On layered triangulations of 3-manifolds: a motivation, a generalisation, and an application

Em K. Thompson

BSc(Hons)

A thesis submitted for the degree of

Doctor of Philosophy

at Monash University in 2024

School of Mathematics

Monash University

Melbourne, Australia

2024

Copyright notice

Abstract

Dehn filling is one of the most important operations in low-dimensional topology. For instance, it allows us to generate *any* (closed, orientable) 3-manifold from an appropriate link complement, and can be used to describe *infinite* families of knots, by adding twists to parallel strands. Meanwhile, one of the most convenient ways to study a 3-manifold is by capturing its topology in a *triangulation*, which can be encoded combinatorially and passed to a computer. In 2006, Jaco and Rubinstein introduced *layered solid tori* as a way to construct **triangulations of Dehn fillings**.

In the first part of this thesis, we study triangulations of 3-manifolds that require the fewest tetrahedra possible. Motivated by the observation that layered solid tori appear frequently within triangulations of the simplest hyperbolic knots, we classify certain families of knots that are related by Dehn filling. In particular, we organise 229 'census knots' into families based on Dehn fillings of the so-called *magic manifold*. The main contribution is the explicit construction of 5 different triangulations of the magic manifold that can be Dehn-filled using layered solid tori to generate minimal triangulations of all 229 of the aforementioned knots. These triangulations are conjectured to extend to minimal triangulations for 42 infinite families of knots related by twisting.

Next, we study Jaco and Rubinstein's *higher-genus layered handlebodies*, which can theoretically be used to construct triangulations with appealing properties such as certain low measures of complexity, and an ability to highlight important topological structures. Unfortunately, the construction of a genus-g layered handlebody is combinatorially challenging, even for $g = 2$. As a result, in the years since their introduction, higher-genus layered handlebodies have received considerably less attention than their genus-1 counterparts. This thesis showcases an algorithm, created in collaboration with He and Morgan, that enables the explicit construction of closely related triangulations using simple combinatorial data as input. By relaxing a single condition in the definition of a layered handlebody, we realise an implementable algorithm to construct explicit triangulations that exhibit the same key measures of complexity and structure-highlighting qualities of Jaco and Rubinstein's triangulations.

Lastly, we demonstrate an application of layered solid tori to a problem in *hyperbolic knot theory*. There is a well-established connection between the *space of deformations* of hyperbolic structures on a knot complement, and the *A-polynomial* of the corresponding knot. In an effort to simplify the notoriously difficult calculation of A-polynomials, Champanerkar (2003) described a way to extract defining equations for the A-polynomial from a triangulation of a knot complement. In 2020, Howie, Mathews and Purcell (HMP) observed that if this triangulation contains a layered solid torus, then the combinatorial structure of the layered solid torus can also be observed in the set of A-polynomial equations. The final contribution of the thesis is a result extending the work of HMP, which harnesses the combinatorics of layered solid tori to further simplify the calculation of A-polynomials for families of knots related by twisting.

Declaration

I hereby declare that this thesis contains no material which has been accepted for the award of any other degree or diploma at any university or equivalent institution and that, to the best of my knowledge and belief, this thesis contains no material previously published or written by another person, except where due reference is made in the text of the thesis.

Em K. Thompson
July 31st, 2024

Publications during enrolment

During my candidature I have had two papers published and another two have been submitted for publication, as detailed below. The inclusion of published and co-authored work in this thesis is as follows.

All figures, including those that appear in co-authored work, are of my own creation.

Chapter 1. This is a background chapter that includes content from the introductory sections of [2] and [3].

Chapter 2. The contents of this chapter will appear in a sole-author manuscript, which is currently in preparation.

Chapter 3. This chapter is based on [3], which is joint work with Alex He and James Morgan. My co-authors and I all made significant contributions to the project and the manuscript, which has been submitted for publication. Much of the introductory content from Sections 1 & 2 in [3], as well as an example that appeared as Appendix A, has been reconfigured to form Section 3.1 of this thesis. Sections 3.2 & 3.3 of this thesis correspond to Sections 3 & 4 of [3], with only minor adjustments. Meanwhile, since I contributed less heavily to Sections 5–7 of [3], that content has been condensed into Section 3.4 of this thesis.

Chapter 4. This chapter is based on my sole-author paper [2], which is published in the *New York Journal of Mathematics* under a CC-BY 4.0 licence. The content from Sections 1 & 2 of [2] has been reconfigured to form Section 4.2 of this thesis. Meanwhile, Sections 4.3 & 4.4 of this thesis correspond to Sections 3 & 4 of [3], with only minor adjustments.

Publications during candidature

[1] Joshua A. Howie, Daniel V. Mathews, Jessica S. Purcell, and **Em K. Thompson**. "A-polynomials of fillings of the Whitehead sister". *International Journal of Mathematics*, 34.13 (2023), Paper No. 2350085.

[2] **Em K. Thompson**. "Twisting, ladder graphs, and A-polynomials". *New York Journal of Mathematics*, 29 (2023), pp. 739–770.

Submitted manuscripts

[3] Alexander He, James Morgan, and **Em K. Thompson**, 2024. "An algorithm to construct one-vertex triangulations of Heegaard splittings". Preprint available at `arXiv:2312.17556`.

[4] Marc Kegel, Arunima Ray, Jonathan Spreer, **Em Thompson**, and Stephan Tillmann, 2024. "On a volume invariant of 3-manifolds". 2024. Preprint available at `arXiv:2402.04839`.

For my younger self.

Acknowledgements

This research was supported by an Australian Government Research Training Program (RTP) Scholarship.

A huge thanks to John Chan and everyone else in the School of Maths at Monash who has helped make it a place that I still haven't left!

Growing up, it never even occurred to me that 'mathematician' was a possible career-path. Every step I have taken down this road has been enabled by the support and encouragement of the people named below.

Of course, the first people to thank are my loving and supportive family, who have always believed in me, and encouraged me to seek fulfilment in all of my pursuits. I am so incredibly grateful. To my mum, my dad, my brother, and my wonderful grandmother – thank you. And a very special happy birthday, Anne.

The first person to actively nudge me in this direction was my Year 12 maths teacher, Anthea. I still remember her excitement for me to encounter completely different types of mathematics at university, including such things as 'geometries in which a line can be parallel to infinitely many others'. I would not be here without her influence.

Even by the time I was finishing my major in pure mathematics, I still didn't recognise that I could *be* a mathematician. If it weren't for Norm Do and Ian Wanless, I would never have considered doing my Honours year. I am extremely appreciative of their ongoing support, as mentors and as friends. I am indebted to Norm, for the countless doors he has opened for me.

To my Honours fam – Will, Ellena, Jenn, Jayden, John, Tim – it was doing maths alongside you that made me want to just keep doing maths.

It was also during Honours that I first got to know Dan and Jessica, and started to envision a world in which I could, perhaps, try my hand at research mathematics. I am incredibly lucky to have worked under two supervisors who are not only brilliant mathematicians, but who are also genuinely kind, honourable, and inspiring humans. Thank you, both, for everything you have done for me, and everything you do for our community.

My day-to-day over the last 4ish years has been heavily shaped by the people 'around' me. My virtual office-mates, Amber, Michael, and Angus, have made me feel connected to my cohort even while working primarily from home. Similarly, the $(GT)^2$ community made me feel more connected to my peers, right around the country, than I could ever have anticipated. To Grace, Alex and James – I'm so glad to call you friends, and I hope we get to keep doing maths together for years to come. Thanks also to Josh, for the various roles you've played – from co-author to conference bud, and everything in between.

A special thank you goes to all the people who've lived with me across the course of this adventure, but most importantly to Winnie, Ebony, and El, who each served a term of being my number-one support person.

Finally, to the people who make me feel utterly blessed – Winnie, Hannah, Marni, Mack, Ellena, Ash, and Will – thank you for being my people. And to El – there just aren't enough words.

Contents

Introduction

This thesis resides in the world of low-dimensional topology. The content relates to triangulations of 3-manifolds, knot theory, and intersections between the two. While we are interested in triangulations of all orientable 3-manifolds, we pay particular attention to triangulations of cusped hyperbolic 3-manifolds. We study triangulations of knot complements both out of interest in the triangulations themselves, but also because they prove to be a powerful tool in characterising certain features of knots. Our focus will be on *layered* triangulations, which we introduce in Chapter 1.

Background

In the meantime, let us begin with some general background. The following landmark result of Wallace [Wal60] and Lickorish [Lic62] serves as motivation for the study of knots and links, and highlights the importance of the operation known as *Dehn filling*.

The Fundamental Theorem of Wallace and Lickorish. Let M be a closed, orientable 3-manifold. Then M is obtained by Dehn filling the exterior of a link in S^3.

Let us take a moment to clarify our use of the key terms in this theorem. We consider a *knot* to be an embedding of S^1 into an ambient 3-manifold M, with equivalence up to ambient isotopy. An *n-component link* is defined similarly as an embedding of n disjoint copies of S^1. We take M to be S^3, unless otherwise specified. The compact manifold $N = M - \nu(L)$, found by removing an open neighbourhood of each component of an n-component link L, is the *exterior of L in M*. In contrast, the *complement of L in M* is the non-compact 3-manifold $\mathring{N} = M - L$. Note that $\mathring{N}$ is homeomorphic to $int(N)$.

Let $[\alpha]$ be an isotopy class of simple closed curves on a torus T, where $\alpha \in \mathbb{Q} \cup \{\infty\}$ is the rational number describing the slope of a geodesic representative of $[\alpha]$. We call α a *slope* on T, and may use 'slope' to refer either to this rational number, or to a curve in the associated isotopy class. When T is a torus boundary component of a manifold M, we may 'fill' T with a solid torus. We say $M(\alpha)$ is the *Dehn filling of M along α* when a solid torus is glued into T so that its meridian is sent to the curve α. In particular, the curve α bounds a disc in $M(\alpha)$, so α is made homotopically trivial by the filling. If M has multiple torus boundary components

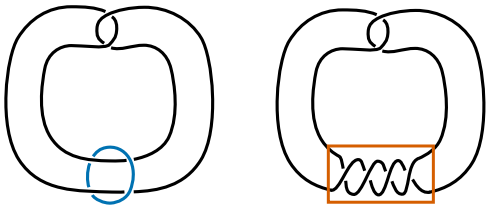

FIGURE 1. The 2-component Whitehead link (left) and the knot obtained by performing a $1/2$ Dehn filling on the blue link component (right). Note that this introduces 2 full negative twists to the 2 parallel strands, which adds 4 negative crossings.

$T_1, \cdots, T_k$, we may Dehn fill distinct boundaries along distinct slopes, in which case we write $M(\alpha_1, \cdots, \alpha_k)$ for the filled manifold.

To reiterate: the Wallace and Lickorish theorem tells us that, for *every* closed, orientable 3-manifold M, there exists some link L, with some number of components k, such that $N = S^3 - \nu(L)$ admits a Dehn filling $N(\alpha_1, \ldots, \alpha_k) = M$. Hence, Dehn filling forms a foundational bridge between the study of knots and links, and the study of 3-manifolds.

Another fundamental result in low-dimensional topology is that 'knots are determined by their complements'.

Theorem. (GORDON–LUECKE, 1989). Suppose K_1 and K_2 are both knots in S^3, with respective exteriors $N_i = S^3 - \nu(K_i)$. Then there is a homeomorphism $f : S^3 \to S^3$ such that $f(K_1) = K_2$ if and only if N_1 and N_2 are themselves homeomorphic. Moreover, if there is an orientation-preserving homeomorphism between N_1 and N_2, then K_1 and K_2 are ambient isotopic.

On the other hand, there may be infinitely many n-component links with homeomorphic complements when $n \geq 2$. This was known to Whitehead [WHI37], who first described the family of *twist knots* via Dehn fillings of the (subsequently named) *Whitehead link* (seen in Figure 1).

This technique of using Dehn filling to add *twists* to a knot diagram can be applied more generally. We consider a *diagram* of a knot in $S^3 = \mathbb{R}^3 \cup \{\infty\}$ to be a projection of the knot onto the xy-plane, with over- and under-crossings indicated by broken arcs. In any portion of a knot diagram where we see p parallel strands, we may 'add twists' as follows. Take a tubular neighbourhood of the knot in S^3 enclosing all p parallel strands; cut along a disc transverse to all strands, then twist (one side of) the cut tube an integer multiple of π times, before regluing so that the strands meet up once again. A rotation of the cut tube by $\pm 2\pi n$ is said to introduce $\pm n$ *full twists*, where the sign is determined by the sign of the crossings added by the twist (for reference, the highlighted crossings in the diagram on the right of Figure 1 are negative). A full twist on p strands results in p over-strands in the knot diagram, creating $p\,(p-1)$ new crossings.

Suppose K is a knot with p parallel strands in a diagram that we wish to add twists to. We may *augment* K by introducing a link component J encircling the p strands. We can realise twists in the diagram of K by performing Dehn fillings on the exterior of $L = K \cup J$. More specifically, by performing a $1/n$ Dehn filling in the torus boundary corresponding to J, we introduce n (negative) full twists to the p strands in the diagram. Given that every full twist adds $p\,(p-1)$ new crossings, this operation is quite 'expensive' in terms of diagram complexity,

as measured by crossing number. However, as we will see in due course, altering a knot in the same way, but from the perspective of Dehn filling its exterior, can be achieved 'relatively cheaply' according to 3-manifold measures of complexity.

This brings us to the question of how to represent and manipulate 3-manifolds, particularly for computational purposes. Our method of choice is, of course, triangulating.

Triangulations of 3-manifolds

In this thesis, we take a *triangulation* to be a decomposition of a manifold into finitely many tetrahedra, with *gluing information* that describes how to affinely identify their triangular faces together in pairs. Some faces may be left unpaired, in which case they form a boundary in the corresponding manifold, with an induced 2-dimensional *boundary triangulation*. Note that the triangulations we work with are sometimes referred to as *generalised* triangulations.[1] This emphasises the fact that we allow our tetrahedra to be flexible, enabling twisting and stretching so that, for example, two faces of the same tetrahedron may glue together. In particular, it is rare for our triangulations to satisfy the (more rigid) conditions required to be a simplicial complex.

One of the operations allowed in our flexible notion of a triangulation is *layering*, which, unsurprisingly, will feature heavily in subsequent chapters.

Definition. (Layering). Given a triangulation with boundary, we may *layer over* a boundary edge $\boldsymbol{e}$ by attaching a tetrahedron to the two faces adjacent to $\boldsymbol{e}$. This is done in the natural way, without twisting or otherwise manipulating the new tetrahedron (see Figure 2).

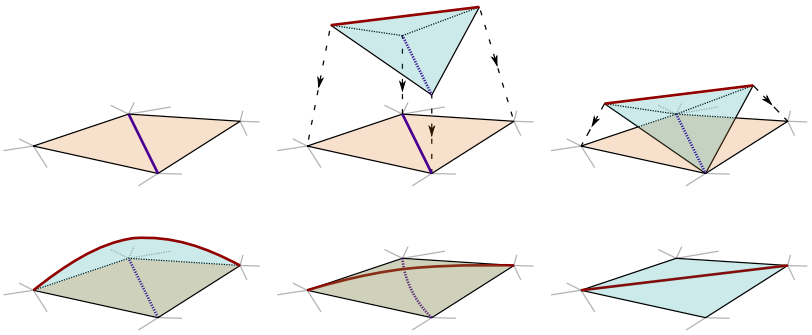

Figure 2. *Layering over a boundary edge.* The blue tetrahedron is glued to the orange boundary faces in such a way that the purple edge is covered and the red edge is introduced as an edge in the new boundary triangulation. The change from the purple edge to the red edge is called a *flip* in the boundary triangulation.

Note that layering is topologically equivalent to attaching a ball, so the underlying 3-manifold is unchanged. However, the induced boundary triangulation is adjusted by *flipping* the edge $\boldsymbol{e}$.

For another example of an operation we allow, again consider a quadrilateral formed by two distinct boundary faces that share an edge $\boldsymbol{e}$. We call $\boldsymbol{e}$ the *diagonal* of this quadrilateral, and we call the other diagonal (which is not a boundary edge) the *off-diagonal* of the quadrilateral.

Definition. (Folding). We may *fold across* the diagonal $\boldsymbol{e}$ to identify the two faces that form the quadrilateral. If γ is the off-diagonal of this quadrilateral, we may also say that we *fold along* γ. See Figure 3.

[1] Indeed, there are many names for triangulations that are not simplicial complexes – *pseudo*-triangulations, *singular* triangulations, *loose* triangulations, *topological* triangulations, *semi-simplicial* triangulations...

When the endpoints of γ are at distinct vertices in the triangulation, folding is equivalent to a *book closing move*. When both endpoints of γ are identified to the same vertex, the fold causes γ to become homotopically trivial as a loop.

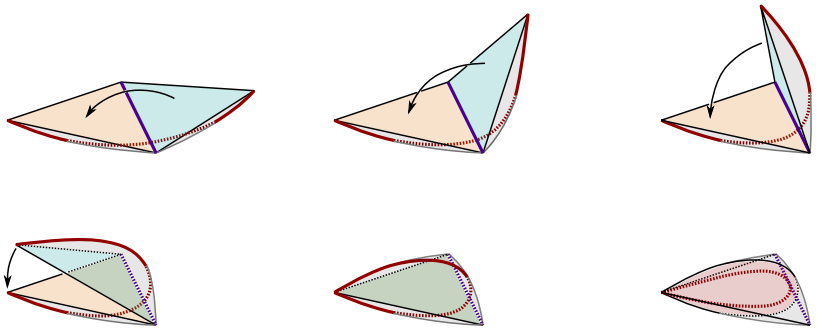

FIGURE 3. *Folding across an edge.* Folding across the purple edge identifies the blue face with the orange face. The red curve in the interior of the manifold is folded back on itself and becomes homotopically trivial. This action may also be described as folding *along* the red curve.

Folding reduces the number of boundary faces by two and, in contrast to layering, *can* change the topology of the triangulation. Indeed, a single fold not only has the potential to change the underlying 3-manifold, but it may also cause a triangulation to become *invalid*.

To understand when triangulations are *valid*, we consider local gluing behaviour around individual vertices. The *link of a vertex* v is the surface S formed by the truncated tips of tetrahedra meeting v. If the link of v is a disc, then v is assumed to be a *boundary vertex* in a triangulation of a 3-manifold with boundary. Note that discs are the *only* bounded surfaces that may occur – if a surface with multiple boundary components or a bounded surface of higher genus arises as a link of any vertex, then the triangulation is considered *invalid*.[2] This is precisely what can go wrong when performing a fold. Thankfully, it is often possible to reinstate the validity of a vertex by performing additional, carefully chosen folds. For a triangulation *without boundary* to be valid, the link of every vertex v must be a closed surface S. If S is a sphere, we say v is a *material vertex*, and if S has genus $g \geq 1$, we say v is an *ideal vertex*.

While it is sometimes convenient to allow a combination of material and ideal vertices in a single triangulation, we follow the common convention of assuming that the vertices in a given triangulation $\mathcal{T}$ are either all material or all ideal. If all vertices are material, then $\mathcal{T}$ is a triangulation of a closed 3-manifold. If all vertices are ideal, there are two interpretations: either $\mathcal{T}$ is a closed triangulation of a *pseudo-manifold*; or, we *remove* the ideal vertices, and say $\mathcal{T}$ is an *ideal triangulation* of a non-compact 3-manifold. The latter interpretation is how we think about triangulations of knot and link complements. In particular, the 'removal' of ideal vertices from a triangulation corresponds precisely to the 'removal' of the 1-dimensional knot or link from S^3.

In this thesis, we encounter triangulations of compact manifolds both with and without boundary, and in the case of ideal triangulations, we restrict our attention to non-compact manifolds whose vertex links are all tori.

[2] A triangulation may also fail to be valid if it contains an edge that is identified to itself in reverse. We will always assume that this situation is avoided.

A NOTE ON SPINES. Another way to represent 3-manifolds combinatorially is to use *spines*. Indeed, many results regarding 3-manifolds were first proved using spines, and in some cases these proofs are arguably more elegant than an analogous argument using triangulations. We will not discuss spines in any particular detail, and instead refer to Matveev's textbook [MAT07] for most omissions. It is important to us, however, that there is a subset of *special* spines, which are dual to triangulations. A nice discussion of this duality, aligned with the language of this thesis, is given in [RST19]. Apart from S^3, $\mathbb{RP}^3$ and $L(3,1)$, which are considered to be exceptional cases, it is reasonable for us to treat special spines and triangulations as dual versions of the same object, as justified by the following:

- One-vertex triangulations of a closed 3-manifold M are in one-to-one correspondence with the special spines of M [MAT07, Corollary 1.1.27].
- If $\mathring{M}$ is the interior of a 3-manifold with at least one boundary component, all of which are tori, then the ideal triangulations of $\mathring{M}$ are in one-to-one correspondence with the special spines of M [MAT07, Corollary 1.1.28].

A related object that we will encounter is the *dual graph* of a triangulation. In a dual graph, each tetrahedron is represented by a node, and two nodes are connected by an arc whenever a face of one tetrahedron is glued to a face of another. As such, it is sometimes referred to as the *face pairing graph*. Note that the flexibility we allow in our triangulations often leads to parallel arcs and self-loops in the dual graph. For a closed triangulation, every node in its dual graph is 4-valent.

BACK TO TRIANGULATIONS. The ubiquity of triangulations in 3-manifold topology stems from the following celebrated fact.

Theorem. (MOISE, 1952). Every 3-manifold admits a triangulation.

For Moise, this meant that every *closed* 3-manifold admits a *simplicial* triangulation. Later, both Moise [MOI54] and Bing [BIN54] extended this result to include compact 3-manifolds with boundary. Meanwhile, parallel progress by Casler [CAS65] on special spines implied that the interior of any bounded 3-manifold admits an ideal triangulation.

Another important research direction at this time was to determine the existence and nature of relationships between distinct triangulations of the same 3-manifold. As it turns out, one triangulation may be transformed into another by a sequence of local moves on tetrahedra. These operations were popularised by Pachner, and as such, are often referred to as the *Pachner moves*. To be more specific, there are four moves that we label A-B to indicate that A tetrahedra are replaced by B tetrahedra. The *1-4 move* introduces a vertex and subdivides a single tetrahedron into four. The *2-3 move* replaces two tetrahedra that meet in a single face with three tetrahedra that share a single edge transverse to the original shared face. The *4-1 and 3-2 moves* are the respective inverses to *1-4* and *2-3* moves. Pachner's work [PAC91] showed that the set of all triangulations of a closed 3-manifold M is connected under these four moves.

Later, using analogous moves in the context of special spines, Matveev [MAT87] and Piergallini [PIE88] showed that the set of all triangulations of a closed 3-manifold with exactly one material vertex (and at least two tetrahedra) is connected under only *2-3* and *3-2* moves. Indeed, the same is true for triangulations of closed 3-manifolds with *any* fixed number of material vertices [see BP95; BP97].

Recall that we may interpret a triangulation containing vertex links of genus $g \geq 1$ as a closed triangulation of a pseudo-manifold (rather than a non-compact ideal triangulation). Amendola [Ame05] proved the following unifying theorem in 2005, again using the technology of special spines.

Theorem. (Amendola, 2005). If M is either a closed 3-manifold or a 3-dimensional pseudo-manifold, the set of triangulations of M with a fixed number (possibly zero) of material vertices (and at least two tetrahedra) is connected under *2-3* and *3-2* moves.

Notation for triangulations

When describing explicit triangulations, we adopt the conventions of Regina. Tetrahedra are labelled 0 through N, and the vertices (material or ideal) of each tetrahedron are labelled 0, 1, 2, 3. A priori, the ordering of vertex labels need not be consistent between different tetrahedra, but we will always choose to ensure consistency by 'orienting' our triangulations. More specifically, we set the convention that, when viewing a tetrahedron from the outside, if the vertex labelled 0 is closest to us, the remaining vertex labels 1, 2, 3 appear in anti-clockwise order.

A face-pairing is described using Regina notation in the format $0(123) \sim 1(032)$, which here means that the face of tetrahedron 0 with vertices 1, 2, 3, is glued to the face of tetrahedron 1 with vertices 0, 3, 2, in that order. For more detail on conventions used by Regina, we defer to [Bur13].

Cusped hyperbolic 3-manifolds

Most of the non-compact manifolds we encounter will be *finite volume, cusped hyperbolic 3-manifolds*. A manifold is considered *hyperbolic* if it can be endowed with a metric of constant curvature -1. A hyperbolic 3-manifold M has *finite volume* if and only if it is either closed or is the interior of a compact manifold $\overline{M}$ with torus boundary components. If B is a torus boundary component in $\overline{M}$ and M admits a hyperbolic metric, then we say that the neighbourhood $T^2 \times [0, \infty) \subset M$ corresponding to $B \subset \overline{M}$ is a *cusp neighbourhood*.

This characterisation means that any knot or link complement that admits a hyperbolic structure has finite hyperbolic volume. Remarkably, Thurston [Thu82] showed that 'most' knots are hyperbolic.

Theorem. (Thurston, 1982). A knot K in S^3 is either a *torus knot*,[3] a *satellite knot*,[4] or its complement $S^3 - K$ is a cusped hyperbolic 3-manifold.

Indeed, hyperbolic knots really do account for the *vast majority* of knots, at least among those with up to 19 crossings.

Theorem. (Burton, 2020). There are 352 152 252 knots admitting a diagram with up to 19 crossings. Amongst these, 14 are torus knots, 380 are satellite knots, and the remaining 352 151 858 are hyperbolic.

Our interactions with hyperbolic geometry will primarily take place in the *upper half space model* of hyperbolic 3-space, $\mathbb{H}^3$. In this model,

$$\mathbb{H}^3 = \{(x + iy, t) \in \mathbb{C} \times \mathbb{R} \,|\, t > 0\}$$

[3] A (p, q)-torus knot is ambient-isotopic to a geodesic on the torus with slope p/q.
[4] A satellite knot is ambient-isotopic to an embedding of S^1 into a solid torus, which is itself also knotted.

with a metric given by the first fundamental form

$$ds^2 = \frac{dx^2 + dy^2 + dt^2}{t^2}.$$

Effectively, under this metric, Euclidean distances are scaled by $1/t$. As a consequence, the entire complex plane at $t = 0$ is *at infinity*. Upper half space also includes the *point at infinity*, and together, $\mathbb{C} \cup \{\infty\}$ is referred to as *the boundary at infinity*. The $1/t$ scaling also means that for each value of $t > 0$, we have a genuine Euclidean plane, which we call a *horosphere* (it is a sphere centred at ∞ that looks like a horizontal plane). In this model of $\mathbb{H}^3$, geodesics are either vertical lines or (segments of) semi-circles that meet $\mathbb{C}$ orthogonally. Hence, totally geodesic planes are either vertical (Euclidean) planes, or hemispheres meeting $\mathbb{C}$ orthogonally.

We will make sense of the hyperbolic structure on a manifold M by embedding an ideal triangulation of M into $\mathbb{H}^3$. To embed an individual ideal tetrahedron into this space, we send the ideal vertices to the boundary at infinity. Possible embeddings take one of the two forms shown in Figure 4.

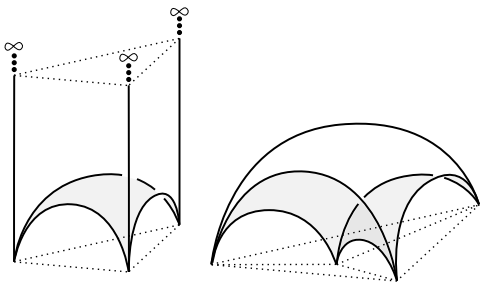

FIGURE 4. The two ways an ideal tetrahedron may appear when embedded in the upper half space model of hyperbolic 3-space.

In Chapter 4, we will see how to use the combinatorics of a triangulation to understand hyperbolic structures on a manifold.

TWISTED TORUS KNOTS

While torus knots themselves are never hyperbolic, there exist many 'almost'-torus knots that are. By adding twists to a subset of parallel strands in a torus knot, we may create a *twisted torus knot*. Most of the knots we encounter in this thesis will be twisted torus knots, although occasionally we will want the flexibility of a *generalised* version. The distinction is that a *true* twisted torus knot only ever adds full twists, whereas a *generalised* twisted torus knot also allows 'partial twists'. To describe these more effectively, let us borrow from the language of braids.

For a braid on p (vertical) strands, we label strands 1 through p from left to right, and use a tuple of integers to encode crossings between adjacent strands in order, as they occur from top to bottom. More specifically, we use n to indicate a positive crossing with the $(n+1)^{st}$ strand crossing over the n^{th} strand, and $-n$ to indicate the respective negative crossing. Note that we use this non-standard version of a 'braid word' to align with the conventions used by SNAPPY [see SNAPCO]. To compress k repeats of the same sequence, we adopt the shorthand $\big[\,(a, \cdots, b)^k\,\big] = \big[\,a, \cdots, b, \cdots^{(k-2 \text{ copies})} \cdots, a, \cdots, b\,\big]$.

Suppose we begin with a (p, q)-torus knot, which we describe as the closure of the braid $[(p-1, p-2, \cdots, 2, 1)^q]$. For a true twisted torus knot, we take the r right-most strands and

introduce a full twists. In our braid notation, this is encoded by

$$\big[\,(p-1,p-2,\cdots,2,1)^q,(p-1,p-2,\cdots,p-r+2,p-r+1)^{ra}\,\big].$$

The generalisation that we adopt realises partial twists by allowing the exponent for the r strands to be any integer $s \neq 0$, indicating s over-strands, with positive or negative slope depending on the sign of s. In particular, when r divides s, the presentation is a true twisted torus knot.

Definition. (Twisted torus knot). Let $0 < r < p$ be positive integers and let q, s be any non-zero integers, provided $\gcd(p,q) = 1$. Then the *(generalised) twisted torus knot* $T(p,q,r,s)$ is the closure of the braid encoded by

$$\big[\,(p-1,p-2,\cdots,2,1)^q,(p-1,p-2,\cdots,p-r+2,p-r+1)^{s}\,\big].$$

From now on, assume all twisted torus knots are in the generalised form, so that the final parameter represents a number of over-strands rather than a number of full twists.

Thesis outline

We dedicate Chapter 1 to introducing the core theme of *layered triangulations*. This includes the definition of an arbitrary-genus *layered handlebody*, with extra attention given to the construction of a genus-1 *layered solid torus*. In Chapter 2, we **motivate** the study of layered solid tori by studying their prevalence among *minimal triangulations*. In Chapter 3, we focus on higher-genus layered handlebodies and **generalise** the construction, resulting in a more practical combinatorial description. Chapter 4 marks a shift in focus away from triangulations themselves, and towards a problem in hyperbolic knot theory where we can **apply** the combinatorial structure of layered solid tori to simplify certain algebraic calculations.

My main contributions are as follows:

- In Chapter 2, I organise 229 hyperbolic census knots into families related by twisting, and describe explicit triangulations for each family, employing layered solid tori to realise each knot as a Dehn filling of the so-called *magic manifold*.
- In Chapter 3, which is joint work with Alex He and James Morgan, I outline an implementable algorithm that enables the explicit construction of layered-type triangulations involving handlebodies of genus $g \geq 1$.
- In Chapter 4, I harness cluster-algebraic structure that arises through the combinatorics of layered solid tori to simplify the (notoriously difficult) calculation of A-polynomials for families of knots related by twisting.

Let us begin!

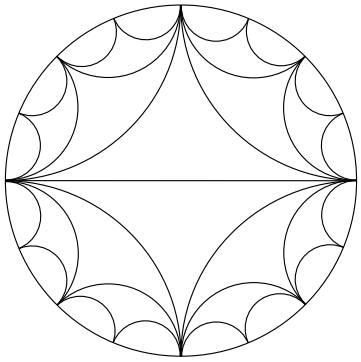

Chapter 1. An overview

Layered triangulations of 3-manifolds

Layered triangulations of 3-manifolds were introduced by Jaco and Rubinstein [JR06] in 2006. The primary focus of their paper was on the construction and classification of *layered solid tori*, including a classification of all normal and almost normal surfaces contained within them. They also described the construction of layered handlebodies with genus $g > 1$, but these were left largely uninvestigated because the construction suffers from combinatorial explosion as genus increases.

SECTION 1.1. *Defining layered handlebodies*

Let us begin by describing the construction of a *layered handlebody*, as given in [JR06, pp. 82–85]. The starting piece of a layered handlebody is a compact surface with one boundary component and Euler characteristic $1 - g$, equipped with a fixed choice of one-vertex triangulation. Jaco and Rubinstein call this a *g-spine*. The first example, when $g = 1$, is the one-triangle Möbius band, which has one vertex and two edges; one edge is interior to the surface and one forms the boundary (see Figure 1.1, left). Notice that, when g is even, the g-spine may be either orientable or non-orientable, but when g is odd, it is necessarily non-orientable. When $g > 1$, many distinct g-spines exist. For example, when considering one-vertex triangulations up to isomorphism, there is one orientable 2-spine (the once-punctured torus, Figure 1.1 centre-left) and four non-orientable 2-spines (the once-punctured Klein bottle equipped with four distinct triangulations, Figure 1.1 centre-right). Jaco and Rubinstein [JR06, p.84] consider the g-spine of a layered handlebody to be the $(-1)^{st}$ *layer*, and label it $\mathscr{T}_{-1}$. In appropriate contexts, a g-spine may also be considered a *degenerate layered handlebody*.

Recall that a non-orientable surface with Euler characteristic $2 - g$ may be realised as the connected sum of g projective planes, which can in turn be represented by a $2g$-gon with g non-orientable edge-pairings. Adding an edge for the boundary component increases the Euler characteristic to $1 - g$, and adds a side to the $2g$-gon. Since any one-vertex triangulation of a $(2g + 1)$-gon requires $2g - 2$ interior (to the polygon) edges, a g-spine contains $3g - 2$ interior (to the surface) edges. Of course, the same is true for orientable g-spines.

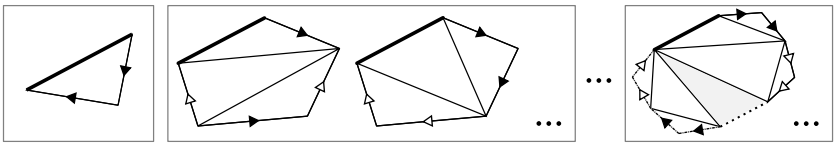

Figure 1.1. The only 1-spine is the one-triangle Möbius band (left). There are five different 2-spines [JR06, p. 84]. Here (centre) we see the unique orientable 2-spine, and one of the four non-orientable 2-spines. On the right is an example of a non-orientable g-spine for arbitrary $g > 4$.

By an Euler characteristic argument [JR06, pp. 82–84], Jaco and Rubinstein show that, at minimum, $3g-2$ tetrahedra are required to build a (not necessarily layered) genus-g handlebody with a one-vertex boundary triangulation. Moreover, they show that by using $3g-2$ tetrahedra to cover each interior edge of a g-spine, the result is guaranteed to be a valid triangulation of a genus-g handlebody, which they define to be a *minimal layered handlebody of genus-g*. To avoid confusion with other notions of a minimal triangulation, let us call this a *basic layered handlebody of genus-g*. A $(3g-2)$-tetrahedron basic layered handlebody is considered to be the 0^{th} *layer* of any layered handlebody, with label $\mathscr{T}_0$.

Finally, for $t \geq 1$, a layered handlebody $\mathscr{T}_t$ of genus-g, with t layers, is defined inductively, adding one tetrahedron at a time, by layering over a boundary edge of $\mathscr{T}_{t-1}$.

We subsequently refer to this as the *JR-construction*. We use the term *layered solid torus* when the focus is specifically on genus-1 layered handlebodies.

Definition 1.1. (Layered triangulation). A *layered triangulation* of a closed, orientable 3-manifold is a one-vertex triangulation consisting of two genus-g layered handlebodies, glued together along a common genus-g surface with an induced one-vertex triangulation.

Remark 1.2. The term 'layered triangulation' also appears in the literature to describe other triangulations that exhibit layering behaviour, most notably in the context of *mapping tori of pseudo-Anosov maps*. In this thesis, the term will be used exclusively in the sense of Definition 1.1.

Section 1.2. *Jaco and Rubinstein's results*

When $g = 1$, a g-spine has one interior edge, so a basic layered solid torus consists of a single tetrahedron, and hence there is only one way to build $\mathscr{T}_0$. For subsequent layers, there are three choices of boundary edge to layer over, and in practice, only two of these are reasonable options, since layering over the most recently introduced edge makes both layers redundant.

In contrast, when $g = 2$, we are flooded with choice at every turn. This begins immediately, when we are forced to choose one of five different g-spines for $\mathscr{T}_{-1}$. Having chosen one, we must then choose how to layer four tetrahedra onto the four interior edges to build $\mathscr{T}_0$, and different choices of ordering can lead to non-isomorphic triangulations. Then, since there are nine edges in the one-vertex triangulation of the genus-2 boundary, we have nine options *for every layer*, as to which edge we layer over.

In light of this, it is no surprise that the most concrete findings of [JR06] are in the genus-1 setting. The main results pertain to the classification of all connected normal and almost normal surfaces in layered solid tori, and layered triangulations of lens spaces. Jaco and Rubinstein demonstrate the power of their combinatorial construction by recovering a number of known

results, using relatively straightforward arguments, including the classification of lens spaces containing embedded non-orientable surfaces.

Perhaps the most important contribution of the paper is the method for triangulating Dehn fillings using layered solid tori, which we describe carefully in the following section, and use repeatedly throughout the thesis.

Interestingly, despite Jaco and Rubinstein's optimism that their higher-genus construction would, "give exciting new ways to study 3-manifolds via Heegaard splittings," very little research to this effect has emerged in the (nearly) two intervening decades. Our discussion of higher-genus layered triangulations resumes in Chapter 3.

SECTION 1.3. *Using layered solid tori to Dehn fill*

Recall that a (topological) Dehn filling is performed by gluing a solid torus along a torus boundary component of a parent manifold. There are infinitely many ways to do this, depending on the slope of the image of the meridian. Jaco and Rubinstein [JR06] form a triangulated Dehn filling by gluing in a layered solid torus, constructed so that its meridian intersects its boundary triangulation in such a way that it is compatible with the boundary triangulation of the parent manifold. Moreover, they outline a way to use the Euclidean algorithm to construct such a layered solid torus for any choice of meridian slope.

1.3.1. Building from the outside inwards

In Jaco and Rubinstein's approach to Dehn filling, the layered solid torus is built up as normal: from the innermost layer, outwards. It turns out to be somewhat more intuitive to 'reverse' this process, and build the layered portion directly onto the boundary of the parent, before forming the Möbius spine by gluing together the exposed faces.

As long as the torus boundary we wish to fill has a one-vertex triangulation, then tetrahedra can be layered on, one-by-one, adjusting the boundary triangulation by a sequence of flips (recall Figure 2), all while leaving the topology of the manifold unchanged. These adjustments to the boundary triangulation change the slopes of the boundary edges, which are well-defined with respect to the framing of the boundary torus. Eventually, once the boundary triangulation consists of edges with appropriate slopes, the two exposed faces can be glued together by folding across an edge, thus forming the Möbius spine.

The 'appropriate slopes' for the boundary edges are dictated by the slopes of the original boundary edges, and the slope of the desired Dehn filling. To describe these more explicitly, we use the language of *the Farey graph*.

1.3.2. The Farey graph

The *Farey sequence of order* n is the list of rational numbers a/n, expressed in their reduced form. Two rational numbers are considered *Farey neighbours* if they appear consecutively in the Farey sequence, for some order n. It turns out that a/b and c/d are Farey neighbours if and only if $|ad - bc| = 1$. Note that one interpretation of the number $|ad - bc|$ is as the intersection number of the geodesics on a torus with slopes a/b and c/d.

The *Farey triangulation* is a triangulation of the hyperbolic plane, where edges are geodesics connecting pairs of Farey neighbours (see Figure 1.2). A face is therefore determined by three

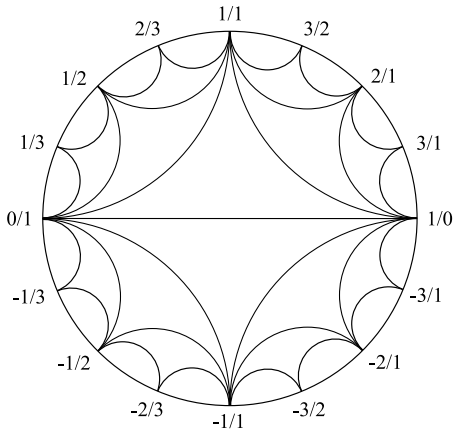

Figure 1.2. The Farey triangulation of $\mathbb{H}^2$ using the Poincaré disk model.

rational numbers with pairwise intersection number 1. Another feature to note is that the sets of rational numbers describing two adjacent Farey triangles differ by exactly one element.

Remark 1.3. While the figures in this thesis depict the Farey triangulation as a triangulation of the Poincaré disc, we make use of graph-theoretic language to avoid confusion and over-use of triangulation terminology. In particular, we appropriate the terminology of the dual *Farey graph*, where each triple of rational numbers with pairwise intersection 1 corresponds to a *node*, and adjacent nodes are connected by *arcs*.

Observe that one-vertex triangulations of the torus are in one-to-one correspondence with triples of slopes with pairwise intersection 1. Moreover, two triples of slopes that differ by only one entry correspond to two triangulations that are related by a flip. As such, the Farey graph is the *flip-graph* for one-vertex triangulations of the torus.

Since layering induces flips in the boundary triangulation, we can encode a sequence of layers in a layered solid torus by a walk in the Farey graph. Note that Jaco and Rubinstein did something similar, using what they called the *L-graph*.

Indeed, the folding of a layered solid torus can also be represented in the Farey graph. Suppose the slopes of three edges in a boundary triangulation are a/b, c/d and e/f. By folding across the edge with slope a/b, and thus identifying the other two edges, the curve with slope $\frac{c+e}{d+f}$ (which is not an edge in the boundary triangulation) is folded back on itself and becomes homotopically trivial. This is the slope that determines the Dehn filling.

1.3.3. Encoding the construction of a layered solid torus

We can now describe a triangulated Dehn filling of any slope in any one-vertex torus boundary.

1. Identify the slopes of the three boundary edges on the boundary of the parent and label the corresponding node in the Farey graph T_0.
2. Identify the closest node containing the target Dehn filling slope, and the unique shortest path between this node and T_0.
3. Label all nodes on this path sequentially from T_0 through to T_{N+1}. Call the arc from T_k to T_{k+1} the k^{th} *step*, and use o_k (for 'old') to refer to the slope that is in T_k but not T_{k+1}.
4. Use steps 0 through to $N-1$ as instructions for how to layer the k^{th} tetrahedron onto the boundary, by covering the edge that has slope o_k.

5. Use the N^{th} step to realise the Möbius spine, by *folding across* the edge with slope o_k.

While the 0^{th} step may go to any of the three nodes adjacent to T_0, each subsequent step has a choice of only two directions, since it never makes sense to go back the way we came. With the Farey graph embedded in the Poincaré disc, it is natural to describe the path from T_0 to T_{N+1} as a sequence of left and right steps. Hence, with the initial information of T_0 and T_1, we can encode the construction of a layered solid torus using a word in L's and R's.

1.3.4. Dehn fillings in ideal triangulations

The preceding discussion focused on the Dehn filling of a torus boundary component in a compact 3-manifold. A layered solid torus can be built from ideal tetrahedra in exactly the same way, and only minor adjustments are required to make sense of a triangulated Dehn filling in a cusped 3-manifold.

Definition 1.4. (Standard cusp). In an ideal triangulation of a manifold with torus cusps, if only two ideal tetrahedra meet a cusp $\mathfrak{c}$, at one ideal vertex each, $\mathfrak{c}$ is called a *standard cusp*.

In Regina notation, the gluing of the two tetrahedra in a standard cusp is (up to relabelling) $0(012) \sim 1(021)$, $0(013) \sim 1(031)$, $0(023) \sim 1(032)$. With this labelling, the cusp $\mathfrak{c}$ is located at ideal vertices $0(0)$ and $1(0)$, and the faces $0(123)$ and $1(123)$ form a once-punctured torus where tetrahedra 0 and 1 are connected to the rest of the triangulation (see Figure 1.3, left).

Provided we start with a triangulation in which $\mathfrak{c}$ is a standard cusp, a Dehn filling of $\mathfrak{c}$ can be triangulated using an ideal layered solid torus. To perform this filling, we must first *remove* the two tetrahedra of the standard cusp (as in Figure 1.3), leaving a once-punctured torus boundary. We can then build the ideal layered solid torus by layering onto this boundary, exactly as we did in the compact case.

Howie, Mathews, and Purcell [HMP20] showed that this requirement is not *too* restrictive, particularly if we are happy to leave at least one cusp unfilled.

Proposition 1.5. (Howie–Mathews–Purcell, Proposition 5.1). If a compact manifold $\overline{M}$ with n_c torus boundary components admits a triangulation with one vertex in each boundary (and no other vertices), then the non-compact interior M admits an ideal triangulation in which any $n_c - 1$ of the cusps can be arranged to be standard cusps.

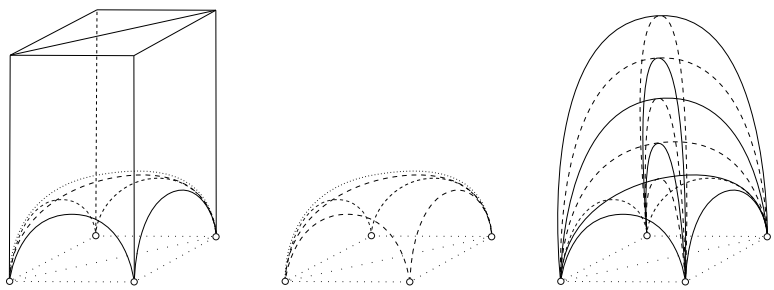

Figure 1.3. Left: A standard cusp, with one ideal vertex from each tetrahedron sent to the point at infinity. Centre: Removing the standard cusp leaves a once-punctured torus boundary. Right: Ideal tetrahedra can be layered directly onto this boundary to form an ideal layered solid torus (note that the layering shown is unrealistic, since the corresponding path in the Farey graph moves back and forth between 2 nodes).

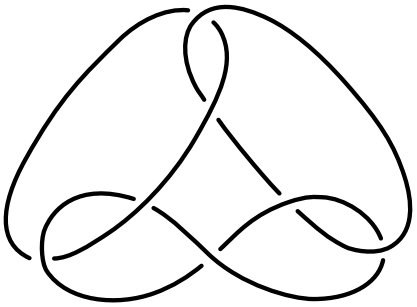

Chapter 2. A motivation

Layered solid tori in minimal triangulations

One compelling reason for studying layered solid tori is their prevalence amongst *minimal triangulations*. In this chapter we delve into the highly studied field of *triangulation complexity*, as measured by number of tetrahedra. We begin in Section 2.1 with a survey of known results, before meeting the so-called *magic manifold* in Section 2.2. In Section 2.3, we use Dehn fillings of the magic manifold to organise low-complexity hyperbolic knots into families that can be extended indefinitely. The main result is presented in Section 2.4, where we describe explicit triangulations of these knot complements, using layered solid tori to Dehn fill. The triangulations are verified to be minimal whenever the knot is simple enough to be recognised, and I conjecture that they extend to minimal triangulations of all knots in each infinite family.

SECTION 2.1. *Minimal triangulations*

Definition 2.1. A triangulation of a 3-manifold M is considered *minimal* if there is no triangulation of the same 3-manifold consisting of fewer tetrahedra. This minimum number of tetrahedra is the *complexity* $c(M)$.

Triangulations are an effective way to represent 3-manifolds for computational purposes, but many 3-manifold algorithms have running times that grow exponentially as the number of tetrahedra increases [HS19]. This alone is sufficient motivation to invest in our understanding of triangulation complexity, but perhaps the more tantalising reason is that, in general, verifying minimality is difficult! For example, the following conjecture [JR06, Conjecture 9.5] remains largely unresolved.

Conjecture 2.2. (Jaco–Rubinstein, 2006). For a genus-g handlebody V with a given one-vertex boundary triangulation τ, a layered triangulation of V corresponding to the shortest path in the flip graph is minimal amongst all triangulations of V with boundary triangulation τ.

In the following, the notation $\{a, b, c\}$ is used to describe the placement of edges in a one-vertex boundary triangulation of a solid torus, with entries representing the number of times the meridian of the solid torus intersects each boundary edge. The following result of Jaco,

Rubinstein, and Tillmann [JRT09] is a corollary to a theorem of theirs regarding minimal triangulations of lens spaces.

Corollary 2.3. (Jaco–Rubinstein–Tillmann, 2009). For the solid torus V with one-vertex boundary triangulation $\tau = \{k+2, k+1, 1\}$, $k \geq 1$, the layered triangulation corresponding to the unique shortest path in the Farey graph is the unique minimal triangulation of V with boundary triangulation τ.

Note that the walk in the Farey graph corresponding to this layered solid torus can be described by a word consisting entirely of either L's or R's. This is, as far as I know, the current extent of the progress towards resolving Conjecture 2.2.

In the remainder of this section we will focus on existing results about minimal triangulations, with a particular emphasis on orientable, cusped hyperbolic 3-manifolds. We first consider low-complexity manifolds found by exhaustive enumeration, followed by more general results regarding the complexity of infinite families of 3-manifolds.

Remark 2.4. Much of what is known about the complexity of 3-manifolds is from the perspective of *Matveev complexity*. This measure of complexity, defined by Matveev [Mat88], counts the number of vertices in a special spine, which corresponds to the number of tetrahedra in a dual triangulation (except in the cases of S^3, $\mathbb{RP}^3$ and $L(3,1)$, which have Matveev complexity 0). For our purposes, there is little need to distinguish the two, so we use both notions of complexity interchangeably.

2.1.1. Exhaustive enumeration

Some of the earliest enumeration of low-complexity 3-manifolds goes back to work of Matveev and Savvateev [MS74] in the 1970s, including the classification of the 61 closed, orientable 3-manifolds with complexity up to 5. This work was built upon by many, not only in the context of closed manifolds [e.g. Mat88; MPe01; Mar10], but also for cusped manifolds [e.g. MF88], and later for manifolds with totally geodesic boundary [FMP03]. Matveev and Tarkaev [MT05] developed the computer program Manifold Recognizer for studying 3-manifolds via spines. The associated website currently hosts a list of the closed orientable prime 3-manifolds up to complexity 12.

Meanwhile, in 1989, Hildebrand and Weeks [HiW89] created a census of cusped, hyperbolic 3-manifolds built from up to 5 ideal tetrahedra, marking the conception of the SnapPea census. This census of cusped, finite-volume hyperbolic 3-manifolds (both orientable and non-orientable) was built upon by Callahan, Hildebrand, and Weeks [CHW99] to include manifolds built by 6 and 7 ideal tetrahedra, then by Thistlethwaite [Thi10], who extended the census to 8 ideal tetrahedra.

It was only later that the SnapPea cusped census (still up to 8 ideal tetrahedra at the time) was verified to contain *only* hyperbolic triangulations by Moser [Mos09], then Hoffman, Ichihara, Kashiwagi, Masai, Oishi, and Takayasu [HIK+16], and only later again when it was verified to contain *all* hyperbolic triangulations by Burton [Bur14]. Indeed, it was at this time that Burton not only extended the SnapPea cusped census to manifolds built from 9 ideal tetrahedra, but also identified *every* minimal triangulation (geometric and otherwise) of every cusped hyperbolic manifold of complexity up to 9. This (and other) exhaustive triangulation data is available through Regina.

Table 2.1. Summary of census knots by complexity. The number of one-cusped hyperbolic manifolds of the same complexity is provided for reference, and the minimum and maximum volumes of knots of each complexity are included for the sake of interest.

T	All 1-cusped	Knots in S^3	Min. vol(KT_v)	Max. vol(KT_v)
2	2	1	2.029883	2.029883
3	9	2	2.828122	2.828122
4	52	4	3.163963	3.608689
5	223	22	3.417915	4.851171
6	913	43	3.526196	5.693021
7	3388	129	3.573883	6.922634
8	12 241	301	3.600467	7.766012
9	42 279	765	3.616793	8.882564

Another approach to enumeration was taken by Fominykh, Garoufalidis, Goerner, Tarkaev, and Vesnin [FGG+16] who classified all cusped, orientable hyperbolic 3-manifolds that can be built from up to 25 *regular* ideal tetrahedra, as well as all cusped, non-orientable hyperbolic 3-manifolds built from up to 21 regular tetrahedra. These are guaranteed to be minimal triangulations by a volume argument of Thurston [Thur, Corollary 6.1.7].

In the current version of SnapPy (v3.1.1), one can access all orientable cusped hyperbolic manifolds up to complexity 9 and all non-orientable cusped hyperbolic manifolds up to complexity 7. SnapPy also hosts a census of closed hyperbolic manifolds built from up to 7 tetrahedra [as tabulated by HoW94] containing 17 non-orientable, and 11 031 orientable manifolds.

Hyperbolic knots in the 3-sphere. With growing censuses generating a rapid increase in available triangulation data, it is natural to narrow one's attention to certain subcategories of manifolds. In this thesis, we focus on the subcategory of orientable, cusped hyperbolic 3-manifolds that can be realised as the complement of a knot in S^3. A specific census for these manifolds was established in 1999 by Callahan, Dean, and Weeks [CDW99], beginning with all knot complements built from up to 6 ideal tetrahedra. This was extended to 7 ideal tetrahedra by Champanerkar, Kofman, and Patterson [CKP04], then to 8 ideal tetrahedra by Champanerkar, Kofman, and Mullen [CKM14]. When Dunfield [Dun20] classified all exceptional fillings of all manifolds in the 9-tetrahedron SnapPea (orientable, cusped) census, the identification of the 9-tetrahedron knots was a pleasant side-effect.

We will refer to the hyperbolic knots built from up to 9 ideal tetrahedra as the *census knots*. The naming convention we use for individual census knots is KT_v, where T is the complexity, and v is an ordering on the hyperbolic volumes of all equal-complexity knots. The numbers of census knots with each complexity from 2 to 9 are shown in Table 2.1 (there are no 1-tetrahedron knot complements).

2.1.2. Infinite families of minimal triangulations

Results that guarantee the exact complexity of infinite families of 3-manifolds are rare. As alluded to earlier, Jaco, Rubinstein, and Tillmann [JRT09] established the exact complexity for certain families of lens spaces, including the result that $c(L(2k,1)) = k$. This led to subsequent findings in [JRT11], by considering manifolds for which $L(2k,1)$ is a connected double cover. In both papers, layered solid tori are central to their arguments. In particular, the *unique* minimal

triangulation for each lens space they study is its minimal *layered* triangulation (corresponding to a shortest path in the Farey graph). Using double covers, they also determined the exact complexity for certain 'generalised quaternionic spaces' [JRT11]. In this case, the key construction is a so-called 'layered chain', which we will encounter towards the end of this chapter.

Results on exact complexity for infinite families of finite volume, cusped hyperbolic 3-manifolds are also rare. Jaco, Rubinstein, Spreer, and Tillmann [JRST20] proved that monodromy ideal triangulations[1] of hyperbolic once-punctured torus bundles are minimal, where minimality is achieved by layering that is once again governed by short paths in the Farey graph. Most recently, Rubinstein, Spreer, and Tillmann [RST21] constructed another infinite class of minimal ideal triangulations that arise as fillings of the 3-component link 'L8a16'. In this case, it is the layered chain construction that seems to hold the key to achieving minimality.

When it comes to explicit minimal triangulations for infinite families of *knot complements*, even less is known. In terms of non-hyperbolic knots, Fominykh and Wiest [FW13] use Farey paths to find upper bounds on the complexity of torus knot complements, and conjecture that their bound is sharp. Of course, any explicit construction of a triangulation automatically provides an upper bound on the complexity of the knot. As such, the triangulated fillings of the Whitehead sister link complement that we used in [HMPT23] provide an upper bound on the complexity of the twisted torus knots $T\big(5, 1-5n, 2, 2\big)$ for all $n \in \mathbb{Z}$.

Perhaps the most extensively studied hyperbolic knots, with respect to complexity, are the 2-bridge knots. Geometric triangulations of 2-bridge knot complements were originally described by Sakuma and Weeks [SW95]. Ishikawa and Nemoto [IN16] showed that many of the Sakuma–Weeks triangulations are not minimal, and presented a new upper bound on the complexity of 2-bridge links, with an example of a particular family that achieves minimality. Morgan and Spreer [MS24] also give lower bounds for the complexity of certain 2-bridge links in terms of the size of the Sakuma–Weeks triangulation. For the special case of the twist knots, Aribi, Guéritaud, and Piguet-Nakazawa [AGP22] recently constructed triangulations consisting of roughly half the number of tetrahedra suggested by the upper bound given in [IN16].

In Section 2.4, I present triangulations for 42 families of knots, which I conjecture to be minimal. In the absence of a proof that these triangulations are indeed minimal, a side-effect of describing an explicit construction is that we obtain upper bounds for the complexity of infinitely many hyperbolic knots.

SECTION 2.2. *Chain links and the magic manifold*

In this section, we consider a family of hyperbolic chain links that have captured the interest of mathematicians for decades. An *n-chain link* is (intuitively) a closed chain with n components, where each component is linked once with each of its two neighbours. In general, such a chain can be twisted an arbitrary number of times, and when n is even, it can also be completely *untwisted*. Consider a chain link *untwisted* if it can be embedded in $\mathbb{R}^3$ so that its components alternate between lying parallel and perpendicular to the xy-plane; call these components *horizontal* and *vertical*, respectively. An n-chain link is considered *minimally twisted* if either: n is even and the chain is untwisted, or: n is odd and $n-1$ of the components alternate between being horizontal

[1] The monodromy is assumed to have trace not equal to $0, \pm 1, \pm 2$.

and vertical, until the n^{th} component closes the chain by connecting a horizontal component with a vertical component using the least amount of twisting necessary (see Figure 2.1).

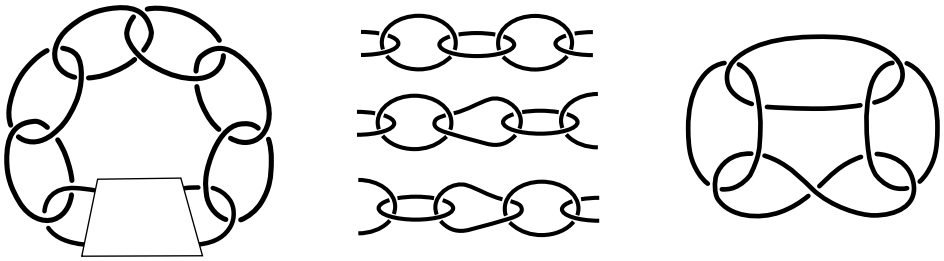

Figure 2.1. Left: A generic chain link with 6 untwisted components, ready to be closed by a 7^{th} component that may be twisted arbitrarily many times. Centre: If n is even (top), the n^{th} component connects two vertical (or horizontal) components, and is itself horizontal (respectively, vertical). When n is odd, the (twice-punctured) disk bounded by the n^{th} component is neither vertical nor horizontal, but instead exhibits partial twisting that may be either right-handed (middle) or left-handed (bottom). Right: A 4-chain link with the least amount of twisting required to admit a hyperbolic complement.

While the minimally twisted n-chain links are hyperbolic for all $n \geq 5$ [NR92], the same is not true for $n = 3, 4$. However, only a single half-twist is required to realise a hyperbolic chain link in each case. A hyperbolic 4-chain link with the least twisting required is shown in Figure 2.1 (right), while a hyperbolic 3-chain link was the featured image at the beginning of this chapter.

These hyperbolic chain links form a family of links $\{n\text{CL}\}$, with their complements forming a family of manifolds $\{M_n\}$. Consecutive members in this family are related by simple surgeries: nCL is obtained by -1 surgery on any single component of $(n+1)$CL, while M_n is homeomorphic to M_{n+1} after performing a -1 Dehn-filling on any single cusp. Indeed, this gives a natural meaning to nCL (and M_n) for $n = 2$ (the Whitehead link), for $n = 1$ (the figure-8 knot), and even for $n = 0$ (the Fomenko-Matveev-Weeks manifold). The members of this family are shown in Figure 2.2, for n between 1 and 7.

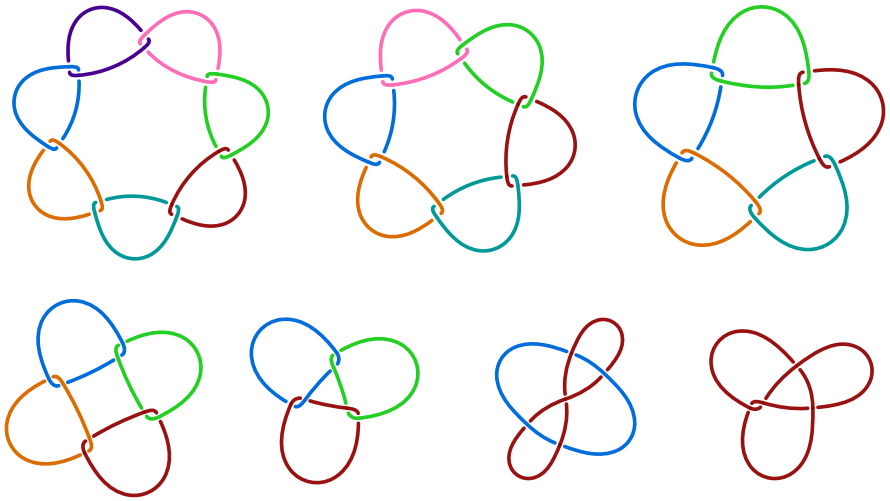

Figure 2.2. The family of links $\{n\text{CL}\}$ for $n = 7$ down to 1. For $n \geq 3$, these are minimally twisted hyperbolic chain links, and for $n = 1, 2$, we rely on the property that nCL is obtained from $(n+1)$CL by performing -1 surgery on one of its components. These figures are adapted from output generated using [KLO].

Remark 2.5. Some notes on chain links:

- There are two choices for the direction of the partial twist when closing an odd-n chain, resulting in opposite-orientation manifolds. We use the orientation given in Figure 2.2, which matches the orientation of M_3 used in [MPE06].
- From now on, any reference to 'chain links' will implicitly mean the family of hyperbolic chain links with minimal twisting, unless otherwise specified.
- The symmetry of chain links means that we can cyclically permute components. We label components $\mathfrak{c}_0, \cdots, \mathfrak{c}_{n-1}$ in a clockwise direction.

Remark 2.6. In his notes, Thurston studied the untwisted even-n chain links, along with what I like to think of as the 'gently twisted' chain links; that is, those with an alternating diagram where no component has self-crossings. Notably, the hyperbolic structure of M_3 was known to Thurston, and he remarked upon its 'particularly low' volume [see Chapter 6.8, THUR].

VOLUMES OF CHAIN LINKS. Indeed, since Thurston's observation about M_3, the volumes of M_n have been seen to be very low in general. In 2001, Cao and Meyerhoff [CM01] proved that M_1 (the figure-8 knot) realises the smallest volume of all 1-cusped hyperbolic manifolds. The '0-cusped' manifold M_0 was confirmed to be the unique minimal volume, closed, orientable hyperbolic 3-manifold in [GMM09]. In 2010, Agol [AGO10] proved that M_2 (the Whitehead link) realises the smallest volume of all 2-cusped hyperbolic manifolds.

In the same paper, Agol referred to a statement of Venzke [VEN08] asserting that M_n is *not* the smallest volume hyperbolic link with n cusps for $n \geq 11$, since the $(n-1)$-fold cyclic cover of the Whitehead link is smaller. In light of this, Agol made the following conjecture.

Conjecture 2.7. (AGOL, 2010). For all $n \leq 10$, the smallest volume amongst all n-cusped hyperbolic manifolds is realised by M_n.

In 2013, Yoshida [YOS13] confirmed that Agol's conjecture holds for $n = 4$ and recently, Zhang [ZHA23] made progress towards a proof for $n = 3$.

Meanwhile, Kaiser, Purcell, and Rollins [KPR12] set out to verify Venzke's claim for $n \geq 11$. They proved the claim for $n \geq 60$ using volume bounds, and the cases $12 \leq n \leq 25$ using rigorous numerical computations. The cases $26 \leq n \leq 59$ were considered extremely likely to hold, based on non-rigorous numerical results, but their techniques and SNAPPY's numerics were not considered sensitive enough to verify the $n = 11$ case.

The chain links have also been shown to be Dehn filling parents of many of the smallest volume hyperbolic manifolds. For instance, Gabai, Meyerhoff, and Milley [GMM09] determined a set $\mathcal{P}$ of 21 manifolds from which all 1-cusped hyperbolic manifolds with volume less than 2.848 must be obtained (by Dehn filling all but one of their cusps). The complement of 3CL was the only 3-cusped manifold in $\mathcal{P}$ and Milley [MIL09] separately showed that 12 of the 20 2-cusped manifolds in $\mathcal{P}$ could themselves be obtained by filling one of 3CL's cusps.

EXCEPTIONAL FILLINGS OF CHAIN LINKS.

Definition 2.8. (Exceptional filling). A Dehn filling of a cusped hyperbolic 3-manifold is considered *exceptional* if the filled manifold fails to be hyperbolic.

In 1999, Gordon and Wu [GW99] were studying the intersection numbers between pairs of

exceptional filling slopes for which one of the filled manifolds contained an essential torus, and the other contained an essential annulus. They proved that the only manifolds for which this intersection number could be greater than 3 were the Whitehead link, the Whitehead sister, and a 2-bridge link determined by the rational number 3/10. Because all three of these manifolds can be realised by Dehn filling M_3, Gordon and Wu described M_3 as the 'magic' manifold, and since then, the name has stuck. This study of intersection numbers between exceptional filling slopes has continued over the years, eventually extending to the classification of distances between filling slopes that realise other pairs of essential surfaces. The chain links continue to feature heavily in this research [ALR18].

In an unpublished manuscript, Berge [Ber90] described twelve families of knots for which some Dehn filling realises a lens space. In the so-called *Berge conjecture*, which appears as Problem 1.78 in [Kir95], Gordon suggests that Berge knots are the only knots admitting lens space surgeries. Baker [Ba08a] showed that ten of the twelve families of Berge knots can be realised by Dehn filling M_5; he also showed that knots in the remaining two families can be obtained by Dehn filling minimally twisted chain links, but these may require arbitrarily many components [Ba08b].

In 2006, Martelli and Petronio [MPe06] completely classified the exceptional fillings of M_3. Then, in 2014, Martelli, Petronio, and Roukema [MPR14] classified all exceptional fillings of M_4 and M_5. Even more recently, Martelli [Mar21] classified all exceptional fillings of M_6 and M_7. It is Martelli and Petronio's classification of exceptional fillings of the magic manifold that we use to identify census knots in Section 2.3.

Complexity of chain links. In 1991, Adams and Sherman [AS91] proved that at least $2n$ ideal tetrahedra are required to triangulate the complement of any link with n components. In this paper, they gave 3CL as an example of a 3-component link whose complement can be built out of 6 ideal tetrahedra. In 1999, the SnapPea census revealed that, in fact, M_3 is the *only* 3-cusped hyperbolic manifold that can be built from 6 tetrahedra.

The census of cusped, orientable hyperbolic 3-manifolds built from up to 25 *regular* ideal tetrahedra [FGG+16] also revealed interesting properties of the chain links. One feature of this census is that it identifies the manifolds that maximise volume amongst all manifolds of a given complexity. Of particular note is the fact that M_5 can be built from 10 regular tetrahedra. This means that M_5 simultaneously realises the maximum volume amongst 10-tetrahedron (orientable, cusped hyperbolic) 3-manifolds *and* is conjectured to be minimal volume amongst 5-cusped (orientable, hyperbolic) 3-manifolds. Note that this is also a minimal triangulation for M_5. The authors of [FGG+16] also draw attention to the only 7-component link complement that appears in their census, which is built from 20 regular ideal tetrahedra, and arises as a 2-fold cover of 5CL.

It is widely accepted (albeit difficult to cite!) that 'many', if not 'most', census manifolds can be realised as fillings of M_3 or M_5. Since this classification is not readily accessible, we dedicate the next section to identifying census knots that arise as Dehn fillings of the magic manifold, and add to our understanding of these census knots by organising them into families related by twisting.

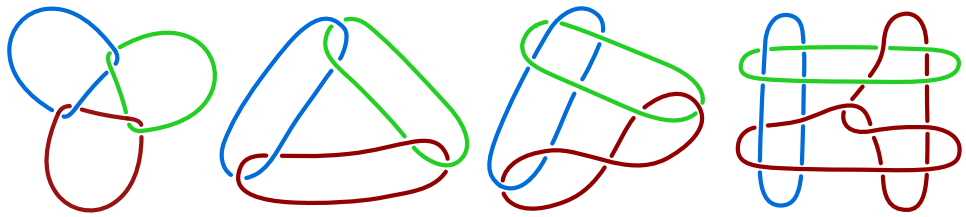

FIGURE 2.3. The chain link diagram of 3CL can be adjusted to appear as on the right, which is a more helpful diagram for our purposes. Two intermediate steps in the sequence of adjustments are shown.

SECTION 2.3. *Families of census knots related by twisting*

In this section we consider fillings of the magic manifold M_3 that result in census knots, ultimately sorting them into families related by twisting. Throughout this section, take n, k, p, q, r, s, t, u to be integers and consider any 'slopes' to be reduced rational numbers, or $1/0$. We will consistently use r/s to denote the filling slope in cusp $\mathfrak{c}_1$ (the blue component in Figure 2.3), and t/u for the filling slope in cusp $\mathfrak{c}_2$ (the green component in Figure 2.3). We refer to these as the *primary slope* and *secondary slope*, respectively.

Since volume decreases under Dehn filling, we restrict our attention to the 278 census knots with volume less than $\mathbf{V} = \mathrm{vol}(M_3) \simeq 5.3335$ (summarised in Table 2.2). Ultimately, we account for 229 of these knots as fillings of M_3.

TABLE 2.2. Summary of 278 census knots with volumes less than that of the magic manifold.

T	Total candidates	Largest candidate	Volume
≤ 5	29	$K5_{22}$	4.85117
6	35	$K6_{35}$	5.32249
7	54	$K7_{54}$	5.26280
8	66	$K8_{66}$	5.32359
9	94	$K9_{94}$	5.24619

A partial filling $M_3(\alpha, \beta)$ obtained from M_3 by filling two components along slopes α, β is confirmed to be a knot in S^3 by identifying a closed filling $M_3(\alpha, \beta, \gamma) = S^3$. In this case, we say that γ is the *trivial filling slope*, which is unique by the GORDON–LUECKE Theorem. The conventions used by Martelli and Petronio [MPE06] mean that instances of an S^3 filling appear in their tables as the lens space $L\big(f(n), \star\big)$ with $f(n) = \pm 1$ and $\star$ an unimportant integer. Let us restate Theorem 1.3. of [MPE06] to emphasise the classification of hyperbolic knots.

Theorem 2.9. (MARTELLI–PETRONIO, 2006). The closed manifold $N = M_3\big(p/q\,,\, r/s\,,\, t/u\big)$ is the S^3 filling of a knot $M_3\big(r/s\,,\, t/u\big)$ if one of the following occurs, up to permutation.

A. The trivial filling slope is $p/q = \infty$, in which case $N = L\big(tr - us, \star\big)$.
   Hence, $M_3\big(r/s\,,\, t/u\big)$ is a knot in S^3 whenever $tr - us = \pm 1$.

B. The trivial filling slope is $p/q = -2$, and $r/s = -2 + 1/k$, in which case

$$N = L\big(3k\,(t + 2u) - 2t - u, \star\big).$$

   Hence, $M_3(-2 + 1/k\,, t/u\big)$ is a knot in S^3 whenever $3k\,(t + 2u) - 2t - u = \pm 1$.

C. The trivial filling slope is $p/q = -1$, and $r/s = -3 + 1/k$, in which case

$$N = L\big(2k\,(t+3u) - t - u, \star\big).$$

Hence, $M_3(-3+1/k\,,\,t/u\,)$ is a knot in S^3 whenever $2k\,(t+3u) - t - u = \pm 1$.

We refer to the filling $M_3\big(r/s\,,\,t/u\,\big)$ as a *knot of Type A, B, or C*, depending on which of these categories the pair of slopes $r/s\,,\,t/u$ falls into.

Remark 2.10. The knots described in Theorem 2.9 are generally hyperbolic, except in the isolated instances where a single exceptional slope is in $\{\,0/1\,,\,-1/1\,,\,-2/1\,,\,-3/1\,,\,1/0\,\}$ or a pair of exceptional slopes is in $\{\,(1/1\,,\,1/1\,)\,,\,(-3/2\,,\,-5/2\,)\,,\,(-4/1\,,\,-1/2\,)\,\}$. Note that there are other instances of $L\big(f(n),\star\big)$ in Martelli and Petronio's tables, however, we have ignored them here if the only solutions to $f(n) = \pm 1$ imply that the corresponding knot is not hyperbolic. Going forward, we denote the set of single exceptional slopes by

$$\mathcal{X} = \{\,0/1\,,\,-1/1\,,\,-2/1\,,\,-3/1\,,\,1/0\,\}\,.$$

In the remainder of this section we describe the organisation of 229 census knots into families that share a primary filling slope. In fact, in Section 2.3.4, we offer descriptions of each family as a sequence of knots related by twisting. In the case of knots with negative primary filling slopes, we describe families of twisted torus knots. For the positive fillings, we define a 'clasped torus knot' (see Figure 2.5), and organise the remaining knots into families of this form.

We choose to interpret the magic manifold using the model shown in Figure 2.4, right. That is, we let $\mathbf{H} = T^2 \times \{-\infty, \infty\} - \mathfrak{c}_0$ be the complement of 3CL, with $\mathfrak{c}_1$ located at $T^2 \times \{+\infty\}$ and $\mathfrak{c}_2$ located at $T^2 \times \{-\infty\}$. At times we also use a compact version of this model, which we denote $\overline{\mathbf{H}}$. In $\overline{\mathbf{H}}$, we truncate cusps $\mathfrak{c}_1$ and $\mathfrak{c}_2$ to get real torus boundaries at $T^2 \times \{1\}$ and $T^2 \times \{-1\}$, respectively, and 'replace' $\mathfrak{c}_0$ so that it is an embedding of S^1 in $T^2 \times [-1, 1]$. Despite no longer being cusps, we will continue to refer to the two $T^2 \times \{\pm 1\}$ boundaries and the embedded curve in $\overline{\mathbf{H}}$ using the same $\mathfrak{c}_i$ notation.

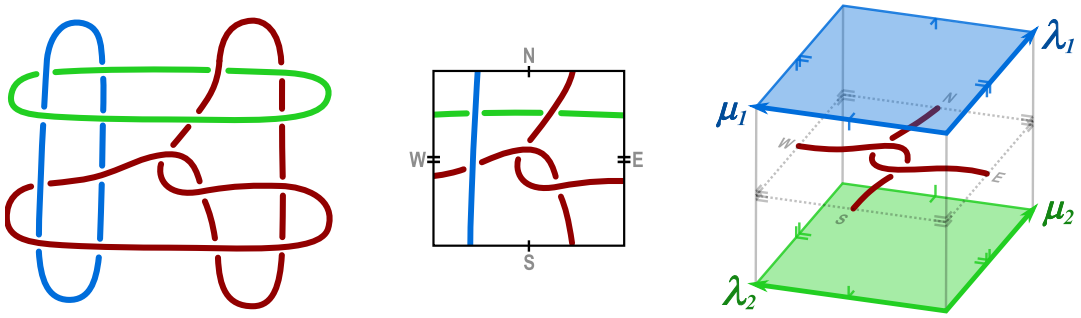

Figure 2.4. Left: Our alternative view of 3CL where, away from a central tangle, $\mathfrak{c}_0$ (shown in red) runs parallel to either one of $\mathfrak{c}_1$ (blue) or $\mathfrak{c}_2$ (green). Centre: Connecting the diagram of 3CL on the left to the model of M_3 on the right. Right: A model of the complement of the Hopf link formed by $\mathfrak{c}_1 \cup \mathfrak{c}_2$ using $T^2 \times I$, with the $\mathfrak{c}_0$ tangle embedded in a neighbourhood of $T^2 \times \{0\}$. The μ_i, λ_i framing shown here is used consistently throughout the remainder of this chapter.

We begin by establishing notation and stating some basic facts about continued fractions and Dehn twists. Using this, we describe families of knots for each category of hyperbolic knots in Theorem 2.9.

2.3.1. Dehn twists and continued fractions

To describe the families of knots that arise from Theorem 2.9, we use continued fraction expansions of filling slopes, which can be interpreted in relation to Dehn twists about annuli in $\overline{\mathbf{H}}$. As discussed in [Gor02], the exterior of a link with two or more components is, in general, not unique. In particular, there are two *cut-twist-reglue* operations that account for 'most' homeomorphisms between homeomorphic exteriors of inequivalent links. These correspond to cutting and twisting along properly embedded *discs* or properly embedded *annuli*, and each can be understood in terms of *Dehn twists* on relevant torus boundary components.

Dehn twists. Recall that a Dehn twist about a curve α on a torus is a homeomorphism of the torus leaving points away from α fixed, and *adding a twist about* α in an open neighbourhood $\nu(\alpha)$. We will apply the same framework to twisting about annuli in $\overline{\mathbf{H}}$ by twisting about α throughout the entire interval $\nu(\alpha) \times [-1, 1]$.

It is well-established [for instance, in Rol76, Lemma 12] that a geodesic with slope r/s on a torus can be reduced by Dehn twists about μ and λ to a geodesic with slope 0 or ∞. Moreover, the precise sequence of twists can be determined using the Euclidean algorithm, whose steps can in turn be encoded by a continued fraction expansion of r/s.

Continued fractions. Of the many conventions that exist for representing continued fractions, we adopt the following. We write a continued fraction expansion for r/s as

$$r/s = \big[\, c_1, c_2, \cdots, c_m \,\big] = c_1 + \cfrac{1}{c_2 + \cfrac{1}{\ddots\ c_{m-1} + \cfrac{1}{c_m}}},$$

where $c_i \in \mathbb{Z}$, and c_1 always represents the 'whole part'. In particular, $c_1 = 0$ when $r < s$. When coefficients other than c_1 are equal to zero we will typically update the continued fraction using the following adjustments. When $c_i = 0$ for $i \neq 0, m$, we can rewrite

$$\big[\, c_1, \cdots, c_{i-1}, 0, c_{i+1}, \cdots, c_m \,\big] = \big[\, c_1, \cdots, c_{i-1} + c_{i+1}, \cdots, c_m \,\big].$$

We can also make sense of a continued fraction with $c_m = 0$. For small cases, we have

$$\big[\, 0 \,\big] = 0, \quad \big[\, c_1, 0 \,\big] = 1/0\,, \quad \text{and} \quad \big[\, c_1, c_2, 0 \,\big] = c_1 + \frac{1}{c_2 + 1/0} = c_1 + \frac{0}{c_2 \cdot 0 + 1} = c_1.$$

From here, one can argue inductively that $\big[\, c_1, \cdots, c_{m-2}, c_{m-1}, 0 \,\big] = \big[\, c_1, \cdots, c_{m-2} \,\big]$.

If a continued fraction expansion of r/s has m coefficients, we say it has *length* m. We will have cause to distinguish between continued fractions of *even length* and *odd length*. Note that a continued fraction with opposite parity can be found by adjusting the final coefficient as follows:

$$\big[\, c_1, \cdots, c_m \,\big] = \big[\, c_1, \cdots, (c_m \pm 1), \mp 1 \,\big].$$

Reducing slopes. Now let us consider the relationship between a continued fraction for the rational number r/s, and a sequence of Dehn twists that reduce r/s to $1/0$, to coincide

with μ. As is common-practice, we conflate Dehn twists about μ, λ with matrices $U^{\pm 1} = \left(\begin{smallmatrix} 1 & 1 \\ 0 & 1 \end{smallmatrix}\right)^{\pm 1}$, $V^{\pm 1} = \left(\begin{smallmatrix} 1 & 0 \\ 1 & 1 \end{smallmatrix}\right)^{\pm 1} \in GL_2(\mathbb{Z})$, respectively. Then the coefficients in a continued fraction can be read as a list of exponents for an alternating product of the matrices U and V (and their inverses).

We can also use continued fractions in this way to describe sequences of Dehn twists about annuli in $\overline{\mathbf{H}}$. We will typically work in the framing of $\mathfrak{c}_1$, with $\mu_1 = \left[\begin{smallmatrix} 1 \\ 0 \end{smallmatrix}\right]$ and $\lambda_1 = \left[\begin{smallmatrix} 0 \\ 1 \end{smallmatrix}\right]$. Note that the framing on $\mathfrak{c}_2$ is related to the framing on $\mathfrak{c}_1$ by the matrix $\left(\begin{smallmatrix} 0 & 1 \\ 1 & 0 \end{smallmatrix}\right)$, so a curve denoted $\left[\begin{smallmatrix} p \\ q \end{smallmatrix}\right]$ has slope q/p with respect to the $\mathfrak{c}_2$ framing. Twists around μ_1 will be extended through $\overline{\mathbf{H}}$ to twists about an annulus A_1, that has μ_1 and λ_2 as boundaries. Similarly, twists about λ_1 will be extended to twists about A_2, which is the annulus bounded by μ_2 and λ_1.

2.3.2. Hyperbolic knots of Type A

Recall from Theorem 2.9 that $M_3\left(r/s\,,\, t/u\right)$ is a knot in S^3 whenever $tr - us = \pm 1$.

Lemma 2.11. Suppose r/s is any reduced rational number not in $\mathcal{X}$, with continued fraction expansion $\left[c_1, \cdots, c_m, k\right]$. Let $r'/s' = \left[c_1, \cdots, c_m\right]$. Then there is a family of knots

$$\mathcal{F}(n) = M_3\left(r/s\,,\, t_n/u_n\right), \text{ with } \frac{t_n}{u_n} = \frac{s \cdot n + s'}{r \cdot n + r'} = \left[0, c_1, \cdots, c_m, k, n\right],$$

where $n \in \mathbb{Z}$ indexes full twists on some number of parallel strands in a diagram of $M_3\left(r/s\right)$.

Proof. Since there is a geodesic connecting r/s and r'/s' in the Farey diagram, $t = s'$ and $u = r'$ is a solution to the equation $tr - us = \pm 1$. Then since $\gcd(r, s) = 1$, we have infinitely many more solutions of the form $t = (s' + s \cdot n)$, $u = (r' + r \cdot n)$. Hence, by [MPe06], all such pairs of slopes result in a knot in S^3.

Next, we argue that $t_n/u_n = \left[0, c_1, \cdots, c_m, k, n\right]$. Recall that t_n/u_n is a slope on $\mathfrak{c}_2$, so the same geodesic has slope u_n/t_n with respect to the framing of $\mathfrak{c}_1$. Therefore, we show that $u_n/t_n = \left[c_1, \cdots, c_m, k, n\right]$. If we were to directly compute a continued fraction expansion for

$$\frac{u_n}{t_n} = \frac{r \cdot n + r'}{s \cdot n + s'},$$

the first step would be to find a coefficient and remainder in the division of u_n by t_n. But we can use the fact that

$$\frac{r}{s} = c_1 + \frac{1}{\left[c_2, \cdots, c_m, k\right]} \quad \text{and} \quad \frac{r'}{s'} = c_1 + \frac{1}{\left[c_2, \cdots, c_m\right]}$$

to see that the same sequence of coefficients will simultaneously reduce all three of r'/s', r/s, and u_n/t_n, until the remainder in the division of u_n by t_n is

$$c_{m-1} + \frac{k \cdot n + 1}{c_m \cdot (k \cdot n + 1) + n} = c_{m-1} + \frac{1}{c_m + \dfrac{n}{k \cdot n + 1}} = c_{m-1} + \frac{1}{c_m + \dfrac{1}{k + 1/n}}.$$

This shows that $u_n/t_n = \left[c_1, \cdots, c_m, k, n\right]$, and hence t_n/u_n is the reciprocal as claimed.

All that remains is to show that n indexes full twists on parallel strands in a diagram of $M_3\left(r/s\right)$. We mark a geodesic α with slope r/s on $\mathfrak{c}_1$. We also mark a geodesic β on $\mathfrak{c}_2$, noting that this geodesic has slope t_n/u_n with respect to the $\mathfrak{c}_2$ framing, but slope u_n/t_n with respect to the $\mathfrak{c}_1$ framing (which is the one we consider).

We then perform a sequence F of Dehn twists along A_1 and A_2 until $F(\alpha)$ has slope $1/0$. The sequence of Dehn twists along A_1 and A_2 is determined from the continued fraction for r/s. Because the continued fractions for r/s and u_n/t_n coincide until the last term, the curves α and β are simultaneously simplified by the twists we perform. Moreover, when $F(\alpha)$ has slope $1/0$, $F(\beta)$ has slope $n'/1$ (but not necessarily $n/1$), which means it can be further reduced to a slope of $0/1$ (so that it coincides with the meridian of $\mathfrak{c}_2$) using only twists about A_1, and therefore leaving $F(\alpha)$ in place.

Performing such a sequence of Dehn twists yields a homeomorphic link complement of an inequivalent link [Gor02], where $\mathfrak{c}_0$ can still be seen as a (now more complicated) knot in the complement of a Hopf link. Filling $\mathfrak{c}_1$ trivially along $F(\alpha) = \left[\begin{smallmatrix}1\\0\end{smallmatrix}\right]$ leaves a 2-component link in S^3, where $\mathfrak{c}_2$ is an unknot around some number of parallel strands of $\mathfrak{c}_0$.

Hence, we can add full twists to these strands by performing $1/n$ fillings in $\mathfrak{c}_2$ (with respect to the current framing in $\mathfrak{c}_2$) for any $n \in \mathbb{Z}$. Note that the exact indexing of n depends on the slope $n'/1$ that we encountered when the $1/0$ slope was first achieved in $\mathfrak{c}_1$.

□

2.3.3. Hyperbolic knots of Type B & C

The two remaining points from Theorem 2.9 allow us to describe two more categories of hyperbolic knots.

From Theorem 2.9, we know that $M_3\big(r/s\,,\,t/u\big)$ is a knot when $r/s = -2 + 1/k$ and t/u is any slope satisfying $3k\,(t+2u) - 2t - u = \pm 1$. Hence, we find solutions for t, u by solving the diophantine equation $(3k-2)\,t + (6k-1)\,u = 1$, which gives

$$\frac{t}{u} = \frac{(2k-1) + n\,(6k-1)}{(1-k) - n\,(3k-2)} \quad \text{for any } k, n \in \mathbb{Z}.$$

A continued fraction expansion for these slopes is $t/u = \big[-2, -k, 1, 2, n\big]$.

We can follow the same procedure for the knots of Type C, which are the fillings $M_3\big(r/s\,,\,t/u\big)$ with $r/s = -3 + 1/k$ and t/u any slope satisfying $2k(t+3u) - t - u = \pm 1$. We again rewrite this as a diophantine equation and solve to find

$$\frac{t}{u} = \frac{(3k-2) + n\,(6k-1)}{(1-k) - n\,(2k-1)} \quad \text{for any } k, n \in \mathbb{Z}.$$

A continued fraction expansion for these slopes is $t/u = \big[-3, -k, 1, 1, n\big]$.

2.3.4. Finding homes for census knots

Recall from the definition in the introduction that a (generalised) twisted torus knot can be obtained from a (p, q)-torus knot by introducing an extra s over-strands, with either a positive or negative slope, that pass over $r-1$ parallel strands. We denote this twisted torus knot by $T(p, q, r, \pm s)$. Now let us define a *clasped* torus knot.

Definition 2.12. We say the *clasped torus knot* $Cl(p, q)$ is the knot obtained from a (p, q)-torus knot by replacing a small section of two parallel strands with a clasp, as shown in Figure 2.5.

The following conjectures assign clasped and twisted torus knot descriptions to the different families of knots we have just described. In Appendix A, we provide SnapPy code to construct

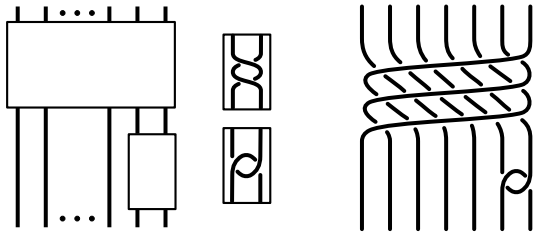

Figure 2.5. Left: A braid representation of a (p, q)-torus knot, with p vertical strands entering the large box, where there will be q over-strands, with positive or negative slope given by the sign of q. By inserting one of the two tangles into the small box, we obtain either the twisted torus knot $T(p, q, 2, -2)$ (using the *twisted tangle*, top) or the *clasped torus knot* $Cl(p, q)$ (using the *clasped tangle*, bottom). Right: The clasped torus knot $Cl(7, 3)$.

these families and to recognise members that are census knots. This code has been used to verify Conjectures 2.13 to 2.17 for all k, n that correspond to census knots in the tables of Appendix A.[2]

Type A knots with negative primary filling slopes. Suppose $r'/s' = [c_1, \cdots, c_m]$ is a continued fraction expansion of length m for some $r'/s' \in \mathbb{Q} \cup \{1/0\}$ (where $1/0$ is represented by $[\emptyset]$). We consider primary slopes $r/s = [c_1, \cdots, c_m, k]$ for a given k, along with secondary slopes $t_n/u_n = [0, c_1, \cdots, c_m, k, n]$, expressed in terms of $n \in \mathbb{Z}$.

Conjecture 2.13. Suppose a family of knots has primary slope $r/s < 0$ with continued fraction expansion and secondary slopes t_n/u_n described as above. Then $M_3\big(r/s\,,\, t_n/u_n\big)$ can be described as a family of twisted torus knots $T\big(a, b_n, 2, -2\big)$, with the parameters a and b_n determined based on the parity of m and the sign of k, as below.

	$k < 0$	$k > 0$
m odd	$a = r - s$ $b_n = t_n - u_n$	$a = s - r$ $b_n = u_n - t_n$
m even	$a = s - r$ $b_n = t_n - u_n$	$a = r - s$ $b_n = u_n - t_n$

Type A knots with positive primary filling slopes.

Conjecture 2.14. For a given $k \in \mathbb{Z} \setminus \{-1, 0\}$, there is a family of clasped torus knots, indexed by $n \in \mathbb{Z}$,

$$M_3\left(\frac{k+1}{k}, \frac{1+kn}{1+(k+1)\,n}\right) = \begin{cases} Cl\big(\,|2k+1|,\, 2-|2k+1|\cdot n\big), & k < -1 \\ Cl\big(\,|2k+1|,\, -2-|2k+1|\cdot n\big), & k > 0. \end{cases}$$

Conjecture 2.15. For a given $k > 0$, there are two families of clasped torus knots, each indexed by $n \in \mathbb{Z}$,

$$M_3\left(\frac{1}{k}, \frac{1+kn}{n}\right) = Cl\big(\,k+1, -1-(k+1)\,n\big),$$
$$M_3\left(\frac{k}{1}, \frac{n}{1+kn}\right) = Cl\big(\,k+1, 1+(k+1)\,n\big).$$

[2]Not all SnapPy computations are 'verified', however, when the `identify` function recognises a hyperbolic manifold M as a census knot N, this means that `M.is_isometric_to(N)` is `True`, which *is* guaranteed to be rigorous [SnapPy].

Families of Type B knots. Recall that the knots of Type B have primary and secondary filling slopes of the form $r/s = [-2, k]$ and $t/u = [-2, -k, 1, 2, n]$, respectively.

Conjecture 2.16. For a given $k \in \mathbb{Z} \setminus \{-1, 0, 1\}$, there is a family of twisted torus knots, indexed by $n \in \mathbb{Z}$,

$$M_3\left(-2 + \frac{1}{k}, \frac{(2k-1) + n\,(6k-1)}{(1-k) - n\,(3k-2)}\right) = \begin{cases} T\big(3k-1, k + (3k-1)\cdot n, k, -2\big), & k \geq 2 \\ T\big(1-3k, k + (3k-1)\cdot n, 1-k, -2\big), & k \leq -2. \end{cases}$$

Families of Type C knots. Recall that the knots of Type C families have primary and secondary filling slopes of the form $r/s = [-3, k]$ and $t/u = [-3, -k, 1, 1, n]$, respectively.

Conjecture 2.17. For a given $k \in \mathbb{Z} \setminus \{0, 1\}$, there is a family of knots, indexed by $n \in \mathbb{Z}$,

$$M_3\left(-3 + \frac{1}{k}, \frac{(3k-2) + n\,(6k-1)}{(1-k) - n\,(2k-1)}\right) = \begin{cases} T\big(4k-1, 1-2k-(4k-1)\cdot n, 2k-1, 1\big), & k \geq 2 \\ T\big(1-4k, 1-2k-(4k-1)\cdot n, 1-2k, 1\big), & k \leq -1. \end{cases}$$

Summary of findings. Recall that there are 278 census knots with volumes lower than $\mathrm{vol}(M_3)$. In Appendix A, we account for 229 of these knots as fillings of M_3. Meanwhile, based on informal experiments using SnapPy, we hypothesise that the remaining 49 census knots *cannot* be realised as fillings of M_3.

Appendix A includes ten tables of census knots organised into Type A families, as well as one table each for census knots that form families of Type B and C. In the following, we refer to $r'/s' = [c_1, \cdots, c_m]$ as the *root* of the family with the primary slope r/s given by $[c_1, \cdots, c_m, k]$. The ten tables of Type A families correspond to the roots

$$r'/s' = 1/0\,,\ 0/1\,,\ 1/1\,,\ -1/1\,,\ -2/1\,,\ -3/1\,,\ -1/2\,,\ -1/3\,,\ -3/2\,,\ -2/3\,.$$

Note that some primary slopes appear in more than one of the Type A tables, since they can be written in terms of more than one of the roots. While each instance of a given primary slope contributes a seemingly different twisted or clasped torus knot description, the difference is only in the indexing of n. Meanwhile, as Martelli and Petronio [MPe06] observed, both $-3/2$ and $-4/1$ give rise to the Whitehead sister link complement, and as such, we do see two genuinely different twisted torus knot descriptions for this family.

In the tables of Appendix A, there are 42 families for which we define a *pair of distinguished fillings*. Given a root $r'/s' = [c_1, \cdots, c_m] = [R_m]$, let us write $r/s = [R_m, k]$ and $t_n/u_n = [0, R_m, k, n]$ for its associated primary and secondary slopes, respectively. For a Type A family with primary slope $r/s = [R_m, k]$, we define its *pair of distinguished fillings* to be $\{M_3(r/s\,,\, t_i/u_i),\ M_3(r/s\,,\, t_j/u_j)\}$, where the secondary slopes are either

$$\begin{aligned} t_i/u_i &= [0, R_m, k, -1] \quad \text{and} \quad t_j/u_j = [0, R_m, k, 2], \qquad \text{if } k < 0, \text{ or} \\ t_i/u_i &= [0, R_m, k, 1] \quad \text{and} \quad t_j/u_j = [0, R_m, k, -2], \qquad \text{if } k > 0. \end{aligned}$$

Meanwhile, for all families of Types B & C, regardless of the sign of k, we define the pair of distinguished fillings to be the two fillings with secondary slopes t_n/u_n for $n = 1, -2$.

Note that a family is assigned a pair of distinguished fillings if it has at least two fillings that are recognised as census knots, and these arise for values of n that are 'sufficiently far apart'. Loosely speaking, the chosen fillings represent the earliest 'symmetric' pair of fillings that are both hyperbolic, where the symmetry in question relates to the positive and negative arms of the sequence of slopes t_n/u_n (best visualised by considering the associated walk in the Farey graph).

For each family with a pair of distinguished fillings K_1, K_2, we find the average of $\mathrm{vol}(K_1)$ and $\mathrm{vol}(K_2)$, then label all families by $\mathcal{F}_v$, where v is an integer assigned in order of increasing average volume. All distinguished fillings, along with their volumes, are summarised in Section A.1. Note that there is an anomaly in the case of $r/s = -1/2$, which is the only family that sees the same knots for both positive and negative n. It has been assigned the label $\mathcal{F}_0$ for this reason. The families of Type B & C have labels marked with an asterisk.

Section 2.4. *Triangulated fillings of the magic manifold*

In this section, we describe several different triangulations of the magic manifold, so that we can ultimately construct minimal triangulations of all census knots classified in the previous section.

2.4.1. Strategy for finding triangulations

Let us describe now the process of triangulating the complement of 3CL in such a way that layered solid tori can be used to Dehn fill the cusps $\mathfrak{c}_1$ and $\mathfrak{c}_2$. In contrast to the previous section, where we preferred the compact $\overline{\mathbf{H}}$ model, in this section, we choose to view the complement of 3CL as $\mathbf{H} = T^2 \times \{-\infty, \infty\} - \mathfrak{c}_0$ (recall Figure 2.4, right). We construct triangulations in which both cusps $\mathfrak{c}_1$ and $\mathfrak{c}_2$ are standard cusps (recall Definition 1.4) as follows: we introduce 3 carefully chosen edges that can be isotoped to lie below the plane $T^2 \times \{0\}$ to form a 2-triangle once-punctured torus, then we cone downwards to cusp $\mathfrak{c}_2$ at $T^2 \times \{-\infty\}$ to form a standard cusp. If we do the same thing above the plane for $\mathfrak{c}_1$, then all that remains is to triangulate the neighbourhood of $T^2 \times \{0\}$.

When decomposing a link complement into ideal tetrahedra from a diagram, we introduce edges that have their endpoints 'on' the link. However, because the link itself is not actually present in the complement, the endpoints of these edges can be isotoped along the link, provided the interior of the edge never passes through a link component or another edge. We will introduce edges in this way, one-by-one, until they can be seen to form a collection of ideal tetrahedra that fill the entire complement. Because we will ultimately decompose the complement into multiple tetrahedra that can be glued back together around each edge, we expect to see copies of the same edge used multiple times during this process, and sometimes in what appear to be completely different positions in the diagram.

We are interested in triangulations with the fewest tetrahedra necessary, so our strategy is to introduce 3 edges below the tangle (which must be distinct), then work upwards through the interval, seeing which edges can be reused and only introducing additional edges as necessary. Eventually, the edges we introduce will span a collection of tetrahedra that fill the entire complement, giving us our ideal triangulation.

Having obtained an appropriate triangulation, we will remove the two pairs of tetrahedra meeting $\mathfrak{c}_1$ and $\mathfrak{c}_2$, leaving some number of tetrahedra, say t_0, that form a *core*. Viewing each

once-punctured boundary torus from its cusp, we can then determine the three boundary slopes (with respect to the framing shown in Figure 2.4), and hence identify the starting point in the Farey graph for the construction of each layered solid torus. We will let $\mathcal{T}(\mathcal{S}_1, \mathcal{S}_2; t_0)$ denote the triangulation of the magic manifold M_3 with two standard cusps and t_0 tetrahedra at its core, with triples of boundary slopes $\mathcal{S}_i$ that are exposed upon removing each of the standard cusps. Let t_1 be the number of tetrahedra required to build a layered solid torus with primary filling slope r/s from a boundary with slopes $\mathcal{S}_1$, and define t_2 similarly for the secondary slope in $\mathfrak{c}_2$ with boundary slopes $\mathcal{S}_2$. The total size of any triangulation obtained from $\mathcal{T}(\mathcal{S}_1, \mathcal{S}_2; t_0)$ by filling both cusps with layered solid tori is then $t_0 + t_1 + t_2$.[3]

The size of any triangulation constructed in this manner can be determined just by considering distances in the Farey graph. In this way, we will determine which fillings of a given triangulation $\mathcal{T}(\mathcal{S}_1, \mathcal{S}_2; t_0)$ realise minimal triangulations of the census knots identified in Section 2.3.

Let $\mathcal{P}_i$, $\mathcal{Q}_i$, $\mathcal{R}_i$ (for $i = 1, 2$) denote the following triples of boundary slopes, with respect to the framing of the cusp they appear in:

$$\mathcal{P}_i = \left\{ {}^{1}/_{0}\,,\ {}^{-1}/_{1}\,,\ {}^{-2}/_{1} \right\}, \quad \mathcal{Q}_i = \left\{ {}^{1}/_{0}\,,\ {}^{-2}/_{1}\,,\ {}^{-3}/_{1} \right\}, \quad \text{and} \quad \mathcal{R}_i = \left\{ {}^{1}/_{0}\,,\ {}^{1}/_{1}\,,\ {}^{0}/_{1} \right\}.$$

Let $\mathbf{C}_{\mathbb{Q}}$ denote the set of census knots identified in Appendix A, for which neither the primary nor secondary filling slope is an integer.

Theorem 2.18. There are three triangulations of M_3,

$$\mathbf{T}_1 = \mathcal{T}(\mathcal{P}_1, \mathcal{P}_2; 2), \quad \mathbf{T}_2 = \mathcal{T}(\mathcal{Q}_1, \mathcal{P}_2; 2), \quad \text{and} \quad \mathbf{T}_3 = \mathcal{T}(\mathcal{R}_1, \mathcal{R}_2; 5),$$

such that a minimal triangulation of knot $K \in \mathbf{C}_{\mathbb{Q}}$ can be realised by filling one of $\mathbf{T}_1, \mathbf{T}_2$ or $\mathbf{T}_3$ with two layered solid tori.

We prove this theorem by constructing each triangulation (in the following two subsections), then presenting tables in Appendix B that verify the number of tetrahedra required for each filling. We then return to the matter of integer slopes in Section 2.4.4.

2.4.2. A first triangulation

We work in the universal cover of $T^2 \times \mathbb{R}$, in a neighbourhood of the $T^2 \times \{0\}$ plane. Take the strands of $\mathfrak{c}_0$ running horizontally in Figure 2.6a to be above the plane, and the strands running vertically to be below it. Introduce three edges as shown in Figure 2.6a. We see two copies of the red and orange edges, which glue to form a one-vertex triangulation of the torus below the plane. We then cone down to cusp $\mathfrak{c}_2$ at $T^2 \times \{-\infty\}$, as described earlier, forming two ideal tetrahedra. Note that this only requires a single new edge, with the two tetrahedra formed being shown in Figure 2.6a.

Next, we drag the endpoints of these edges along $\mathfrak{c}_0$ and see that the pink edge can actually be pulled through so that it lies completely above the plane. In Figure 2.6b, we have included additional copies of the red edge, which are all either isotopic to each other or they are different lifts in the universal cover. Introducing one more edge (the teal edge in Figure 2.7a) we can see two new tetrahedra. At this point we have a second one-vertex triangulation of the torus above

[3] Hopefully this notation will not confuse numbers of tetrahedra t_0, t_1, t_2 with indexed slopes ${}^{t_n}/_{u_n}$.

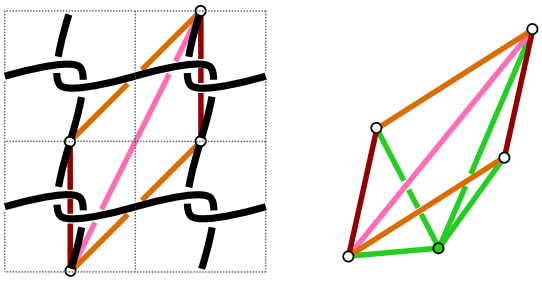

(a) We introduce three edges below the plane to form a one-vertex triangulation of the torus, from which we cone down to cusp $\mathfrak{c}_2$ to find our first two tetrahedra.

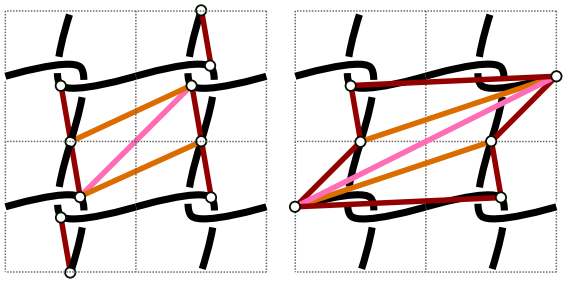

(b) We can drag the endpoints of each edge along cusp $\mathfrak{c}_0$ and reuse them in new positions. Here we also include extra copies of the red edge.

Figure 2.6. Beginning with a standard cusp for $\mathfrak{c}_2$, then dragging the edges upwards.

the plane (see Figure 2.7b), so we can cone up to $\mathfrak{c}_1$ at $T^2 \times \{-\infty\}$, resulting in another pair of tetrahedra.

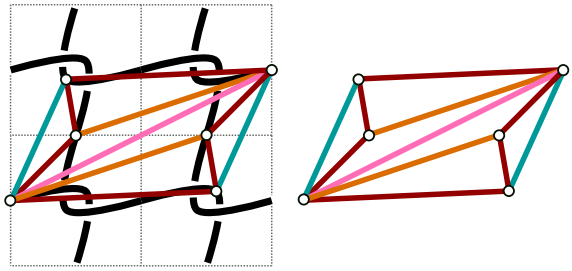

(a) By adding only one extra edge, we form two more tetrahedra. Note that the two 'inner' vertices in this figure are lower than the others.

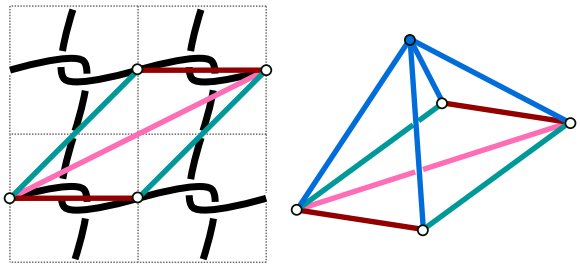

(b) The top faces of the new tetrahedra form a one-vertex triangulation of the torus above the plane, and so we may cone upwards to cusp $\mathfrak{c}_1$, forming our final two tetrahedra.

Figure 2.7. Forming the centre tetrahedra, then coning up to cusp $\mathfrak{c}_1$.

Note that there are two pairs of faces that were not implicitly paired in our construction (faces 012 and 013 of tetrahedra 0 and 1, using the labelling of Figure 2.9), but it is not too difficult to see that different lifts of the two tetrahedra can be isotoped so that these faces coincide. Regardless, we enter our triangulation as in Figure 2.8 into Regina, where it is recognised as `s776 #3`. Since the complement of M_3 is homeomorphic to the SnapPea census manifold `s776`, this confirms that we have built the correct manifold. Moreover, the '`#3`' tells us that this is the third *minimal* triangulation of M_3 that appears in Burton's census [Bur14].

Tetrahedron	Face 012	Face 013	Face 023	Face 123
0	1(210)	1(031)	2(123)	4(132)
1	0(210)	0(031)	3(123)	5(132)
2	3(021)	3(031)	3(032)	0(023)
3	2(021)	2(031)	2(032)	1(023)
4	5(021)	5(031)	5(032)	0(132)
5	4(021)	4(031)	4(032)	1(132)

Figure 2.8. The first 6-tetrahedron triangulation of M_3, which is recognised as `s776 #3`.

Removing the four tetrahedra corresponding to the two standard cusps, we have a core

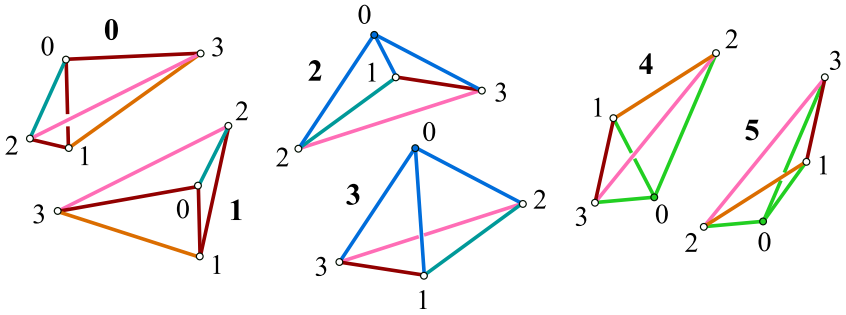

FIGURE 2.9. All tetrahedra with edges coloured as in Figures 2.6 and 2.7, and vertices labelled as in Figure 2.8.

consisting of two tetrahedra. As seen in Figure 2.10, the boundary edges visible from above the plane have slopes $\mathcal{P}_1 = \{ {}^1\!/_0, -{}^1\!/_1, -{}^2\!/_1 \}$, using the framing of $\mathfrak{c}_1$. It turns out that the boundary edges visible from below the plane also have slopes $\mathcal{P}_2 = \{ {}^1\!/_0, -{}^1\!/_1, -{}^2\!/_1 \}$, with respect to the framing of $\mathfrak{c}_2$ (also shown in Figure 2.10). We have therefore constructed $\mathbf{T}_1 = \mathcal{T}(\mathcal{P}_1, \mathcal{P}_2; 2)$.

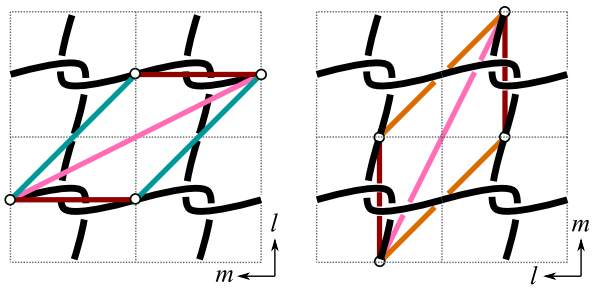

FIGURE 2.10. The boundary edges for $\mathbf{T}_1$. In cusp $\mathfrak{c}_1$ (left), we see that the red edge has slope $1/0$, the teal edge has slope $-1/1$, and the pink slope has slope $-2/1$. In cusp $\mathfrak{c}_2$ (right), we see that the red and pink edges also have slopes $1/0$ and $-2/1$ with respect to the $\mathfrak{c}_2$ framing, and the orange edge has slope $-1/1$.

2.4.3. Additional triangulations

The second triangulation we construct starts with the same edges below the plane, with slopes ${}^1\!/_0, -{}^1\!/_1, -{}^2\!/_1$. We repeat the same process as for the first triangulation, except that the new edge we introduce above the plane is the opposite diagonal to the one chosen previously. That is, when we introduce the teal edge, instead of placing it where it has slope $-{}^1\!/_1$, we place it as in Figure 2.11, where it has slope $-{}^3\!/_1$. In this way we obtain $\mathbf{T}_2 = \mathcal{T}(\mathcal{Q}_1, \mathcal{P}_2; 2)$, with gluing information as in Figure 2.12. Recall that the symmetry of M_3 allows us to interchange cusps, and so the same triangulation can be used as $\mathbf{T}_2' = \mathcal{T}(\mathcal{P}_1, \mathcal{Q}_2; 2)$.

Finally, for a triangulation with non-negative boundary slopes, we construct the triangulation $\mathbf{T}_3 = \mathcal{T}(\mathcal{R}_1, \mathcal{R}_2; 5)$. Starting with the edges below the plane with slopes ${}^0\!/_1, {}^1\!/_1, {}^1\!/_0$, we form two tetrahedra by coning down to $T^2 \times \{-\infty\}$, as before. Next, by viewing the two triangles of this once-punctured torus as a quadrilateral with the ${}^1\!/_1$ slope as the diagonal, we cone *into* a point on $\mathfrak{c}_0$ above the plane to form another two tetrahedra (see Figure 2.13, left).

Observe that we can drag the red edge along the link to account for two of these edges, but we need to introduce an additional two edges for the others. This time, we repeat the

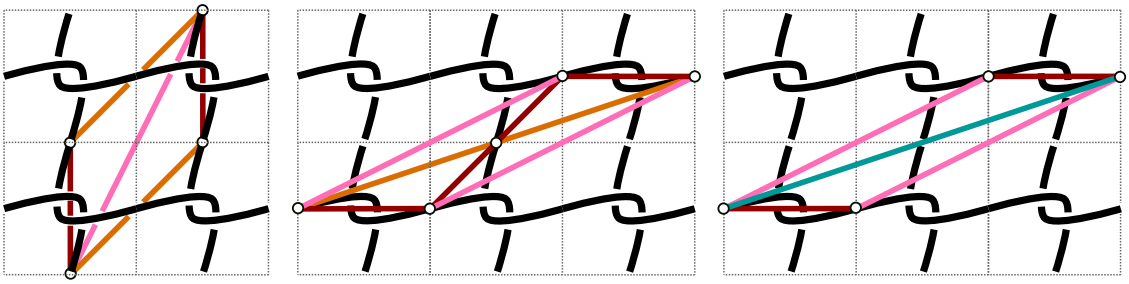

Figure 2.11. For $\mathbf{T}_2$, we start with the same edges below the plane but this time we consider different lifts in the universal cover, and introduce the teal edge so that it now has slope $-3/1$ with respect to the framing of $\mathfrak{c}_1$.

Tetrahedron	Face 012	Face 013	Face 023	Face 123
0	1(102)	1(310)	2(123)	4(132)
1	0(102)	0(310)	3(123)	5(132)
2	3(021)	3(031)	3(032)	0(023)
3	2(021)	2(031)	2(032)	1(023)
4	5(021)	5(031)	5(032)	0(132)
5	4(021)	4(031)	4(032)	1(132)

Figure 2.12. The second 6-tetrahedron triangulation of M_3, which is recognised as `s776 #4`. Note that the highlighted cells are the only places this triangulation differs from the previous one.

same process from above the plane; introducing 2 edges with slopes $^0/_1$ and $^1/_1$, and reusing the red edge, which has slope $^1/_0$ (with respect to the framing of $\mathfrak{c}_1$). We then cone into the centre again from above, making use of edges previously introduced (see Figure 2.13, right). At this point we notice that the edges we have introduced from above and below actually enclose another tetrahedron in the centre. Finally, we can cone up to $\mathfrak{c}_1$ as usual. In total, this yields a 9-tetrahedron triangulation of M_3. While this triangulation is not immediately recognisable to Regina (see gluing information in Figure 2.14), simplification confirms that it is indeed `s776`, and we have therefore constructed $\mathbf{T}_3 = \mathcal{T}(\mathcal{R}_1, \mathcal{R}_2; 5)$.

In the tables of Appendix B, we determine the number of tetrahedra t_1, t_2 required to construct layered solid tori for filling slopes r/s, t/u, relative to the boundary slopes of the chosen triangulation $\mathcal{T}(\mathcal{S}_1, \mathcal{S}_2; t_0)$, by counting the number of steps in the Farey graph. The total number of tetrahedra required for our triangulation of any filling $M_3(r/s, t/u)$ can be read off these tables as $t_0 + t_1 + t_2$. Meanwhile, using SnapPy to recognise a filling of M_3 as a census knot KT_v immediately tells us that T is the complexity of the knot. Hence, for each

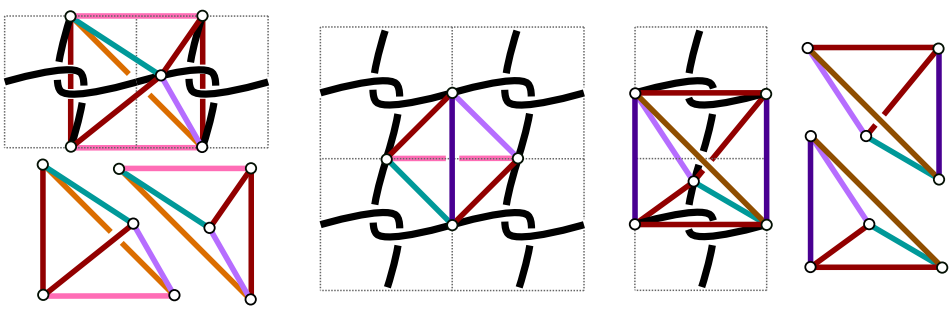

Figure 2.13. Edges forming 5 tetrahedra, as described in the construction of $\mathbf{T}_3$.

Tetrahedron	Face 012	Face 013	Face 023	Face 123
0	1(021)	2(023)	3(203)	5(213)
1	0(021)	2(132)	4(203)	6(213)
2	3(130)	4(310)	0(013)	1(031)
3	4(021)	2(201)	0(023)	7(213)
4	3(021)	2(310)	1(203)	8(213)
5	6(021)	6(031)	6(032)	0(213)
6	5(102)	5(031)	5(032)	1(213)
7	8(102)	8(031)	8(032)	3(213)
8	7(021)	3(031)	7(032)	4(213)

FIGURE 2.14. The 9-tetrahedron triangulation $\mathbf{T}_3$ of M_3, which is recognised as `s776` after simplification. Tetrahedra 5, 6 and 7, 8 form two standard cusps, while tetrahedra 0-4 form the core. Labelling of the core tetrahedra is as in Figure 2.15.

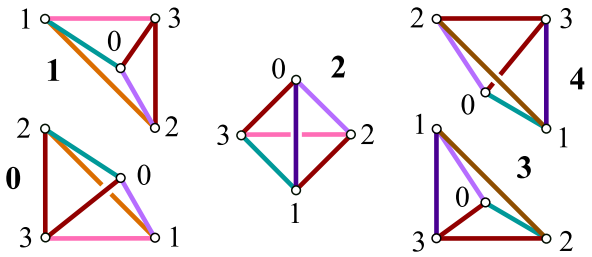

FIGURE 2.15. Labelling of the 5 tetrahedra that make up the core of $\mathbf{T}_3$.

knot in Tables B.2 to B.9, we can quickly see that $T = t_0 + t_1 + t_2$, unless one of the slopes r/s, t/u is an integer. Since every knot in $\mathbf{C}_{\mathbb{Q}}$ is accounted for in Appendix B, we consider the proof of Theorem 2.18 complete.

2.4.4. Triangulations of integer fillings

If we study the behaviour of the triangulations $\mathbf{T}_1$, $\mathbf{T}_2$, and $\mathbf{T}_3$ when a layered solid torus is used to realise an *integer* filling, there are elementary moves that can reduce the number of tetrahedra required.

It turns out that these elementary moves essentially convert one of our layered solid tori into a *layered chain*, as described by Burton in his PhD thesis [Bur03]. Like a layered solid torus, a layered chain is built up by layering some number of tetrahedra onto a surface, except in this case there are minor restrictions on which edges can be covered. At the end of the layering step, exposed faces are identified to each other by folding. In general, the starting surface for this construction is a twice-punctured annulus, triangulated by four faces.

However, if an appropriate 4-face triangulation of a boundary *torus*, as seen in Figure 2.16, is found in a manifold, then a layered chain can be used to realise a Dehn filling. This was done in [RST21]. We call a boundary triangulation *permissible* if it has one of the forms shown in Figure 2.16. In order to describe fillings of a permissible cusp using a layered chain, we let α be the curve parallel to edges a and b in Figure 2.16, and let β be the curve parallel to the concatenation of edges c and e. As usual, we take α, β to mean either the curve itself or the slope of the curve, depending on context.

The slope of the filling can be determined in the familiar way, by locating the curve made homotopically trivial by the closing fold, and tracing this curve back through the layers until

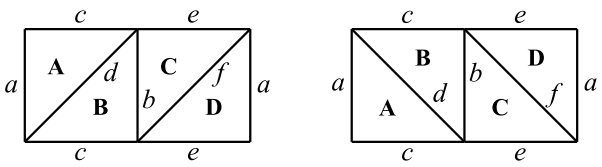

Figure 2.16. A *permissible boundary* that a layered chain may be attached to. We say that the boundary on the left has *positive diagonals*, while the boundary on the right has *negative diagonals*.

it can be seen with respect to the original boundary triangulation. See [RST21, Fig.2] for an example of this. The aforementioned restriction that affects layering in this construction is that the edges labelled a and b in Figure 2.16 can never be covered. As a result, the α curve can never be made trivial by a fold. Moreover, the only Dehn fillings in a permissible cusp that can be realised using a layered chain are those with slopes $p \cdot \alpha + \beta$, $p \in \mathbb{Z}$.

Now, note that we can form a 4-tetrahedron cusp from a permissible boundary triangulation by coning up to a point, just as we did to form a standard cusp from a one-vertex boundary. Hence, if a link complement admits a triangulation with such a 4-tetrahedron cusp, we can remove these tetrahedra, determine the slopes of α and β, then perform $p \cdot \alpha + \beta$ Dehn fillings by attaching an appropriate layered chain.

In the following, we distinguish between the two boundary triangulations shown in Figure 2.16, based on whether their diagonals have positive or negative slope in the figure, and determine the slopes α and β with respect to the framing of cusp $\mathfrak{c}_i$ in M_3. Let $\hat{\mathcal{S}}_i = \{\alpha, \beta; \pm\}$ be the *slope information* for a permissible boundary, where $\alpha, \beta \in \mathbb{Q} \cup \{ 1/0 \}$ and the '$\pm$' refers to the slope of the diagonals.

Lemma 2.19. The number of tetrahedra t required to Dehn fill a permissible cusp $\mathfrak{c}$ with slope information $\{\alpha, \beta; \pm\}$ along the filling slope $p \cdot \alpha + \beta$ is

$$t = \begin{cases} |\, p - 1 \,|, & \text{if } \mathfrak{c} \text{ has positive diagonals, or} \\ |\, p + 1 \,| & \text{if } \mathfrak{c} \text{ has negative diagonals.} \end{cases}$$

Proof. We focus on the $t = 0$ case. For both of the permissible cusps shown in Figure 2.16, consider the alternative fundamental domain realised by cutting along f and regluing face **D** along the edge e. In each case, faces **B** and **C** can be identified by folding across edge b, which causes edge e and edge d to be identified in the process. Then, faces **A** and **D** can be identified by folding across $e \sim d$.

In the boundary with positive diagonals, the curve made trivial by these folds is $\alpha + \beta$, whereas in the boundary with negative diagonals, the curve made trivial is $-\alpha + \beta$.

For $t > 0$, layering is first used to achieve a fundamental domain with enough skewing so that the analogous folds make the desired slope trivial. Each increase in $|p|$ requires one additional tetrahedron. □

Recall from Section 2.4.1 the notation $\mathcal{T}(\mathcal{S}_1, \mathcal{S}_2; t_0)$, used to describe a triangulation of M_3. Such a triangulation is assumed to have two standard cusps, so that by removing a pair of tetrahedra from the cusp $\mathfrak{c}_i$, a 2-triangle torus boundary is revealed. The $\mathcal{S}_i$ describe the boundary slopes of each such boundary, with respect to the framing of that cusp. Then t_0 is the number of tetrahedra left over in the 'core'.

Now, we use $\mathcal{T}(\hat{\mathcal{S}}_1, \mathcal{S}_2; t_0)$ to describe a triangulation of M_3 where this time we assume $\mathfrak{c}_1$ is a *permissible* cusp with slope information given by $\hat{\mathcal{S}}_i = \{\alpha, \beta; \pm\}$. We can construct triangulated Dehn fillings of M_3 from this triangulation by removing the $2 + 4 = 6$ tetrahedra from the standard and permissible cusps, before attaching a layered solid torus to the $\mathfrak{c}_2$ boundary and a layered chain to the $\mathfrak{c}_1$ boundary. Moreover, the size of such a triangulation can again be determined as the sum of t_0 and the number of tetrahedra required for each Dehn filling: say t_1 for the layered chain, and t_2 for the layered solid torus.

Recall that $\mathcal{R}$ is the set of slopes $\{{}^1\!/_0, {}^1\!/_1, {}^0\!/_1\}$. Let $\mathcal{R}' = \{{}^1\!/_0, -{}^1\!/_1, {}^0\!/_1\}$. In addition, let $\hat{\mathcal{V}} = \{{}^1\!/_0, {}^1\!/_1; -\}$ and $\hat{\mathcal{U}} = \{{}^1\!/_0, -{}^5\!/_1; +\}$. Also, let $\mathbf{C}_{\mathbb{Z}}$ be the set of census knots identified in Appendix A with at least one integer filling slope.

Theorem 2.20. There exist triangulations $\hat{\mathbf{T}}_4$ and $\hat{\mathbf{T}}_5$ of the magic manifold with

$$\hat{\mathbf{T}}_4 = \mathcal{T}(\hat{\mathcal{V}}_1, \mathcal{R}_2; 2), \text{ and } \hat{\mathbf{T}}_5 = \mathcal{T}(\hat{\mathcal{U}}_1, \mathcal{R}'_2; 2),$$

such that a minimal triangulation of any $K \in \mathbf{C}_{\mathbb{Z}} \setminus \{K2_1\}$ can be realised by filling either $\hat{\mathbf{T}}_4$ or $\hat{\mathbf{T}}_5$ with a layered chain in $\mathfrak{c}_1$ and a layered solid torus in $\mathfrak{c}_2$.

Remark 2.21. After describing $\hat{\mathbf{T}}_4$, we will see that it *can* be used to build a triangulation of $K2_1 = M_3({}^2\!/_1, {}^1\!/_1)$, however, it requires 5 tetrahedra: 2 in the core, 2 in the layered chain for the ${}^2\!/_1$ filling, and 1 in the layered solid torus for the ${}^1\!/_1$ filling. It turns out that this triangulation can be simplified by two elementary moves. First, the layering of the single tetrahedron in the layered solid torus introduces a degree-3 edge, so a *3-2* move can be performed. Then, the folding that realises the ${}^1\!/_1$ filling results in a degree-2 edge, so a *2-0* move can be performed. Hence, we get a triangulation consisting of $5 - 1 - 2 = 2$ tetrahedra.

Proof of Theorem 2.20. The core of $\hat{\mathbf{T}}_4$ is shown in Figure 2.17. Note that tetrahedra 0 and 1 are taken directly from $\mathbf{T}_3$. On the right, we see the four faces that form the permissible boundary, which has negative diagonals. This view also shows that the α curve has slope ${}^1\!/_0$, while the β curve has slope ${}^1\!/_1$, each with respect to the $\mathfrak{c}_1$ framing. The full triangulation including the six cusp tetrahedra is given in Figure 2.18.

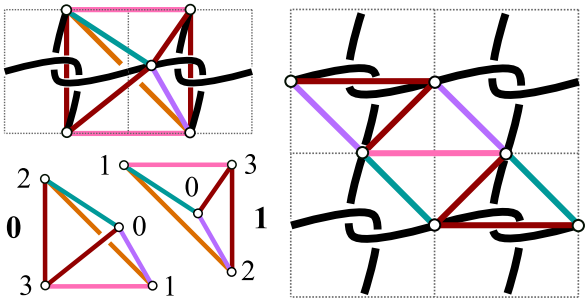

FIGURE 2.17. The two core tetrahedra in $\hat{\mathbf{T}}_4$, with the labelling used in Figure 2.18. Recall the framing of each cusp from Figure 2.4.

The 2-tetrahedron core of $\hat{\mathbf{T}}_5$ is shown in the top of Figure 2.19. A considerable amount of skewing is required to visualise the $\mathfrak{c}_1$ and $\mathfrak{c}_2$ boundaries, as we see in Figure 2.19, bottom. The red, pink and orange edges form the boundary triangulation for cusp $\mathfrak{c}_2$. It is relatively easy to see that their slopes are indeed ${}^1\!/_0$, ${}^0\!/_1$ and $-{}^1\!/_1$, respectively, with respect to the framing of $\mathfrak{c}_2$.

Tetrahedron	Face 012	Face 013	Face 023	Face 123
0	1(021)	5(321)	7(231)	2(213)
1	0(021)	6(321)	4(231)	3(213)
2	3(021)	3(031)	3(032)	0(213)
3	2(021)	2(031)	2(032)	1(213)
4	7(021)	5(031)	5(032)	1(302)
5	6(021)	4(031)	4(032)	0(310)
6	5(021)	7(031)	7(032)	1(310)
7	4(021)	6(031)	6(032)	0(302)

Figure 2.18. The triangulation $\hat{\mathbf{T}}_4$ of M_3 (recognised as `s776` after simplification). Tetrahedra 2 and 3 form a standard cusp, tetrahedra 4-7 form a permissible cusp, and tetrahedra 0 and 1 form the core.

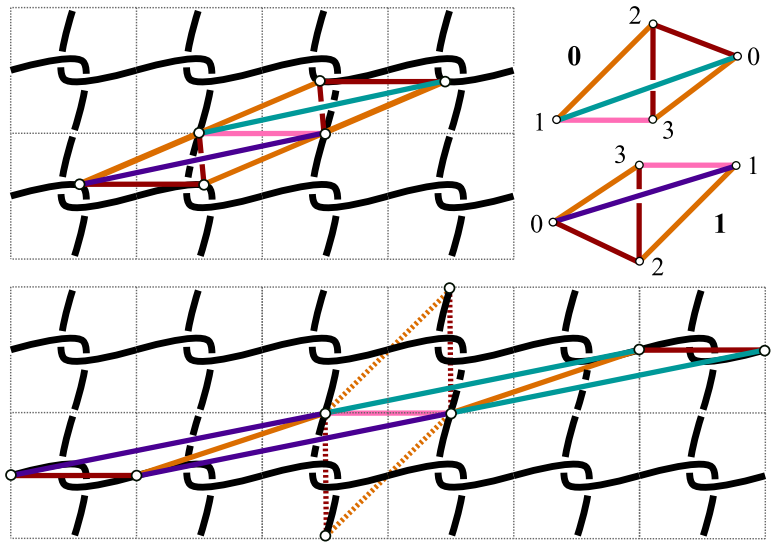

Figure 2.19. The two core tetrahedra in $\hat{\mathbf{T}}_5$, with the labelling used in Figure 2.20.

For the permissible boundary in $\mathfrak{c}_1$, we first skew the tetrahedra in Figure 2.19, top, by sliding the top-right red edge further right and the bottom-left red edge further left. Then we use different lifts of two of the faces, stretching our fundamental domain even further to the top-right and bottom-left, as seen in Figure 2.19, bottom.

This realises a permissible boundary with positive diagonals. Here, α is again equal to $1/0$, and we can see that the β slope is $-5/1$, with respect to the $\mathfrak{c}_1$ framing. The gluing information for the complete triangulation is given in Figure 2.20. On this occasion we label vertices with the opposite orientation to our established anti-clockwise convention, since this allows us to reuse most of the gluing information from $\hat{\mathbf{T}}_4$.

For the permissible cusp with slope information $\hat{\mathcal{V}} = \{1/0, 1/1; -\}$, Lemma 2.19 tells us that a Dehn filling with slope $k/1$ given by $(k-1)\left[\begin{smallmatrix}1\\0\end{smallmatrix}\right] + \left[\begin{smallmatrix}1\\1\end{smallmatrix}\right]$ requires a layered chain of $\left|(k-1)+1\right| = |k|$ tetrahedra. In Table B.10, we demonstrate that the knots in $\mathbf{C}_{\mathbb{Z}} \setminus \{K2_1\}$ with positive slopes achieve minimal triangulations using $\hat{\mathbf{T}}_4$.

Meanwhile, in the permissible cusp with slope information $\hat{\mathcal{U}} = \{1/0, -5/1; +\}$, a Dehn filling with slope $k/1$ given by $(k+5)\left[\begin{smallmatrix}1\\0\end{smallmatrix}\right] + \left[\begin{smallmatrix}-5\\1\end{smallmatrix}\right]$ requires a layered chain of $\left|(k+5)-1\right| = \left|k+4\right|$ tetrahedra. As such, the knots in $\mathbf{C}_{\mathbb{Z}}$ with negative slopes achieve minimal triangulations using $\hat{\mathbf{T}}_5$, as can be seen in Table B.11. □

Tetrahedron	Face 012	Face 013	Face 023	Face 123
0	4(231)	5(321)	1(320)	2(213)
1	7(231)	6(321)	0(320)	3(213)
2	3(021)	3(031)	3(032)	0(213)
3	2(021)	2(031)	2(032)	1(213)
4	7(021)	5(031)	5(032)	1(302)
5	6(021)	4(031)	4(032)	0(310)
6	5(021)	7(031)	7(032)	1(310)
7	4(021)	6(031)	6(032)	0(302)

FIGURE 2.20. The 8-tetrahedron triangulation $\hat{\mathbf{T}}_5$ of M_3, which is recognised as `s776` after simplification. The only differences between this and $\hat{\mathbf{T}}_4$ are the shaded cells, but note that on this occasion the vertex labels have the opposite orientation to our established convention.

Remark 2.22. The intuition behind 'distinguished fillings' is made more apparent by the tables of Appendix B. In each family of knots related by twisting, from the distinguished fillings onwards, only a single additional tetrahedron is required to realise each additional twist.

BEYOND THE CENSUS KNOTS. Note that all families with distinguished fillings contain two 9-tetrahedron census knots, with one occurring for a positive value of n, and the other for a negative n. In the case of $\mathcal{F}_0$, the same 9-tetrahedron knot is seen twice, so we choose to ignore the negative value. We label these values n^+ and n^- and refer to them as the *known limits* for a family of census knots.

Suppose $\mathcal{T}(\mathcal{S}_1, \mathcal{S}_2; t_0)$ is the triangulation that achieves minimality for the census knots in a family $\mathcal{F}_i$ with primary slope r/s. Here, we let $\mathcal{S}_1$ represent either the boundary slopes for a standard cusp or the slope information for a permissible cusp. Similarly, we use t_1 to denote the number of tetrahedra in either the layered solid torus or the layered chain that realises the r/s filling. Furthermore, let $t_2^{\pm}$ be the number of tetrahedra in the layered solid torus that realises the filling for the census knots at the $n^{\pm}$ known limits of this family.

If $\mathcal{F}_i(n)$ is the knot in family $\mathcal{F}_i$ corresponding to the secondary slope with index n, then we write its complexity as $c(\mathcal{F}_i(n)) = t_0 + t_1 + t_2$. Using the notation of the known limits, we have $c(\mathcal{F}_i(n^{\pm})) = t_0 + t_1 + t_2^{\pm} = 9$.

Conjecture 2.23. For all $\mathcal{F}_i$ listed in Section A.1, with known limits $n^{\pm}$, the extension of the layered solid torus in cusp $\mathfrak{c}_2$ will generate minimal triangulations for all other knots in the family, with $c(\mathcal{F}_i(n^{\pm} \pm j)) = 9 + j$.

An *attaching circle* on a genus-2 boundary surface, which will bound a disc after filling.

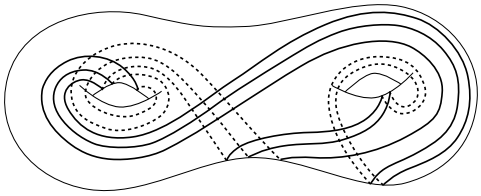

Chapter 3. A generalisation

Reimagining layered handlebodies for a constructive algorithm

While layered solid tori are frequently used and extremely well-understood, their higher genus counterparts have received much less attention. This is because, as genus grows, the combinatorics involved in constructing a layered handlebody becomes increasingly unmanageable. In this chapter, we take a closer look at higher-genus layered handlebodies, and describe a construction more convenient to work with. The main contribution is an implementable algorithm that can be used to construct explicit triangulations exhibiting all of the most desirable features of a layered triangulation.

SECTION 3.1. *Higher-genus layered handlebodies*

Recall that the JR-construction of a genus-g layered handlebody begins by layering a minimum of $3g-2$ tetrahedra onto a triangulated g-spine with Euler characteristic $1-g$. As we have seen, when $g=1$, the Farey graph acts as a vast but well-structured playground, from which we continue to uncover properties related to layered solid tori. However, the moment we step into the world of higher-genus layered handlebodies, we are met with overwhelming levels of choice:

- Where the one-triangle Möbius band was the unique 1-spine, there are five different 2-spines, and increasingly many for $g \geq 3$;
- Where there was a single internal edge on the Möbius triangle to layer over, there are $3g-2$ internal edges in a g-spine, and the order of layering matters;
- Where there were 3 boundary edges in the one-vertex triangulation of a torus, there are $6g-3$ boundary edges in a one-vertex triangulation of a genus-g surface, so the valence of the flip graph is $6g-3$;
- Where the flip graph for genus 1 was a tree, a higher-genus flip graph is *not* a tree, and shortest paths may not be unique.

To emphasise the second point, even after restricting to one of the five spines in genus 2, Jaco and Rubinstein state that there are 384 ways to layer four tetrahedra and obtain a genus-2 handlebody [JR06, p.84]. They note that this count does include duplicates up to isomorphism,

but that tabulation using Regina determined there are still 196 distinct 4-tetrahedron genus-2 handlebodies.

Despite the impracticality of working concretely with higher-genus handlebodies, Jaco and Rubinstein described how to build a closed manifold from two genus-g handlebodies, and proved the following theorem.

Theorem 3.1. (Jaco–Rubinstein, Theorem 10.1). Every closed, orientable 3-manifold admits a layered (and therefore one-vertex) triangulation.

Proof. We outline the sequence of results in [JR06] that contribute to the proof. Firstly, a compact 3-manifold whose boundary components each have a one-vertex triangulation may be extended to a triangulation of the entire manifold, without introducing new vertices [Lemma 9.3 of JR06]. In particular, any one-vertex triangulation on the boundary of a genus-g handlebody may be extended to a layered triangulation of the handlebody [Corollory 9.4 of JR06]. Moreover, any two distinct one-vertex triangulations of a closed orientable surface are related by a finite sequence of flips. This last point is stated in relevant terminology as Lemma 3.4 of [JR06], but can be traced back to Harer [Har86], Hatcher [Hat91], and Mosher [Mos96]. Since flips can be realised by layering, the boundary of one genus-g handlebody can always be adjusted to match the boundary of any other genus-g handlebody. Finally, since every closed, orientable 3-manifold admits a Heegaard splitting (which can be argued as a result of Moise's Theorem [Moi52]), a layered triangulation must also exist. □

To construct such a triangulation, the preceding existence argument would suggest starting with a triangulated genus-g Heegaard surface and a basic layered handlebody on each side. One would then identify a sequence of flips that can be realised by layering to match the boundary triangulations of each handlebody to the Heegaard surface. The slightly more practical approach that Jaco and Rubinstein [JR06, pp. 91–92] identified is to do all of the layering on one side of this picture, passing through the Heegaard surface, and continuing until the boundary triangulation can be folded to form the g-spine of the second handlebody.

Note that the folding described here requires a reflective symmetry across an edge in the boundary triangulation, since the second g-spine is formed by identifying all $4g-2$ boundary faces in pairs *simultaneously* by folding the $4g$-gon in half. To distinguish from the *local* folding defined in the introduction (where only two neighbouring faces are glued together), we will refer to the folding of an entire $4g$-gon as a *global fold*. Boundary triangulations that admit a global fold are called 2-*symmetric* in [JR06]. Understanding these special boundary triangulations for genus $g \geq 2$ (including their prevalence and distribution in the flip graph) is therefore important to understanding the JR-construction of a triangulated Heegaard splitting.

There are 9 distinct one-vertex triangulations of the genus-2 surface, which were classified using *chord diagrams* in [Mos96]. However, only five of these possess the 2-symmetry required for a global fold, corresponding to the five different 2-spines shown in Figure 30 of [JR06]. Indeed, Jaco and Rubinstein note that the non-isomorphic 2-symmetric triangulations of any genus-g surface are in one-to-one correspondence with the distinct g-spines of Euler characteristic $1-g$. Thus, the percentage of triangulations with this 2-symmetry goes to zero as genus increases [JR06, p.91].

With 9 distinct genus-2 boundary triangulations, the prospect of mapping out relationships between 2-symmetric triangulations is daunting, but not unfathomable. Unfortunately, the same cannot be said for $g \geq 3$. In 2002, Bacher and Vdovina [BV02] showed that this number skyrockets, with 1726 distinct one-vertex triangulations of a genus-3 boundary surface, 1 349 005 for genus 4, 2 169 056 374 for genus 5, and so on. The largest count they recorded was the number of distinct one-vertex triangulations of the genus-15 surface, which is

$$19\,903\,817\,294\,929\,565\,349\,602\,352\,185\,144\,632\,327\,980\,494\,486\,370.$$

3.1.1. Measuring complexity by width

As we saw in Chapter 2, layered solid tori appear frequently in minimal triangulations. While Jaco and Rubinstein [JR06] conjectured that layered handlebodies of *any* genus are likely to be minimal, we know considerably less about the prevalence of higher-genus handlebodies appearing as subcomplexes in low-complexity triangulations.

However, the complexity of a triangulation as defined by the number of its tetrahedra is not the only sensible measure of complexity. In the past decade or so, there has been increasing interest in 'widths' of triangulations, which are defined by applying graph-theoretical notions of width to the dual graphs of triangulations. For example, the *treewidth* of a triangulation is, loosely speaking, a measure of how 'tree-like' its dual graph is. Interest in treewidth is driven by algorithms that are *fixed parameter tractable* in the treewidth, meaning that the computation time is bounded above by a product of a polynomial function of the number of tetrahedra, and an exponential function of the treewidth; this means that for any fixed treewidth, the computation time reduces to a polynomial function, and hence the algorithm becomes 'tractable'. For examples of such fixed parameter tractable algorithms for solving various problems in 3-manifold topology, see [BD17; BLPS16; BMS18; BP14; BS13].

A related measure that gives an upper bound for treewidth is the *cutwidth* of a triangulation, which we formally define in Section 3.4.1. In 2019, Huszár and Spreer [HS19] proved that if M is a closed 3-manifold with Heegaard genus g, then the cutwidth of M is bounded above by $4g-2$. More accurately, they showed that the JR-construction of a genus-g layered triangulation satisfies this bound, so every manifold has at least one such triangulation. It is reasonable to predict that there may be manifolds for which a minimal triangulation is too large to feasibly compute with, while a layered triangulation has low enough cutwidth to be useful. Unfortunately, this feature is difficult to exploit in practice because the JR-construction is difficult to implement.

3.1.2. A more flexible construction

We overcome the issue of sparse 2-symmetric triangulations in the construction of triangulated Heegaard splittings by removing the requirement to form a second g-spine from a global fold. We still insist that faces are only ever glued by layering or folding, but because we perform folds locally between two faces at a time, we allow the instances of folding to be interspersed with additional layering, until no exposed faces remain.

To compare, note that the JR-construction of a triangulated splitting would have us traverse the flip graph by layering until we found a 2-symmetric triangulation that admits a global fold achieving the desired topology. In essence, this means finding a 2-symmetry that, upon folding, will kill the appropriate elements of the fundamental group. We achieve the same topology by

making curves homotopically trivial one-by-one.

This adjustment means that we may not have a g-spine at the centre of our handlebody. However, we still avoid introducing new vertices and, as we show in Theorem 3.33, the same cutwidth bound applies to our construction. Most importantly, we have an algorithm that has been successfully implemented using Regina to construct these triangulations explicitly. The algorithm executes a sequence of layering and folding to make specified curves homotopically trivial. This of course applies to the construction of triangulated Heegaard splittings, but may also be applied to the higher-genus analogue of Dehn filling, whereby a boundary component of genus g is filled so that g specified curves each bound a disc in the closed manifold [see, for example Lac02; Eas06].

In principle, our algorithm can be used to construct one-vertex triangulations in a variety of settings:

A. Starting with any one-vertex triangulation of a genus-g surface, we may build inwards to form a triangulated handlebody with the prescribed boundary triangulation.

B. Given a Heegaard splitting specified by a Heegaard diagram—that is, a closed orientable surface S marked with two sets of attaching circles, where each set specifies how to attach a handlebody on one of the sides of S—we can attach handlebodies to both sides of the splitting surface. The result is a triangulation of the closed 3-manifold corresponding to the given splitting.

C. Given any compact orientable 3-manifold M with boundary, together with a set of attaching circles in a boundary component B of M, we can build a triangulation of the generalised Dehn filling of B, as specified by the given attaching circles.

The version of our algorithm that is currently implemented requires a one-vertex triangulation of a 3-manifold (as in Setting C) with the added condition that there be only one boundary component.[1] As discussed, triangulated Heegaard splittings may be constructed in this setting, by taking the starting manifold to be a handlebody itself.

The remainder of this chapter proceeds as follows. In the next section, we study the 4-tetrahedron genus-2 handlebody with isomorphism signature `eHuGabdes`, to get a sense of how higher-genus layered handlebodies behave; particularly in comparison to layered solid tori. In Section 3.2, we introduce the notion of a *combinatorial filling diagram* as a way to encode the topological instructions of a Heegaard splitting (or generalised Dehn filling) combinatorially, with respect to a given triangulation. Our main algorithm is detailed in Section 3.3, and in Section 3.4, we prove Theorem 3.33, demonstrate our algorithm on simple examples, and summarise findings from some preliminary experimentation.

3.1.3. A case study

In recent years, a function has been incorporated into Regina, which generates a $(3g-2)$-tetrahedron triangulation of a genus-g handlebody. The triangulation generated by this function is a layered handlebody. The 4-tetrahedron genus-2 handlebody that Regina builds has isomorphism signature `eHuGabdes`, with gluing information as in Figure 3.1.

[1] An implementation compatible with Settings A and B would require tedious bookkeeping to move between 2- and 3-dimensional triangulations, but should otherwise be conceptually straightforward. Similarly, the restriction to a single boundary component is purely for the sake of more streamlined code.

Tetrahedron	Face 012	Face 013	Face 023	Face 123
0	–	1(023)	–	1(132)
1	2(013)	3(012)	0(013)	0(132)
2	3(301)	1(012)	–	–
3	1(013)	2(120)	–	–

Figure 3.1. Triangulation of a basic (4 tetrahedron) genus-2 handlebody built in Regina from the isomorphism signature `eHuGabdes`. Note that the labelling has been 'oriented' so that the order of vertex labels is consistent between tetrahedra.

We use this triangulation as a case study, reconstructing it from the outside inwards. We also highlight how folding relates to the location of compression discs, and how the curves bounding these discs can be traced through the layers of the handlebody. This information allows us to recover the $\mathbb{R}^3$ embedding of `eHuGabdes` shown in Figure 3.2.

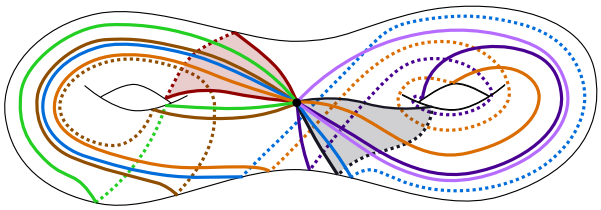

Figure 3.2. An embedding of the `eHuGabdes` handlebody into $\mathbb{R}^3$. The red and blue curves are those that are made homotopically trivial by folds (see Section 3.1.5), and thus bound discs in the handlebody (shaded). The remaining curves represent 6 of the 9 edges in the boundary triangulation of `eHuGadbes`, shown here only to demonstrate that an $\mathbb{R}^3$ embedding that places the compression discs in a natural position is not necessarily the simplest embedding with respect to the boundary triangulation.

3.1.4. Tracing layers from the outside inwards

From the gluing information in Figure 3.1, we see that the unglued faces that form the boundary are: 0(012), 0(023), 2(023), 2(123), 3(023) and 3(123). Figure 3.3 shows all four tetrahedra, with tetrahedra 0, 2 and 3, oriented so that we are looking at the six boundary faces. Note that the colour of each edge is dictated by its *edge class*, which can be easily read off from the 'Skeletal Components' tab in the Regina GUI.

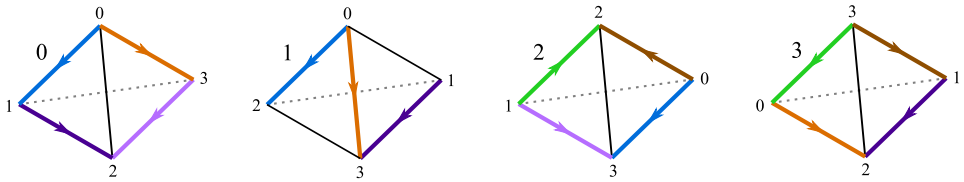

Figure 3.3. The four tetrahedra with labels corresponding to the gluing information in Figure 3.1. The coloured edges are those that help us reconstruct the triangulation in Figure 3.4.

We start reconstructing the triangulation by forming an octagon from the six boundary faces. There are multiple ways to do this; we choose to keep faces of the same tetrahedron connected, and otherwise make choices that are convenient for subsequent steps. In the following, we are viewing the triangulation of the handlebody from the outside. Hence, by 'inwards' we mean 'into the screen', or perhaps 'behind the page'. We also use 'layer' to mean a 2-dimensional sub-skeleton consisting of either 'outer' or 'inner' faces of each tetrahedron.

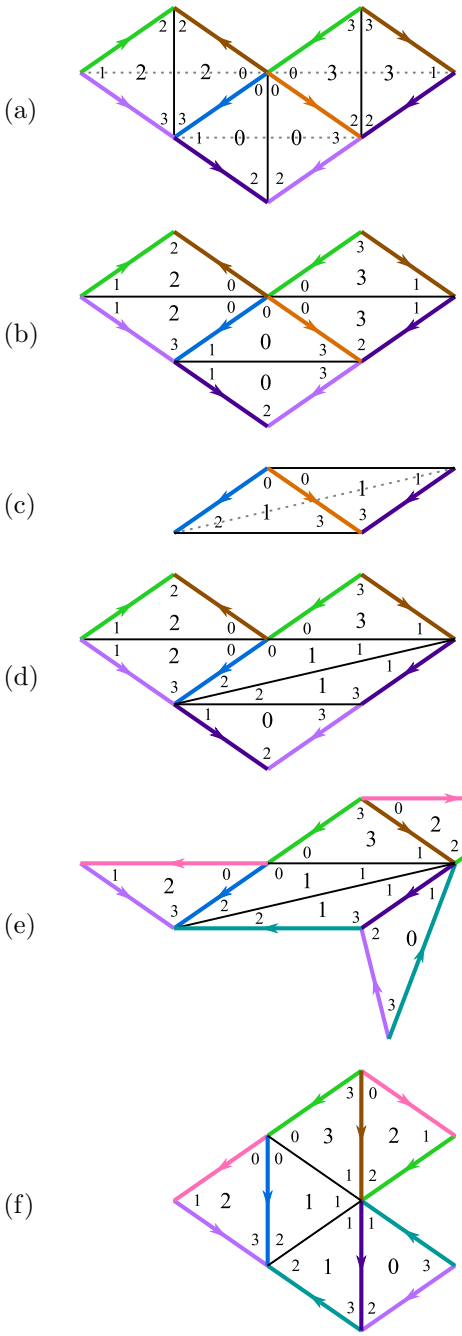

(a) Identifying the orange edges 0(03) and 3(02) of tetrahedra 0 and 3, and the blue edges 0(01) and 2(03) of tetrahedra 0 and 2, we form the outermost layer of the triangulation.

(b) Disregarding the outer faces now, we see the inner faces of these three tetrahedra, which form the next layer in.

(c) Recalling the gluing information from Figure 3.1, we attach tetrahedron 1 from behind, to the faces 0(013) and 3(012).

(d) The new innermost layer includes the two inner faces 1(012) and 1(123) of tetrahedron 1, the two inner faces of tetrahedron 2, and faces 0(123) and 3(013).

(e) At this point, we choose a new octagon to represent the same layer. We can describe this adjustment as 'cutting' along edges 2(01) and 0(13), and 'regluing' along edges 2(02) and 0(12), respectively.

(f) This is the same representation as the previous one, but it has been isotoped so that the three remaining face pairings $0(123) \sim 1(132)$, $1(012) \sim 2(013)$, and $2(012) \sim 3(301)$ can be seen as natural folds across the purple, blue, and brown edges, respectively.

FIGURE 3.4. Reconstructing `eHuGabdes` from the outside inwards.

3.1.5. IDENTIFYING MERIDIAN CURVES FROM FOLDS

In genus 1, a layered solid torus is completely determined by the slope of a curve that bounds the (unique) meridian disc, and the way this curve intersects the boundary edges. For higher-genus handlebodies, there are multiple curves that bound non-isotopic compression discs, and we no longer have the convenience of a 2-dimensional basis to describe each such curve in terms of a slope. Nonetheless, any fold causes some curve to be made homotopically trivial.

In the following sequence, we identify the curves made trivial by folds, and follow them back through the steps in Figure 3.4, to see how they appear on the boundary of the layered handlebody. Since we are particularly interested in curves that correspond to meridians of handles, we typically ignore separating curves.

(a)

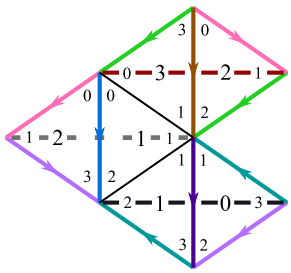

The three folds are made across the three vertical edges, as stated in Figure 3.4(f). The curves that are made homotopically trivial by these folds are indicated by the dashed lines. Note that the curve cutting across 1(012) and 2(013) is a separating curve, so we are less interested in its fate.

(b)

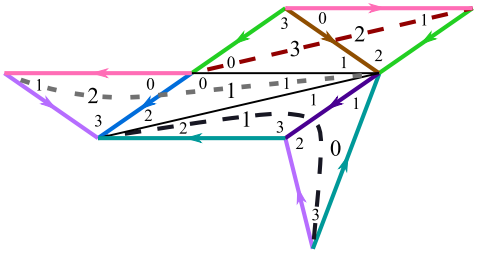

We then retrace the steps in Figure 3.4, keeping track of these curves. When we isotope the octagon, the embedding of each curve follows.

(c)

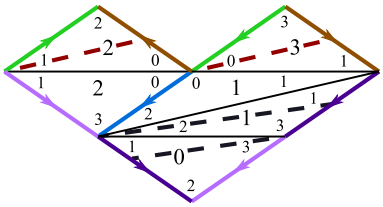

After reversing the 'cutting' and 'regluing' of Figure 3.4(e), the red and blue curves are each split into two segments that meet via the brown and purple edge identifications, respectively.

(d)

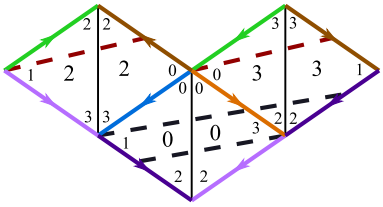

Having identified the location of the red and blue curves with respect to the original octagon, their position with respect to the boundary triangulation becomes apparent.

Figure 3.5. Following the position of homotopically trivial curves back through the sequence in Figure 3.4, to determine their location with respect to the boundary triangulation.

This process gives insight into our philosophy for defining *combinatorial filling diagrams*, as detailed in the following section. Where a layered solid torus is characterised by one curve that bounds a unique meridian, we use g non-separating curves to specify the location of handles that characterise the topology of a genus-g filling. And since we cannot describe these curves using slopes, we instead describe them by their position with respect to a boundary triangulation.

Section 3.2. *Combinatorial filling diagrams*

We begin by defining a *topological* filling diagram as a Heegaard-type diagram. We then introduce *pinched* filling diagrams, and justify their equivalence to topological filling diagrams. The remainder of this section is then dedicated to introducing *combinatorial filling diagrams*, which consist of a one-vertex triangulation of a compact orientable 3-manifold, along with combinatorial data encoding the position of attaching circles with respect to the boundary triangulation.

3.2.1. Topological filling diagrams

Given a closed orientable surface Σ of genus g, a *system of attaching circles* $\gamma = \{\gamma_1, \ldots, \gamma_g\}$ on Σ is a collection of g embedded closed curves that are disjoint, and are non-separating as a multicurve on Σ. Define a *topological filling diagram* D to be a compact orientable 3-manifold

M, along with a non-empty union $B = B^1 \cup \cdots \cup B^k$ of boundary components of M, where each boundary component B^i is marked with a system γ^i of attaching circles; we write $D = (M, B, \gamma)$, where $\gamma = \gamma^1 \cup \cdots \cup \gamma^k$. Occasionally, when it is necessary to make a clear distinction from attaching circles in some other context (such as Heegaard diagrams, as described in Setting B), we might instead refer to the attaching circles in a topological filling diagram as *filling curves*.

For simplicity, we focus on the case where M has exactly one boundary component, in which case $B = \partial M$.

Recall from Setting B that a Heegaard diagram consists of a surface Σ with two systems β and γ of attaching circles; this specifies a closed 3-manifold M^* because β and γ specify how to glue two handlebodies together along Σ. From such a Heegaard diagram, we can easily obtain a topological filling diagram D that specifies the same 3-manifold M^*: simply take $D = (M, \partial M, \gamma)$, where M is a handlebody obtained by filling Σ according to β.

A topological filling diagram can be used to build the corresponding filled manifold as described in the following 'folklore' algorithm. For the case of Heegaard diagrams see, for example, Rolfsen's textbook [Rol76, Chapter 9.].

Algorithm 3.2. (Topological filling algorithm). As input, take the filling diagram $\mathcal{D} = (M, B, \gamma)$, where M is a compact orientable 3-manifold with a genus-g boundary B marked with the system of attaching circles γ, as well as a genus-g handlebody H.

1. Remove a collar neighbourhood of the discs in H bounded by the meridians of its handles. These pieces are 2-handles. Set $H' = H - \{\text{2-handles}\}$ and note that H' is homeomorphic to a 3-ball with $2g$ marked discs.
2. Attach the 2-handles to M, by identifying the meridian curves from H to the attaching circles γ in ∂M. Set $M' = M \cup \{\text{2-handles}\}$ and note that the boundary of M is homeomorphic to S^2 with $2g$ marked discs.
3. Glue H' to the S^2 boundary of M', ensuring that the marked discs are glued back to each other, as they were in H. [2]
4. Return the filled 3-manifold $M(\gamma)$.

3.2.2. Pinched filling diagrams

Let us introduce an adaptation of Algorithm 3.2, which is more directly comparable to the triangulation built by our combinatorial algorithm. We refer to this as the *pinched filling algorithm*.

Suppose $D^2 \times [-1, 1]$ is a collar neighbourhood of a properly embedded disc, with a point $(p, 0) \in \partial D^2 \times \{0\}$. We define the corresponding *wedge neighbourhood* to be a quotient of the collar neighbourhood, found by collapsing the segment $\{p\} \times [-1, 1]$ to the single point $(p, 0)$.

In the pinched filling algorithm, instead of removing collar neighbourhoods of the discs in H bounded by meridians, we remove wedge neighbourhoods (as in Figure 3.6) and set $\hat{H}$ to be $H - \{\text{wedges}\}$. Note that $\hat{H}$ is homeomorphic to a 3-ball with $2g$ marked discs, each with a marked point.

On the boundary of M, before attaching the wedge pieces, we isotope each attaching circle so that they all intersect at a single point (but remain pairwise disjoint away from this common point). This is always possible since the complement of the attaching circles in ∂M is path-connected. We denote the set of pinched attaching circles by $\hat{\gamma}$.

[2] This is always possible due to Alexander's lemma.

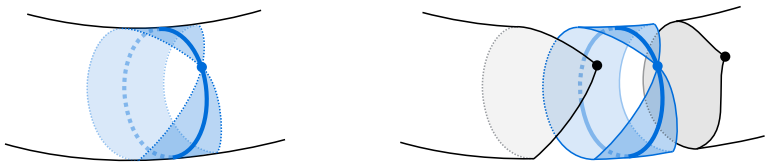

Figure 3.6. A wedge neighbourhood of a meridian disc. Removing a wedge from H leaves two marked discs on ∂H, each with a marked point.

The wedges from H can be attached to the pinched attaching circles on M, with the point of each wedge meeting the pinched point of the attaching circle. We set $\hat{M} = M \cup \{\text{wedges}\}$ and claim that the boundary of $\hat{M}$ is homeomorphic to a pinched 2-sphere (see Proposition 3.3 below).

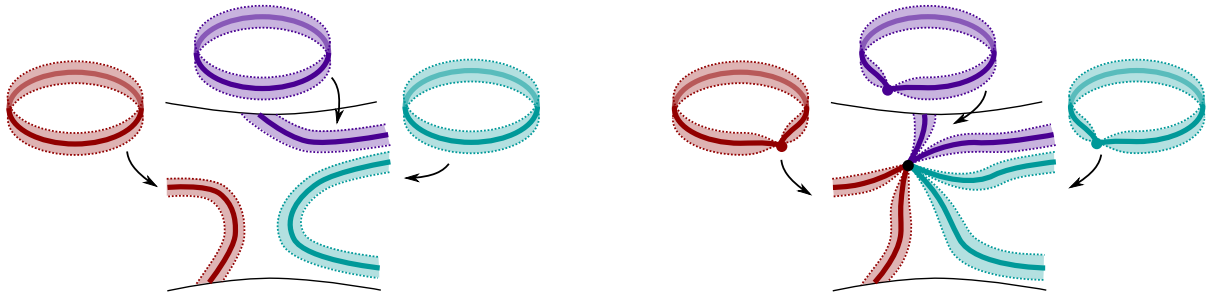

(a) Attaching 2-handles to attaching circles in the standard algorithm.

(b) Attaching wedges to pinched attaching circles in the pinched algorithm.

Figure 3.7. Comparing Step 2 of Algorithm 3.2 with the corresponding step in the pinched filling algorithm.

To conclude, we glue $\hat{H}$ to the boundary of $\hat{M}$, ensuring that the marked discs and marked points are glued to each other, as they were in H. This is possible due to Alexander's lemma.

In summary, the pinched filling algorithm takes a pinched filling diagram $\hat{D} = (M, B, \hat{\gamma})$, where the $\hat{\gamma}$ curves have been isotoped to meet at a point, and proceeds as in Algorithm 3.2, except that it uses wedges instead of 2-handles.

Proposition 3.3. The boundary of $\hat{M} = M \cup \{\text{wedges}\}$ is homeomorphic to a pinched 2-sphere and the pinched filling algorithm builds the same 3-manifold $M(\gamma)$ as Algorithm 3.2.

Proof. Recall that $M' = M \cup \{\text{2-handles}\}$ is the object obtained in Step 2 of Algorithm 3.2, and that its boundary is a 2-sphere.

We show that we can deformation retract M' to $\hat{M}$ inside $M(\gamma)$, without changing the topology of $M(\gamma)$; Figure 3.8 illustrates the idea of the proof in the genus 2 case. Note that since the algorithm fills the 2-sphere component with a 3-ball, we may assume that $M(\gamma) - M'$ is simply connected.

First, convert each 2-handle inside M' into a wedge by contracting a line segment on the interval boundary of the 2-handle to a point. This brings together two points on $\partial M'$ by pinching inwards into M', resulting in a pinched 2-sphere boundary.

Note that there is a path on the pinched 2-sphere boundary connecting any two distinct wedge points. Contract $g - 1$ such paths so that all wedge points are pulled together. This yields $\hat{M}$, which is the pinched version of M', and its boundary is still a pinched 2-sphere.

Since $\hat{M}$ exists inside $M(\gamma)$, the changes we made to the algorithm are valid. Moreover, the changes do not affect the topology of $M(\gamma)$, so the pinched version of the algorithm also builds the desired 3-manifold. □

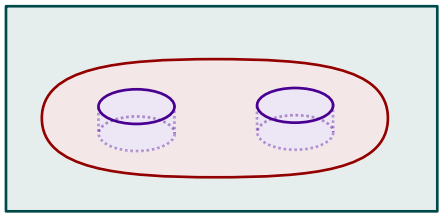

(a) The output of Step 2 in Algorithm 3.2.

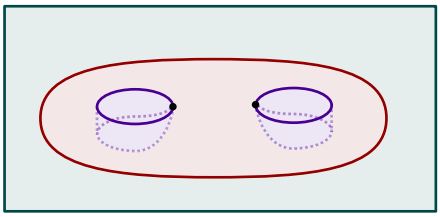

(b) Pinching 2-handles to wedges through the 2-handles.

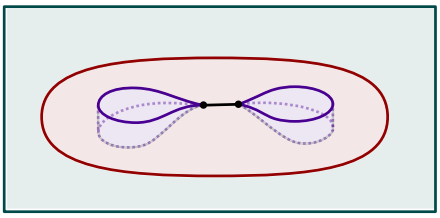

(c) Contracting wedge points along a path in the boundary of the 3-ball.

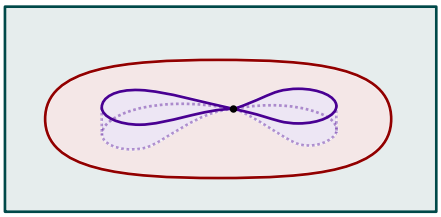

(d) The pinched version of 3.8a, obtained by contracting paths within $M(\gamma)$.

FIGURE 3.8. An example when ∂M is genus 2, justifying the equivalence of Algorithm 3.2 and the pinched filling algorithm. The red region represents M, the purple regions represent the 2-handles and wedge pieces, and the green region represents the 3-ball that is glued to the boundary of M'.

3.2.3. Input for the main algorithm

Here we introduce the *combinatorial filling diagram*, which is used as input for Algorithm 3.29. Later, in Theorem 3.30, we prove that the construction of a 3-manifold from a combinatorial filling diagram is essentially a triangulated version of the pinched filling algorithm.

Suppose M_Δ and H_Δ are analogues of M and H, respectively, in Algorithm 3.2. In the combinatorial setting, we assume M_Δ comes equipped with a one-vertex triangulation, and our strategy is to build H_Δ directly onto the boundary of M_Δ; we ultimately define H_Δ to be the complement of M_Δ in the triangulation constructed by Algorithm 3.29.

Rooted normal curves. Since the boundary of M_Δ inherits a (one-vertex) triangulation, it is helpful to isotope the attaching circles so that they intersect nicely with the edges of the boundary triangulation. We may assume that they are in *normal position* with respect to the triangulation, meaning that the curves: are disjoint from the vertex, intersect edges transversely, and intersect faces in *normal arcs* (see Definition 3.4). However, for input into our algorithm, we ask that the attaching circles be *rooted*: that is, we isotope the curves so that each one meets the vertex in exactly one point.

Definition 3.4. A *normal arc* in a triangle is a simple curve that enters a face from one edge and leaves from a different edge, thus cutting off one of the three corners. A *rooted arc* is a simple curve that runs from one corner, across the face and leaves via the opposite edge. See Figure 3.9.

Definition 3.5. The number of normal and rooted arcs in a triangle Δ are encoded using *(rooted normal) arc coordinates*. If e_0, e_1, e_2 denote the edges of Δ, we let n_i be the number of

normal arcs opposite the edge e_i and let r_i be the number of rooted arcs through the edge e_i. See Figure 3.9.

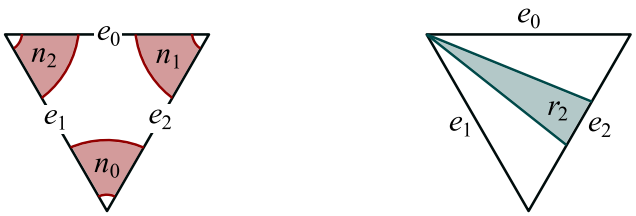

Figure 3.9. Left: Normal arcs and their coordinates. Right: A rooted arc and its coordinate.

Definition 3.6. An embedded curve γ in a (2-dimensional) one-vertex triangulation is in *rooted normal position* if either:

- γ coincides with an edge of the triangulation, in which case we say that γ is *resolved*; or
- γ consists of exactly two rooted arcs together with some finite number (possibly zero) of normal arcs, in which case we say that γ is *unresolved*.

A collection of curves is in *rooted normal position* if each individual curve is in rooted normal position, the curves are all pairwise disjoint away from the vertex, and no two such curves cross at the vertex.

In Proposition 3.8 below, we show that on a one-vertex triangulation of a genus-g surface, we can always isotope a system of attaching circles to be in rooted normal position. Before we prove this, it is worth commenting on why we develop this notion of rooted normal curves, rather than using the well-studied and widely-used notion of normal curves:

Remark 3.7. Our main algorithm relies on the following useful property of rooted normal curves: the number of times that such a curve intersects the (interiors of) edges of the triangulation can be reduced right down to zero, until the curve is resolved. Our algorithm is then able to ignore resolved curves while it deals with all the other unresolved curves. An earlier version of our algorithm attempted to apply a similar philosophy directly to normal curves. This was surprisingly complicated and inelegant, and we found that rooted normal curves solved many of the problems that we had with normal curves; in particular, our proof of Proposition 3.19 later on relies crucially on the curves being rooted, and provides a glimpse of the complications that arise if one tries to use normal curves instead.

Proposition 3.8. Let B_Δ be a closed orientable genus-g surface equipped with a one-vertex triangulation. A system of attaching circles on B_Δ, in normal position with respect to the triangulation, can be isotoped to be in rooted normal position.

Proof. Recall that a valid system of attaching circles consists of g non-intersecting curves that are collectively non-separating. By cutting B_Δ along all attaching circles, we obtain a surface homeomorphic to S^2 with $2g$ discs removed. In particular, the complement of the attaching circles in B_Δ is path-connected. Moreover, disjoint paths connecting each curve to the vertex can be embedded in B_Δ simultaneously.

In fact, these paths can be positioned with respect to the triangulation in such a way that for each attaching circle γ, there is at least one triangle in which a path can be drawn between a

normal arc belonging to γ and one of the corners of the triangle. Note that if this were not the case, every corner of every triangle would be separated from γ by at least one arc of some other attaching circle, and hence, cutting B_Δ along all attaching circles other than γ would yield at least two disconnected components: one containing the vertex, and one containing γ. Since a valid set of attaching circles is non-separating, this is a contradiction.

Now, consider a triangle that admits a path between an arc of γ and one of its corners. Up to symmetry, there are two possible configurations of arcs in this triangle, depending on whether γ is connected to the corner it cuts off, or to one of the corners across the triangle (see Figure 3.10). For each attaching circle γ, we choose one normal arc with a path connecting it to the vertex, then isotope along the path so that γ becomes rooted; in the context of a single triangle, call this corner the *root corner*.

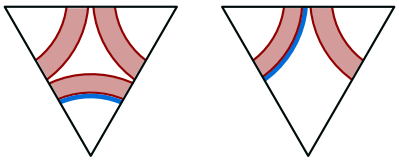

FIGURE 3.10. For each attaching circle γ in normal position, there exists a triangle exhibiting one of these two configurations. In particular, there is a normal arc belonging to γ that appears as either: the innermost normal arc in one of the three corners of the triangle (left); or the outermost normal arc in one of the three corners of a triangle where one of the other two corners of the triangle has no normal arcs (right). The shaded regions indicate the possible positions for other normal arcs appearing in each triangle.

This process introduces arcs that are no longer normal with respect to the triangulation, as seen in Figure 3.11. In particular, we see arcs that meet a corner at one end and cross an adjacent edge at the other, forming bigons between the edges of the triangulation and the rooted attaching circle.

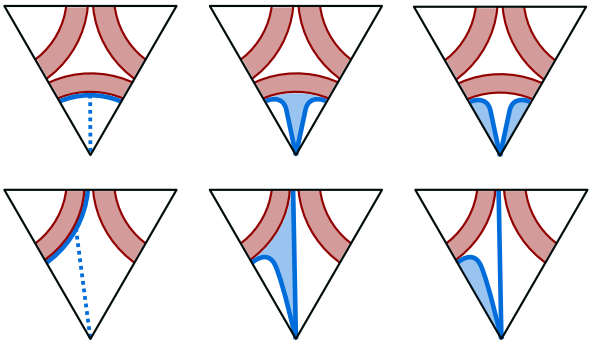

FIGURE 3.11. In either of the cases shown in Figure 3.10, there is a path connecting the distinguished normal arc to the bottom corner of the triangle. Isotoping along this path to the corner introduces one or two bigons, depending on the configuration of arcs. At this point, the curve is rooted but no longer normal. Again, there are shaded regions corresponding to other compatible normal arcs in the triangle, but here we also shade the regions through which we isotope the curve of interest.

To remove bigons, we isotope across the edge into the adjacent triangle. The isotoped arc either leaves the adjacent triangle via the edge opposite the root corner (as in Figure 3.12a, left), or it leaves via the edge adjacent to the root corner (as in Figure 3.12b, left). In the first of these cases, the result is a rooted arc (as in Figure 3.12a, right). In the second case, we have

created a new bigon (as in Figure 3.12b, right). When this happens, we continue isotoping the curve across edges until all such bigons are removed. Note that this process must terminate and result in a rooted arc because the attaching circle cannot fully encircle the vertex.

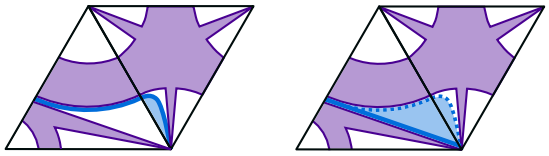

(a) If the continuation of the curve leaves the adjacent triangle via the edge opposite the root corner, then we obtain a rooted arc.

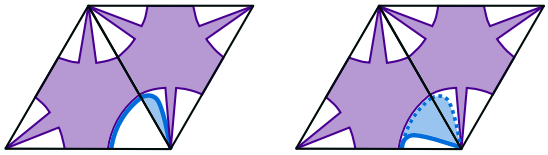

(b) If the continuation of the curve leaves the adjacent triangle via the other edge meeting the root corner, then we have created a new bigon in this triangle and we continue recursively.

Figure 3.12. The two possible scenarios that arise when we isotope a bigon across an edge into the adjacent triangle. The purple shaded regions indicate the possible positions of other arcs in each triangle and the blue shaded regions again indicate the region through which we isotope the arcs of interest.

The process of removing these bigons terminates in one of three ways; note that having rooted each distinct attaching circle in one place, there are two 'ends' where the circle leaves and then returns to the vertex. The first way the process may terminate is when both ends of the rooted attaching circle form a rooted arc in different triangles, like in Figure 3.13a. The second possibility is similar, except that both ends appear as rooted arcs in the same triangle, from the same corner, as in Figure 3.13b. Finally, the two ends of the rooted attaching circle may be rooted at two distinct corners in the same triangle, without leaving the triangle, as in Figure 3.13c. In this last case, the attaching circle is isotopic to an edge of the triangle, and is therefore resolved.

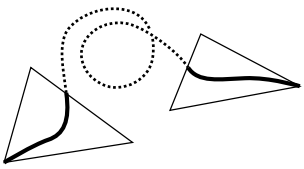

(a) Each of the two ends are rooted in distinct triangles.

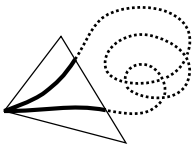

(b) Both ends are rooted in the same triangle, in the same corner.

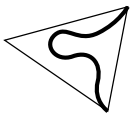

(c) Both ends are rooted in the same triangle but at different corners.

Figure 3.13. After removing bigons, the two endpoints of a rooted attaching circle may appear in one of three configurations.

Arcs where no isotopy was required remain in normal position. Hence, at the end of this process the attaching circles are positioned such that they either coincide with edges of the triangulation, or they consist entirely of normal and rooted arcs. Thus, they are in rooted normal position, as claimed. □

The collection of rooted attaching circles form a bouquet, in the graph-theoretical sense, so we refer to the set of rooted attaching circles as a *filling bouquet*, and individual curves as

(filling) petals. As shown above, each unresolved petal intersects the vertex once (in two rooted arcs) and all other intersections with the triangulation are transverse. When a filling bouquet is understood to be valid, we will say that the petals are disjoint, even though they technically meet at the vertex.

DESCRIBING CURVES VIA EDGE WEIGHTS. Let B_Δ denote a one-vertex triangulation of a closed orientable surface of genus g, and suppose we have a system of attaching circles in rooted normal position in B_Δ. We define the *weight* of an edge e in B_Δ to be the number of transverse intersections between all attaching circles and the interior of e (this does not include any intersections at the vertex). An edge e in B_Δ has *maximal weight* if there is no edge in B_Δ with strictly higher weight than e. The *total weight* of B_Δ is the sum of all edge weights. We use edge weights to encode the unresolved attaching circles.

Recall that a triangle Δ with edges e_0, e_1, e_2 contains normal arcs n_0, n_1, n_2 and rooted arcs r_0, r_1, r_2. Denote the weight of edge e_i by w_i. Observe that $w_i = r_i + n_{i+1} + n_{i-1}$, where subscripts are taken to be in $\mathbb{Z}_3$.

Proposition 3.9. (Edge weights determine rooted normal curves). There is at most one choice of rooted normal arc coordinates that is compatible with the edge weights around a face Δ.

Before proving this proposition, we collect some useful observations and basic facts about arc coordinates and their restrictions. Throughout this section we continue to assume that subscripts are in $\mathbb{Z}_3$.

Lemma 3.10. (Fundamental observation). Only one of the three rooted arc coordinates may be positive in a given triangle, and the normal coordinate corresponding to the positive root coordinate must be 0. That is, if $r_i > 0$ then we must have $n_i = 0$ and $r_{i\pm1} = 0$, as in Figure 3.14.

FIGURE 3.14. When a rooted arc is present, meaning $r_i > 0$, then there can be no normal arcs in that corner, so $n_i = 0$, and the other rooted arc coordinates $r_{i\pm1}$ must also be 0.

Lemma 3.11. If $r_i > 0$, then $w_i > w_{i+1} + w_{i-1}$.

Proof. With reference to Figure 3.15, we have

$$r_i > 0 \implies w_i = r_i + n_{i-1} + n_{i+1} > n_{i-1} + n_{i+1} = w_{i+1} + w_{i-1}. \qquad \square$$

Corollary 3.12. If edge e_i has maximal weight, then the only rooted arc coordinate that can possibly be positive is r_i.

Lemma 3.13. If $w_0 \leqslant w_1 \leqslant w_2$, then $r_0 = r_1 = 0$.

Proof. If $r_0 > 0$ then $w_0 > w_1 + w_2$ by Lemma 3.11, but this implies that $w_0 > w_2$, which is a contradiction to our assumed ordering. A similar argument applies to r_1. $\square$

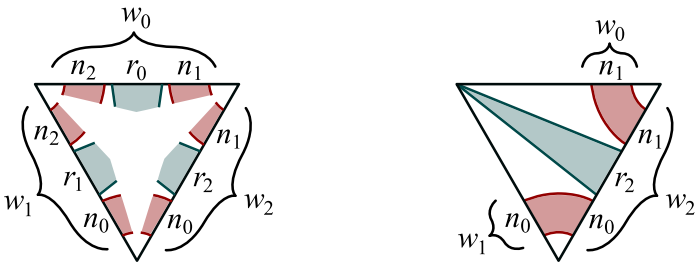

Figure 3.15. Left: In general, $w_i = n_{i-1} + r_i + n_{i+1}$. Right: If the root coordinate r_i is positive then $w_{i-1} = n_{i+1}$, $w_{i+1} = n_{i-1}$, and $w_i = w_{i+1} + r_i + w_{i-1}$.

Lemma 3.14. If $w_0 \leqslant w_1 \leqslant w_2$, then $r_2 \geqslant w_2 - w_1 - w_0$.

Proof. By definition, $r_2 = w_2 - n_0 - n_1$. By the fundamental observation, we have $w_1 = n_0 + n_2$ and $w_0 = n_1 + n_2$, so this becomes $r_2 = w_2 + (n_2 - w_1) + (n_2 - w_0)$. Then by expanding we see that $r_2 = w_2 + 2n_2 - w_1 - w_0 \geqslant w_2 - w_1 - w_0$. □

Proof of Proposition 3.9. Assume, without loss of generality, that $w_0 \leqslant w_1 \leqslant w_2$. Hence, $r_0 = r_1 = 0$ (by Lemma 3.13) and it remains to be shown what values r_2, n_0, n_1 and n_2 can take. Note that all possible sets of edge weights fall into one of the following cases:

(a) $w_0 + w_1 < w_2$,
(b) $w_0 + w_1 \geqslant w_2$ and $w_0 + w_1 + w_2$ is even,
(c) $w_0 + w_1 \geqslant w_2$ and $w_0 + w_1 + w_2$ is odd.

It turns out that the possible arc coordinates are completely determined by which of these edge weight conditions are satisfied. We will show that: in (a), there must be at least one rooted arc; in (b), the only realisation of compatible edge weights consists of entirely normal arcs; and in (c), there is no realisation of the edge weights as compatible rooted and normal arcs.

First consider when $w_0 + w_1 < w_2$. We have

$$\begin{aligned} w_2 - w_1 - w_0 > 0 &\implies r_2 > 0 && \text{(Lemma 3.14)} \\ &\implies n_2 = 0 && \text{(Fundamental observation)} \\ &\implies n_0 = w_1,\ n_1 = w_0 \text{ and } r_2 = w_2 - n_0 - n_1 && \text{(see Figure 3.15)} \\ &\implies r_2 = w_2 - w_1 - w_0. \end{aligned}$$

Thus, when $w_0 + w_1 < w_2$, the rooted normal arc coordinates may be expressed in terms of edge weights as follows:

$$n_0 = w_1, \quad n_1 = w_0, \quad n_2 = 0, \quad r_0 = r_1 = 0, \quad r_2 = w_2 - w_0 - w_1.$$

Now suppose $w_0 + w_1 \geqslant w_2$. Recall, by Lemma 3.13, that $r_0 = r_1 = 0$. Note that r_2 must also be 0, since otherwise our inequality would contradict Lemma 3.11. When there are no rooted arcs, as in Figure 3.9 (left), we see that

$$w_0 + w_1 + w_2 = 2(n_0 + n_1 + n_2) \quad \implies \quad w_0 + w_1 + w_2 \text{ is even.}$$

In particular, case (c) is incompatible with any valid set of rooted normal arc coordinates.

When $w_0 + w_1 + w_2$ is even, we can turn the edge weights into normal arc coordinates in the usual way. In detail, for each $i \in \mathbb{Z}_3$ we have

$$w_i + w_{i+1} + w_{i-1} = 2(n_i + n_{i+1} + n_{i-1}) = 2n_i + 2w_i, \quad \text{as in Figure 3.9 (left).}$$

This implies that $n_i = \frac{1}{2}(w_{i+1} + w_{i-1} - w_i)$. Thus, when $w_0 + w_1 \geq w_2$ and $w_0 + w_1 + w_2$ is even, the rooted normal arc coordinates may be expressed in terms of edge weights as follows:

$$n_0 = \frac{w_1 + w_2 - w_0}{2}, \quad n_1 = \frac{w_0 + w_2 - w_1}{2}, \quad n_2 = \frac{w_0 + w_1 - w_2}{2}, \quad r_0 = r_1 = r_2 = 0.$$

This completes the proof of the proposition. □

Remark 3.15. In general, even if a set of edge weights is compatible with some choice of rooted normal arc coordinates, the corresponding collection of curves need not form a filling bouquet: there might be curves formed entirely by normal arcs, which are therefore not rooted; and there might also be rooted curves that intersect each other transversely at the vertex. We use the term *valid* to describe a set of edge weights or a collection of filling petals that avoids these features.

Defining combinatorial filling diagrams. Now that we have established the fact that attaching circles can be isotoped to rooted normal position, and that a valid set of edge weights uniquely determines a collection of attaching circles, we are ready to define a combinatorial filling diagram. Although our definition is restricted to the case where the input manifold has only one boundary component, this is not necessary in principle.

Definition 3.16. (Combinatorial filling diagram). Let $\mathcal{T}$ be a one-vertex triangulation of a compact orientable 3-manifold with a single genus-g boundary. Let $\mathcal{R}$ be a (possibly empty) set of edges in $\mathcal{T}$ corresponding to resolved attaching circles. Let $\mathcal{W}$ be the tuple of edge weights encoding the unresolved attaching circles. We call $(\mathcal{T}, \mathcal{R}, \mathcal{W})$ a *combinatorial filling diagram*.

Proposition 3.17. (Equivalence). A topological filling diagram (M, B, γ) can be converted to a combinatorial filling diagram $(M_\Delta, \mathcal{R}, \mathcal{W})$, and vice versa.

Proof. Topological to combinatorial. Let M_Δ denote the manifold M endowed with a one-vertex triangulation; there are many ways to verify that such a triangulation exists, for example using tools discussed in [JR06, Section 5.2] or [Wee05, Section 3]. After a small perturbation, we can ensure that the system γ of attaching circles is disjoint from the vertex of ∂M_Δ, and transverse to the edges of ∂M_Δ; we can then minimise edge weights in the usual way to ensure that γ is normal with respect to ∂M_Δ. We complete the conversion by using Proposition 3.8 to turn the attaching circles into a filling bouquet, which we encode using edge weights $\mathcal{W}$ and resolved edges $\mathcal{R}$.

Combinatorial to topological. First, we can use the edge weights $\mathcal{W}$ to reconstruct the unresolved curves (uniquely, by Proposition 3.9). Provided that these unresolved curves, together with the resolved curves given by $\mathcal{R}$, form a valid set of rooted attaching circles, we can isotope all of these rooted circles away from each other to give a system γ of attaching circles on $B = \partial M_\Delta$. □

Our algorithm consists of four subroutines. We begin with an overview of the main algorithm before describing each subroutine in greater detail.

The input for our algorithm is a combinatorial filling diagram. Recall that this consists of:

- a one-vertex triangulation of a compact orientable 3-manifold with a single genus-g boundary component;
- a tuple of edge weights encoding the unresolved filling petals on the genus-g boundary; and
- a set of boundary edges corresponding to the resolved filling petals.

The first step of the algorithm is to layer tetrahedra onto the boundary, and hence perform flips on the boundary 2-triangulation until all filling petals are resolved. We call the subroutine that achieves this the *Petal-Resolver*. At the end of this step all filling petals coincide with edges in the (new) boundary triangulation.

Next, we ensure each resolved filling petal is *isolated*, meaning that the two triangles adjacent to this petal have no other resolved petals as edges. If any of the resolved petals appear in the same triangle, then we adjust the triangulation by layering more tetrahedra; an easy case is shown in Figure 3.16. We call this subroutine the *Quad-Isolator*. At the end of this step, the g resolved filling petals appear as the diagonals of mutually disjoint quadrilaterals.

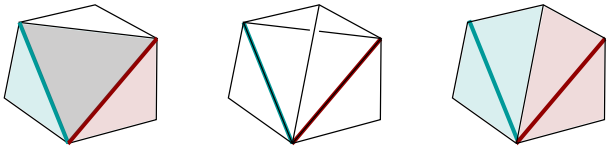

Figure 3.16. The red and blue filling petals share a triangle and are therefore *not isolated* (left). The triangulation is adjusted by layering (centre) so that the red and blue edges are contained in mutually disjoint quadrilaterals (right).

The first topological change we make to the triangulation is done by *folding*. To prepare for folding, we layer an extra tetrahedron over each resolved filling petal. The two exposed faces of each newly-layered tetrahedron are then identified by folding across the newly introduced edge. This makes each of the filling petals homotopically trivial (recall Figure 3 from the introduction), which we claim is analogous to attaching the wedges in the pinched filling algorithm. Hence, we call this subroutine the *Wedge-Folder*. At the end of this step, the triangulation will be *invalid*, in the sense that the link of the 3-vertex is not a closed surface or a disc.

The remaining unidentified faces form a 2-triangulation of a (pinched) 2-sphere that we wish to fill trivially. This is analogous to the step in the topological filling algorithm where we attach a 3-ball. Hence, we refer to the final subroutine as the *Ball-Filler*. This routine may require further layering to adjust the boundary triangulation, but ultimately the 2-sphere boundary is closed by again folding across edges to identify adjacent faces.

Once all this is done, the algorithm returns a one-vertex triangulation of a closed 3-manifold. For the remainder of this section, we consider each subroutine in more detail.

3.3.1. Petal-Resolver

The Petal-Resolver layers tetrahedra onto the genus-g boundary to adjust the triangulation in such a way that each filling petal becomes resolved (that is, each petal appears as a boundary

edge of the triangulation). We say that an edge in the triangulation is *reducible* if performing the flip to replace it strictly decreases the total weight of edges in the boundary of the triangulation; we emphasise that the weight only counts the points where edges meet *unresolved* petals. On the other hand, if flipping an edge introduces a new edge with equal or higher edge weight, we say the original edge is *irreducible*.

Algorithm 3.18. (Petal-Resolver). Given a one-vertex 3-manifold triangulation with genus-g boundary, together with a valid collection of filling petals:

1. If all filling petals are resolved, then terminate and return the triangulation. Otherwise, find a reducible boundary edge e.
2. Layer a tetrahedron over e, and then return to Step 1.

Proposition 3.19. If one or more filling petals remains unresolved, then there must be at least one reducible edge. Hence, the Petal-Resolver is guaranteed to terminate.

Proof. We prove that at least one of the *maximal-weight* edges is reducible.

Consider two adjacent triangles where the shared edge $\boldsymbol{e}$ has maximal weight amongst all edges in the boundary triangulation. The two triangles must be distinct, since a triangle cannot be adjacent to itself in the boundary triangulation (this would require either an extra vertex or that the boundary were non-orientable).

For the quadrilateral formed by these two triangles, we label vertices and edges as in Figure 3.17. We know that the four vertices are actually copies of the same vertex, and the edges may also be identified in pairs; however, we assign them distinct labels for clarity. We label the types of arcs that appear in a quadrilateral as per Figure 3.17. Let v_i be the number of arcs in the quadrilateral cutting off vertex $i \in \{1, 2, 3, 4\}$. Let x be the number of arcs that cut across the quadrilateral, either through edges $\boldsymbol{a}$, $\boldsymbol{e}$, $\boldsymbol{b}$ or edges $\boldsymbol{d}$, $\boldsymbol{e}$, $\boldsymbol{c}$. Let $r_{\boldsymbol{a}}$ and $r_{\boldsymbol{d}}$ be the number of arcs that are rooted at vertex 3, and that leave the quadrilateral via edge $\boldsymbol{a}$ and $\boldsymbol{d}$, respectively. Define $r_{\boldsymbol{b}}$ and $r_{\boldsymbol{c}}$ similarly, but for arcs rooted at vertex 4. Since we assume $\boldsymbol{e}$ is maximal-weight, Corollary 3.12 implies that there can be no arcs rooted at vertices 1 or 2.

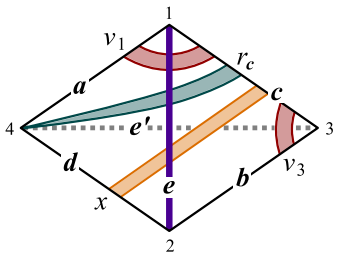

FIGURE 3.17. Labels for edges and arcs in a quadrilateral that are used in the proof of Proposition 3.19.

Case 1: Both triangles contain rooted arcs.

(i) If a filling petal appears as an off-diagonal of the quadrilateral, as in Figure 3.18a or Figure 3.18b, then performing the flip realises the petal as an edge in the triangulation. In particular, $\boldsymbol{e}$ is reducible.

(ii) If there is no filling petal appearing as an off-diagonal of the quadrilateral, we have the scenario shown in Figure 3.18c (up to symmetry). Suppose there are $x \geq 0$ normal arcs that cross the quadrilateral between the rooted arcs. Further suppose that there

are $v_1 \geq 0$ normal arcs cutting off vertex 1, and $v_2 \geq 0$ cutting off vertex 2. Finally, suppose there are $r_c \geq 1$ arcs rooted at vertex 4 and $r_d \geq 1$ rooted arcs rooted at vertex 3. In this case, performing the flip strictly reduces the edge weight, since $w(e) = v_1 + r_c + x + r_d + v_2$, while the weight of the flipped edge would be $w(e') = x$. Therefore e is reducible.

Case 2: Only one triangle contains rooted arcs.

(i) If there are multiple rooted arcs that leave the quadrilateral through each of the two opposite edges, we have the scenario shown in Figure 3.18d (up to symmetry). In this case, $w(e) = v_1 + r_c + r_b + v_2$, with $v_1, v_2 \geq 0$ and $r_c, r_b \geq 1$. Meanwhile, the weight of the flipped edge is $v_3 \geq 0$. Note that $w(c) = v_1 + r_c + v_3$ can be at most equal to the weight of e, by the maximality assumption, so $v_1 + r_c + r_b + v_2 \geq v_1 + r_c + v_3 > v_3$. Since the flipped edge would have weight $w(e') = v_3$, performing the flip strictly reduces the total weight, and hence e is reducible.

(ii) If all rooted arcs leave the quadrilateral through the same opposite edge, then we have the scenario shown in Figure 3.18e (up to symmetry). Similar to the previous case, we have $w(e) = v_1 + r_c + x + v_2$, which (by the maximality assumption) is at least as big as the weight of edge c, $w(c) = v_1 + r_c + x + v_3$. Together with the fact that $r_c \geq 1$, this gives us that $v_1 + r_c + x + v_2 \geq v_1 + r_c + x + v_3 > x + v_3$. Since the flipped edge would have weight $w(e') = x + v_3$ we again see that performing the flip strictly reduces the total weight, and hence that e is reducible.

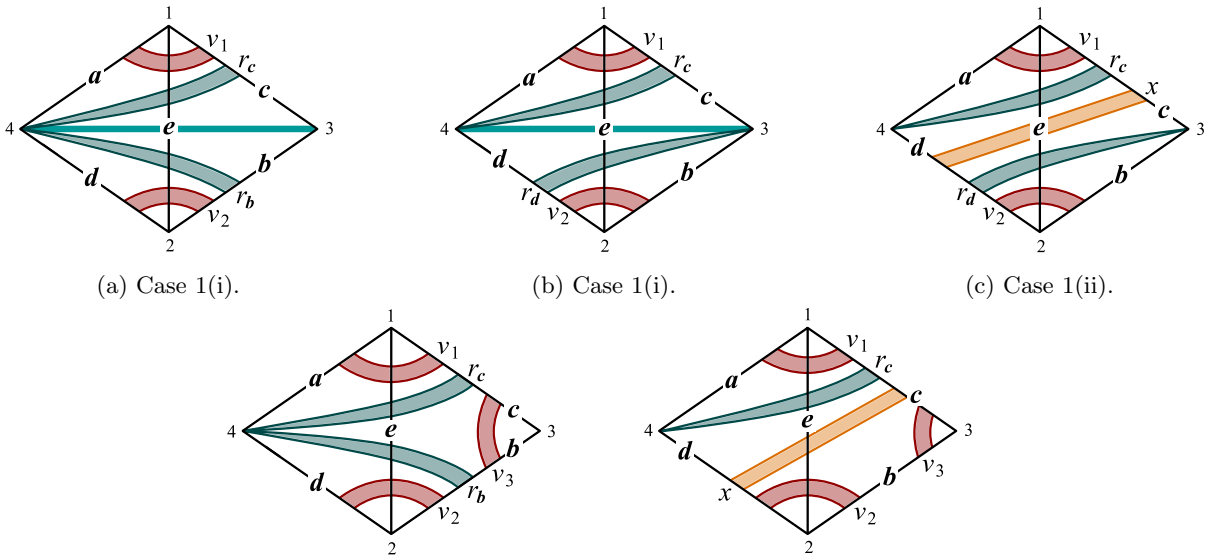

(a) Case 1(i). (b) Case 1(i). (c) Case 1(ii).

(d) Case 2(i). (e) Case 2(ii).

Figure 3.18. All possible configurations of arcs when one or both of the triangles contain rooted arcs.

Case 3: Neither triangle contains a rooted arc. If e is reducible then we are done, so assume it is irreducible. We will show that there must be some other (maximal-weight) edge that is reducible.

To this end, first notice that there can never be arcs that cut the quadrilateral in half in both directions at the same time, since such arcs would intersect. Without loss of generality, we assume x is the number of arcs cutting through edges $\mathbf{d}, \mathbf{e}, \mathbf{c}$, as in Figure 3.19.

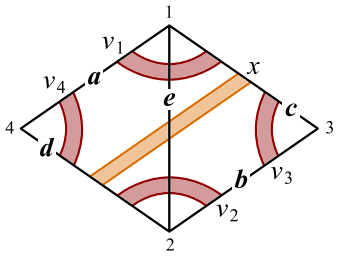

FIGURE 3.19. Configuration of arcs in a quadrilateral where neither triangle contains a root, as in Case 3.

Under the maximality assumption, we have that $w(\boldsymbol{e}) = v_1 + x + v_2 \geq v_1 + x + v_3 = w(\boldsymbol{c})$ and $w(\boldsymbol{e}) = v_1 + x + v_2 \geq v_4 + x + v_2 = w(\boldsymbol{d})$. These respectively imply that $v_2 \geq v_3$ and $v_1 \geq v_4$.

Note that performing the flip will result in an edge of weight $w(\boldsymbol{e}') = v_3 + x + v_4$. Under the assumption that $\boldsymbol{e}$ is irreducible, $w(\boldsymbol{e}') \geq w(\boldsymbol{e})$, which implies that $v_3 + v_4 \geq v_1 + v_2$. In summary, $v_3 + v_4 \geq v_1 + v_2$ by the irreducibility assumption, and the maximality assumption implies both $v_2 \geq v_3$ and $v_1 \geq v_4$, so altogether we have $v_2 = v_3$ and $v_1 = v_4$.

This means that edges $\boldsymbol{d}$ and $\boldsymbol{c}$, which have weights given by $w(\boldsymbol{c}) = v_1 + x + v_3$ and $w(\boldsymbol{d}) = v_2 + x + v_4$, are also maximal-weight edges. Note that one or both of $\boldsymbol{a}$ and $\boldsymbol{b}$ may also be maximal weight edges. If any of the additional maximal-weight edges are reducible, then we are done.

Hence, let us consider the case where all maximal-weight edges are also irreducible; by our previous arguments, this means that none of these maximal-weight edges are incident to triangles containing rooted arcs. Beginning with the quadrilateral just discussed, inductively build an *irreducible region* by including the triangles adjacent to each maximal-weight irreducible edge (if they are not already included). That is, for each maximal-weight edge $\boldsymbol{f}$ along which we include an additional triangle, we can make the same arguments for the quadrilateral at $\boldsymbol{f}$; this yields additional maximal-weight edges, along which we might need to include further triangles. This process must terminate, since the total triangulation is finite. The result is a subcomplex in which all interior edges are maximal-weight and irreducible.

Using the labels of Figure 3.19, and assuming the quadrilateral is contained inside the irreducible region, notice that $\boldsymbol{c}$, $\boldsymbol{d}$ and $\boldsymbol{e}$ must each be maximal-weight and irreducible, and that each of $\boldsymbol{a}$ and $\boldsymbol{b}$ may also be maximal-weight and irreducible. In particular, notice that each triangle in the irreducible region must be incident to at least two maximal-weight irreducible edges. We call a triangle *equilateral* if all three of its edges are maximal-weight and irreducible, and we call it *isosceles* if exactly two of its edges are maximal-weight and irreducible. With this terminology, we can say that every triangle in the irreducible region is either isosceles or equilateral.

From here, we argue that there must be at least one curve contained entirely in the irreducible region. Such a curve must consist entirely of normal arcs, and is therefore not rooted. This contradicts the assumption that we started with a valid collection of filling petals.

To find such an unrooted curve, let m denote the maximal weight, and consider an arbitrary weight-m edge e in the irreducible region. Let $p_1, \ldots, p_m$ denote the points at which the filling petals intersect e, labelled in the order that they appear along e. If m is odd, then we write $m = 2k + 1$ and call the point p_{k+1} the *innermost intersection*; otherwise, if m is even, then we write $m = 2k$ and call the points p_k and p_{k+1} the *innermost intersections*.

With this terminology in mind, consider an arbitrary triangle Δ in the irreducible region. If Δ is equilateral, then observe that m must be even; moreover, the innermost intersections are all paired together by three *innermost arcs*, as shown in Figure 3.20 (left). On the other hand, if Δ is isosceles, then the innermost intersections are paired together by either one or two (depending on the parity of m) *innermost arcs*, as shown in Figure 3.20 (right and centre).

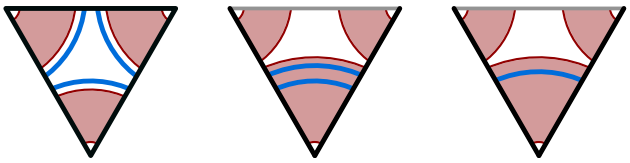

Figure 3.20. Depending on the parity of m, and the type of triangle, the innermost arcs (blue) appear as shown. Left: When Δ is equilateral and m is even. Centre: When Δ is isosceles and m is even. Right: When Δ is isosceles and m is odd.

Observe that the innermost arcs must all join together to give at least one curve that never leaves the irreducible region, which produces the desired contradiction. Thus, we conclude that we are guaranteed to find a reducible maximal-weight edge.

Since there is always a reducible edge, the Petal-Resolver is able to strictly reduce the total edge weight until it reaches 0, at which point all filling petals are resolved. □

3.3.2. Quad-Isolator

The algorithm makes the filling petals homotopically trivial by folding them back on themselves. To be able to perform such a fold along all the petals simultaneously, we need the petals to belong to disjoint quadrilaterals. That is, if for each (resolved) filling petal we consider the quadrilateral formed by the two triangles incident to the petal, then we require the interiors of these quadrilaterals to be mutually disjoint. The following algorithm uses layering to ensure that this requirement is satisfied:

Algorithm 3.20. (Quad-Isolator). Given a one-vertex 3-manifold triangulation with genus-g boundary, along with g distinguished edges corresponding to resolved filling petals:

1. Label all edges corresponding to resolved filling petals with a 0.
2. Starting with $i = 1$, repeat the following until there are no triangles with exactly two labelled edges:
   (a) Identify all triangles for which exactly two edges have labels (each of these labels will be less than i).
   (b) For each triangle identified above, assign the third edge the label i.
   (c) Increase i by one.
3. Starting with i equal to the largest edge label in the triangulation, repeat the following:
   (a) Layer a tetrahedron over each i-labelled edge.
   (b) Decrease i by one. Terminate if $i = 0$.

We refer to an edge labelled i as an i-edge. Call any triangle with exactly two 0-edges a *seed*. For $i > 0$, define a *flip region of depth* i to be a collection of triangles bounded by some number of 0-edges and a single i-edge, where all edges interior to this region are assigned labels strictly

between 0 and i; define a flip region of depth 0 to be an isolated 0-edge. The two possible flip regions of depth 2 (up to symmetry) are shown in Figure 3.21.

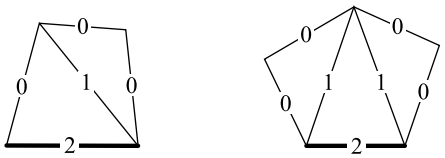

FIGURE 3.21. The two flip regions of depth 2 (up to symmetry).

Lemma 3.21. If an edge is labelled i, then it must belong to a flip region of depth i.

Proof. First consider $i = 1$. Edges with label 1 only ever appear as the third edge in a seed. A seed is exactly a flip region of depth 1.

Next consider $i = 2$. An edge with label 2 belongs to a triangle Δ for which the other edges are labelled either 0 and 1, or 1 and 1. In either case, the edges with label 1 must belong to a seed on the other side of Δ, so altogether, both scenarios imply that the 2-edge is the only non-zero labelled boundary edge of a region otherwise bounded by 0-edges, whose interior edges are all labelled 1. Recall the possibilities from Figure 3.21.

Now consider an arbitrary integer $k > 2$. An edge will only ever be labelled with a k if it belongs to a triangle Δ in which one of the other edges is labelled $k - 1$, and the third edge is labelled with some integer from 0 to $k - 1$. Assuming that the lemma is true for all $i < k$, we see that Δ must be incident to two flip regions of depth less than k. The union of Δ with these two flip regions forms a flip region of depth k. By induction, this proves the lemma. □

Proposition 3.22. The Quad-Isolator terminates and is guaranteed to return a triangulation in which all filling petals are contained within mutually disjoint quadrilaterals.

Proof. First, notice that Step 2 must terminate since the triangulation has finitely many triangles.

For each iteration of Step 3, the set of edges with maximum valued i-labels must be contained within mutually disjoint quadrilaterals. To see why this holds, consider an arbitrary edge $\boldsymbol{e}$ with label i. By Lemma 3.21, we know that $\boldsymbol{e}$ must form part of the boundary of a flip region of depth i on one side. Now consider the triangle Δ on the other side of $\boldsymbol{e}$. The other two edges of Δ must be either both labelled or both unlabelled.

It turns out that if both edges are labelled, as in Figure 3.22a, then we reach a contradiction. To see this, recall that we are assuming i is the maximum value a label can take, so the two edges in question have labels $j, k \leq i$. Lemma 3.21 implies that these edges must bound their own flip regions of depths j and k, respectively. However, altogether this produces a region entirely bounded by 0-edges. Since there are at most g edges with 0-labels, which can bound at most $g - 2$ triangles, and there are $4g - 2$ triangles in the triangulation of the genus-g surface, this implies that the set of 0-edges form a separating multicurve. This contradicts the fact that the 0-edges correspond to a valid collection of filling petals.

The upshot is that the other two edges of Δ must both be unlabelled. In other words, all edges with maximum valued i-labels appear in a quadrilateral for which: one triangle has two unlabelled edges; and the other triangle has an $(i - 1)$-edge and an $(i - j)$-edge, for some

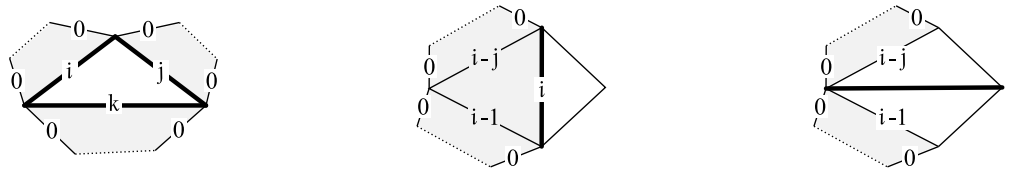

(a) If both edges are labelled, we reach a contradiction.

(b) The generic configuration when both edges are unlabelled.

(c) Layering over the i-edge leaves flip regions of depths $i-j$ and $i-1$.

Figure 3.22. Different configurations of flip regions in the proof of Proposition 3.22.

$0 < j \leq i$. This is illustrated in Figure 3.22b. The i-edges are therefore contained in mutually disjoint quadrilaterals, so we may simultaneously layer over all of these edges.

After such a layering, the flip region of depth i is split into two flip regions of depths $i-1$ and $i-j$, respectively (see Figure 3.22c). Each iteration of Step 3 therefore reduces the depths of flip regions until the only remaining labelled edges are the 0-edges. By induction, the 0-edges all belong to disjoint quadrilaterals, as required. □

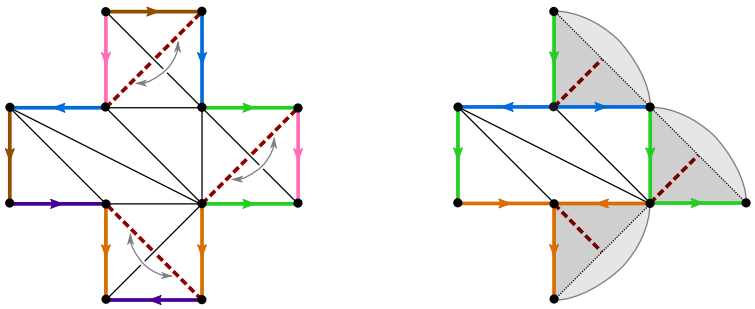

Figure 3.23. (Example 3.24). A genus-3 boundary triangulation, with filling petals indicated by dashed red lines, and the result of performing the folds that make them trivial. Folding causes the brown edge to be identified with the pink edge, which is in turn identified with the green edge, while the purple edge is identified with the orange edge.

3.3.3. Wedge-Folder

The following subroutine layers and folds tetrahedra that correspond to the wedges of the pinched filling algorithm, thus making the filling petals homotopically trivial.

Algorithm 3.23. (Wedge-Folder). Given a one-vertex 3-manifold triangulation with genus-g boundary, along with g resolved filling petals that are isolated within disjoint quadrilaterals:

1. *Layer over each filling petal.* Before we can fold each filling petal back on itself, it must appear as an *off-diagonal*. We achieve this by layering a tetrahedron over each filling petal.
2. *Fold along the filling petals.* We identify the two boundary faces of each newly layered tetrahedron by folding across the edge that was introduced by the layering.

This subroutine involves layering on g tetrahedra and performing g folds, so it terminates, and leaves $2g-2$ remaining boundary faces.

Example 3.24. Consider the boundary triangulation for a genus-3 handlebody shown in Figure 3.23. We see (schematically) what happens when we perform the folds to make the filling

petals homotopically trivial. Notice that the folds identify edges that were not previously in the same edge class, and the remaining boundary faces form a four-vertex triangulation of S^2. While the 2-triangulation of the S^2 boundary contains four distinct 2-vertices, in the 3-triangulation these are all pinched together at the single 3-vertex.

Proposition 3.25. When the Wedge-Folder routine terminates, the remaining boundary faces form a 2-triangulation of a pinched 2-sphere.

Proof. We compare the process of attaching a folded tetrahedron along a filling petal to the process of attaching a wedge piece in the pinched filling algorithm.

Attaching a tetrahedron by first layering over the petal, then folding along it is equivalent to folding the tetrahedron first, *then* attaching it along the filling petal. Figure 3.24 compares this process with the analogous step in the pinched filling algorithm.

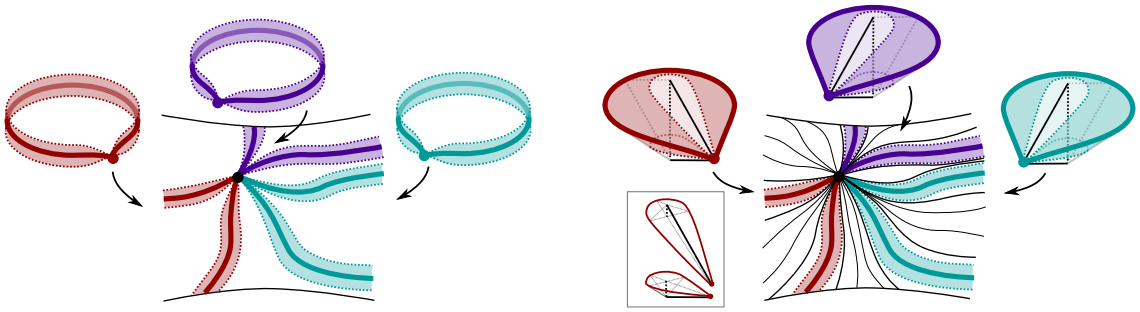

FIGURE 3.24. Comparing Step 2 of the pinched filling algorithm (left) with the corresponding step in the combinatorial filling algorithm (right). INSET: The two cone pieces from a folded tetrahedron.

Notice that the wedge pieces can be embedded inside the folded tetrahedra. In particular, attaching a folded tetrahedron has the same effect as attaching a wedge piece, except for some additional identification corresponding to the *cone pieces* at the vertices away from the Heegaard petal (shown in Figure 3.24, inset). Let us consider the effect of these cone pieces.

Figure 3.25a shows how the six corners of the tetrahedron meet around the vertex before folding, and how the gluing identifies them. We can expand the neighbourhood of the filling petal to cover most of each of the faces, leaving only the tips of four of the corners as in Figure 3.25b. If we identify the tips first, as in Figure 3.25c, we see that they just pinch off part of the 2-sphere boundary as a ball. Hence, we can think of the extra identification as premature filling of part of the 3-ball.

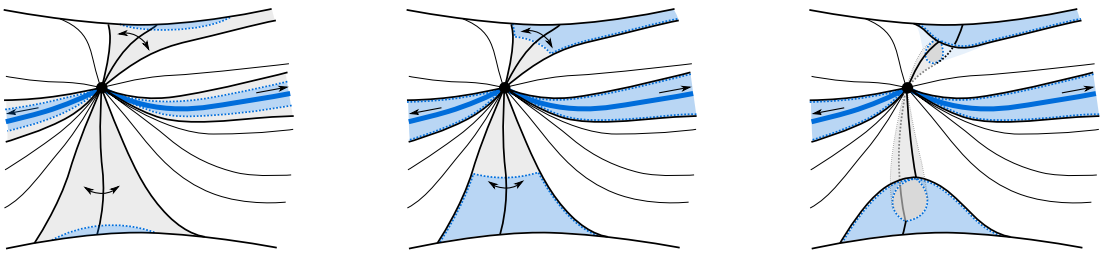

(a) A local view of the six corners meeting the vertex.

(b) Expanding the neighbourhood of the filling petal.

(c) Pinching closed just the tips that correspond to the cone pieces.

FIGURE 3.25. Understanding how the boundary is affected by attaching a folded tetrahedron.

Without the cone pieces, we know from the pinched filling algorithm that the boundary is a pinched 2-sphere. Then by considering the cone pieces alone, as in Figure 3.25c, we see that they just pinch the pinched boundary even more. In particular, the boundary is still a pinched 2-sphere. The fact that we still have a 2-sphere can also be verified by observing that folding preserves the Euler characteristic: two vertices are identified to become one, and two faces are glued together so that they no longer appear in the boundary, but the resulting reduction in the Euler characteristic is exactly cancelled out by the fact that five boundary edges become two after the fold. □

3.3.4. Ball-Filler

After making the filling petals homotopically trivial using the Wedge-Folder routine, we need to close up the remaining boundary faces in such a way that no new topology is introduced. This is analogous to the step in the topological filling algorithm where a ball is glued in. Hence, we refer to this subroutine as the Ball-Filler.

Let us introduce some terminology before detailing the Ball-Filler subroutine. We call a one-vertex 3-triangulation $\mathcal{T}_0$ *fillable* if its boundary consists of zero or more (pinched) 2-sphere components. The closed 3-manifold M_0 obtained by filling in each 2-sphere boundary component of $\mathcal{T}_0$ with a 3-ball is called the *filled manifold* associated to $\mathcal{T}_0$. We call another fillable triangulation $\mathcal{T}_1$ a *refinement* of $\mathcal{T}_0$ if:

- the filled manifolds associated to $\mathcal{T}_0$ and $\mathcal{T}_1$ are homeomorphic; and
- $\mathcal{T}_1$ has strictly fewer boundary triangles than $\mathcal{T}_0$.

Note that, with this terminology, the output from the Wedge-Folder subroutine is considered a fillable triangulation.

Algorithm 3.26. (Ball-Filler). For a fillable triangulation $\mathcal{T}_i$ with non-empty (and possibly disconnected) boundary B_i, iteratively construct a refinement $\mathcal{T}_{i+1}$ as follows, until no boundary faces remain:

1. Attempt to build a refinement $\mathcal{T}_{i+1}$ in one of the following ways:
   (a) If there is an off-diagonal in the triangulation of B_i that realises a closed curve γ, then build $\mathcal{T}_{i+1}$ by folding along γ.
   (b) If there is an edge $\boldsymbol{e}$ in the triangulation of B_i that realises a closed curve γ, build $\mathcal{T}_{i+1}$ by first layering a tetrahedron over $\boldsymbol{e}$, then folding along γ.

   Whenever this attempt is successful, check whether $\mathcal{T}_{i+1}$ is closed. If so, terminate and return $\mathcal{T}_{i+1}$; otherwise, go back to the start of this algorithm, using $\mathcal{T}_{i+1}$ in place of $\mathcal{T}_i$.
2. Build a refinement as follows:
   (a) Fix a vertex v of B_i.
   (b) Flip edges incident to v by layering tetrahedra until a closed curve is realised by either an edge or an off-diagonal in the triangulation of B_i.
   (c) Return to step 1 (which is now guaranteed to succeed).

Example 3.27. Recall Figure 3.23 from the previous example. At the end of the Wedge-Folder routine, the remaining boundary was a four-vertex triangulation of a pinched 2-sphere (redrawn

in Figure 3.26a). Running Ball-Filler on this triangulation requires no additional tetrahedra, since there are two closed curves that appear as off-diagonals.

Notice that if the original triangulation was slightly different, the 2-sphere triangulation could instead have been one of those shown in Figures 3.26b or 3.26c. In these cases, layering is required before folding, as dictated by Steps 1b and 2 in the Ball-Filler algorithm. The pale dotted edge in Figure 3.26c indicates a layering that would realise the same triangulation as in Figure 3.26a.

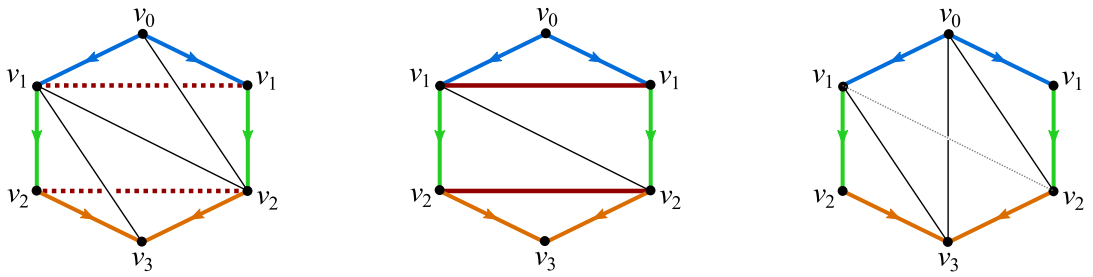

(a) There are two closed curves, rooted at v_1 and v_2 respectively, that appear as **off-diagonals**.

(b) There are two closed curves, rooted at v_1 and v_2 respectively, that appear as **edges**.

(c) There are **no** closed curves that can be realised as edges or off-diagonals.

FIGURE 3.26. Examples of triangulations of the pinched 2-sphere that require each of the cases in Algorithm 3.26.

Proposition 3.28. Given a fillable triangulation with non-empty boundary, it is always possible to construct a refinement. Hence, the Ball-Filler algorithm is guaranteed to terminate and return a triangulation of a closed 3-manifold.

Proof. Let $\mathcal{T}_i$ be a fillable triangulation with non-empty boundary B_i. Our goal is to eventually close the boundary using only layering and folding. Recall that all the vertices in the boundary 2-triangulation are anchored to the single 3-vertex in the 3-triangulation, so we cannot identify two distinct 2-vertices together without disrupting the topology of the 3-manifold. As such, the folds need to be performed so that no new identifications are made between 2-vertices. This can be achieved by folding along curves that: begin and end at the same 2-vertex, and can be realised as off-diagonals in the boundary triangulation (possibly after layering).

Hence, to prove that it is always possible to build a refinement, we show that there is always a sequence of flips that leads to a boundary triangulation where there is at least one quadrilateral whose off-diagonal begins and ends at the same 2-vertex. In particular, we show that Step 2 terminates.

We first eliminate cases where Step 1 immediately succeeds in building a refinement:

- If there is a vertex of degree 1 or 2, then there must be a closed curve realised by an edge or an off-diagonal, respectively (see Figure 3.27).
- If there is a triangle with more than one corner identified to a single vertex, then there must be a closed curve realised by an edge (all the possible cases are summarised in Figure 3.28).

With this in mind, consider the case where Step 1 does not immediately succeed in building a refinement. In this case, we know in particular that every vertex has degree at least 3, and that no triangle contributes more than once to the degree of any vertex. Fixing an arbitrary

(a) A degree 1 vertex, with one edge (red) forming a closed curve. Layering over this edge results in the situation in 3.27b.

(b) A degree 2 vertex, with a closed curve appearing as an off-diagonal. These two faces can be identified by folding.

Figure 3.27. If there is a vertex of degree 1 or 2, then we can build a refinement after layering at most one extra tetrahedron.

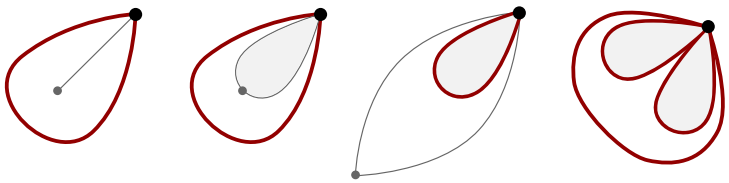

Figure 3.28. A single triangle that contributes more than one of its corners to the degree of a vertex must be in one the four configurations shown. In each case there is at least one edge (indicated in red) that forms a closed curve.

vertex v, and letting d denote the degree of v, we therefore know that there are d distinct triangles meeting v. Thus, flipping edges incident to v, as in Step 2 of the Ball-Filler routine, iteratively reduces the degree of v (see Figure 3.29). Observe that this is guaranteed to lead to a scenario where Step 1 will successfully build a refinement; in the worst case, we might need to reduce the degree of v all the way down to 2, but then we would be done at that point, since there would be an off-diagonal that realises a closed curve.

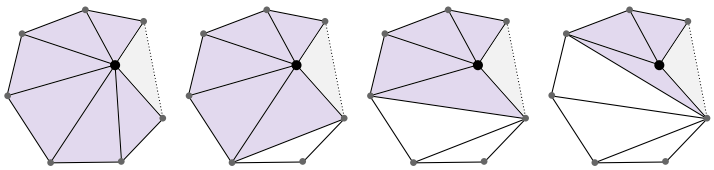

Figure 3.29. When no triangle contributes more than one of its corners to the degree of a vertex, they must be arranged as shown, and the degree can be reduced by layering.

Finally, notice the effect on the number of boundary faces: any layering covers two boundary faces but replaces them with two new ones, so the number of boundary faces is unchanged; whereas any fold identifies two boundary faces to each other, so the number of boundary faces decreases by two. Therefore, each refinement decreases the number of boundary faces, until no boundary faces remain. □

3.3.5. Full algorithm

Putting all of the subroutines together, we get our main algorithm, which allows us to fill in the boundary component of any one-vertex triangulation of a 3-manifold with boundary. In particular, by filling in the boundary of a handlebody, we can effectively construct a one-vertex triangulation of a 3-manifold from a Heegaard diagram.

Suppose (M, B, γ) is a topological filling diagram for $M(\gamma)$, defined by a compact orientable 3-manifold M with a single genus-g boundary component B, together with g attaching circles

given by γ. Let $\mathcal{T}$ be a one-vertex triangulation of M, with B_Δ the induced triangulation on B. Let $\mathcal{R}$ and $\mathcal{W}$ encode the curves γ on B_Δ.

Algorithm 3.29. (Combinatorial filling algorithm). Given a combinatorial filling diagram $(\mathcal{T}, \mathcal{R}, \mathcal{W})$, as described above, build a one-vertex triangulation of $M(\gamma)$ as follows:

1. *Run Petal-Resolver.* Layer tetrahedra over reducible edges until all filling petals appear as (boundary) edges in the triangulation.
2. *Run Quad-Isolator.* Layer tetrahedra until each filling petal is contained within its own quadrilateral.
3. *Run Wedge-Folder.* For each filling petal, layer a tetrahedron over it to make it an off-diagonal, and then fold to make the filling petal homotopically trivial.
4. *Run Ball-Filler.* Iteratively identify remaining boundary faces by folding without introducing new topology. Terminate and return the resulting triangulation.

Theorem 3.30. The combinatorial filling algorithm terminates and returns a one-vertex triangulation of the filled manifold $M(\gamma)$.

Proof. We have seen that each subroutine terminates and yields output that is valid as input for the subsequent subroutine. Hence, the overall algorithm is guaranteed to terminate.

The triangulation is one-vertex by construction.

It remains to be shown that the output is indeed a valid triangulation of the manifold $M(\gamma)$ described by the input. Recall from Proposition 3.3 that the pinched filling algorithm constructs the same manifold as the topological filling algorithm. Here we show that the combinatorial filling algorithm builds the same manifold as the pinched filling algorithm.

Recall (from Proposition 3.17) that a topological filling diagram can be converted to a combinatorial one by: assigning a one-vertex triangulation to the manifold M, and isotoping the attaching circles so that they are in rooted normal position with respect to the induced boundary triangulation B_Δ. In particular, by ignoring the triangulation, this also determines a pinched filling diagram.

Since Petal-Resolver and Quad-Isolator only involve layering, the effect of these subroutines on the combinatorial filling diagram is just to change the boundary triangulation. Since the pinched filling diagram does not see the triangulation, the pinched and combinatorial filling diagrams are still equivalent by the end of the Quad-Isolator routine.

From here, the pinched filling algorithm proceeds by attaching a collection W of wedges to turn the boundary into a pinched 2-sphere, and then filling the pinched 2-sphere with a ball B to obtain the 3-manifold $M(\gamma)$. By construction, the triangulation at the end of the Quad-Isolator routine coincides with the closure of $M(\gamma) - (W \cup B)$; in other words, this triangulation embeds inside $M(\gamma)$. As described in the proof of Proposition 3.25, the Wedge-Folder routine effectively attaches a collection F of folded tetrahedra, and we can view F as a union of the wedges W with some cone pieces. We can think of the cone pieces as forming part of the ball B, so that our triangulation is still embedded inside $M(\gamma)$ at the end of the Wedge-Folder routine; in fact, our triangulation coincides with $M(\gamma)$ minus the interior of a pinched ball.

The final step of the combinatorial filling algorithm is to use the Ball-Filler routine to close the pinched 2-sphere boundary of our triangulation. This involves layering and folding operations

that can be performed inside $M(\gamma)$, preserving the property that the triangulation is embedded in $M(\gamma)$. At the end of the Ball-Filler routine, our triangulation coincides with the entirety of $M(\gamma)$, and is therefore homeomorphic to $M(\gamma)$. □

Section 3.4. *Putting the algorithm to work*

In this final section, we discuss measures of complexity, demonstrate the algorithm on some simple genus-2 Heegaard splittings, and summarise our preliminary experimentation using the algorithm. Note that this section is an abridged version of Sections 5–7 in the full preprint [HMT24a]. For the remainder of this chapter, we will refer to the triangulations constructed by Algorithm 3.29 as *petal-filled* triangulations.

3.4.1. Triangulation complexity

In this section, we consider the complexity of petal-filled triangulations, particularly in the case where the input filling diagram describes a Heegaard splitting.

Cutwidth.

Definition 3.31. (Cutwidth). Let $G = (V, E)$ be a multigraph (i.e. a graph in which two nodes may be connected by multiple 'parallel' arcs). For a given ordering $(v_1, \cdots, v_n)$ of the nodes in V, define a *cutset* C_ℓ for each $\ell \in \{1, \cdots, n-1\}$ to be the set of arcs joining all nodes v_i for $i \leq \ell$ to any nodes v_j with $j > \ell$. The *width* of this ordering is the maximum of $|C_\ell|$ across all ℓ. The *cutwidth* of G is the minimum width across all possible orderings of V. The cutwidth of a triangulation $\mathcal{T}$ is defined to be the cutwidth of the dual graph of $\mathcal{T}$.

Remark 3.32. We can find an upper bound on cutwidth by calculating the width of a single choice of ordering of tetrahedra (which corresponds to an ordering of the nodes of the dual graph).

Theorem 3.33. (Bounded cutwidth). When the input triangulation for Algorithm 3.29 is a layered handlebody of genus g, the petal-filled triangulation obtained as output has cutwidth bounded above by $4g - 2$.

Proof. The boundary of the initial layered handlebody consists of $4g - 2$ triangles. Layering tetrahedra onto the boundary preserves the number of triangles on the boundary.

Layering tetrahedra induces a natural ordering of tetrahedra in a given triangulation. Starting with the layered handlebody, we label the tetrahedra in the order they are layered.

Our algorithm modifies the given triangulation via a sequence of layering and folding. We continue numbering the newly-added tetrahedra according to the order in which they are layered. Let Δ_i denote the i^{th} tetrahedron in this ordering.

At every stage, we have at most $4g - 2$ boundary triangles, since layering preserves this number and folding reduces this number by two. Consider the ℓth cutset under this ordering; this corresponds to gluings between tetrahedra of the form Δ_i and Δ_j, where $i \leqslant \ell < j$. The size of this cutset is bounded above by the number of boundary faces remaining after the ℓth layering, and is therefore bounded above by $4g - 2$. □

In Section 3.4.3, we discuss cutwidths for different triangulations of the same manifolds; in particular, we construct many petal-filled triangulations, and examine how the cutwidth changes after simplifying using Regina.

Minimal layerings. Recall that there is a unique shortest path in the flip graph that corresponds to a *minimal layered solid torus*.

Proposition 3.34. In the case where the boundary component to be filled has genus 1—in which case, a filling diagram just describes a Dehn filling—our algorithm constructs the standard layered solid torus that realises the desired Dehn filling. The sequence of layerings corresponds to the unique non-backtracking path between two triangulations in the flip graph.

Proof. Recall that we can describe layered solid tori by the edge weights of the meridian curve in (unrooted) normal position. The notation $\mathrm{LST}(a, b, c)$ describes the layered solid torus in which the unrooted meridian curve intersects the three boundary edges in a, b and c points, respectively. Without loss of generality, we can assume $a \leq b \leq c$. It is well-established that $a + b = c$, and by layering over each edge, the resulting layered solid torus is: $\mathrm{LST}(b, c, b + c)$ if the edge with weight a was covered; $\mathrm{LST}(a, c, a + c)$ if the edge with weight b was covered; and $\mathrm{LST}(a, b, b - a)$ if the edge with weight c was covered. In particular, the only layering that results in a reduction of total edge weight is the layering that covers the maximal-weight edge.

To see that the same logic holds when the meridian is rooted, we can do everything in the universal cover, and observe that changing the position of the meridian by translations has no effect on the procedure.

Hence, our algorithm never needs to make any arbitrary choices when $g = 1$, and it will always build the layered solid torus corresponding to the unique shortest path in the flip graph. □

The situation for genus 2 and higher is more complicated. There are no longer unique paths between any pair of boundary triangulations, and there is not a unique 2-triangulation that realises the filling petals as edges. It would be an interesting challenge to try to improve our algorithm by analysing paths in the flip graph and optimising the number of tetrahedra we use in the construction of handlebodies of genus $g > 1$.

3.4.2. Using the algorithm

The algorithm is available on GitHub [HMT24b] and can be implemented using Regina.

To build a petal-filled triangulation using our algorithm, we set `tri` to be any one-vertex 3-triangulation with a single genus-g boundary component. We set `weights` to be an n-tuple, where n is the total number of edges in `tri`; entries for boundary edges correspond to the weights on those edges, and entries for non-boundary edges must be 0. We set `resolved` to be a (possibly empty) set of edge labels corresponding to pre-resolved edges. We then use the sequence of commands shown in Figure 3.30 to build the petal-filled triangulation determined by the input. More detailed instructions for using our algorithm can be found in the preprint [HMT24a].

Let us demonstrate our algorithm by constructing one-vertex petal-filled triangulations for some simple genus-2 Heegaard splittings. Recall that we apply our algorithm to Heegaard diagrams (in the sense of Setting B) by assuming that one side of the diagram has already been filled, so that the first set of attaching circles corresponds to the meridians of an input

```
H = HeegaardBuilder()
H.setBouquet(Triangulation3(tri), weights, resolved)
H.resolveGreedily()
H.fillHandlebody()
filled = H.triangulation()
```

FIGURE 3.30. A basic sequence of commands to construct a petal-filled triangulation using our algorithm.

handlebody M, and the second set corresponds to filling curves on ∂M. Figure 3.31 shows the filling curves that we use to represent Heegaard splittings of S^3, $(S^2 \times S^1)\#(S^2 \times S^1)$ and $L(3,1)$.

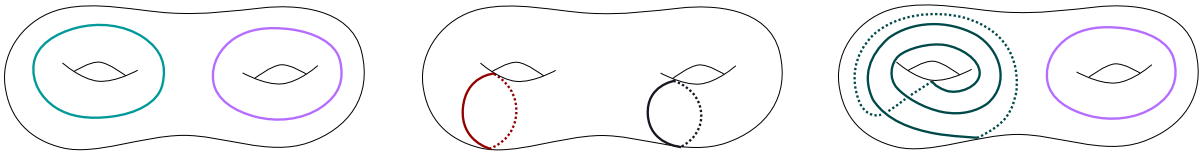

FIGURE 3.31. Topological filling diagrams for (left to right): S^3, $(S^2 \times S^1)\#(S^2 \times S^1)$, and $L(3,1)$

To convert the topological filling diagrams of Figure 3.31 into combinatorial filling diagrams, we endow the input handlebody M with the triangulation given by the isomorphism signature `eHuGabdes` (recall that this is the genus-2 handlebody we studied in Section 3.1.3).

Since we are assuming that one set of attaching circles (of the Heegaard diagram) corresponds to the meridians of the starting handlebody, we must locate the meridians of M with respect to the triangulation. This was done in Section 3.1.3, and the corresponding embedding of the boundary triangulation into $\mathbb{R}^3$ is shown in Figure 3.32.

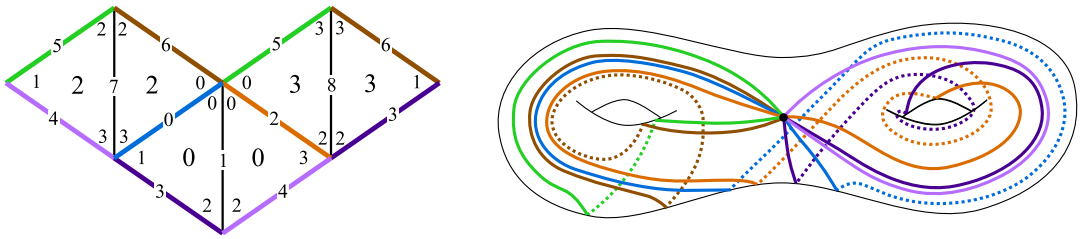

FIGURE 3.32. LEFT: The boundary triangulation of `eHuGabdes`, using labels from REGINA (as in Section 3.1.3). Note that there are three types of labels: tetrahedron number (in the centre of each face), edge number (in the centre of each edge), and vertex number (in the corners of each face). RIGHT: An embedding of this marked genus-2 boundary surface into $\mathbb{R}^3$, with edges 1, 7 and 8 omitted for simplicity.

For each example topological filling diagram, we copy the filling curves onto the triangulation in Figure 3.32, and then isotope these circles so that they are rooted and compatible with the boundary triangulation. We can then determine which edges correspond to pre-resolved attaching circles, and can also read off the edge-weight tuple. This gives all the required data to input into our algorithm.

We set `tri` to be the genus-2 layered handlebody with isomorphism signature `eHuGabdes`, and run the sequence of commands described above for each example filling diagram.

A GENUS-2 SPLITTING OF S^3. Figure 3.33 visualises a combinatorial filling diagram for S^3.

Having set `weights=(0,0,0,0,0,0,0,0,1)` and `resolved={4}`, we run the algorithm, followed by `filled.isoSig()`, to find that the isomorphism signature is `gLLAQaddefefbpupcgo`.

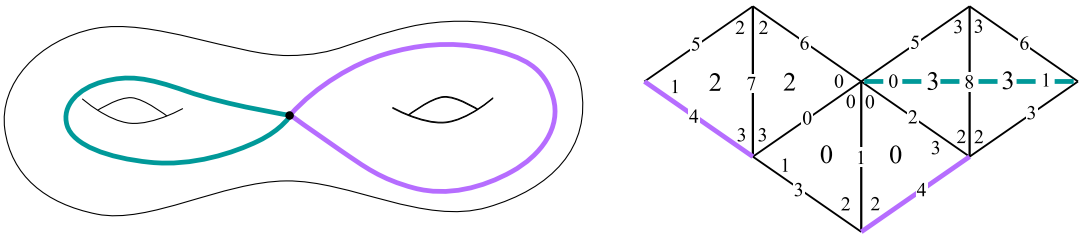

FIGURE 3.33. The rooted version of the topological filling diagram for S^3 (left), and how these filling curves appear with respect to the boundary triangulation (right). From this, we know to set `resolved={4}` and `weights=(0,0,0,0,0,0,0,0,1)`.

.

To confirm that we have built a triangulation of S^3, we run `filled.isSphere()`, which returns `True`, as expected.

A GENUS-2 SPLITTING OF $(S^2 \times S^1)\#(S^2 \times S^1)$. Figure 3.34 visualises a combinatorial filling diagram for $(S^2 \times S^1)\#(S^2 \times S^1)$.

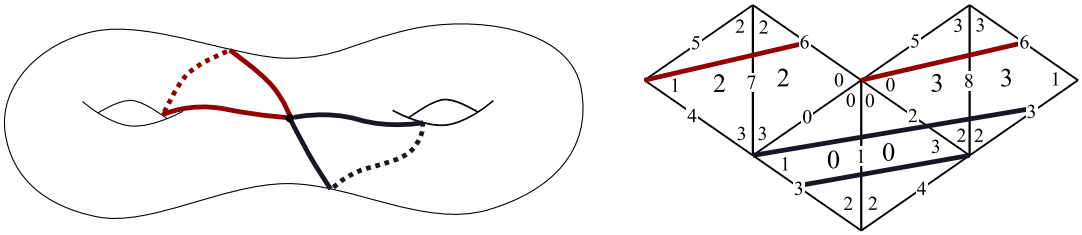

FIGURE 3.34. The rooted version of the topological filling diagram for $(S^2 \times S^1)\#(S^2 \times S^1)$ (left), and how these filling curves appear with respect to the boundary triangulation (right). From this, we know to set `resolved` to be empty and `weights=(0,2,1,1,0,0,1,1,2)`.

.

Having set `weights=(0,2,1,1,0,0,1,1,2)` and `resolved` to be empty, we run the algorithm, followed by `summands = filled.summands()`, which tells us that `filled` has two summands in its connected sum decomposition. We can check the isomorphism signatures of the two summands using `summands[0].isoSig()` and `summands[1].isoSig()`. Both return the isomorphism signature `cMcabbjaj`, which represents a triangulation of $S^2 \times S^1$. This confirms that `filled` is a triangulation of $(S^2 \times S^1)\#(S^2 \times S^1)$.

A GENUS-2 SPLITTING OF THE LENS SPACE $L(3,1)$. Figure 3.35 visualises a combinatorial filling diagram for $L(3,1)$.

Having set `weights=(0,0,0,0,0,1,0,1,1)` and `resolved={4}`, we run the algorithm, followed by `filled.isoSig()`, which returns the isomorphism signature

`hLLAAkcdeeffggawadaudg`.

After simplifying this filled triangulation, REGINA recognises it as $L(3,1)$.

3.4.3. EXPERIMENTATION

We used our algorithm to construct triangulations of genus-2 and 3 Heegaard splittings. Full details are given in the preprint [HMT24a]. We constructed genus-2 Heegaard splittings using

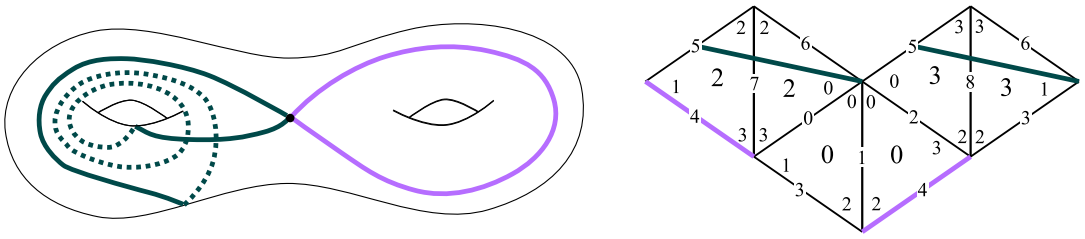

Figure 3.35. The rooted version of the topological filling diagram for $L(3,1)$ (left), and how these filling curves appear with respect to the boundary triangulation (right). From this, we know to set `resolved={4}` and `weights=(0,0,0,0,0,1,0,1,1)`.

.

the layered handlebody `eHuGabdes`, with filling bouquets determined purely combinatorially by enumerating all possible filling bouquets with total weights between 2 and 40. We built a total of 115 237 petal-filled triangulations of prime 3-manifolds in this way (with no expectation of uniqueness).

After simplifying and removing identifiable duplicates, we were left with 38 855 different simplified triangulations, 7804 of which were successfully identified as distinct minimal triangulations in the Regina closed orientable 3-manifold census [Bur11] and Hodgson-Weeks closed hyperbolic census [HoW94]. Amongst these 7804 triangulations, we saw 3006 different census manifolds.

From the 3006 census manifolds, we identified 509 lens spaces. In particular, we conclude that for the other 2497 census manifolds that we found, the Heegaard genus is equal to 2.

Delving a little deeper into the topology of the triangulations that we found, we identified 2108 triangulations of *hyperbolic* 3-manifolds using the Regina closed census and Hodgson-Weeks closed hyperbolic census, corresponding to 303 unique census manifolds. The first such manifold that we encountered was generated by the filling bouquet with edge weights `(2,1,0,3,2,3,1,1,1)` (total weight 14) and no pre-resolved edges; we can recreate the filling bouquet on the boundary triangulation of `eHuGabdes` using these edge weights, as shown in Figure 3.36. The isomorphism signature of the resulting petal-filled triangulation was

`kLvAAPPkcefehijijjuxdxasalalw`.

After simplifying this triangulation, we identified the manifold as `Hyp_0.94270736` from the Regina closed census.

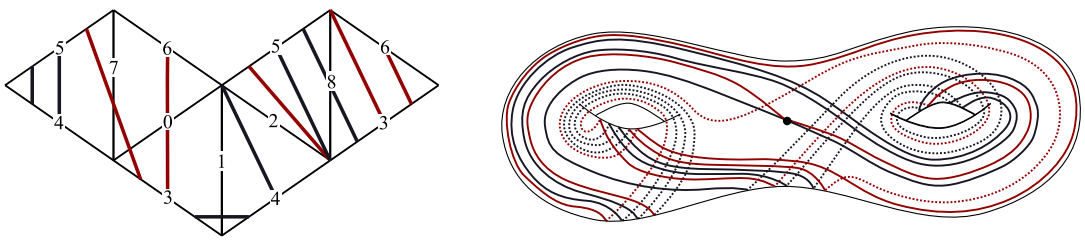

Figure 3.36. Left: Curves reconstructed from the edge weights $(2,1,0,3,2,3,1,1,1)$. Right: How these curves appear in our $\mathbb{R}^3$ embedding of `eHuGabdes` (recall Figure 3.32).

We also constructed some genus-3 Heegaard splittings, using the layered handlebody with isomorphism signature `hHbLbqiabegeti`. For this handlebody, we generated filling bouquets

with total edge weight between 3 and 20, and constructed a total of 25 343 petal-filled triangulations of prime 3-manifolds. After simplifying these petal-filled triangulations and removing duplicates, we were left with 6929 different simplified triangulations. We successfully identified 5428 of these as distinct minimal triangulations in the Regina closed orientable census and the Hodgson-Weeks census, corresponding to 2222 unique census manifolds.

From these 2222 census manifolds, we observed 679 manifolds not seen in our genus 2 experiments. Of these, 83 were identified as lens spaces. We identified 1093 triangulations of hyperbolic manifolds using the Regina closed census and Hodgson-Weeks closed hyperbolic census, corresponding to 151 unique census manifolds.

Cutwidth observations. We used Sage to compute cutwidths (recall Definition 3.31) for the triangulations that we found in the experiments discussed above. Full details are given in the preprint [HMT24a] (where we also consider treewidth, and discuss results for genus-3). From the 38 855 different simplified triangulations constructed from the genus-2 handlebody, we found that 34 419 of the corresponding petal-filled triangulations had cutwidth equal to 6 (i.e. the upper bound in Theorem 3.33). For 874 of these, we found that the 'simplified' triangulation (with fewer tetrahedra) actually had higher cutwidth. Indeed, 254 of these had an increase of (at least) 2 in their cutwidth after simplification.

An *incomplete hyperbolic structure*, as seen in the universal cover of a torus cusp.

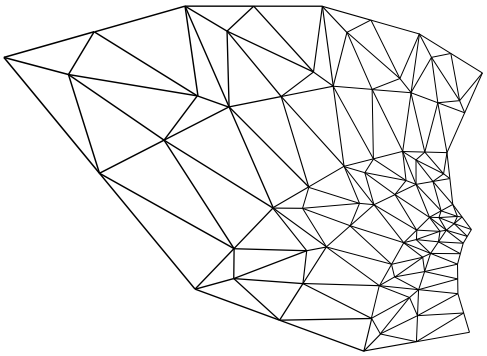

Chapter 4. An application

Describing deformations of hyperbolic structures

In this chapter, we use triangulations as a tool to study the hyperbolic geometry of cusped 3-manifolds. We see how a strategic choice of triangulation can highlight or reveal topological features of a manifold that may have otherwise been obscured. We consider deformations of hyperbolic structures on knot complements – a geometric problem that appears heavily algebraic – and show that the combinatorics of layered solid tori can be exploited to simplify the associated calculations. We begin with an introduction to hyperbolic triangulations in Section 4.1, followed by necessary background on describing deformations in Section 4.2. The main results are presented in Section 4.3, and we conclude in Section 4.4 with example calculations to demonstrate the main theorem.

SECTION 4.1. *Hyperbolic structures from triangulations*

Recall that an ideal tetrahedron can be embedded in hyperbolic 3-space by sending its ideal vertices to points on the boundary at infinity. In the process, edges are sent to hyperbolic geodesics, and faces are sent to totally geodesic planes. An entire triangulation of a manifold may be placed into $\mathbb{H}^3$ inductively using the so-called *developing map*, which introduces successive tetrahedra to $\mathbb{H}^3$ according to the prescribed face pairings. A triangulation is considered to have a hyperbolic structure if 'nothing goes wrong' in this process. Let us say this more carefully in the following.

4.1.1. Encoding geometry

It is a convenient fact that each edge in a hyperbolic ideal tetrahedron can be associated with a complex number z. This is possible since, for any ideal tetrahedron, there is an isometry of $\mathbb{H}^3$ that sends the endpoints of the edge of interest to 0 and ∞, while also sending one ideal vertex to 1 and the fourth ideal vertex to a point on the complex plane with $\mathrm{im}(z) > 0$ (as in Figure 4.1).

These parameters encode the geometry of the ideal tetrahedron. For example, if the edge parameter associated to an edge is z, then the dihedral angle between the adjacent faces of the

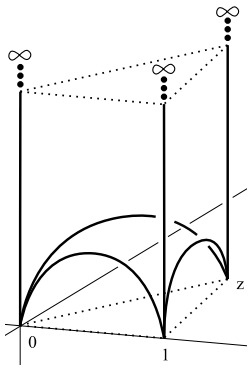

FIGURE 4.1. A standard embedding of an ideal tetrahedron into $\mathbb{H}^3$, with ideal points at 0, 1, ∞ and z.

tetrahedron is $\text{Arg}(z)$. If any of the edge parameters in an ideal tetrahedron Δ are 0 or 1, we say that the tetrahedron is *degenerate*. This cannot occur in a hyperbolic triangulation, so for now, assume this situation is avoided. It turns out that opposite edges in an ideal tetrahedron always have the same edge parameter, and in fact, all edge parameters in a non-degenerate tetrahedron can be written in terms of a single complex number. Suppose a tetrahedron Δ has vertices labelled as standard, and call the edges 0(01) and 0(23) the *a-edges*, 0(02) and 0(13) the *b-edges*, and 0(03) and 0(12) the *c-edges*. Without loss of generality, if the edge parameter for the a-edges is $z_\Delta^a = z$, then the edge parameters for the b-edges may be expressed as $z_\Delta^b = \frac{1}{1-z}$, and the edge parameters for the c-edges may be expressed as $z_\Delta^c = \frac{z-1}{z}$. We say that z is the *shape* of the tetrahedron.

To ensure that a tetrahedron Δ is not degenerate, we insist that z_Δ^a, z_Δ^b, z_Δ^c satisfy the following *degeneracy equations*:

$$z_\Delta^a z_\Delta^b z_\Delta^c = -1 \quad \text{and} \quad z_\Delta^a + (z_\Delta^b)^{-1} + 1 = 0.$$

To describe the remaining conditions required for a triangulation to be hyperbolic, we consider a specific triangulation. We study the complement of the hyperbolic knot $K5_4$, with triangulation as given in Figure 4.2.

	012	013	023	123
0	2(021)	1(023)	1(312)	1(031)
1	2(301)	0(132)	0(013)	0(230)
2	0(021)	1(120)	3(021)	3(103)
3	2(032)	2(213)	4(021)	4(103)
4	3(032)	3(213)	4(312)	4(230)

(a) Face pairings for the triangulation of $K5_4$ in *Regina* notation.

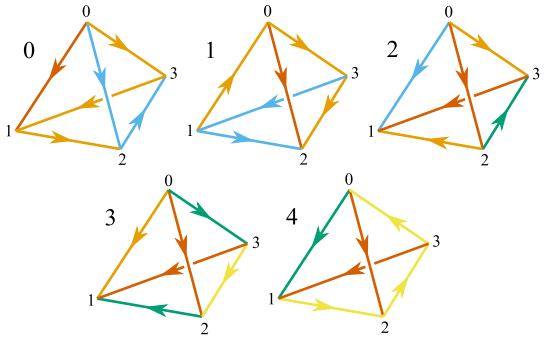

(b) A visual representation of the gluing information, with edge colours to be used in subsequent figures.

FIGURE 4.2. A triangulation of the knot $K5_4$.

For a triangulation to make sense after embedding in hyperbolic space, each pair of faces that glue together must have the same geometry. We ensure this is the case globally by en-

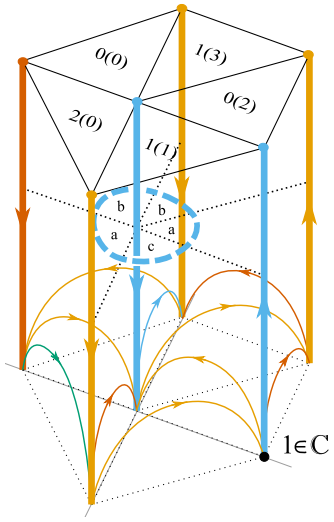

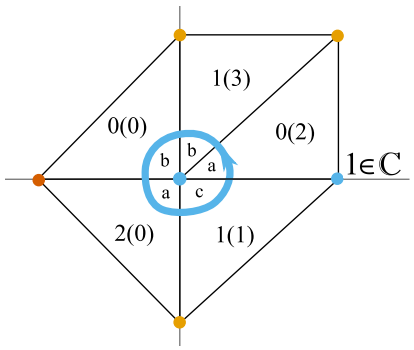

(a) All the information from the 3-dimensional picture can be summarised in this 2-dimensional picture of the induced *cusp triangulation*.

Figure 4.3. On the left we see the 3-dimensional picture of how tetrahedra glue together around the blue edge. The corresponding gluing equation is $z_0^a \cdot z_1^b \cdot z_0^b \cdot z_2^a \cdot z_1^c = 1$.

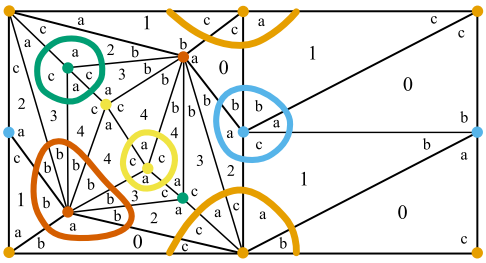

Figure 4.4. The cusp triangulation for $K5_4$. Coloured curves correspond to the product of edge parameters that make up each gluing equation.

suring it is the case around each edge in the triangulation. This condition is captured by the *gluing equations*, which require the product of edge parameters seen around each edge to be 1. Figure 4.3 shows the gluing around the blue edge for $K5_4$.

There is actually no need to consider the 3-dimensional picture, because all the information we require can be seen in the 2-dimensional *cusp triangulation*. The cusp triangulation is the induced triangulation where tetrahedra intersect a given horosphere. As such, the triangles in a cusp triangulation correspond to truncated tips of tetrahedra, and the 2-vertices represent 3-edges meeting the cusp transversely. In Figure 4.4, the labels in the centre of each triangle refer to the tetrahedron, and the labels in the corners indicate whether each vertex corresponds to an a-, b-, or c-edge. Note that the cusp triangulation is reconstructed from the gluing information in Table 4.2a (which is not an insignificant task).

From Figure 4.4, we extract the following gluing equations for $K5_4$:

$$\begin{aligned}
\text{Red edge:} \quad & 1 = z_0^a \cdot z_2^b \cdot z_3^b \cdot z_4^b \cdot z_4^b \cdot z_3^b \cdot z_2^b \cdot z_1^b \\
\text{Yellow edge:} \quad & 1 = z_4^c \cdot z_4^a \cdot z_4^c \cdot z_3^a \\
\text{Green edge:} \quad & 1 = z_3^c \cdot z_2^a \cdot z_3^c \cdot z_4^a \\
\text{Blue edge:} \quad & 1 = z_0^a \cdot z_1^b \cdot z_0^b \cdot z_2^a \cdot z_1^c
\end{aligned}$$

Having established that tetrahedra glue together nicely around each edge, we next consider how they glue together globally around a cusp. To do this, we compute *holonomies* of the

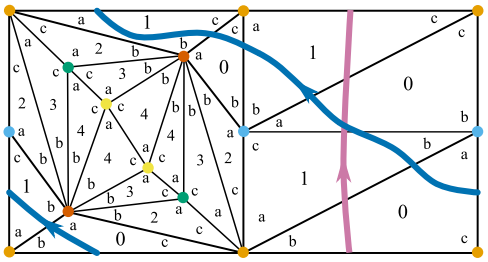

FIGURE 4.5. The meridian (pink) and longitude (blue), with orientations used to determine their holonomies.

meridian and longitude of the cusp. The holonomy of an oriented closed curve is represented by a product of edge parameters as they are encountered along the curve. If an edge parameter is seen to the right of the curve, its inverse is contributed to the product; otherwise, the edge parameter is contributed as normal. Figure 4.5 shows the meridian and longitude of $K5_4$, from which we can extract the holonomies

$$h(\mu) = z_0^b \cdot (z_1^b)^{-1} \cdot z_0^a \cdot (z_1^c)^{-1}$$
$$h(\lambda) = (z_0^a)^{-1} \cdot (z_1^b)^{-1} \cdot z_0^a \cdot z_1^b \cdot (z_0^c)^{-1} \cdot (z_1^c)^{-1} \cdot z_0^b \cdot z_1^a.$$

If a triangulation satisfies the gluing and degeneracy equations, then it has a hyperbolic structure. However, this structure is in general *incomplete*. By Mostow-Prasad rigidity, there is a unique *complete* hyperbolic structure on any finite-volume hyperbolic 3-manifold. We can use the holonomies, in terms of the shape parameters, to determine when a hyperbolic structure is complete. The complete hyperbolic structure occurs when the holonomies of the meridian and longitude are pure translations, without rotation or scaling. This condition is captured by the *completeness equations*, $h(\mu) = 1$ and $h(\lambda) = 1$.

Neumann and Zagier [NZ85] defined an integer matrix that encodes the gluing and completeness equations via the exponents of each edge parameter. This can be constructed by first writing out an *incidence matrix* with one row per gluing or completeness equation, and one column each for all edge parameters over all tetrahedra in the triangulation. For each edge-type $e \in \{a, b, c\}$ in the tetrahedron Δ, let $\mathbf{z}_\Delta^e$ be the column vector that encodes the integer exponents of z_Δ^e in each of the gluing and completeness equations. The *Neumann-Zagier matrix NZ*, as it is now known, consists of pairs of columns $\mathbf{z}_\Delta$, $\mathbf{z}'_\Delta$ found by subtracting each 'c' column from the corresponding 'a' and 'b' columns, i.e.

$$\mathbf{z}_\Delta = \mathbf{z}_\Delta^a - \mathbf{z}_\Delta^c \quad \text{and} \quad \mathbf{z}'_\Delta = \mathbf{z}_\Delta^b - \mathbf{z}_\Delta^c.$$

By an Euler characteristic argument, the number of edges in an ideal triangulation is equal to the number of tetrahedra, but Neumann and Zagier [NZ85] showed that one of the n gluing equations in an n-tetrahedron triangulation is always redundant, and can be safely ignored. Hence, the Neumann-Zagier matrix is an $(n+1) \times (2n)$ matrix with $n-1$ rows corresponding to gluing equations, as well as a row for each of the meridian and longitude holonomies; and two columns per tetrahedron, namely $\mathbf{z}_\Delta$, $\mathbf{z}'_\Delta$. This matrix will be important for us later on. Figure 4.6 shows the entries for the *NZ* matrix from our example of $K5_4$.

	$\mathbf{z}_0$	$\mathbf{z}'_0$	$\mathbf{z}_1$	$\mathbf{z}'_1$	$\mathbf{z}_2$	$\mathbf{z}'_2$	$\mathbf{z}_3$	$\mathbf{z}'_3$	$\mathbf{z}_4$	$\mathbf{z}'_4$
Red edge	1	0	0	1	0	2	0	2	0	2
Yellow edge	0	0	0	0	0	0	1	0	−1	−2
Green edge	0	0	0	0	1	0	−2	−2	1	0
Blue edge	1	1	−1	0	1	0	0	0	0	0
Meridian	1	1	1	0	0	0	0	0	0	0
Longitude	1	2	2	1	0	0	0	0	0	0

Figure 4.6. Entries for the *NZ* matrix corresponding to our example of $K5_4$.

section 4.2. *Deformations of hyperbolic structures*

While the complete hyperbolic structure on a cusped hyperbolic 3-manifold is unique, there are infinitely many incomplete hyperbolic structures. For a 1-cusped hyperbolic manifold, Thurston showed that there is a complex 1-dimensional space of incomplete hyperbolic structures that arise as *deformations* of the complete structure [see Chapter 5.5, Thur]. The space of deformations of the hyperbolic structures on an ideal triangulation is now known as the *deformation variety* or the *gluing variety*.

One way to parametrise the space of incomplete structures is using the gluing equations and the holonomies of the meridian and longitude. Instead of setting the holonomies of the meridian and longitude equal to 1, we may set them equal to variables M and L, respectively. This system of equations can then be reduced to obtain a polynomial in L and M. This was originally done by Champanerkar [Cha03], who called this polynomial $H(L, M)$. He showed that $H(L, M)$ is closely related to a knot invariant known as the *A-polynomial*.

The A-polynomial $A(L, M)$ is an invariant of a (framed) one-cusped 3-manifold that was originally introduced in 1994 [CCGLS]. It is a 2-variable polynomial describing the relationship between the eigenvalues of the meridian and longitude of the cusp under representations of the fundamental group into $\mathrm{SL}(2, \mathbb{C})$. An analogous polynomial, which we denote by $\overline{A}(L, M)$ can be defined similarly but with $\mathrm{PSL}(2, \mathbb{C})$ representations. This was studied by Boyer and Zhang [BZ98].

The A-polynomial exhibits a number of important properties, including the ability to detect boundary slopes of incompressible surfaces in the knot complement. The A-polynomial is also known in connection to the coloured Jones polynomial through the so-called AJ conjecture [Gar04].

Connections to hyperbolic geometry. The group of isometries of $\mathbb{H}^3$ is isomorphic to $\mathrm{PSL}(2, \mathbb{C})$, which is what enabled Champanerkar to connect $H(L, M)$ to $A(L, M)$ via $\overline{A}(L, M)$. This connection uses the fact that the completeness equations determining the complete hyperbolic structure on a knot complement K also determine a discrete, faithful representation $\overline{p} : \pi_1(K) \to \mathrm{PSL}(2, \mathbb{C})$. This distinguished representation can be tracked throughout each step in defining $\overline{A}(L, M)$, and can ultimately be associated to one of the factors of $\overline{A}(L, M)$. Furthermore, $\overline{p}$ always lifts to a representation $p : \pi_1(K) \to \mathrm{SL}(2, \mathbb{C})$ [Thur; CS83], and a factor of $A(L, M)$ can similarly be identified. We refer to this factor of either $\overline{A}(L, M)$ or $A(L, M)$, and the corresponding factor of $H(L, M)$, as the *geometric factor* of the respective polynomial.

While $H(L, M)$ necessarily depends on the given triangulation (and in general will not detect all factors of the $\mathrm{PSL}(2, \mathbb{C})$ A-polynomial [see Seg12]), Champanerkar showed that $H(L, M)$ is always a *divisor* of $\overline{A}(L, M)$ [Cha03, Theorem 2.1]. Moreover, the geometric factor of $H(L, M)$ is *equal to* the geometric factor of $\overline{A}(L, M)$, and hence, this factor is triangulation-independent [Cha03, Theorem 2.2].

Since $H(L, M)$ exhibits many of the important properties of the A-polynomial, it has become common for authors to conflate $H(L, M)$, $\overline{A}(L, M)$ and $A(L, M)$ to various degrees. For us, 'the A-polynomial' may, at various times, be used to mean any of the aforementioned polynomials, but since we are primarily concerned with hyperbolic knots we will always assume that the geometric factor is included.

The A-polynomials we know. To date, A-polynomials (or divisors containing the geometric factor) are known for all knots with up to eight crossings, many knots with nine crossings and some knots with ten crossings, as well as all hyperbolic knots that can be triangulated by up to seven ideal tetrahedra [Cul; LM24]. There also exist explicit formulas for the A-polynomials of the torus knots [CCGLS], the twist knots [Mat14a; Mat14b], iterated torus knots [NiZ17], and knots with Conway's notation $C(2m, 3)$ [HL16]. Recursive formulas exist for the A-polynomials of certain classes of two-bridge knots [HS04; Pet15], and a family of pretzel knots [GM11; TY04].

This family of pretzel knots is found by $1/m$ Dehn fillings of what Garoufalidis calls a *favorable link* [Gar14]. That is, the geometric factors of A-polynomials for the $1/m$ fillings of this link satisfy a particular recurrence. Indeed, Garoufalidis proves more generally that there exists a recurrent sequence of rational functions containing the geometric factor of the A-polynomial for any family of knots related by twisting [see Theorem 3.1 of Gar14]. My results lead to a similar observation but where the rational functions are given explicitly rather than recursively.

A problem in elimination theory. The A-polynomial is notoriously difficult to compute, in general. A direct approach to computing the A-polynomial of a knot via representations into $\mathrm{SL}(2, \mathbb{C})$ is to assign arbitrary matrices to each generator in the knot group and set up a system of equations that ensure the group relations are satisfied. By considering words in the generators corresponding to the meridian and longitude, and by declaring the eigenvalues of their images to be M and L, respectively, we obtain further equations involving these variables.

The number of equations in this system scales linearly with the number of relations in the fundamental group. Eliminating all variables other than M and L gives the A-polynomial. This approach is effective so long as the number of relations is small, and as such, the A-polynomial is readily computable for knots with small crossing number (using, for instance, the Wirtinger presentation, which requires one less relation than there are crossings in a diagram). The A-polynomial has also been calculated for some infinite families of knots with simple fundamental group presentations, such as the twist knots: a recursive formula was given by Hoste and Shanahan [HS04] (recovered and generalised later by Petersen [Pet15]), and then made explicit by Mathews [Mat14a; Mat14b]. It is a well known problem in elimination theory that finding resultants in a system of polynomial equations becomes computationally difficult when the num-

ber of equations is large or the degree of the polynomials is high. This is a recurring challenge in the calculation of A-polynomials.

As discussed, Champanerkar's polynomial can be calculated directly for hyperbolic knots by reducing the system of gluing equations along with the holonomy equations in terms of L and M. This calculation is feasible for knot complements that are built from a small number of tetrahedra; however, once the number of tetrahedra becomes too large, calculations are again impeded by the limitations of elimination theory. Culler developed a numerical method for computing divisors of the $\mathrm{SL}(2,\mathbb{C})$ A-polynomial that contain the geometric factor, which also uses the deformation variety. He set up a database of these polynomials for knots with small crossing numbers and knots with low triangulation complexity [available via Cul; LM24].

Ptolemy equations. Recall that the gluing and holonomy equations can be stored in the $(n+1)\times(2n)$-dimensional NZ matrix. Neumann and Zagier [NZ85] showed that this matrix exhibits *symplectic* properties. In particular, NZ can be extended to a square matrix in which rows come in pairs that are symplectically dual to each other. The rows corresponding to the meridian and longitude holonomies form a dual pair, and $n-1$ additional rows can be introduced to form dual pairs with each of the rows corresponding to gluing equations. Mathews and Purcell [MPu22] have recently described a geometric interpretation of the rows that are added in this way.

Dimofte [Dim13], and later Howie, Mathews, and Purcell [HMP20], used the $(2n)\times(2n)$ symplectic version of NZ to perform a change of basis on the system of gluing and holonomy equations. This process converts the one equation per edge class and one equation per cusp generator (all in terms of variables associated to each tetrahedron) to one equation per tetrahedron (in terms of variables associated to each edge class and each cusp generator). We give a broad overview of this process here, but refer to [HMP20] for the details.

To begin, the gluing and holonomy equations are converted into a logarithmic form, which can then be summarised by the matrix equation $NZ\cdot Z = H+\pi i C$, where Z is a vector consisting of the logarithmic analogues of z_Δ, z'_Δ, H is a vector in terms of the holonomy variables L, M, and C is a vector in terms of the exponents of z^c_Δ [see Definition 2.22 in HMP20]. As alluded to above, the matrix NZ can be extended to a symplectic matrix, called SY in [HMP20], by introducing $n-1$ (appropriately chosen) additional rows. Using SY, Howie, Mathews, and Purcell obtain a new set of variables, including one for each of the edge classes and cusp generators, summarised in a vector $\Gamma = SY\cdot Z$. They prove [in Proposition 2.53, HMP20] that the logarithmic gluing and holonomy equations are equivalent to $Z = (-J)\cdot NZ'\cdot\Gamma' + \pi i B$, where NZ' and Γ' are (loosely speaking) just rearranged versions of NZ and Γ, the matrix J is skew-symmetric (with $J^2 = -\mathrm{Id}$), and B is an integer vector satisfying $NZ\cdot B = C$ [whose existence was guaranteed in NZ85].

By re-exponentiating, Howie, Mathews, and Purcell [HMP20] obtain variables $\gamma_j = e^{\Gamma_j}$ corresponding to each edge class that allow them to rewrite z^a_Δ, z^b_Δ in terms of the γ_j variables and the holonomy variables L, M. The degeneracy equations $z^a_\Delta + (z^b_\Delta)^{-1} + 1 = 0$ for each tetrahedron can then be re-expressed in terms of the new variables. Howie, Mathews, and Purcell noticed that these new equations exhibit Ptolemy-like structure similar to the equations defining Goerner and Zickert's *enhanced Ptolemy variety* [GZ18]. The key observation in [HMP20] is

that, for any tetrahedron belonging to a **layered solid torus**, the associated Ptolemy-like equation has the form

$$\pm\gamma_{\Delta(01)}\gamma_{\Delta(23)} \pm \gamma_{\Delta(02)}\gamma_{\Delta(13)} = \gamma_{\Delta(03)}\gamma_{\Delta(12)}. \tag{4.1}$$

Returning to our example of $K5_4$, we associate the variables $\gamma_b, \gamma_g, \gamma_o, \gamma_r, \gamma_y$ with the edges coloured blue, green, orange, red, and yellow, respectively. In [HMPT23], my coauthors and I determined the equations associated to each tetrahedron to be:

$$\begin{aligned}
\Delta_0: \quad \gamma_o^2 &= L^{-1}M\,\gamma_r\gamma_b - L^{-1}M^2\gamma_b\gamma_o \\
\Delta_1: \quad \gamma_o\gamma_b &= -L^{-1}M^2\gamma_o^2 + M\,\gamma_r\gamma_b \\
\Delta_2: \quad \gamma_r^2 &= \gamma_b\gamma_g + \gamma_o^2 \\
\Delta_3: \quad \gamma_g^2 &= \gamma_o\gamma_y + \gamma_r^2 \\
\Delta_4: \quad \gamma_y^2 &= \gamma_g\gamma_y + \gamma_r^2.
\end{aligned}$$

Cluster algebras. Howie, Mathews, and Purcell [HMP20] observed that the Ptolemy-like equations associated to tetrahedra in a layered solid torus are reminiscent of so-called *exchange relations* in a *cluster algebra*.

Cluster algebras are commutative rings with rich combinatorial structure. Generators and relations are not defined at the outset, but rather, sets (called *clusters*) of *cluster variables* are generated recursively using a process called *mutation*. A formal definition of this process is unnecessary for our purposes, however, we may think of mutation informally as the replacement of one cluster variable in a cluster with a new cluster variable, according to an *exchange relation*. For example, the "simplest cluster algebra of infinite type" [as described in Zel07], is defined by the initial cluster $\{x_1, x_2\}$ and the exchange relation

$$x_{i-1}\,x_{i+1} = x_i^2 + 1.$$

The main arguments in Section 4.3 are inspired by a loose connection drawn between this exchange relation and the Ptolemy-like equation (4.1), after replacing the cluster variables x_i with (appropriately indexed) edge class variables γ_j.

Originally, cluster algebras were defined by Fomin and Zelevinsky [FZ02] when they were studying dual canonical bases and total positivity in semisimple Lie groups. Since then, applications of cluster algebras have been found in a wide range of contexts, including quiver representations, discrete dynamical systems, tropical geometry, and Teichmüller theory [FZ03]. One intriguing property of a cluster algebra, known as the *Laurent phenomenon*, is that every cluster variable can be written as an integer Laurent polynomial in the initial cluster variables [FZ02].

Cluster algebras also arise naturally in relation to triangulations of surfaces, and in this context, Fomin, Shapiro, and Thurston [FST08] proved that the cluster variables carry information about certain intersection numbers. In particular, the exponents of the terms in the denominator of the Laurent polynomial are equal to intersection numbers in the corresponding triangulation [see Theorem 8.6 in FST08, for details].

Combinatorial structure. Cluster algebras capture rich combinatorial structure in the settings where they arise. It is therefore unsurprising that many results in this field can be

proven via overtly combinatorial arguments. For example, there are three separate proofs [CZ06; MuP07; Zel07] that the inductively defined cluster variables for the simplest infinite-type cluster algebra (recall the exchange relation above) can be defined explicitly by a closed formula in terms of only the initial cluster variables.

We take particular inspiration from the proof given by Musiker and Propp [MuP07], which uses *perfect matchings* of *weighted ladder graphs*. Let us introduce the relevant terminology.

Informally, a *ladder graph* L_r is the graph that resembles a ladder with r rungs. It is a $2r$-node graph with two rows of r node and arcs connecting adjacent nodes in each row and column. A *weighted graph* is a graph in which each arc is assigned a number or variable, called a *weight*. A *perfect matching* of a graph G is a subset S of arcs in G such that each node belongs to exactly one arc in S (see Figure 4.7 for an example). The *weight* $w(S)$ of a perfect matching is defined to be the product of the weights of its constituent arcs.

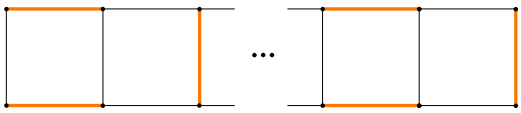

Figure 4.7. A perfect matching of the ladder graph L_r.

In a perfect matching of a ladder graph, if one horizontal arc is included, then the horizontal arc directly above or below it must also be included. Notice that a perfect matching of a ladder graph is completely determined by which pairs of horizontal arcs are contained in the perfect matching. Moreover, adjacent horizontal arcs cannot be simultaneously included. Choosing a perfect matching of the ladder graph L_r is therefore equivalent to choosing a subset of the integers $\{1, \cdots, r-1\}$ without choosing any consecutive integers.

With this in mind we state the following combinatorial result, which is an important piece in the proof of Theorem 4.8.

Theorem 4.1. (Musiker–Propp, Theorem 3). The number of ways to choose a subset S of $\{1, 2, \cdots, 2r-1\}$ such that S contains a odd elements, b even elements, and no consecutive elements is

$$\binom{r-1-a}{b}\binom{r-b}{a}.$$

Remark 4.2. This differs from the statement in [MuP07] in the following ways: we require only the first of the two cases (where Musiker and Propp's N is odd), and we replace their n, q, and r with $r-1$, a, and b, respectively.

4.2.1. Using layered solid tori to simplify A-polynomial calculations

In the remainder of this chapter, we pull together the various threads discussed so far, and prove the following theorem.

Theorem 4.3. Let $K_{\pm m}$ be the sequence of knots obtained by performing $\pm 1/m$ Dehn fillings on an unknotted component of a two-component link in S^3. Then, for sufficiently large m, the A-polynomial of $K_{\pm m}$ may be defined by a finite number of fixed polynomial equations corresponding to the parent link and a single polynomial equation depending on m that corresponds to the Dehn filling.

We approach this from the perspective of cluster algebras, first proving that the Ptolemy-like equations corresponding to tetrahedra in a layered solid torus exhibit the Laurent phenomenon (Theorem 4.8), and that the exponents in the denominator of the associated Laurent polynomial may be interpreted as certain intersection numbers in the Farey triangulation (Theorem 4.16). Our main arguments rely on perfect matchings of ladder graphs, as inspired by [MuP07].

Implications of these results for the calculation of A-polynomials are presented in Theorem 4.17 and Corollary 4.18. Then, in Section 4.4.1, I add to the list of known A-polynomials by giving explicit formulas for rational functions that contain the geometric factor of the A-polynomials for the twisted torus knots $T(5, -5n-14, 2, 2)$ and $T(5, 5n+11, 2, 2)$ for $n \geq 1$.

SECTION 4.3. *Simplifying A-polynomial calculations*

Let us begin by establishing notation for the slopes in a layered solid torus, with reference to the corresponding walk in the Farey triangulation. Our notation differs to that used in [HMP20], where slopes are labelled according to the *absolute* direction of the associated step (that is, using *port* for the slope to the left and *starboard* for the slope to the right). Here we label slopes according to the direction of the associated step *relative* to the previous step. For the k^{th} step, we label the *old* slope o_k and the slope we are *heading* towards h_k, as in [HMP20]. Knowing the $(k-1)^{st}$ step, we label the slope that the k^{th} step *pivots* around p_k and the slope that *fans* out f_k (as in Figure 4.8, right). For the initial step, the old and heading slopes are labelled o_0 and h_0, respectively. However, because there is no previous step, the pivot and fan slopes are ill-defined. Hence, for this step we declare the slope to the left in the Farey triangulation to be f_0 and the slope to the right to be p_0 (see Figure 4.8, left). Note that the labelling of the initial step is as though it were a right step.

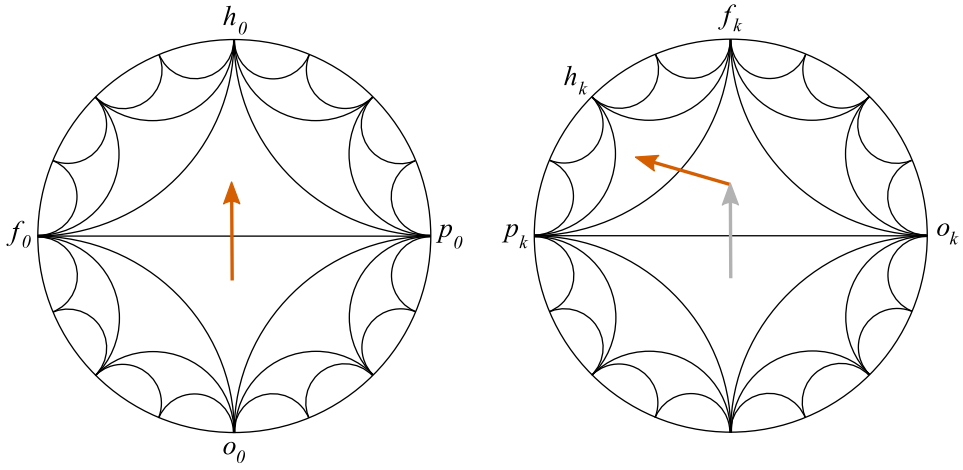

FIGURE 4.8. LEFT: Slope labels for the initial step. RIGHT: Slope labels for the k^{th} step.

Following Howie, Mathews, and Purcell [HMP20], we assign γ variables to each edge class in the triangulation and label these variables by the slope of the edge. There are two formats we use, depending on the context. When referring to a slope s_k associated to the k^{th} step in the construction of a layered solid torus, we use the notation γ_{s_k}. When the actual slope is known, as is the case throughout Section 4.4, we use the notation $\gamma_{p/q}$ for the edge with slope p/q.

Here we restate Theorem 3.17(ii) of [HMP20] using the relative slope labels discussed above.

Theorem 4.4. (Howie–Mathews–Purcell, Theorem 3.17(ii)). With slopes labelled according to the corresponding walk of length N in the Farey triangulation, the Ptolemy equations for the tetrahedra in a layered solid torus are

$$\gamma_{o_k}\gamma_{h_k} + \gamma_{p_k}^2 - \gamma_{f_k}^2 = 0, \text{ for } 0 \leq k \leq N-1.$$

When $k = N$ we pick up the *folding equation* $\gamma_{p_N} = \gamma_{f_N}$.

Remark 4.5. By labelling slopes according to their relative direction, we remove the need to distinguish between left and right steps, as in [HMP20].

Definition 4.6. (Anatomy of a layered solid torus). Let W be a word in L's and R's describing the sequence of left and right steps in the construction of a layered solid torus X.

- The final letter in W, corresponding to the fold in X, is the *tip of* W.
- The maximal string of either L's or R's immediately preceding the tip of W is the *tail of* W and the corresponding tetrahedra form the *tail of* X.
- The string of L's and R's in W preceding the tail of W form the *body of* W and the corresponding tetrahedra form the *body of* X.
- The tetrahedron in X that corresponds to the 0^{th} step is the *head of* X. For reasons that are not important at this point, we may sometimes denote the head by (R) in W.

Throughout this chapter, when referring to the length of a walk that describes the construction of a layered solid torus (that is, including the head, body, tail and tip) we use N, whereas when only considering the length of a tail we use n.

Observe that the Ptolemy equations for $0 \leq k \leq N-1$ in Theorem 4.4 encompass those associated with the head, body and tail of the layered solid torus, while the folding equation corresponds to the tip.

4.3.1. Results related to cluster algebras

Throughout this section, take k to be fixed. For ease of notation, we define the following family of polynomials.

Definition 4.7.

$$H_n = \gamma_{f_k}^{2n} + \sum_{a+b\leq n-1} (-1)^{n-a-b} \binom{n-1-a}{b} \binom{n-b}{a} \gamma_{f_k}^{2a} \gamma_{o_k}^{2b} \gamma_{p_k}^{2(n-a-b)}, \text{ for } n \in \mathbb{Z}^+.$$

Theorem 4.8. Suppose a layered solid torus has a tail of length $n \geq 1$ beginning at the k^{th} step. Then, using the Ptolemy equations corresponding to each tetrahedron, the variable $\gamma_{h_{k+n-1}}$ can be expressed as

$$\gamma_{h_{k+n-1}} = \frac{H_n}{\gamma_{f_k}^{n-1}\gamma_{o_k}^{n}}.$$

Thus, $\gamma_{h_{k+n-1}}$ can be expressed as an integer Laurent polynomial in the variables $\gamma_{f_k}, \gamma_{o_k}$ and γ_{p_k}.

To prove this theorem we first establish a relationship between H_n and the perfect matchings of a weighted ladder graph G_r. Let G_r be the ladder graph L_r with arcs weighted as in Figure 4.9. Vertical arc weights alternate between γ_{p_k} and $-\gamma_{p_k}$, starting with γ_{p_k} on the left. Horizontal arc weights alternate between γ_{f_k} and γ_{o_k}, starting with γ_{f_k} on the left.

Definition 4.9. Let $\mathcal{S}$ be the set of all perfect matchings of the graph G_r. We define a polynomial P_r in the variables $\gamma_{f_k}, \gamma_{o_k}$ and γ_{p_k} to be the sum of the weights of all perfect matchings in $\mathcal{S}$. That is,

$$P_r(\gamma_{f_k}, \gamma_{o_k}, \gamma_{p_k}) = \sum_{S \in \mathcal{S}} w(S).$$

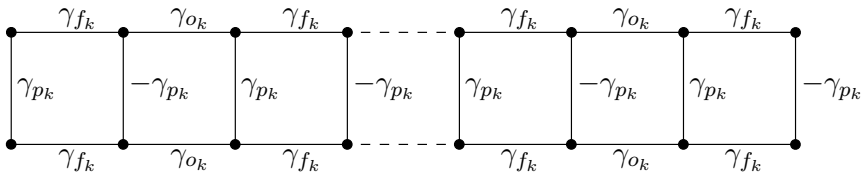

FIGURE 4.9. The graph G_r for even r, with arcs weighted as described.

We show that H_n is equivalent to P_{2n}.

Lemma 4.10. (MUSIKER–PROPP, Lemma 2). The number of ways to choose a perfect matching of G_r with a pairs of arcs weighted γ_{f_k} and b pairs of arcs weighted γ_{o_k} is the number of ways to choose a subset $S \subset \{1, 2, \ldots, r-1\}$ such that S contains a odd elements, b even elements, and no consecutive elements.

Proof. To see this, note that all perfect matchings of G_r can be found by choosing pairs of parallel horizontal arcs with the condition that no consecutive arcs are chosen. Pairs of parallel arcs weighted γ_{f_k} are in one-to-one correspondence with the odd integers between 1 and $r-1$, while pairs of parallel arcs weighted γ_{o_k} are in one-to-one correspondence with the even integers between 1 and $r-1$. □

Remark 4.11. Note that a perfect matching as described above must also include $\lceil r/2 \rceil - a - b$ vertical arcs each weighted γ_{p_k} and $\lfloor r/2 \rfloor - a - b$ vertical arcs each weighted $-\gamma_{p_k}$. Hence, when $r = 2n$, the number described in Lemma 4.10 is the coefficient in P_{2n} of the term

$$(-1)^{n-a-b} \gamma_{f_k}^{2a} \gamma_{o_k}^{2b} \gamma_{p_k}^{2(n-a-b)}.$$

Recall from Theorem 4.1 that the number of ways to choose a subset $S \subset \{1, 2, \ldots, 2r-1\}$ such that S contains a odd elements, b even elements, and no consecutive elements is

$$\binom{r-1-a}{b}\binom{r-b}{a}.$$

Lemma 4.12. For H_n and P_r as described above, we have $H_n = P_{2n}$.

Proof. Consider the graph G_{2n}. With notation as above, observe that a can range between 0 and n, since there are n odd integers between 1 and $2n-1$. Similarly, b can range between 0 and $n-1$, since there are $n-1$ even integers between 1 and $2n-1$. Moreover, since we cannot choose consecutive integers, the sum of a and b is at most $n-1$, except in the case where $b = 0$ and $a = n$. With this, along with the observation in Remark 4.11, we have

$$P_{2n} = \gamma_{f_k}^{2n} + \sum_{a+b \leq n-1} (-1)^{n-a-b} \binom{n-1-a}{b}\binom{n-b}{a} \gamma_{f_k}^{2a} \gamma_{o_k}^{2b} \gamma_{p_k}^{2(n-a-b)} = H_n.$$ □

Lemma 4.13 and Lemma 4.14 establish recursive properties of the polynomials P_r.

Lemma 4.13. The polynomials P_r satisfy the recurrence

$$P_{2r} = P_{2r-2}(\gamma_{f_k}^2 + \gamma_{o_k}^2 - \gamma_{p_k}^2) - \gamma_{f_k}^2\gamma_{o_k}^2 P_{2r-4}, \text{ for all } r \geq 3.$$

Proof. Assume $r \geq 3$. A perfect matching of G_r can be considered as either: a perfect matching of G_{r-1}, plus the vertical arc at the far right of weight $-\gamma_{p_k}$ (if r is even) or γ_{p_k} (if r is odd); or a perfect matching of G_{r-2}, plus the pair of horizontal arcs on the far right, which are weighted either γ_{f_k} (if r is even) or γ_{o_k} (if r is odd). This observation gives us the following:

$$\begin{aligned} P_{2r} &= -\gamma_{p_k} P_{2r-1} + \gamma_{f_k}^2 P_{2r-2}, \\ P_{2r-1} &= \gamma_{p_k} P_{2r-2} + \gamma_{o_k}^2 P_{2r-3}, \\ P_{2r-2} &= -\gamma_{p_k} P_{2r-3} + \gamma_{f_k}^2 P_{2r-4}. \end{aligned}$$

We solve the first and third equations for P_{2r-1} and P_{2r-3}, respectively, then substitute these into the second equation to get

$$\begin{aligned} \frac{\gamma_{f_k}^2 P_{2r-2} - P_{2r}}{\gamma_{p_k}} &= \gamma_{p_k} P_{2r-2} + \gamma_{o_k}^2 \frac{\gamma_{f_k}^2 P_{2r-4} - P_{2r-2}}{\gamma_{p_k}} \\ \gamma_{f_k}^2 P_{2r-2} - P_{2r} &= \gamma_{p_k}^2 P_{2r-2} + \gamma_{o_k}^2 (\gamma_{f_k}^2 P_{2r-4} - P_{2r-2}) \\ P_{2r} &= \gamma_{f_k}^2 P_{2r-2} + \gamma_{o_k}^2 P_{2r-2} - \gamma_{p_k}^2 P_{2r-2} - \gamma_{f_k}^2\gamma_{o_k}^2 P_{2r-4} \\ P_{2r} &= P_{2r-2}(\gamma_{f_k}^2 + \gamma_{o_k}^2 - \gamma_{p_k}^2) - \gamma_{f_k}^2\gamma_{o_k}^2 P_{2r-4}. \end{aligned}$$

□

Lemma 4.14. The polynomials P_r satisfy the recurrence

$$P_{2r-2} \cdot P_{2r-6} = P_{2r-4}^2 - (\gamma_{f_k}^{r-3}\gamma_{o_k}^{r-2}\gamma_{p_k})^2, \text{ for } r \geq 4.$$

Proof. Note that $P_2 = \gamma_{f_k}^2 - \gamma_{p_k}^2$ and $P_4 = \gamma_{f_k}^4 + \gamma_{p_k}^4 - 2\gamma_{f_k}^2\gamma_{p_k}^2 - \gamma_{o_k}^2\gamma_{p_k}^2$.

All perfect matchings of G_6 are shown in Figure 4.10. From this, we have that

$$P_6 = \gamma_{f_k}^6 - \gamma_{o_k}^4\gamma_{p_k}^2 - 2\gamma_{f_k}^2\gamma_{o_k}^2\gamma_{p_k}^2 - 3\gamma_{f_k}^4\gamma_{p_k}^2 + 2\gamma_{o_k}^2\gamma_{p_k}^4 + 3\gamma_{f_k}^2\gamma_{p_k}^4 - \gamma_{p_k}^6.$$

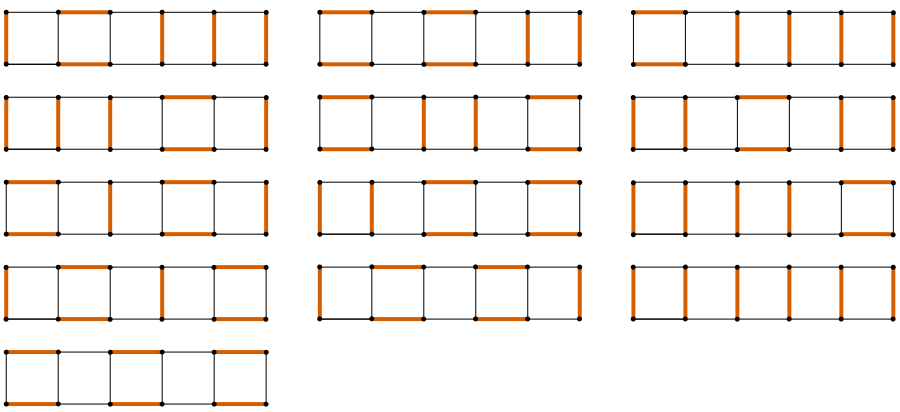

Figure 4.10. All perfect matchings of the graph G_6 (with weights omitted for clarity).

So, when $r = 4$, we have

$$\begin{aligned}
P_6 \cdot P_2 &= (\gamma_{f_k}^6 - \gamma_{o_k}^4\gamma_{p_k}^2 - 2\gamma_{f_k}^2\gamma_{o_k}^2\gamma_{p_k}^2 - 3\gamma_{f_k}^4\gamma_{p_k}^2 + 2\gamma_{o_k}^2\gamma_{p_k}^4 + 3\gamma_{f_k}^2\gamma_{p_k}^4 - \gamma_{p_k}^6) \\
&\quad \cdot (\gamma_{f_k}^2 - \gamma_{p_k}^2) \\
&= \gamma_{f_k}^8 - \gamma_{f_k}^2\gamma_{o_k}^4\gamma_{p_k}^2 - 2\gamma_{f_k}^4\gamma_{o_k}^2\gamma_{p_k}^2 - 4\gamma_{f_k}^6\gamma_{p_k}^2 + 4\gamma_{f_k}^2\gamma_{o_k}^2\gamma_{p_k}^4 + 6\gamma_{f_k}^4\gamma_{p_k}^4 \\
&\quad - 4\gamma_{f_k}^2\gamma_{p_k}^6 + \gamma_{o_k}^4\gamma_{p_k}^4 - 2\gamma_{o_k}^2\gamma_{p_k}^6 + \gamma_{p_k}^8 \\
&= (\gamma_{f_k}^4 + \gamma_{p_k}^4 - 2\gamma_{f_k}^2\gamma_{p_k}^2 - \gamma_{o_k}^2\gamma_{p_k}^2)^2 - \gamma_{f_k}^2\gamma_{o_k}^4\gamma_{p_k}^2 \\
&= P_4^2 - \gamma_{f_k}^2\gamma_{o_k}^4\gamma_{p_k}^2.
\end{aligned}$$

This establishes the base case.

Now consider $r > 4$ and assume for induction that

$$P_{2r-2} \cdot P_{2r-6} = P_{2r-4}^2 - (\gamma_{f_k}^{r-3}\gamma_{o_k}^{r-2}\gamma_{p_k})^2.$$

Considering $P_{2(r+1)-2} \cdot P_{2(r+1)-6}$ we have

$$\begin{aligned}
P_{2r} \cdot P_{2r-4} &= \big(P_{2r-2}(\gamma_{f_k}^2 + \gamma_{o_k}^2 - \gamma_{p_k}^2) - \gamma_{f_k}^2\gamma_{o_k}^2 P_{2r-4}\big) \cdot P_{2r-4}, && \text{from Lemma 4.13} \\
&= P_{2r-2} \cdot P_{2r-4}(\gamma_{f_k}^2 + \gamma_{o_k}^2 - \gamma_{p_k}^2) - \gamma_{f_k}^2\gamma_{o_k}^2 P_{2r-4}^2 \\
&= P_{2r-2} \cdot P_{2r-4}(\gamma_{f_k}^2 + \gamma_{o_k}^2 - \gamma_{p_k}^2) \\
&\quad - \gamma_{f_k}^2\gamma_{o_k}^2 \left(P_{2r-2} \cdot P_{2r-6} + (\gamma_{f_k}^{r-3}\gamma_{o_k}^{r-2}\gamma_{p_k})^2\right) && \text{by assumption} \\
&= P_{2r-2} \cdot \big(P_{2r-4}(\gamma_{f_k}^2 + \gamma_{o_k}^2 - \gamma_{p_k}^2) \\
&\quad -\gamma_{f_k}^2\gamma_{o_k}^2 P_{2r-6}\big) - \gamma_{f_k}^2\gamma_{o_k}^2(\gamma_{f_k}^{r-3}\gamma_{o_k}^{r-2}\gamma_{p_k})^2 \\
&= P_{2r-2} \cdot P_{2r-2} - (\gamma_{f_k}^{r-2}\gamma_{o_k}^{r-1}\gamma_{p_k})^2 && \text{from Lemma 4.13.}
\end{aligned}$$

Hence, by induction, $P_{2r-2} \cdot P_{2r-6} = P_{2r-4}^2 - (\gamma_{f_k}^{r-3}\gamma_{o_k}^{r-2}\gamma_{p_k})^2$, for $r \geq 4$. □

Lemma 4.15. The polynomials H_n satisfy the following recurrence, for any $n \geq 3$.

$$H_n \cdot H_{n-2} = H_{n-1}^2 - (\gamma_{f_k}^{n-2}\gamma_{o_k}^{n-1}\gamma_{p_k})^2.$$

Proof. We have $H_n = P_{2n}$ by Lemma 4.12, so the result follows by setting $r = n + 1$ in Lemma 4.14. □

We are now in a position to prove Theorem 4.8. Recall that the equations involved in this proof are those associated with the tail of the layered solid torus, and we ignore equations related to the head, body and tip of the layered solid torus (recall Definition 4.6).

Proof of Theorem 4.8. We proceed by induction on n, the length of the tail.

When $n = 1$, the tail of the layered solid torus consists of one tetrahedron. The corresponding Ptolemy equation (from Theorem 4.4) is the one for the k^{th} step: $\gamma_{o_k}\gamma_{h_k} + \gamma_{p_k}^2 - \gamma_{f_k}^2 = 0$, which we rewrite as

$$\gamma_{h_k} = \frac{\gamma_{f_k}^2 - \gamma_{p_k}^2}{\gamma_{o_k}}. \tag{4.2}$$

Recalling Definition 4.7, we have

$$H_1 = \gamma_{f_k}^2 + \sum_{a=b=0} (-1)^{1-a-b} \binom{0-a}{b} \binom{1-b}{a} \gamma_{f_k}^{2a} \gamma_{o_k}^{2b} \gamma_{p_k}^{2(1-a-b)} = \gamma_{f_k}^2 - \gamma_{p_k}^2,$$

$$\text{so we have} \quad \gamma_{h_k} = \frac{H_1}{\gamma_{o_k}}.$$

When $n = 2$, the tail of the layered solid torus consists of two tetrahedra and the corresponding Ptolemy equations are those corresponding to the k^{th} and $(k+1)^{st}$ steps, namely $\gamma_{o_k}\gamma_{h_k} + \gamma_{p_k}^2 - \gamma_{f_k}^2 = 0$ (as above) and $\gamma_{o_{k+1}}\gamma_{h_{k+1}} + \gamma_{p_{k+1}}^2 - \gamma_{f_{k+1}}^2 = 0$. Rearranging the second equation gives

$$\gamma_{h_{k+1}} = \frac{\gamma_{f_{k+1}}^2 - \gamma_{p_{k+1}}^2}{\gamma_{o_{k+1}}}.$$

However, in a tail we know that certain slopes are equal, as seen in Figure 4.11.

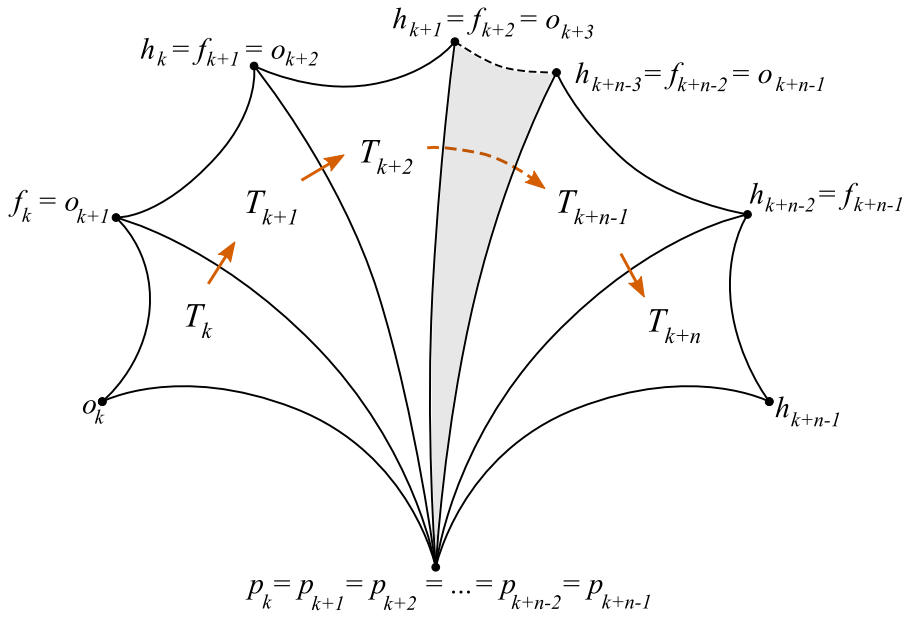

Figure 4.11. A tail of length n beginning at step k. The tail starts in triangle T_k and ends in triangle T_{k+n}. Each vertex is labelled by multiple slopes, since they are relevant to multiple steps in the tail (except for the vertices corresponding to o_k and h_{k+n-1}). In particular, all pivot slopes are the same, the heading slope for one step is the fan slope for the next, and the fan slope for one step is the old slope for the next.

In particular, we have $\gamma_{p_{k+1}} = \gamma_{p_k}$, $\gamma_{f_{k+1}} = \gamma_{h_k}$, and $\gamma_{o_{k+1}} = \gamma_{f_k}$.

Hence, making these substitutions and using equation (4.2), we have

$$\gamma_{h_{k+1}} = \frac{\gamma_{h_k}^2 - \gamma_{p_k}^2}{\gamma_{f_k}} = \frac{\left(\frac{\gamma_{f_k}^2 - \gamma_{p_k}^2}{\gamma_{o_k}}\right)^2 - \gamma_{p_k}^2}{\gamma_{f_k}} = \frac{\gamma_{f_k}^4 + \gamma_{p_k}^4 - 2\gamma_{f_k}^2\gamma_{p_k}^2 - \gamma_{o_k}^2\gamma_{p_k}^2}{\gamma_{f_k}\gamma_{o_k}^2}.$$

Meanwhile,

$$\begin{aligned} H_2 &= \gamma_{f_k}^4 + \sum_{a+b\leq 1} (-1)^{2-a-b} \binom{1-a}{b} \binom{2-b}{a} \gamma_{f_k}^{2a} \gamma_{o_k}^{2b} \gamma_{p_k}^{2(2-a-b)} \\ &= \gamma_{f_k}^4 + \gamma_{p_k}^4 - 2\gamma_{f_k}^2\gamma_{p_k}^2 - \gamma_{o_k}^2\gamma_{p_k}^2. \end{aligned}$$

Thus, $\gamma_{h_{k+1}} = \dfrac{H_2}{\gamma_{f_k}\gamma_{o_k}^2}$.

Now, suppose $n > 2$ and assume for induction that $\gamma_{h_{k+i-1}} = \dfrac{H_i}{\gamma_{f_k}^{i-1}\gamma_{o_k}^i}$, for all $i < n$.

In a tail of length n there are n tetrahedra. The Ptolemy equation corresponding to the n^{th} tetrahedron is the one from Theorem 4.4 associated to the $(k+n-1)^{st}$ step, which can be written as

$$\gamma_{h_{k+n-1}} = \frac{\gamma_{f_{k+n-1}}^2 - \gamma_{p_{k+n-1}}^2}{\gamma_{o_{k+n-1}}}. \tag{4.3}$$

Again, with reference to Figure 4.11, observe that the following variables are equivalent in the tail: $\gamma_{p_{k+n-1}} = \gamma_{p_k}$, $\gamma_{f_{k+n-1}} = \gamma_{h_{k+n-2}}$, and $\gamma_{o_{k+n-1}} = \gamma_{h_{k+n-3}}$, so (4.3) becomes

$$\gamma_{h_{k+n-1}} = \frac{\gamma_{h_{k+n-2}}^2 - \gamma_{p_k}^2}{\gamma_{h_{k+n-3}}}.$$

Now, using the inductive assumption we write

$$\begin{aligned}\gamma_{h_{k+n-1}} &= \left[\left(\frac{H_{n-1}}{\gamma_{f_k}^{n-2}\gamma_{o_k}^{n-1}}\right)^2 - \gamma_{p_k}^2\right] \Bigg/ \left(\frac{H_{n-2}}{\gamma_{f_k}^{n-3}\gamma_{o_k}^{n-2}}\right) \\ &= \frac{H_{n-1}^2 - (\gamma_{f_k}^{n-2}\gamma_{o_k}^{n-1}\gamma_{p_k})^2}{\gamma_{f_k}^{n-1}\gamma_{o_k}^n H_{n-2}}.\end{aligned}$$

Hence, to prove the result, we need

$$\frac{H_{n-1}^2 - (\gamma_{f_k}^{n-2}\gamma_{o_k}^{n-1}\gamma_{p_k})^2}{\gamma_{f_k}^{n-1}\gamma_{o_k}^n H_{n-2}} = \frac{H_n}{\gamma_{f_k}^{n-1}\gamma_{o_k}^n}.$$

But this is equivalent to showing that

$$H_n \cdot H_{n-2} = H_{n-1}^2 - (\gamma_{f_k}^{n-2}\gamma_{o_k}^{n-1}\gamma_{p_k})^2, \quad \text{for } n > 2,$$

which is the recurrence in Lemma 4.15. Hence, the claim follows by induction. □

Theorem 4.16. Suppose the tail of a layered solid torus has length $n \geq 1$ and begins at step k. Let α_s be the geodesic in $\mathbb{H}^2$ whose endpoints are the vertices corresponding to the slopes h_{k+n-1} (the heading slope at the end of the tail) and s, where s is one of f_k, o_k or p_k (the fan, old and pivot slopes at the beginning of the tail). The exponent of γ_s in the denominator of the Laurent polynomial for $\gamma_{h_{k+n-1}}$ is given by the intersection number of α_s with edges it intersects in the Farey triangulation.

Proof. Denote the set of edges in the Farey triangulation by $\mathcal{F}$ and let $|\alpha_s \cap \mathcal{F}|$ be the number of transverse intersections between the geodesic α_s and all edges in $\mathcal{F}$. In each of the accompanying figures, α_{f_k} is shown in dark blue, α_{o_k} is shown in green, and α_{p_k} is shown in light blue.

For this proof we consider the Farey triangulation of the upper half-space model of $\mathbb{H}^2$. After applying the appropriate (not necessarily orientation-preserving) isometry of $\mathbb{H}^2$, we may assume that $f_k = {}^1\!/_0$, $o_k = {}^{-1}\!/_1$, $p_k = {}^0\!/_1$ and $h_k = {}^1\!/_1$. Note that this choice of slopes

ensures that $h_{k+n-1} = {}^1\!/\!_n$ for all $n \geq 1$. In other words, when considering a tail of length n, the common endpoint of $\alpha_{f_k}, \alpha_{o_k}$ and α_{p_k} is ${}^1\!/\!_n$.

We prove the claim by induction on the length of the tail. When $n = 1$ we have the situation shown in Figure 4.12. In particular, we see that α_{f_k} and α_{p_k} are each parallel to edges in the Farey triangulation and therefore $|\alpha_{f_k} \cap \mathcal{F}| = |\alpha_{p_k} \cap \mathcal{F}| = 0$. Meanwhile, α_{o_k} intersects one edge in the Farey triangulation so $|\alpha_{o_k} \cap \mathcal{F}| = 1$. From Theorem 4.8, we know that the denominator of the Laurent polynomial for γ_{h_k} is

$$\gamma_{f_k}^0 \gamma_{o_k}^1 \gamma_{p_k}^0 = \gamma_{f_k}^{|\alpha_{f_k} \cap \mathcal{F}|} \gamma_{o_k}^{|\alpha_{o_k} \cap \mathcal{F}|} \gamma_{p_k}^{|\alpha_{p_k} \cap \mathcal{F}|}.$$

Hence, the base case holds.

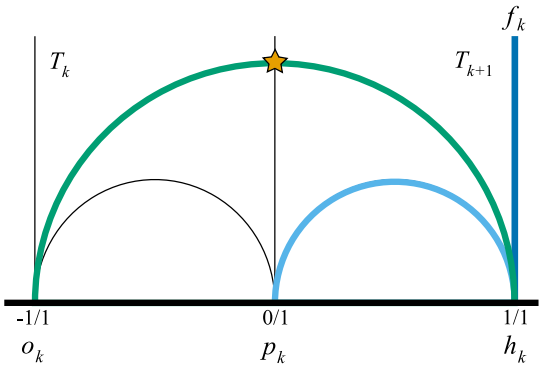

Figure 4.12. The geodesics corresponding to a tail of length $n = 1$ beginning at step k. The star indicates the intersection between α_{o_k} and $\mathcal{F}$.

In Figure 4.13 we see that increasing the length of the tail by 1 increases each of $|\alpha_{o_k} \cap \mathcal{F}|$ and $|\alpha_{f_k} \cap \mathcal{F}|$ by 1, while $|\alpha_{p_k} \cap \mathcal{F}|$ is always 0. Hence, the claim follows by induction. □

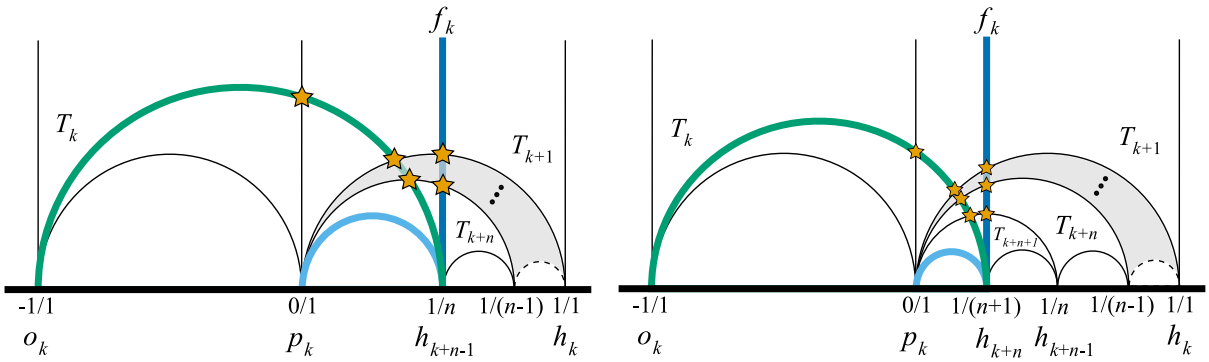

Figure 4.13. The geodesics corresponding to a tail of length n (left) and length $n+1$ (right) beginning at step k. The shaded segments are where one should imagine the fan of triangles T_{k+2} through T_{k+n-1}. Stars indicate transverse intersections. Note that $|\alpha_{p_k} \cap \mathcal{F}| = 0$ for both the tails of length n and $n+1$. Meanwhile, each of $|\alpha_{o_k} \cap \mathcal{F}|$ and $|\alpha_{f_k} \cap \mathcal{F}|$ increase by 1 as the length of the tail increases by 1.

4.3.2. Applications to A-polynomial calculations

Recall that, apart from changing the labels of slopes from absolute to relative directions, our equations are the same as those in [HMP20]. As such, from Theorem 2.58 in [HMP20], we know that setting one of the γ variables to 1 and solving the system of Ptolemy equations gives the geometric factor of the $\mathrm{PSL}(2, \mathbb{C})$ A-polynomial. Moreover, by first making appropriate

substitutions for the variables corresponding to the meridian and longitude, we obtain a rational function in L and M that contains the geometric factor of the $\mathrm{SL}(2,\mathbb{C})$ A-polynomial [see HMP20, Corollary 2.59]. However, finding solutions to such a system directly is again impeded by the increasing number of equations as the triangulation grows. Fortunately, we may use Theorem 4.8 to simplify this computation.

Theorem 4.17. Suppose a knot is obtained from a link complement by Dehn filling using a layered solid torus. Suppose the tail of the layered solid torus has length $n \geq 1$ and begins at step k, and suppose the folding equation corresponds to the tip being in the same direction as the tail. The folding equation, along with the set of tail equations, is equivalent to the equation

$$H_n - \gamma_{f_k}^{n-1}\gamma_{o_k}^{n}\gamma_{p_k} = 0.$$

Proof. In the proof of Theorem 4.8, we saw that the set of n tail equations is equivalent to the equation

$$\gamma_{h_{k+n-1}} = \frac{H_n}{\gamma_{f_k}^{n-1}\gamma_{o_k}^{n}}.$$

The folding equation corresponding to the tip in the same direction as the tail is $\gamma_{p_{k+n}} = \gamma_{f_{k+n}}$ (from Theorem 4.4 with $N = n + k$). However, recall from Figure 4.11 that: all pivot slopes in the tail are equal, so $\gamma_{p_{k+n}} = \gamma_{p_k}$; and the fan slope of the $(k+n)^{th}$ step is equal to the heading slope of the $(k+n-1)^{st}$ step, so $\gamma_{f_{k+n}} = \gamma_{h_{k+n-1}}$. Hence, we set $\gamma_{h_{k+n-1}}$ equal to γ_{p_k} and rearrange to get

$$H_n - \gamma_{f_k}^{n-1}\gamma_{o_k}^{n}\gamma_{p_k} = 0, \text{ as desired.}$$ □

The above result consolidates all equations associated with the tip and tail of a layered solid torus, however, to compute A-polynomials, we also require: the finitely many equations coming from the head and body of the layered solid torus; and the finitely many equations corresponding to the tetrahedra that triangulate the parent link. As seen in [HMP20], when the meridian or longitude intersect a tetrahedron in the parent link, the corresponding equation involves the variables L and M. Such equations can be used to express γ variables in terms of L and M.

Corollary 4.18. When $\gamma_{f_k}, \gamma_{o_k}$, and γ_{p_k} are expressed in terms of L and M (using the equations from the parent link and the body of the Dehn filling), the rational function $H_n - \gamma_{f_k}^{n-1}\gamma_{o_k}^{n}\gamma_{p_k}$ contains the geometric factor of the $\mathrm{SL}(2,\mathbb{C})$ A-polynomial for the corresponding knot.

Proof. This follows from the previous theorem and Corollary 2.59 of [HMP20]. □

Once we have $\gamma_{f_k}, \gamma_{o_k}$, and γ_{p_k} expressed in terms of L and M, Theorem 4.17 gives a family of rational functions in L and M depending only on n. This means that the main barrier to effective computation of these rational functions is in finding $\gamma_{f_k}, \gamma_{o_k}$, and γ_{p_k} in terms of L and M, which depends on the Ptolemy equations of the tetrahedra required to triangulate the parent link complement. In particular, this means that if a parent link admits an appropriate triangulation consisting of few tetrahedra, the A-polynomials for fillings of this link are readily computable. We now demonstrate the power of this result by applying it in the context of two families of knots related by twisting.

Tetrahedron	Face 012	Face 013	Face 023	Face 123
0	2(312)	1(023)	1(312)	1(031)
1	3(123)	0(132)	0(013)	0(230)
2	3(021)	3(031)	3(032)	0(120)
3	2(021)	2(031)	2(032)	1(012)

Table 4.1. A triangulation of the Whitehead sister link complement in Regina notation.

Section 4.4. *Example A-polynomial calculations*

In this section we see how Theorem 4.17 can be applied to A-polynomial calculations for two families of knots related by twisting: the twisted torus knots $T(5, 1-5m, 2, 2)$ and the twist knots $J(2, 2m)$. Throughout this section the variable m is used in relation to $1/m$ Dehn fillings and the variable n is used with reference to the length of a tail in a layered solid torus.

4.4.1. Fillings of the Whitehead sister

The Whitehead sister link is often presented as the $(-2, 3, 8)$-pretzel link, shown on the left of Figure 4.14. Unsurprisingly, we will instead view it as the augmented twisted torus knot shown on the right of Figure 4.14. By performing $1/m$ Dehn fillings on the unknotted component (blue) we generate the infinite family of twisted torus knots $T(5, 1-5m, 2, 2)$ [HMPT23].

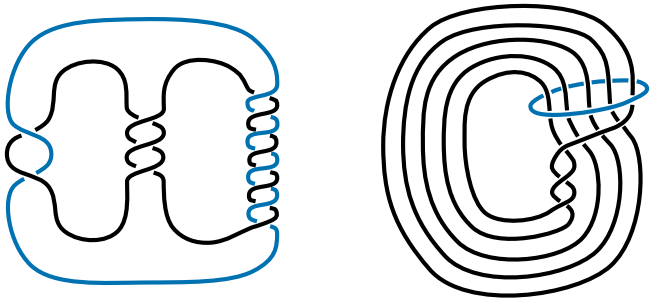

Figure 4.14. The Whitehead sister link with unknotted component shown in blue. On the left is the standard pretzel diagram and on the right, we see an alternative diagram that elucidates why $1/m$ Dehn fillings generate the $T(5, 1-5m, 2, 2)$ twisted torus knots.

Howie, Mathews, Purcell and I studied this link in [HMPT23], using the triangulation given in Table 4.1 (with notation as in Regina). Observe that tetrahedra 2 and 3 glue only to each other and one face each of tetrahedra 0 and 1. Vertices 2(0) and 3(0) meet the unknotted cusp and all other vertices meet the other cusp. To perform Dehn fillings on the unknotted cusp we remove tetrahedra 2 and 3, leaving a once-punctured torus boundary triangulated by the faces 0(012) and 1(012). We may then glue an appropriate layered solid torus to these exposed faces to make the Dehn filling slope homotopically trivial.

We determined the Ptolemy equations for the outside tetrahedra in [HMPT23]. Note that we saw a version of these equations in the $K5_4$ example in Section 4.2. Here we have moved all terms to one side, and multiplied through by powers of L and M to remove negative exponents.

$$M\gamma_{1/0}\gamma_{4/1} - M^2\gamma_{4/1}\gamma_{3/1} - L\gamma_{3/1}^2 = 0 \text{ for tetrahedron 0, and} \tag{4.4}$$

$$-M^2\gamma_{3/1}^2 + LM\gamma_{1/0}\gamma_{4/1} - L\gamma_{3/1}\gamma_{4/1} = 0 \text{ for tetrahedron 1.} \tag{4.5}$$

These γ variables are labelled according to the slopes of the corresponding edge classes. These slopes were determined in [HMPT23], and we can relate them to the $K5_4$ example, where the edges with slopes $1/0$, $3/1$, $4/1$, $2/1$, and $0/1$, are coloured red, orange, blue, green, and yellow, respectively.

Using the Farey triangulation. To apply Theorem 4.17, we must determine paths in the Farey triangulation describing the construction of appropriate layered solid tori. This was done in [HMPT23]. Since the slopes of the boundary edges are $3/1$, $4/1$, and $1/0$, the starting Farey triangle is the one with vertices labelled by these rational numbers.

To perform $+1/m$ Dehn fillings we follow the path indicated in blue in Figure 4.15 and to perform $-1/m$ Dehn fillings we follow the path indicated in orange. These paths can be described by the words $\mathrm{L}^2\,\mathrm{RL}^{m-2}$ and $\mathrm{L}^3\,\mathrm{R}^{m-1}$, respectively. Recall that the final L or R corresponds to the tip representing the fold, so this means that the layered solid torus used for a $+1/m$ Dehn filling has a tail of length $n = m - 3$, while the layered solid torus used for a $-1/m$ Dehn filling has a tail of length $n = m - 2$.

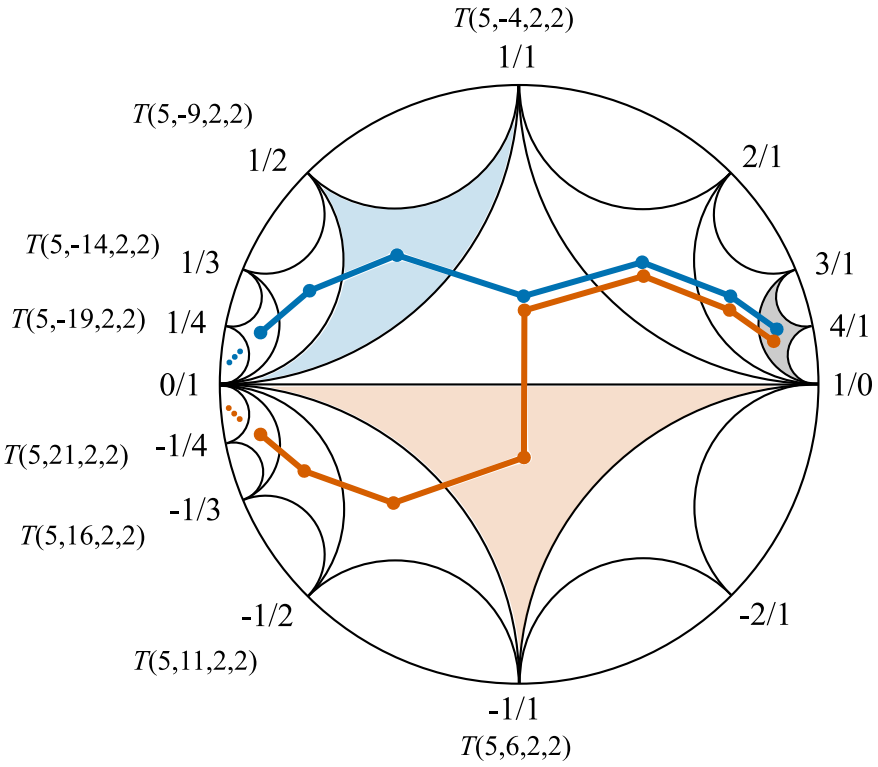

Figure 4.15. Paths in the Farey diagram corresponding to $\pm 1/m$ Dehn fillings of the Whitehead sister link. The starting triangle is shaded grey and the triangles where each of the tails begin are indicated in blue and orange, for the positive and negative Dehn fillings, respectively. The twisted torus knot obtained by performing each Dehn filling is also noted.

Theorem 4.17 applies for tails of length $n \geq 1$ with the tip in the same direction, so here we consider Dehn fillings with slopes $+1/m$ for $m \geq 4$ and $-1/m$ for $m \geq 3$. The tails for both

the positive and negative Dehn fillings each start at step 4. Steps 0, 1 and 2 are the same for both paths, and using Theorem 4.4, we obtain their corresponding Ptolemy equations

$$\gamma_{4/1}\gamma_{2/1} + \gamma_{3/1}^2 - \gamma_{1/0}^2 = 0, \tag{4.6}$$

$$\gamma_{3/1}\gamma_{1/1} + \gamma_{1/0}^2 - \gamma_{2/1}^2 = 0, \tag{4.7}$$

$$\gamma_{2/1}\gamma_{0/1} + \gamma_{1/0}^2 - \gamma_{1/1}^2 = 0. \tag{4.8}$$

For positive Dehn fillings, step 3 is a right step and hence corresponds to the Ptolemy equation

$$\gamma_{1/0}\gamma_{1/2} + \gamma_{1/1}^2 - \gamma_{0/1}^2 = 0. \tag{4.9}$$

The tail begins at step 4 and we have $o_4 = {}^1\!/\!_1$, $p_4 = {}^0\!/\!_1$ and $f_4 = {}^1\!/\!_2$. Hence, by Theorem 4.17, the equations for the tail of length $n \geq 1$ (corresponding to Dehn fillings of slope $+{}^1\!/\!_m$ for $m \geq 4$) are equivalent to the equation

$$\gamma_{1/2}^{2n} + \sum_{a+b\leq n-1} (-1)^{n-a-b}\binom{n-1-a}{b}\binom{n-b}{a}\gamma_{1/2}^{2a}\gamma_{1/1}^{2b}\gamma_{0/1}^{2(n-a-b)} - \gamma_{1/1}^{n}\gamma_{1/2}^{n-1}\gamma_{0/1} = 0. \tag{4.10}$$

For negative Dehn fillings, step 3 is a left step and therefore corresponds to the Ptolemy equation

$$\gamma_{1/1}\gamma_{-1/1} + \gamma_{1/0}^2 - \gamma_{0/1}^2 = 0. \tag{4.11}$$

The tail begins at step 4 and we have $o_4 = {}^1\!/\!_0$, $p_4 = {}^0\!/\!_1$ and $f_4 = -1/1$. Hence, by Theorem 4.17, the equations for the tail of length $n \geq 1$ (corresponding to Dehn fillings of slope $-{}^1\!/\!_m$ for $m \geq 3$) are equivalent to the equation

$$\gamma_{-1/1}^{2n} + \sum_{a+b\leq n-1} (-1)^{n-a-b}\binom{n-1-a}{b}\binom{n-b}{a}\gamma_{-1/1}^{2a}\gamma_{1/0}^{2b}\gamma_{0/1}^{2(n-a-b)} - \gamma_{1/0}^{n}\gamma_{-1/1}^{n-1}\gamma_{0/1} = 0. \tag{4.12}$$

A-polynomials for positive Dehn fillings. The equations (4.4) through (4.10) define a rational function that contains the geometric factor of the A-polynomial of the knot obtained by $1/(n+3)$ Dehn filling of the Whitehead sister link, for $n \geq 1$.

We set $\gamma_{3/1} = 1$ and use equations (4.4) through (4.9) to write $\gamma_{0/1}$, $\gamma_{1/1}$ and $\gamma_{1/2}$ entirely in terms of L and M. These can be found in Appendix C. With these substitutions, (4.10) becomes a formula for rational functions that contain the geometric factor of the A-polynomials for the twisted torus knots $T(5, 1-5(n+3), 2, 2)$, with $n \geq 1$.

A-polynomials for negative Dehn fillings. The equations (4.4) through (4.8), along with equations (4.11) and (4.12) define a rational function that contains the geometric factor of the A-polynomial of the knot obtained by $-1/(n+2)$ Dehn filling of the Whitehead sister link, for $n \geq 1$.

Again, we set $\gamma_{3/1} = 1$ and use equations (4.4) through (4.8) and equation (4.11) to write $\gamma_{1/0}$, $\gamma_{-1/1}$ and $\gamma_{0/1}$ entirely in terms of L and M. These can also be found in Appendix C. With these substitutions, (4.12) becomes a formula for rational functions that contain the geometric factor of the A-polynomials for the twisted torus knots $T(5, 1+5(n+2), 2, 2)$, with $n \geq 1$.

Changing basis. As discussed in [HMPT23], the choice of generators for the cusp homology were not the standard basis for the link in S^3. While we used the actual meridian, we did not use the preferred longitude. For the positive Dehn fillings, the required change of basis in the

A-polynomial variables is $(L, M) \mapsto (LM^{8-25m}, M)$ for each $m = n + 3 \geq 4$. For the negative Dehn fillings, the required change of basis is $(L, M) \mapsto (LM^{8+25m}, M)$ for each $m = n + 2 \geq 3$.

Comparing with what is known. The twisted torus knots $T(5, 16, 2, 2)$ and $T(5, -19, 2, 2)$ are equivalent to the census knots $K7_3$ and $K7_4$, respectively. After changing basis as above, and multiplying through by powers of L and M to remove negative exponents, the largest factors seen in the output of our formulas match the A-polynomials found by Culler [Cul]. For example, with substitutions as given in Appendix C, and with $n = 1$, equation (4.12) gives a polynomial with four factors, the largest of which has 455 terms. After changing basis, this factor is identical to the A-polynomial given for $K7_3$ on Culler's website [Cul].

The knots $T(5, 21, 2, 2)$ and $T(5, -24, 2, 2)$ are equivalent to the census knots $K8_3$ and $K8_4$, respectively, and our formula immediately gives a rational function containing the geometric factor of their A-polynomials despite their very large size; the largest factors of these have 784 and 952 terms, respectively. Since the A-polynomials for these knots do not appear on Culler's database we cannot compare.

4.4.2. The twist knots

It is well known that the twist knots may be obtained by $1/m$ Dehn fillings of the complement of the Whitehead link (recall Figure 1 from the introduction). We use the notation $J(2, l)$ to mean the twist knot with l right-handed crossings in one of its twist regions (indicated by the orange box in Figure 1). The $+1/m$ Dehn fillings of the Whitehead link therefore generate the family of twist knots $J(2, 2m)$ and $-1/m$ Dehn fillings generate the family $J(2, -2m)$.

Tetrahedron	Face 012	Face 013	Face 023	Face 123
0	3(021)	1(213)	2(130)	1(230)
1	4(102)	2(132)	0(312)	0(103)
2	2(203)	0(302)	2(102)	1(031)
3	0(021)	4(103)	4(203)	4(213)
4	1(102)	3(103)	3(203)	3(213)

Figure 4.16. A triangulation of the Whitehead link complement in Regina notation.

In this section we apply Theorem 4.17 to the family of twist knots obtained by Dehn filling the Whitehead link using layered solid tori. We use the same triangulation as in [HMP20], which is given in Regina notation in Figure 4.16. The Dehn fillings are performed by replacing tetrahedra 3 and 4 with layered solid tori. Each of the three outside tetrahedra contribute a Ptolemy equation, which were found in [HMP20]. We make the substitutions $\ell = L^2$ and $m = M^2$, and multiply through by powers of L and M to remove negative exponents. We use the same γ labels, including $\gamma_{0(23)}$, which is associated to the edge class in the triangulation that contains the 23 edge of tetrahedron 0. This labelling reflects the fact that this edge class does not appear in the cusp being filled and therefore does not have a well-defined slope. The equations are

$$-LM\gamma_{0(23)}\gamma_{2/1} - L\gamma_{3/1}\gamma_{1/0} - M^2\gamma_{1/0}^2 = 0, \tag{4.13}$$

$$-M^2\gamma_{3/1}\gamma_{1/0} - L\gamma_{1/0}^2 - M\gamma_{0(23)}\gamma_{2/1} = 0, \tag{4.14}$$

$$\gamma_{1/0}^2 - \gamma_{1/0}\gamma_{3/1} - \gamma_{0(23)}^2 = 0. \tag{4.15}$$

The paths in the Farey triangulation corresponding to the $\pm 1/m$ Dehn fillings of the Whitehead link were determined by Howie, Mathews and Purcell in [HMP20] and are shown in Figure 4.17. The words describing the positive and negative paths are LRL^{m-2} and $\mathrm{L}^2\mathrm{R}^{m-1}$, respectively. Given that the final L or R corresponds to the tip representing the fold, we have tails of lengths $n = m - 3$ and $n = m - 2$, respectively. From this we see that Theorem 4.17 applies to the calculation of A-polynomials for the twist knots $J(2, 2m)$ for $m \geq 4$ and $J(2, -2m)$ for $m \geq 3$. The tails of each of the positive and negative Dehn fillings start at step 3, with both paths sharing steps 0 and 1. The Ptolemy equations for steps 0 and 1 are

$$\gamma_{3/1}\gamma_{1/1} + \gamma_{2/1}^2 - \gamma_{1/0}^2 = 0, \text{ and} \tag{4.16}$$

$$-\gamma_{2/1}\gamma_{0/1} + \gamma_{1/1}^2 - \gamma_{1/0}^2 = 0. \tag{4.17}$$

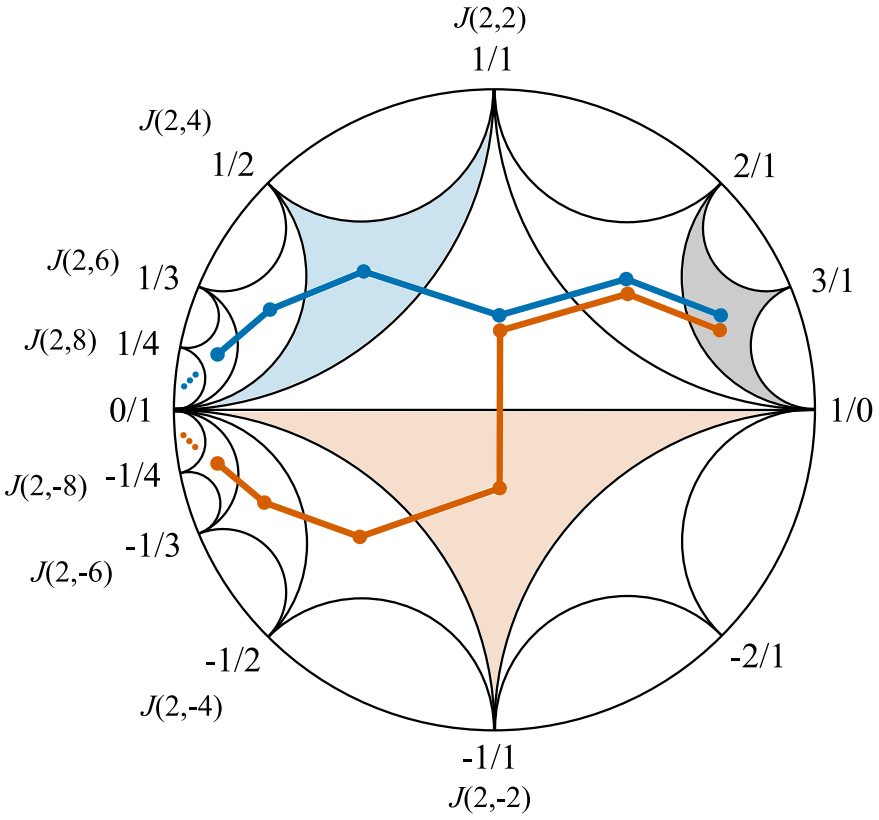

Figure 4.17. Paths in the Farey diagram corresponding to $\pm 1/m$ Dehn fillings of the Whitehead link. The starting triangle is shaded grey and the triangles where each of the tails begin are indicated in blue and orange, for the positive and negative Dehn fillings, respectively. The twist knot obtained by performing each Dehn filling is also noted.

For $+1/m$ Dehn fillings, step 2 is a right step and therefore corresponds to the Ptolemy equation

$$\gamma_{1/2}\gamma_{1/0} + \gamma_{0/1}^2 - \gamma_{1/1}^2 = 0. \tag{4.18}$$

Meanwhile, for $-1/m$ Dehn fillings, step 2 is a left step, so corresponds to the Ptolemy equation

$$\gamma_{-1/1}\gamma_{1/1} + \gamma_{0/1}^2 - \gamma_{1/0}^2 = 0. \tag{4.19}$$

Next we express $\gamma_{1/1}$, $\gamma_{0/1}$, $\gamma_{1/2}$, $\gamma_{-1/1}$ and $\gamma_{1/0}$ in terms of only L and M. We set $\gamma_{1/0}$ equal to 1 and use equations (4.13) through (4.17) to express $\gamma_{1/1}$ and $\gamma_{0/1}$ as follows:

$$\begin{aligned}\gamma_{1/1} &= M^{-2}(L-1)^{-1}(L-M^4)\\ \gamma_{0/1} &= -M^{-3}L^{1/2}(L-1)^{-3/2}(M-1)(M+1)(M^2-1)^{1/2}(M^2+1)(L+M^2)^{1/2}.\end{aligned}$$

For $+1/m$ Dehn fillings, we rearrange (4.18) to get

$$\begin{aligned}\gamma_{1/2} = M^{-6}(L-1)^{-3}(&L^2 + LM^2 - 2L^2M^2 + L^3M^2 - LM^4 - 2L^2M^4\\ &+ 2LM^8 + L^2M^8 - M^{10} + 2LM^{10} - L^2M^{10} - LM^{12}).\end{aligned}$$

For $-1/m$ Dehn fillings, we rearrange (4.19) to get

$$\gamma_{-1/1} = M^{-4}(L-1)^{-2}(L + M^2 - LM^2 - 2LM^4 - LM^6 + L^2M^6 + LM^8).$$

For the positive Dehn fillings, Theorem 4.17 tells us that the A-polynomial for $J(2, 2(n+3))$, for $n \geq 1$, contains a factor of the rational function given by

$$\gamma_{1/2}^{2n} + \sum_{a+b\leq n-1} (-1)^{n-a-b}\binom{n-1-a}{b}\binom{n-b}{a}\gamma_{1/2}^{2a}\gamma_{1/1}^{2b}\gamma_{0/1}^{2(n-a-b)} - \gamma_{1/1}^{n}\gamma_{1/2}^{n-1}\gamma_{0/1} = 0. \tag{4.20}$$

Remark 4.19. As stated, the output of this equation involves fractional exponents, however, these can be removed by conjugating appropriately.

Meanwhile, for negative Dehn fillings, the A-polynomial for $J(2, -2(n+2))$ contains a factor of the rational function given by

$$\gamma_{1/2}^{2n} + \sum_{a+b\leq n-1} (-1)^{n-a-b}\binom{n-1-a}{b}\binom{n-b}{a}\gamma_{-1/1}^{2a}\gamma_{1/0}^{2b}\gamma_{0/1}^{2(n-a-b)} - \gamma_{1/0}^{n}\gamma_{-1/1}^{n-1}\gamma_{0/1} = 0. \tag{4.21}$$

Again, conjugation is needed to remove fractional exponents.

Comparing with what is known. The A-polynomials for the twist knots were shown by Hoste and Shanahan to be irreducible. As such, we expect the output of our formulas to contain precisely the A-polynomial of each twist knot. Using the explicit formulas of Mathews [Mat14a; Mat14b], we verify that the largest factor of our output is indeed the A-polynomial for each of the twist knots $J(2, 2m)$ for $m \in [-8, -3] \cup [4, 8]$. Note that a change of basis is required, namely $(L, M) \mapsto (-LM^{-2}, M)$. This change of basis does not depend on the Dehn filling slope, since the linking number of the two components of the Whitehead link is 0.

The behaviour seen in the output of our formulas uncovers a new recursive relationship in the A-polynomials of twist knots. In the following, we let

$$\begin{aligned}x &= -L + L^2 + 2LM^2 + M^4 + 2LM^4 + L^2M^4 + 2LM^6 + M^8 - LM^8,\\ y &= M^4(L+M^2)^4, \text{ and}\\ z &= L(M^2-1)^3(M^2+1)^2(L-M^4).\end{aligned}$$

Theorem 4.20. Let A_m^+ be the A-polynomial of the twist knot $J(2,2m)$ and let A_m^- be the A-polynomial of the twist knot $J(2,-2m)$. With initial conditions below,

$$A_{m-1}^+ \cdot A_{m+1}^+ = (A_m^+)^2 + y^{m-2} z M^4 (L+M^2)^3, \text{ for } m > 1, \text{ and}$$
$$A_{m-1}^- \cdot A_{m+1}^- = (A_m^-)^2 + y^{m-1} z (L+M^2), \text{ for } m > 0.$$

Initial conditions:

$$\begin{aligned}
A_1^- &= -L + LM^2 + M^4 + 2LM^4 + L^2M^4 + LM^6 - LM^8 \\
A_0^- &= 1 \\
A_1^+ &= L + M^6 \\
A_2^+ &= -L^2 + L^3 + 2L^2M^2 + LM^4 + 2L^2M^4 - LM^6 - L^2M^8 + 2LM^{10} \\
&\quad + L^2M^{10} + 2LM^{12} + M^{14} - LM^{14}
\end{aligned}$$

Proof. We use the recursive relationship found by Hoste and Shanahan [HS04], which can be rewritten in our notation as follows, with x, y, and initial conditions as above.

$$A_m^+ = xA_{m-1}^+ - yA_{m-2}^+,$$
$$A_m^- = xA_{m-1}^- - yA_{m-2}^-.$$

We prove the positive case by showing that

$$A_{m-1}^+ \cdot A_{m+1}^+ - (A_m^+)^2 = y^{m-2} z M^4 (L+M^2)^3.$$

Applying Hoste and Shanahan's relation repeatedly to the left-hand side gives

$$\begin{aligned}
A_{m-1}^+ \cdot A_{m+1}^+ - (A_m^+)^2 &= xA_{m-1}^+ \cdot A_m^+ - y(A_{m-1}^+)^2 - (A_m^+)^2 \\
&= y\left(xA_{m-2}^+ \cdot A_{m-1}^+ - y(A_{m-2}^+)^2 - (A_{m-1}^+)^2\right) \\
&\;\;\vdots \\
&= y^k\left(xA_{m-k-1}^+ \cdot A_{m-k}^+ - y(A_{m-k-1}^+)^2 - (A_{m-k}^+)^2\right) \\
&\;\;\vdots \\
&= y^{m-2}\left(xA_1^+ \cdot A_2^+ - y(A_1^+)^2 - (A_2^+)^2\right).
\end{aligned}$$

Substituting in the expressions for x, y, A_1^+ and A_2^+, we find that

$$xA_1^+ \cdot A_2^+ - y(A_1^+)^2 - (A_2^+)^2 = zM^4(L+M^2)^3,$$

thus recovering the right-hand side.

An analogous argument shows that

$$A_{m-1}^- \cdot A_{m+1}^- - (A_m^-)^2 = y^{m-1}\left(xA_0^- \cdot A_1^- - y(A_0^-)^2 - (A_1^-)^2\right).$$

Again by substituting, we find that

$$xA_0^- \cdot A_1^- - y(A_0^-)^2 - (A_1^-)^2 = z(L+M^2),$$

which proves the negative case. □

Concluding remarks

Ongoing work

Each of the projects covered in this thesis offer exciting avenues for continued exploration. Extensions to the results of both Chapter 2 and 4 are currently in preparation, and the algorithm from Chapter 3 is already proving useful in others' work.

Take-away

Layered triangulations are a powerful tool in the study of 3-manifolds. From a complexity perspective, we saw just how prevalent layered solid tori are amongst known minimal triangulations, and I have conjectured that they hold the key to minimal triangulations for 42 infinite families of knots. We also saw how a slight relaxing of the JR-construction allows us to produce petal-filled triangulations that offer the same bounded cut-width of Jaco and Rubinstein's layered handlebodies, with the added advantage of an implementable algorithm to construct them.

These examples are direct demonstrations of how layered triangulations are useful in computation, but in the most recent chapter, we saw how the combinatorial structure of a layered solid torus can be exploited to improve computations in a less direct way. In the context of hyperbolic structures on cusped 3-manifolds, we were able to leverage the power of a triangulation in which twisting behaviour is combinatorially encoded.

While layered triangulations were our main focus, similar lessons apply to any type of triangulation that emphasises or reveals topological features of a manifold. In particular, a triangulation that is minimal (for some measure of complexity) should not automatically be assumed to be the 'best' triangulation. By being selective about the triangulations we use, and taking advantage of their inherent structures, we can change the way we study 3-manifolds.

Bibliography

[Ago10] Ian Agol. "The minimal volume orientable hyperbolic 2-cusped 3-manifolds". In: *Proc. Amer. Math. Soc.* 138.10 (2010), pp. 3723–3732. ISSN: 0002-9939,1088-6826. DOI: 10.1090/S0002-9939-10-10364-5.

[AGP22] Fathi Ben Aribi, François Guéritaud, and Eiichi Piguet-Nakazawa. *Geometric triangulations and the Teichmüller TQFT volume conjecture for twist knots*. 2022. arXiv: 1903.09480 [math.GT].

[ALR18] Benjamin Audoux, Ana G. Lecuona, and Fionntan Roukema. "On hyperbolic knots in S^3 with exceptional surgeries at maximal distance". In: *Algebraic & Geometric Topology* 18.4 (2018), pp. 2371–2417. DOI: 10.2140/agt.2018.18.2371.

[Ame05] Gennaro Amendola. "A calculus for ideal triangulations of three-manifolds with embedded arcs". In: *Math. Nachr.* 278.9 (2005), pp. 975–994. ISSN: 0025-584X,1522-2616. DOI: 10.1002/mana.200310285.

[AS91] Colin Adams and William Sherman. "Minimum ideal triangulations of hyperbolic 3-manifolds". In: *Discrete Comput. Geom.* 6.2 (1991), pp. 135–153. ISSN: 0179-5376,1432-0444. DOI: 10.1007/BF02574680.

[Ba08a] Kenneth L. Baker. "Surgery descriptions and volumes of Berge knots. I. Large volume Berge knots". In: *J. Knot Theory Ramifications* 17.9 (2008), pp. 1077–1097. ISSN: 0218-2165,1793-6527. DOI: 10.1142/S0218216508006518.

[Ba08b] Kenneth L. Baker. "Surgery descriptions and volumes of Berge knots. II. Descriptions on the minimally twisted five chain link". In: *J. Knot Theory Ramifications* 17.9 (2008), pp. 1099–1120. ISSN: 0218-2165,1793-6527. DOI: 10.1142/S021821650800652X.

[BD17] Benjamin A. Burton and Rodney G. Downey. "Courcelle's theorem for triangulations". In: *Journal of Combinatorial Theory*. Series A 146 (2017), pp. 264–294. DOI: 10.1016/j.jcta.2016.10.001.

[Ber90] John Berge. *Some knots with surgeries yielding lens spaces*. (facsimile of 1990 unpublished manuscript). 2018. arXiv: 1802.09722 [math.GT].

[Bin54] R. H. Bing. "Locally tame sets are tame". In: *Ann. of Math.* 2nd ser. 59 (1954), pp. 145–158. ISSN: 0003-486X. DOI: 10.2307/1969836.

[BLPS16] Benjamin A. Burton, Thomas Lewiner, João Paixão, and Jonathan Spreer. "Parameterized Complexity of Discrete Morse Theory". In: *ACM Trans. Math. Softw.* 42.1 (2016). DOI: 10.1145/2738034.

[BMS18] Benjamin A. Burton, Clément Maria, and Jonathan Spreer. "Algorithms and complexity for Turaev-Viro invariants". In: *Journal of Applied and Computational Topology* 2 (2018), pp. 33–53. DOI: 10.1007/s41468-018-0016-2.

[BP14] Benjamin A. Burton and William Pettersson. "Fixed Parameter Tractable Algorithms in Combinatorial Topology". In: *Computing and Combinatorics*. Ed. by Zhipeng Cai, Alex Zelikovsky, and Anu Bourgeois. Springer International Publishing, 2014, pp. 300–311. DOI: 10.1007/978-3-319-08783-2_26.

[BP95] Riccardo Benedetti and Carlo Petronio. "A finite graphic calculus for 3-manifolds". In: *Manuscripta Math.* 88.3 (1995), pp. 291–310. ISSN: 0025-2611,1432-1785. DOI: 10.1007/BF02567824.

[BP97] Riccardo Benedetti and Carlo Petronio. *Branched standard spines of 3-manifolds*. Vol. 1653. Lecture Notes in Mathematics. Springer-Verlag, Berlin, 1997, pp. viii+132. ISBN: 3-540-62627-1. DOI: 10.1007/BFb0093620.

[BS13] Benjamin A. Burton and Jonathan Spreer. "The complexity of detecting taut angle structures on triangulations". In: *Proceedings of the 2013 Annual ACM-SIAM Symposium on Discrete Algorithms (SODA)*. Society for Industrial and Applied Mathematics, 2013, pp. 168–183. DOI: 10.1137/1.9781611973105.13.

[Bur03] Benjamin A. Burton. "Minimal triangulations and normal surfaces". PhD thesis. The University of Melbourne, 2003.

[Bur11] Benjamin A. Burton. "Detecting genus in vertex links for the fast enumeration of 3-manifold triangulations". In: *Proceedings of the 36th International Symposium on Symbolic and Algebraic Computation*. Association for Computing Machinery, 2011, pp. 59–66. DOI: 10.1145/1993886.1993901.

[Bur13] Benjamin A. Burton. "Computational topology with Regina: algorithms, heuristics and implementations". In: *Geometry and topology down under*. Vol. 597. Contemp. Math. Amer. Math. Soc., Providence, RI, 2013, pp. 195–224. ISBN: 978-0-8218-8480-5. DOI: 10.1090/conm/597/11877.

[Bur14] Benjamin A. Burton. *The cusped hyperbolic census is complete*. 2014. arXiv: 1405.2695 [math.GT].

[Bur20] Benjamin A Burton. "The next 350 million knots". In: *36th International Symposium on Computational Geometry (SoCG 2020)*. Schloss-Dagstuhl-Leibniz Zentrum für Informatik. 2020.

[BV02] Roland Bacher and Alina Vdovina. "Counting 1-vertex triangulations of oriented surfaces". In: *Discrete Math.* 246.1-3 (2002). Formal power series and algebraic combinatorics (Barcelona, 1999), pp. 13–27. ISSN: 0012-365X,1872-681X. DOI: 10.1016/S0012-365X(01)00249-7.

[BZ98] S. Boyer and X. Zhang. "On Culler-Shalen Seminorms and Dehn Filling". In: *Annals of Mathematics* 148.3 (1998), pp. 737–801. ISSN: 0003486X.

[Cas65] B. G. Casler. "An imbedding theorem for connected 3-manifolds with boundary". In: *Proc. Amer. Math. Soc.* 16 (1965), pp. 559–566. ISSN: 0002-9939,1088-6826. DOI: 10.2307/2033878.

[CCGLS] D. Cooper, M. Culler, H. Gillet, D. D. Long, and P. B. Shalen. "Plane curves associated to character varieties of 3-manifolds". In: *Invent. Math.* 118.1 (1994), pp. 47–84. ISSN: 0020-9910. DOI: 10.1007/BF01231526.

[CDW99] Patrick J. Callahan, John C. Dean, and Jeffrey R. Weeks. "The simplest hyperbolic knots". In: *J. Knot Theory Ramifications* 8.3 (1999), pp. 279–297. ISSN: 0218-2165. DOI: 10.1142/S0218216599000195.

[Cha03] Abhijit Champanerkar. *A-polynomial and Bloch invariants of hyperbolic 3-manifolds*. Thesis (Ph.D.)–Columbia University. ProQuest LLC, Ann Arbor, MI, 2003, p. 108. ISBN: 978-0496-36046-8.

[CHW99] Patrick J. Callahan, Martin V. Hildebrand, and Jeffrey R. Weeks. "A census of cusped hyperbolic 3-manifolds". In: *Math. Comp.* 68.225 (1999). With microfiche supplement, pp. 321–332. ISSN: 0025-5718,1088-6842. DOI: 10.1090/S0025-5718-99-01036-4.

[CKM14] Abhijit Champanerkar, Ilya Kofman, and Timothy Mullen. "The 500 simplest hyperbolic knots". In: *J. Knot Theory Ramifications* 23.12 (2014), pp. 1450055, 34. ISSN: 0218-2165. DOI: 10.1142/S0218216514500552.

[CKP04] Abhijit Champanerkar, Ilya Kofman, and Eric Patterson. "The next simplest hyperbolic knots". In: *J. Knot Theory Ramifications* 13.7 (2004), pp. 965–987. ISSN: 0218-2165.

[CM01] Chun Cao and Robert G. Meyerhoff. "The orientable cusped hyperbolic 3-manifolds of minimum volume". In: *Invent. Math.* 146.3 (2001), pp. 451–478. ISSN: 0020-9910,1432-1297. DOI: 10.1007/s002220100167.

[CS83] Marc Culler and Peter B. Shalen. "Varieties of group representations and splittings of 3-manifolds". In: *Ann. of Math. (2)* 117.1 (1983), pp. 109–146. ISSN: 0003-486X. DOI: 10.2307/2006973.

[Cul] Marc Culler. *A-polynomials*. http://homepages.math.uic.edu/ culler/Apolynomials/.

[CZ06] Philippe Caldero and Andrei Zelevinsky. "Laurent expansions in cluster algebras via quiver representations". In: *Mosc. Math. J.* 6.3 (2006), pp. 411–429, 587. ISSN: 1609-3321. DOI: 10.17323/1609-4514-2006-6-3-411-429.

[Dim13] Tudor Dimofte. "Quantum Riemann surfaces in Chern-Simons theory". In: *Adv. Theor. Math. Phys.* 17.3 (2013), pp. 479–599. ISSN: 1095-0761.

[Dun20] Nathan M. Dunfield. "A census of exceptional Dehn fillings". In: *Characters in low-dimensional topology*. Vol. 760. Contemp. Math. Amer. Math. Soc., [Providence], RI, 2020, pp. 143–155. ISBN: 978-1-4704-5209-4; 978-1-4704-6135-5. DOI: 10.1090/conm/760/15289.

[Eas06] Vivien R. Easson. "Surface subgroups and handlebody attachment". In: *Geometry & Topology* 10.1 (2006), pp. 557–591. DOI: 10.2140/gt.2006.10.557.

[FGG+16] Evgeny Fominykh, Stavros Garoufalidis, Matthias Goerner, Vladimir Tarkaev, and Andrei Vesnin. "A census of tetrahedral hyperbolic manifolds". In: *Experimental Mathematics* 25.4 (2016), pp. 466–481.

[FMP03] Roberto Frigerio, Bruno Martelli, and Carlo Petronio. "Complexity and Heegaard genus of an infinite class of compact 3-manifolds". In: *Pacific J. Math.* 210.2 (2003), pp. 283–297. ISSN: 0030-8730,1945-5844. DOI: 10.2140/pjm.2003.210.283.

[FST08] Sergey Fomin, Michael Shapiro, and Dylan Thurston. "Cluster algebras and triangulated surfaces. I. Cluster complexes". In: *Acta Math.* 201.1 (2008), pp. 83–146. ISSN: 0001-5962. DOI: 10.1007/s11511-008-0030-7.

[FW13] E. Fominykh and B. Wiest. "Upper bounds for the complexity of torus knot complements". In: *Journal of Knot Theory and Its Ramifications* 22.10 (2013), pp. 1350053–1350053.

[FZ02] Sergey Fomin and Andrei Zelevinsky. "Cluster algebras. I. Foundations". In: *J. Amer. Math. Soc.* 15.2 (2002), pp. 497–529. ISSN: 0894-0347. DOI: 10.1090/S0894-0347-01-00385-X.

[FZ03] Sergey Fomin and Andrei Zelevinsky. "Cluster algebras: notes for the CDM-03 conference". In: *Current developments in mathematics, 2003*. Int. Press, Somerville, MA, 2003, pp. 1–34.

[Gar04] Stavros Garoufalidis. "On the characteristic and deformation varieties of a knot". In: *Geom. Topol. Monogr* 7 (2004), pp. 291–304. DOI: 10.2140/gtm.2004.7.291.

[Gar14] Stavros Garoufalidis. "Recurrent sequences of polynomials in three-dimensional topology". In: *Acta Math. Vietnam.* 39.4 (2014), pp. 541–548. ISSN: 0251-4184. DOI: 10.1007/s40306-014-0086-8.

[GL89] C. McA. Gordon and J. Luecke. "Knots are determined by their complements". In: *J. Amer. Math. Soc.* 2.2 (1989), pp. 371–415. ISSN: 0894-0347,1088-6834. DOI: 10.2307/1990979.

[GM11] Stavros Garoufalidis and Thomas W. Mattman. "The A-polynomial of the $(-2, 3, 3 + 2n)$ pretzel knots". In: *New York J. Math.* 17 (2011), pp. 269–279.

[GMM09] David Gabai, Robert Meyerhoff, and Peter Milley. "Minimum volume cusped hyperbolic three-manifolds". In: *J. Amer. Math. Soc.* 22.4 (2009), pp. 1157–1215. ISSN: 0894-0347,1088-6834. DOI: 10.1090/S0894-0347-09-00639-0.

[Gor02] C. McA. Gordon. "Links and their complements". In: *Topology and geometry: commemorating SISTAG*. Vol. 314. Contemp. Math. Amer. Math. Soc., Providence, RI, 2002, pp. 71–82. ISBN: 0-8218-2820-7. DOI: 10.1090/conm/314/05423.

[GW99] C. McA. Gordon and Ying-Qing Wu. "Toroidal and Annular Dehn Fillings". In: *Proceedings of the London Mathematical Society* 78.3 (1999), pp. 662–700. DOI: 10.1112/S0024611599001823.

[GZ18] M. Goerner and C. K. Zickert. "Triangulation independent Ptolemy varieties". In: *Math. Z.* 289.1-2 (2018), pp. 663–693. ISSN: 0025-5874. DOI: 10.1007/s00209-017-1970-4.

[Har86] John L. Harer. "The virtual cohomological dimension of the mapping class group of an orientable surface". In: *Inventiones mathematicae* 84.1 (1986), pp. 157–176. ISSN: 0020-9910.

[Hat91] Allen Hatcher. "On triangulations of surfaces". In: *Topology and its applications* 40.2 (1991), pp. 189–194. ISSN: 0166-8641.

[HIK+16] Neil Hoffman, Kazuhiro Ichihara, Masahide Kashiwagi, Hidetoshi Masai, Shin'ichi Oishi, and Akitoshi Takayasu. "Verified computations for hyperbolic 3-manifolds". In: *Exp. Math.* 25.1 (2016), pp. 66–78. ISSN: 1058-6458,1944-950X. DOI: 10.1080/10586458.2015.1029599.

[HiW89] Martin Hildebrand and Jeffrey R. Weeks. "A computer generated census of cusped hyperbolic 3-manifolds". In: *Computers and mathematics (Cambridge, MA, 1989)*. Springer, New York, 1989, pp. 53–59. ISBN: 0-387-97019-3.

[HL16] Ji-Young Ham and Joongul Lee. "An explicit formula for the A-polynomial of the knot with Conway's notation $C(2n, 3)$". In: *J. Knot Theory Ramifications* 25.10 (2016), pp. 1650057, 9. ISSN: 0218-2165. DOI: 10.1142/S0218216516500577.

[HMP20] Joshua A. Howie, Daniel V. Mathews, and Jessica S. Purcell. *A-polynomials, Ptolemy varieties and Dehn filling*. To appear in: *Algebraic & Geometric Topology*. 2020. arXiv: 2002.10356 [math.GT].

[HMPT23] Joshua A. Howie, Daniel V. Mathews, Jessica S. Purcell, and Em K. Thompson. "A-polynomials of fillings of the Whitehead sister". In: *International Journal of Mathematics* 34.13 (2023), p. 2350085.

[HMT24a] Alexander He, James Morgan, and Em K. Thompson. *An algorithm to construct one-vertex triangulations of Heegaard splittings*. 2024. arXiv: 2312.17556 [math.GT].

[HMT24b] Alexander He, James Morgan, and Em K. Thompson. *Heegaard builder*. https://github.com/AlexHe98/heegaardbuilder/. 2024.

[HoW94] Craig D. Hodgson and Jeffrey R. Weeks. "Symmetries, isometries and length spectra of closed hyperbolic three-manifolds". In: *Experiment. Math.* 3.4 (1994), pp. 261–274.

[HS04] Jim Hoste and Patrick D. Shanahan. "A formula for the A-polynomial of twist knots". In: *J. Knot Theory Ramifications* 13.2 (2004), pp. 193–209. ISSN: 0218-2165. DOI: 10.1142/S0218216504003081.

[HS19] Kristóf Huszár and Jonathan Spreer. "3-manifold triangulations with small treewidth". In: *35th International Symposium on Computational Geometry*. Vol. 129. LIPIcs. Leibniz Int. Proc. Inform. Schloss Dagstuhl. Leibniz-Zent. Inform., Wadern, 2019, Art. No. 44, 20. ISBN: 978-3-95977-104-7.

[IN16] Masaharu Ishikawa and Keisuke Nemoto. "Construction of spines of two-bridge link complements and upper bounds of their Matveev complexities". In: *Hiroshima Math. J* 46 (2016), pp. 149–162.

[JR06] William Jaco and J. Hyam Rubinstein. *Layered-triangulations of 3-manifolds*. 2006. arXiv: math/0603601 [math.GT].

[JRST20] William Jaco, J. Hyam Rubinstein, Jonathan Spreer, and Stephan Tillmann. "On minimal ideal triangulations of cusped hyperbolic 3-manifolds". In: *Journal of Topology* 13.1 (2020), pp. 308–342.

[JRT09] William Jaco, J. Hyam Rubinstein, and Stephan Tillmann. "Minimal triangulations for an infinite family of lens spaces". In: *J. Topol.* 2.1 (2009), pp. 157–180. ISSN: 1753-8416,1753-8424. DOI: 10.1112/jtopol/jtp004.

[JRT11] William Jaco, J. Hyam Rubinstein, and Stephan Tillmann. "Coverings and minimal triangulations of 3–manifolds". In: *Algebraic & Geometric Topology* 11.3 (2011), pp. 1257–1265.

[Kir95] Rob Kirby, ed. *Kirby's List: Problems in Low Dimensional Topology*. Available at https://homepages.warwick.ac.uk/~masaw/ftp/kirby_list.pdf. 1995.

[KLO] Frank Swenton. *Knot-Like Objects (KLO) software (v0.979 alpha)*. http://www.klo-software.net. 2024.

[KPR12] James Kaiser, Jessica S. Purcell, and Clint Rollins. "Volumes of chain links". In: *J. Knot Theory Ramifications* 21.11 (2012), pp. 1250115, 17. ISSN: 0218-2165,1793-6527. DOI: 10.1142/S0218216512501155.

[Lac02] Marc Lackenby. "Attaching handlebodies to 3–manifolds". In: *Geometry & Topology* 6.2 (Dec. 2002), pp. 889–904. DOI: 10.2140/gt.2002.6.889.

[Lic62] W. B. R. Lickorish. "A representation of orientable combinatorial 3-manifolds". In: *Ann. of Math.* 2nd ser. 76 (1962), pp. 531–540. ISSN: 0003-486X. DOI: 10.2307/1970373.

[LM24] Charles Livingston and Allison H. Moore. *KnotInfo: Table of Knot Invariants*. URL: knotinfo.math.indiana.edu. July 2024.

[Mar10] Bruno Martelli. "Complexity of PL manifolds". In: *Algebr. Geom. Topol.* 10.2 (2010), pp. 1107–1164. ISSN: 1472-2747,1472-2739. DOI: 10.2140/agt.2010.10.1107.

[Mar21] Bruno Martelli. "Dehn surgery on the minimally twisted seven-chain link". In: *Comm. Anal. Geom.* 29.7 (2021), pp. 1597–1641. ISSN: 1019-8385,1944-9992.

[Mat07] S. V. Matveev. *Algorithmic topology and classification of 3-manifolds*. Second. Vol. 9. Algorithms and Computation in Mathematics. Springer, Berlin, 2007, pp. xiv+492. ISBN: 978-3-540-45898-2.

[Mat14a] Daniel V. Mathews. "An explicit formula for the A-polynomial of twist knots". In: *J. Knot Theory Ramifications* 23.9 (2014), pp. 1450044, 5. ISSN: 0218-2165. DOI: 10.1142/S0218216514500448.

[Mat14b] Daniel V. Mathews. "Erratum: An explicit formula for the A-polynomial of twist knots [MR3268980]". In: *J. Knot Theory Ramifications* 23.11 (2014), pp. 1492001, 1. ISSN: 0218-2165. DOI: 10.1142/S0218216514920011.

[Mat87] S. V. Matveev. "Transformations of special spines, and the Zeeman conjecture". In: *Izv. Akad. Nauk SSSR Ser. Mat.* 51.5 (1987), pp. 1104–1116, 1119. ISSN: 0373-2436. DOI: 10.1070/IM1988v031n02ABEH001083.

[Mat88] S. V. Matveev. "The complexity of three-dimensional manifolds and their enumeration in the order of increasing complexity increase". In: *Dokl. Akad. Nauk SSSR* 301.2 (1988), pp. 280–283. ISSN: 0002-3264.

[MF88] S. V. Matveev and A. T. Fomenko. "Isoenergetic surfaces of Hamiltonian systems, the enumeration of three-dimensional manifolds in order of growth of their complexity, and the calculation of the volumes of closed hyperbolic manifolds". In: *Uspekhi Mat. Nauk* 43.1(259) (1988), pp. 5–22, 247. ISSN: 0042-1316. DOI: 10.1070/RM1988v043n01ABEH001554.

[Mil09] Peter Milley. "Minimum volume hyperbolic 3-manifolds". In: *J. Topol.* 2.1 (2009), pp. 181–192. ISSN: 1753-8416,1753-8424. DOI: 10.1112/jtopol/jtp006.

[Moi52] Edwin E. Moise. "Affine Structures in 3-Manifolds: V. The Triangulation Theorem and Hauptvermutung". In: *Annals of Mathematics* 56.1 (1952), pp. 96–114. ISSN: 0003-486X. DOI: 10.2307/1969769.

[Moi54] Edwin E. Moise. "Affine structures in 3-manifolds. VIII. Invariance of the knot-types; local tame imbedding". In: *Ann. of Math.* 2nd ser. 59 (1954), pp. 159–170. ISSN: 0003-486X. DOI: 10.2307/1969837.

[Mos09] Harriet Moser. "Proving a manifold to be hyperbolic once it has been approximated to be so". In: *Algebr. Geom. Topol.* 9.1 (2009), pp. 103–133. ISSN: 1472-2747,1472-2739. DOI: 10.2140/agt.2009.9.103.

[Mos96] Lee Mosher. "A user's guide to the mapping class group: once punctured surfaces". In: *Geometric and computational perspectives on infinite groups (Minneapolis, MN and New Brunswick, NJ, 1994)*. Vol. 25. DIMACS Ser. Discrete Math. Theoret. Comput. Sci. Amer. Math. Soc., Providence, RI, 1996, pp. 101–174. ISBN: 0-8218-0449-9. DOI: 10.1090/dimacs/025/08.

[MPe01] Bruno Martelli and Carlo Petronio. "Three-manifolds having complexity at most 9". In: *Experiment. Math.* 10.2 (2001), pp. 207–236. ISSN: 1058-6458,1944-950X.

[MPe06] Bruno Martelli and Carlo Petronio. "Dehn filling of the "magic" 3-manifold". In: *Comm. Anal. Geom.* 14.5 (2006), pp. 969–1026. ISSN: 1019-8385.

[MPR14] Bruno Martelli, Carlo Petronio, and Fionntan Roukema. "Exceptional Dehn surgery on the minimally twisted five-chain link". In: *Comm. Anal. Geom.* 22.4 (2014), pp. 689–735. ISSN: 1019-8385,1944-9992. DOI: 10.4310/CAG.2014.v22.n4.a4.

[MPu22] Daniel V. Mathews and Jessica S. Purcell. *A symplectic basis for 3-manifold triangulations*. 2022. arXiv: 2208.06969 [math.GT].

[MS24] James Morgan and Jonathan Spreer. *On the complexity of 2-bridge link complements*. 2024. arXiv: 2406.09629 [math.GT].

[MS74] S. V. Matveev and V. V. Savvateev. "Three-dimensional manifolds having simple special spines". In: *Colloq. Math.* 32 (1974), pp. 83–97. ISSN: 0010-1354,1730-6302.

[MT05] S. V. Matveev and V.V. Tarkaev. "Three-manifold recognizer". In: *Computer program* (2005). http://www.matlas.math.csu.ru/?page=about.

[MuP07] G. Musiker and J. Propp. "Combinatorial interpretations for rank-two cluster algebras of affine type". In: *Electron. J. Combin.* 14.1 (2007), Research Paper 15, 23.

[NiZ17] Yi Ni and Xingru Zhang. "Detection of knots and a cabling formula for A-polynomials". In: *Algebr. Geom. Topol.* 17.1 (2017), pp. 65–109. ISSN: 1472-2747. DOI: 10.2140/agt.2017.17.65.

[NR92] Walter D. Neumann and Alan W. Reid. "Arithmetic of hyperbolic manifolds". In: *Topology '90 (Columbus, OH, 1990)*. Vol. 1. Ohio State Univ. Math. Res. Inst. Publ. de Gruyter, Berlin, 1992, pp. 273–310. ISBN: 3-11-012598-6.

[NZ85] Walter D. Neumann and Don Zagier. "Volumes of hyperbolic three-manifolds". In: *Topology* 24.3 (1985), pp. 307–332. ISSN: 0040-9383. DOI: 10.1016/0040-9383(85)90004-7.

[Pac91] Udo Pachner. "PL homeomorphic manifolds are equivalent by elementary shellings". In: *European journal of Combinatorics* 12.2 (1991), pp. 129–145.

[Pet15] Kathleen L. Petersen. "A-polynomials of a family of two-bridge knots". In: *New York J. Math.* 21 (2015), pp. 847–881.

[Pie88] Riccardo Piergallini. "Standard moves for standard polyhedra and spines". In: *Rend. Circ. Mat. Palermo (2) Suppl.* 18 (1988). Third National Conference on Topology (Italian) (Trieste, 1986), pp. 391–414. ISSN: 1592-9531.

[Regina] Benjamin A. Burton, Ryan Budney, William Pettersson, et al. *Regina: Software for low-dimensional topology*. http://regina-normal.github.io/. 1999–2024.

[Rol76] Dale Rolfsen. *Knots and links*. Vol. No. 7. Mathematics Lecture Series. Publish or Perish, Inc., Berkeley, CA, 1976, pp. ix+439.

[RST19] J. Hyam Rubinstein, Henry Segerman, and Stephan Tillmann. "Traversing three-manifold triangulations and spines". In: *Enseign. Math.* 65.1-2 (2019), pp. 155–206. ISSN: 0013-8584,2309-4672. DOI: 10.4171/lem/65-1/2-5.

[RST21] J. Hyam Rubinstein, Jonathan Spreer, and Stephan Tillmann. *A new family of minimal ideal triangulations of cusped hyperbolic 3-manifolds*. 2021. arXiv: 2112.01654 [math.GT].

[Sage] W. A. Stein et al. *Sage Mathematics Software (v10.1)*. http://www.sagemath.org. The Sage Development Team. 2023.

[Seg12] Henry Segerman. "A generalisation of the deformation variety". In: *Algebr. Geom. Topol.* 12.4 (2012), pp. 2179–2244. ISSN: 1472-2747,1472-2739. DOI: 10.2140/agt.2012.12.2179.

[SnapPy] Marc Culler, Nathan M. Dunfield, Matthias Goerner, and Jeffrey R. Weeks. *SnapPy, a computer program for studying the geometry and topology of 3-manifolds (v3.1.1)*. http://snappy.computop.org. 2024.

[SnapCo] Nathan M. Dunfield. *SnapPy graphical conventions*. https://github.com/3-manifolds/Spherogram/blob/master/spherogram_src/links/doc.pdf. 2021.

[SW95] Makoto Sakuma and Jeffrey R. Weeks. "Examples of canonical decompositions of hyperbolic link complements". In: *Japanese Journal of Mathematics*. New series 21.2 (1995), pp. 393–439.

[Thi10] Morwen Thistlethwaite. *Cusped hyperbolic manifolds with 8 tetrahedra*. https://web.math.utk.edu/ morwen/8tet/readme.txt. 2010.

[Thu82] William P. Thurston. "Three dimensional manifolds, Kleinian groups and hyperbolic geometry". In: *Bulletin of the American Mathematical Society*. New series 6.3 (1982), pp. 357–381. ISSN: 0273-0979.

[Thur] William P. Thurston. *The geometry and topology of three-manifolds: With a preface by Steven P. Kerckhoff*. Vol. 27. American Mathematical Society, 2022.

[TY04] N. Tamura and Y. Yokota. "A formula for the A-polynomials of $(-2, 3, 1 + 2n)$-pretzel knots". In: *Tokyo J. Math.* 27.1 (2004), pp. 263–273. ISSN: 0387-3870. DOI: 10.3836/tjm/1244208490.

[Ven08] Rupert William Venzke. *Braid Forcing, Hyperbolic Geometry, and Pseudo-Anosov Sequences of Low Entropy*. Thesis (Ph.D.)–California Institute of Technology. ProQuest LLC, Ann Arbor, MI, 2008, p. 124. ISBN: 978-1267-59751-9.

[Wal60] Andrew H. Wallace. "Modifications and cobounding manifolds". In: *Canadian J. Math.* 12 (1960), pp. 503–528. ISSN: 0008-414X,1496-4279. DOI: 10.4153/CJM-1960-045-7.

[Wee05] Jeffrey R. Weeks. "Computation of hyperbolic structures in knot theory". In: *Handbook of knot theory*. Ed. by William Menasco and Morwen Thistlethwaite. Elsevier Science, 2005. Chap. 10, pp. 461–480. DOI: 10.1016/B978-044451452-3/50011-3.

[Whi37] J. H. C. Whitehead. "On Doubled Knots". In: *Journal of the London Mathematical Society* 1.1 (1937), pp. 63–71. ISSN: 0024-6107.

[Yos13] Ken'ichi Yoshida. "The minimal volume orientable hyperbolic 3-manifold with 4 cusps". In: *Pacific J. Math.* 266.2 (2013), pp. 457–476. ISSN: 0030-8730,1945-5844. DOI: 10.2140/pjm.2013.266.457.

[Zel07] Andrei Zelevinsky. "Semicanonical basis generators of the cluster algebra of type A". In: *Electron. J. Comb.* 14.4 (2007), pp. 1–5.

[Zha23] Yue Zhang. *Guts and The Minimal Volume Orientable Hyperbolic 3-Manifold with 3 Cusps*. 2023. arXiv: 2304.09950 [math.GT].

Appendix A. Families of census knots

This appendix classifies all of the families of census knots that are discussed in Section 2.3. Each knot arises as a filling of two cusps of the magic manifold M_3. For each filling, one of the slopes is designated the *primary slope* and is consistently denoted by r/s, while subsequent slopes are called *secondary slopes* and are consistently labelled t/u.

The census knots are organised into families based on their primary slope. In the tables of Section A.3, each column represents a family of knots. In the case of Tables A.1 to A.10, we proved in Lemma 2.11 that filling cusp $\mathfrak{c}_1$ along a primary slope r/s leaves a 2-component link in which cusp $\mathfrak{c}_2$ forms an unknot around some number of parallel strands of $\mathfrak{c}_0$. Moreover, the secondary slopes are of an appropriate form so that the filling in $\mathfrak{c}_2$ along t/u realises some number of full twists on the encircled strands.

The secondary slopes t_n/u_n for each column are given in terms of n, and any knots that SnapPy recognises after filling $M_3(r/s)$ along t_n/u_n are listed in the appropriate column in order of increasing n. When a primary slope is exceptional, i.e. $r/s \in \mathcal{X}$, the column is omitted (a double vertical line makes this apparent). When a secondary slope is exceptional, i.e. $t_n/u_n \in \mathcal{X}$, the corresponding cell is shaded red and contains an X. Vertical dots in each column emphasise the fact that each family has infinitely many members for positive and negative n, despite no further census knots being recognised. For families with a distinguished pair of fillings, which are shaded blue, the family receives a label $\mathcal{F}_v$ based on the ordering by average volume assigned in Section A.1.

As per the claims of Section 2.3.4, every family is assigned either a twisted torus knot description or a clasped torus knot description. The SnapPy code used to verify each claim is provided in Section A.2.

A.1. Distinguished families

The following table describes an ordering on the 42 families with a distinguished pair of fillings, based on the average volume of K_1, K_2. Distinguished fillings are shaded in Tables A.1 to A.12. Families marked with an asterisk are those of Type B & C.

	r/s	K_1	vol_1	K_2	vol_2	vol_{av}	Description
$\mathcal{F}_0$	$-1/2$	NH	N/A	$K3_1$	2.82812	1.414061044	$T(3, 1-3n, 2, -2)$
$\mathcal{F}_1$	$1/1$	$K2_1$	2.02988	$K3_2$	2.82812	2.429002651	$Cl(2, 1+2n)$
$\mathcal{F}_2$	$-1/3$	$K3_1$	2.82812	$K4_4$	3.60869	3.218405575	$T(4, 1-4n, 2, -2)$
$\mathcal{F}_3$	$-4/1$	$K5_1$	3.41791	$K5_4$	3.52851	3.473212167	$T(5, -1+5n, 2, -2)$
$\mathcal{F}_4$	$-5/2$	$K6_6$	3.96785	$K6_7$	3.99350	3.980678137	$T(7, 3-7n, 2, -2)$
$\mathcal{F}_5$	$-2/3$	$K5_6$	4.02612	$K5_7$	4.05450	4.040312077	$T(5, -2-5n, 2, -2)$
$\mathcal{F}_6$	$2/1$	$K5_9$	4.05686	$K5_{13}$	4.12490	4.090881738	$Cl(3, 1+3n)$
$\mathcal{F}_7$	$1/2$	$K5_8$	4.05686	$K6_{10}$	4.40083	4.228846370	$Cl(3, -1-3n)$
$\mathcal{F}_8$	$-1/4$	$K5_{10}$	4.08209	$K6_{11}$	4.46180	4.271945154	$T(5, 1-5n, 2, -2)$
$\mathcal{F}_9$	$-5/1$	$K7_8$	4.27986	$K7_9$	4.35277	4.316314380	$T(6, -1+6n, 2, -2)$
$\mathcal{F}_{10}$	$-4/3$	$K7_{12}$	4.36003	$K7_{13}$	4.46284	4.411435232	$T(7, 2-7n, 2, -2)$
$\mathcal{F}_{11}$	$-5/3$	$K7_{14}$	4.46826	$K7_{16}$	4.48570	4.476983629	$T(8, -3-8n, 2, -2)$
$\mathcal{F}^*_{12}$	$-5/3$	$K7_{15}$	4.47895	$K7_{17}$	4.51181	4.495378459	$T(8, 3+8n, 3, -2)$
$\mathcal{F}_{13}$	$3/1$	$K7_{19}$	4.55377	$K7_{26}$	4.63782	4.595794761	$Cl(4, 1+4n)$
$\mathcal{F}_{14}$	$-2/5$	$K6_{16}$	4.54952	$K6_{21}$	4.66383	4.606674615	$T(7, -3+7n, 2, -2)$
$\mathcal{F}_{15}$	$-3/4$	$K7_{21}$	4.57465	$K7_{33}$	4.70790	4.641272953	$T(7, -2-7n, 2, -2)$
$\mathcal{F}^*_{16}$	$-7/2$	$K7_{29}$	4.66731	$K7_{31}$	4.68948	4.678393829	$T(9, 5+9n, 5, 1)$
$\mathcal{F}_{17}$	$-7/3$	$K8_{21}$	4.66915	$K8_{25}$	4.69458	4.681864567	$T(10, 3-10n, 2, -2)$
$\mathcal{F}_{18}$	$-6/1$	$K9_{18}$	4.66305	$K9_{26}$	4.71487	4.688959756	$T(7, -1+7n, 2, -2)$
$\mathcal{F}^*_{19}$	$-7/3$	$K8_{23}$	4.68667	$K8_{26}$	4.69840	4.692537260	$T(10, -3-10n, 4, -2)$
$\mathcal{F}_{20}$	$-7/2$	$K8_{27}$	4.70222	$K8_{29}$	4.71136	4.706790724	$T(9, 4-9n, 2, -2)$
$\mathcal{F}_{21}$	$-1/5$	$K7_{20}$	4.56838	$K8_{40}$	4.86208	4.715232947	$T(6, 1-6n, 2, -2)$
$\mathcal{F}_{22}$	$1/3$	$K7_{25}$	4.60993	$K8_{39}$	4.84818	4.729051162	$Cl(4, -1-4n)$
$\mathcal{F}_{23}$	$-3/5$	$K7_{32}$	4.70156	$K7_{38}$	4.84805	4.774803122	$T(8, 3+8n, 2, -2)$
$\mathcal{F}_{24}$	$-5/4$	$K9_{34}$	4.74474	$K9_{39}$	4.83021	4.787476299	$T(9, 2-9n, 2, -2)$
$\mathcal{F}^*_{25}$	$-8/3$	$K8_{34}$	4.80673	$K8_{36}$	4.81573	4.811228191	$T(11, -5-11n, 5, 1)$
$\mathcal{F}_{26}$	$-8/3$	$K8_{35}$	4.81395	$K8_{37}$	4.82404	4.818990733	$T(11, -4-11n, 2, -2)$
$\mathcal{F}_{27}$	$4/1$	$K9_{37}$	4.80707	$K9_{50}$	4.87261	4.839837081	$Cl(5, 1+5n)$
$\mathcal{F}_{28}$	$-7/4$	$K9_{42}$	4.83695	$K9_{48}$	4.86112	4.849033552	$T(11, -3-11n, 2, -2)$
$\mathcal{F}^*_{29}$	$-7/4$	$K9_{47}$	4.85708	$K9_{49}$	4.87213	4.864606297	$T(11, 4+11n, 4, -2)$
$\mathcal{F}_{30}$	$-4/5$	$K9_{40}$	4.83520	$K9_{56}$	4.96004	4.897618266	$T(9, -2-9n, 2, -2)$
$\mathcal{F}_{31}$	$3/2$	$K8_{44}$	4.89986	$K8_{47}$	4.93820	4.919029453	$Cl(5, -2-5n)$
$\mathcal{F}_{32}$	$-3/7$	$K8_{43}$	4.88501	$K8_{58}$	5.03400	4.959506169	$T(10, -3+10n, 2, -2)$
$\mathcal{F}_{33}$	$2/3$	$K8_{48}$	4.94967	$K8_{51}$	4.97601	4.962841237	$Cl(5, 2-5n)$
$\mathcal{F}_{34}$	$-2/7$	$K8_{50}$	4.95642	$K8_{57}$	5.01830	4.987360888	$T(9, -4+9n, 2, -2)$
$\mathcal{F}_{35}$	$-7/5$	$K9_{62}$	4.99142	$K9_{64}$	4.99947	4.995447408	$T(12, -5+12n, 2, -2)$
$\mathcal{F}_{36}$	$-8/5$	$K9_{65}$	5.00158	$K9_{70}$	5.01370	5.007640743	$T(13, 5+13n, 2, -2)$
$\mathcal{F}^*_{37}$	$-10/3$	$K9_{67}$	5.00603	$K9_{68}$	5.01349	5.009763914	$T(13, 7+13n, 7, 1)$
$\mathcal{F}_{38}$	$-4/7$	$K9_{55}$	4.95474	$K9_{79}$	5.08627	5.020503376	$T(11, 3+11n, 2, -2)$
$\mathcal{F}_{39}$	$-3/8$	$K8_{55}$	5.01245	$K8_{63}$	5.08584	5.049147425	$T(11, 4+11n, 2, -2)$
$\mathcal{F}_{40}$	$-5/7$	$K9_{76}$	5.07393	$K9_{84}$	5.10882	5.091376989	$T(12, 5-12n, 2, -2)$
$\mathcal{F}_{41}$	$-5/8$	$K9_{82}$	5.10425	$K9_{87}$	5.13908	5.121663684	$T(13, -5-13n, 2, -2)$

A.2. Code to verify claims

The conventions used in SnapPy are summarised in [SnapCo]. In particular, note that a $+1$ rational tangle gives a negative crossing while a -1 rational tangle gives a positive crossing.

Twisted torus knots. The twisted torus knot $T(a, b, c, d)$ can be constructed in SnapPy by first describing an appropriate braid word, then taking the braid closure. This can be achieved using the following function.

```
def TTK(a,b,c,d):
    ...:     B=[]
    ...:     if b>0:
    ...:         for i in range(1,b+1):
    ...:             for j in range(1,a):
    ...:                 B.append(a-j)
    ...:     else:
    ...:         for i in range(1,1-b):
    ...:             for j in range(1,a):
    ...:                 B.append(-j)
    ...:     if d>0:
    ...:         for i in range(1,d+1):
    ...:             for j in range(1,c):
    ...:                 B.append(a-j)
    ...:     else:
    ...:         for i in range(1,1-d):
    ...:             for j in range(1,c):
    ...:                 B.append(c-a-j)
    ...:     return Link(braid_closure=B)
```

Clasped torus knots. Since clasped torus knots are not easily described as the closure of a braid, we instead construct them in SnapPy using *tangles*. The knot $Cl(a, b)$ is built up from 'rows', which each consist of $a-2$ vertical strands and one rational tangle (involving 2 strands).

```
def row(a,p,s):
   ...:     return(IdentityBraid(p-1)|RationalTangle(-s)|IdentityBraid(a-p-1))

def overstrand(a,s):
   ...:     strand = []
   ...:     for p in range(1,a):
   ...:         rowp = row(a,p,s)
   ...:         strand.append(rowp)
   ...:     if s>0:
   ...:         strand.reverse()
   ...:     ostrand = strand[0]
   ...:     for p in range(1,a-1):
   ...:         ostrand *= strand[p]
   ...:     return ostrand

def torusRegion(a,b):
   ...:     if b<0:
   ...:         s = -1
   ...:         b = -b
   ...:     else:
   ...:         s = 1
   ...:     tReg = overstrand(a,s)
   ...:     for i in range(2,b+1):
   ...:         tReg *= overstrand(a,s)
   ...:     return tReg
```

Note that `torusRegion(a,b).denominator_closure()` describes the torus knot $T(a, b)$. By adding just one more 'clasp row' before taking the denominator closure, we obtain the knot $Cl(a, b)$.

```
def clasp(a):
   ...:     return IdentityBraid(a-2)|RationalTangle(-2)

def Cl(a,b):
   ...:     tReg = torusRegion(a,b)
   ...:     cRow = clasp(a)
   ...:     joined = tReg * cRow
   ...:     closed = joined.denominator_closure()
   ...:     return closed
```

Recognising census knots. The descriptions of clasped and twisted torus knots given in Section 2.3.4 can be input into SnapPy using the functions just described, then the following function can be used to recognise census knots.

```
def censusID(link):
   ...:     E = link.exterior()
   ...:     if CensusKnots.identify(E) is False:
   ...:         if len(E.identify())>0:
   ...:             return E.identify()[0]
   ...:         else:
   ...:             return "NR"
   ...:     else:
   ...:         return CensusKnots.identify(E)
```

A.3. Tables

The remainder of this appendix consists of 12 tables containing the 229 census knots found by filling M_3.

TABLE A.1. Families of knots with slopes $r/s = [k]$ and $t/u = [0, k, n]$.

(a) In this table, $r = k$, $s = 1$, $t = n$, and $u = 1 + kn$. Columns for $k = -3, -2, -1, 0$ are omitted, since these correspond to exceptional slopes. The 7 columns with two distinguished fillings are labelled with their family name, as assigned in Section A.1.

		$\mathcal{F}_{18}$	$\mathcal{F}_9$	$\mathcal{F}_3$	$\mathcal{F}_1$	$\mathcal{F}_6$	$\mathcal{F}_{13}$	$\mathcal{F}_{27}$	
k	-7	-6	-5	-4	1	2	3	4	5
r/s	$-7/1$	$-6/1$	$-5/1$	$-4/1$	$1/1$	$2/1$	$3/1$	$4/1$	$5/1$
t/u	$\frac{n}{1-7n}$	$\frac{n}{1-6n}$	$\frac{n}{1-5n}$	$\frac{n}{1-4n}$	$\frac{n}{n+1}$	$\frac{n}{2n+1}$	$\frac{n}{3n+1}$	$\frac{n}{4n+1}$	$\frac{n}{5n+1}$
⋮					⋮				
-8					$K9_1$				
-7					$K8_1$	⋮			
-6				⋮	$K7_1$	$K9_9$			
-5				$K9_3$	$K6_1$	$K8_{10}$	⋮		
-4			⋮	$K8_3$	$K5_2$	$K7_{11}$	$K9_{29}$		
-3			$K9_{10}$	$K7_3$	$K4_1$	$K6_9$	$K8_{28}$	⋮	
-2		⋮	$K8_8$	$K6_3$	$K2_1$	$K5_{13}$	$K7_{26}$	$K9_{50}$	⋮
-1	⋮	$K9_{18}$	$K7_8$	$K5_1$	X	$K2_1$	$K5_8$	$K7_{25}$	$K9_{46}$
$n = 0$	X	X	X	X	X	X	X	X	X
1	$K9_{38}$	$K7_{20}$	$K5_{10}$	$K3_1$	$K3_2$	$K5_9$	$K7_{19}$	$K9_{37}$	⋮
2	⋮	$K9_{26}$	$K7_9$	$K5_4$	$K4_2$	$K6_8$	$K8_{24}$	⋮	
3		⋮	$K8_{11}$	$K6_4$	$K5_3$	$K7_{10}$	$K9_{28}$		
4			$K9_{11}$	$K7_4$	$K6_2$	$K8_9$	⋮		
5			⋮	$K8_4$	$K7_2$	$K9_8$			
6				$K9_4$	$K8_2$	⋮			
7				⋮	$K9_2$				
⋮					⋮				

(b) Twisted torus knot descriptions for families with $-7 \le k \le -4$.

	k	$T(1-k, -1+(1-k)\cdot n, 2, -2)$
$\mathcal{F}_3$	-4	$T(5, -1+5n, 2, -2)$
$\mathcal{F}_9$	-5	$T(6, -1+6n, 2, -2)$
$\mathcal{F}_{18}$	-6	$T(7, -1+7n, 2, -2)$
	-7	$T(8, -1+8n, 2, -2)$

(c) Clasped torus knot descriptions for families with $1 \le k \le 5$.

	k	$Cl\,(k+1, 1+(k+1)\cdot n)$
$\mathcal{F}_1$	1	$Cl(2, 1+2n)$
$\mathcal{F}_6$	2	$Cl(3, 1+3n)$
$\mathcal{F}_{13}$	3	$Cl(4, 1+4n)$
$\mathcal{F}_{27}$	4	$Cl(5, 1+5n)$
	5	$Cl(6, 1+6n)$

Table A.2. Families of knots with slopes $r/s = [0, k]$ and $t/u = [k, n]$.

(a) In this table, $r = 1$, $s = k$, $t = 1 + kn$, and $u = n$. Columns for $k = -1, 0$ are omitted, since these correspond to exceptional slopes. The 7 columns with distinguished fillings highlighted are labelled with their family name, as assigned in Section A.1.

			$\mathcal{F}_{21}$	$\mathcal{F}_8$	$\mathcal{F}_2$	$\mathcal{F}_0$	$\mathcal{F}_1$	$\mathcal{F}_7$	$\mathcal{F}_{22}$		
k	-7	-6	-5	-4	-3	-2	1	2	3	4	5
r/s	$-1/7$	$-1/6$	$-1/5$	$-1/4$	$-1/3$	$-1/2$	$1/1$	$1/2$	$1/3$	$1/4$	$1/5$
t/u	$\frac{1-7n}{n}$	$\frac{1-6n}{n}$	$\frac{1-5n}{n}$	$\frac{1-4n}{n}$	$\frac{1-3n}{n}$	$\frac{1-2n}{n}$	$\frac{n+1}{n}$	$\frac{2n+1}{n}$	$\frac{3n+1}{n}$	$\frac{4n+1}{n}$	$\frac{5n+1}{n}$
⋮						⋮	⋮				
-8						$K9_5$	$K9_2$				
-7					⋮	$K8_5$	$K8_2$				
-6					$K9_{35}$	$K7_5$	$K7_2$	⋮			
-5				⋮	$K8_{31}$	$K6_5$	$K6_2$	$K9_{22}$			
-4				$K9_{61}$	$K7_{27}$	$K5_5$	$K5_3$	$K8_{22}$	⋮		
-3			⋮	$K8_{46}$	$K6_{14}$	$K4_3$	$K4_2$	$K7_{24}$	$K9_{57}$		
-2		⋮	$K9_{60}$	$K7_{34}$	$K5_{14}$	$K3_1$	$K3_2$	$K6_{10}$	$K8_{39}$	⋮	⋮
-1	⋮	$K9_{38}$	$K7_{20}$	$K5_{10}$	$K3_1$	X	X	$K3_2$	$K5_9$	$K7_{19}$	$K9_{37}$
$n = 0$	X	X	X	X	X	X	X	X	X	X	X
1	$K9_{18}$	$K7_8$	$K5_1$	X	X	X	$K2_1$	$K5_8$	$K7_{25}$	$K9_{46}$	⋮
2	⋮	⋮	$K8_{40}$	$K6_{11}$	$K4_4$	$K3_1$	$K4_1$	$K7_{18}$	$K9_{53}$	⋮	
3			$K9_{71}$	$K7_{37}$	$K5_{18}$	$K4_3$	$K5_2$	$K8_{20}$	⋮		
4			⋮	$K8_{49}$	$K6_{17}$	$K5_5$	$K6_1$	$K9_{21}$			
5				$K9_{66}$	$K7_{30}$	$K6_5$	$K7_1$	⋮			
6				⋮	$K8_{33}$	$K7_5$	$K8_1$				
7					$K9_{36}$	$K8_5$	$K9_1$				
8					⋮	$K9_5$	⋮				
⋮						⋮					

(b) Twisted torus knot descriptions for families with $-7 \le k \le -2$.

	k	$T(1-k, 1-(1-k)\cdot n, 2, -2)$
$\mathcal{F}_0$	-2	$T(3, 1-3n, 2, -2)$
$\mathcal{F}_2$	-3	$T(4, 1-4n, 2, -2)$
$\mathcal{F}_8$	-4	$T(5, 1-5n, 2, -2)$
$\mathcal{F}_{21}$	-5	$T(6, 1-6n, 2, -2)$
	-6	$T(7, 1-7n, 2, -2)$
	-7	$T(8, 1-8n, 2, -2)$

(c) Clasped torus knot descriptions for families with $1 \le k \le 5$.

	k	$Cl\,(k+1, -1-(k+1)\cdot n)$
$\mathcal{F}_1$	1	$Cl(2, -1-2n)$
$\mathcal{F}_7$	2	$Cl(3, -1-3n)$
$\mathcal{F}_{22}$	3	$Cl(4, -1-4n)$
	4	$Cl(5, -1-5n)$
	5	$Cl(6, -1-6n)$

TABLE A.3. Families of knots with slopes $r/s = [1, k]$ and $t/u = [0, 1, k, n]$.

(a) In this table, $r = k + 1$, $s = k$, $t = 1 + kn$, and $u = 1 + (k + 1)n$. Columns for $k = -1, 0$ are omitted, since these correspond to exceptional slopes. Horizontal dots indicate that several more census knots were identified for $k < -5$ and $k > 4$, but these appear in other tables, so have been omitted to save space. The 4 columns with two distinguished fillings are labelled with their family name, as assigned in Section A.1.

			$\mathcal{F}_{33}$	$\mathcal{F}_7$	$\mathcal{F}_6$	$\mathcal{F}_{31}$		
k	-5	-4	-3	-2	1	2	3	4
r/s	$4/5$	$3/4$	$2/3$	$1/2$	$2/1$	$3/2$	$4/3$	$5/4$
t/u	$\frac{1-5n}{1-4n}$	$\frac{1-4n}{1-3n}$	$\frac{1-3n}{1-2n}$	$\frac{1-2n}{1-n}$	$\frac{n+1}{2n+1}$	$\frac{2n+1}{3n+1}$	$\frac{3n+1}{4n+1}$	$\frac{4n+1}{5n+1}$
$\vdots$					$\vdots$			
-6					$K9_8$			
-5				$\vdots$	$K8_9$			
-4				$K9_{22}$	$K7_{10}$	$\vdots$		
-3			$\vdots$	$K8_{22}$	$K6_8$	$K9_{63}$		
-2			$K9_{72}$	$K7_{24}$	$K5_9$	$K8_{47}$	$\vdots$	
-1		$\vdots$	$K8_{48}$	$K6_{10}$	X	$K6_{10}$	$K8_{48}$	$\vdots$
$n = 0$	$\cdots\ K6_2$	$K5_3$	$K4_2$	$K3_2$	$K2_1$	$K4_1$	$K5_2$	$K6_1\ \cdots$
1	$\vdots$	$K8_{44}$	$K5_{13}$	X	$K5_{13}$	$K8_{44}$	$\vdots$	$\vdots$
2		$\vdots$	$K8_{51}$	$K5_8$	$K6_9$	$K9_{59}$		
3			$K9_{74}$	$K7_{18}$	$K7_{11}$	$\vdots$		
4			$\vdots$	$K8_{20}$	$K8_{10}$			
5				$K9_{21}$	$K9_9$			
$\vdots$				$\vdots$	$\vdots$			

(b) Clasped torus knot descriptions for families with $-5 \le k \le -2$. Here $a = |r+s| = |2k+1|$.

	k	$Cl(a, 2 - a \cdot n)$
$\mathcal{F}_7$	-2	$Cl(3, 2 - 3n)$
$\mathcal{F}_{33}$	-3	$Cl(5, 2 - 5n)$
	-4	$Cl(7, 2 - 7n)$
	-5	$Cl(9, 2 - 9n)$

(c) Clasped torus knot descriptions for families with $1 \le k \le 4$. Again, $a = |r + s| = |2k + 1|$.

	k	$Cl(a, -2 - a \cdot n)$
$\mathcal{F}_6$	1	$Cl(3, -2 - 3n)$
$\mathcal{F}_{31}$	2	$Cl(5, -2 - 5n)$
	3	$Cl(7, -2 - 7n)$
	4	$Cl(9, -2 - 9n)$

Table A.4. Families of knots with slopes $r/s = [-1, k]$ and $t/u = [0, -1, k, n]$.

(a) In this table, $r = 1-k$, $s = k$, $t = 1+kn$, and $u = -1+(1-k)n$. Columns for $k = -1, 0, 1$ are omitted, since these correspond to exceptional slopes. The 7 columns with distinguished fillings highlighted are labelled with their family name, as assigned in Section A.1. Note that the family labelled $\mathcal{F}_0$ is the only family with only one distinguished filling. It is also the only family that generates the same knots for positive and negative n.

		$\mathcal{F}_{24}$	$\mathcal{F}_{10}$	$\mathcal{F}_3$	$\mathcal{F}_0$	$\mathcal{F}_5$	$\mathcal{F}_{15}$	$\mathcal{F}_{30}$	
k	-5	-4	-3	-2	2	3	4	5	6
r/s	$-6/5$	$-5/4$	$-4/3$	$-3/2$	$-1/2$	$-2/3$	$-3/4$	$-4/5$	$-5/6$
t/u	$\frac{1-5n}{6n-1}$	$\frac{1-4n}{5n-1}$	$\frac{1-3n}{4n-1}$	$\frac{1-2n}{3n-1}$	$\frac{2n+1}{-n-1}$	$\frac{3n+1}{-2n-1}$	$\frac{4n+1}{-3n-1}$	$\frac{5n+1}{-4n-1}$	$\frac{6n+1}{-5n-1}$
$\vdots$					$\vdots$				
-7					$K7_5$	$\vdots$			
-6				$\vdots$	$K6_5$	$K9_{19}$			
-5				$K9_3$	$K5_5$	$K8_{18}$	$\vdots$		
-4			$\vdots$	$K8_3$	$K4_3$	$K7_{22}$	$K9_{54}$		
-3			$K9_{12}$	$K7_3$	$K3_1$	$K6_{12}$	$K8_{41}$	$\vdots$	
-2		$\vdots$	$K8_{12}$	$K6_3$	X	$K5_6$	$K7_{33}$	$K9_{56}$	$\vdots$
-1	$\vdots$	$K9_{34}$	$K7_{12}$	$K5_1$	X	X	$K5_1$	$K7_{12}$	$K9_{34}$
$n=0$	X	X	X	X	X	X	X	X	X
1	$K9_{40}$	$K7_{21}$	$K5_7$	$K3_1$	$K3_1$	$K5_7$	$K7_{21}$	$K9_{40}$	$\vdots$
2	$\vdots$	$K9_{39}$	$K7_{13}$	$K5_4$	$K4_3$	$K6_{13}$	$K8_{38}$	$\vdots$	
3		$\vdots$	$K8_{13}$	$K6_4$	$K5_5$	$K7_{23}$	$K9_{52}$		
4			$K9_{13}$	$K7_4$	$K6_5$	$K8_{19}$	$\vdots$		
5			$\vdots$	$K8_4$	$K7_5$	$K9_{20}$			
6				$K9_4$	$K8_5$	$\vdots$			
7				$\vdots$	$K9_5$				
$\vdots$					$\vdots$				

(b) Twisted torus knot descriptions for families with $-5 \le k \le -2$.

	k	$T(1-2k, 2-(1-2k)\cdot n, 2, -2)$
$\mathcal{F}_3$	-2	$T(5, 2-5n, 2, -2)$
$\mathcal{F}_{10}$	-3	$T(7, 2-7n, 2, -2)$
$\mathcal{F}_{24}$	-4	$T(9, 2-9n, 2, -2)$
	-5	$T(11, 2-11n, 2, -2)$

(c) Twisted torus knot descriptions for families with $2 \le k \le 6$.

	k	$T(2k-1, -2-(2k-1)\cdot n, 2, -2)$
$\mathcal{F}_0$	2	$T(3, -2-3n, 2, -2)$
$\mathcal{F}_5$	3	$T(5, -2-5n, 2, -2)$
$\mathcal{F}_{15}$	4	$T(7, -2-7n, 2, -2)$
$\mathcal{F}_{30}$	5	$T(9, -2-9n, 2, -2)$
	6	$T(11, -2-11n, 2, -2)$

TABLE A.5. Families of knots with slopes $r/s = [-2, k]$ and $t/u = [0, -2, k, n]$.

(a) In this table, $r = 1 - 2k$, $s = k$, $t = 1 + kn$, and $u = -2 + (1 - 2k)\, n$. Columns for $k = -1, 0, 1$ are omitted, since these correspond to exceptional slopes. Horizontal dots indicate that several more census knots were identified for $k < -5$ and $k > 6$, but these already appear elsewhere, so have been omitted to save space. The 5 columns with two distinguished fillings are labelled with their family name, as assigned in Section A.1.

			$\mathcal{F}_{17}$	$\mathcal{F}_4$	$\mathcal{F}_3$	$\mathcal{F}_{11}$	$\mathcal{F}_{28}$		
k	-5	-4	-3	-2	2	3	4	5	6
r/s	$-11/5$	$-9/4$	$-7/3$	$-5/2$	$-3/2$	$-5/3$	$-7/4$	$-9/5$	$-11/6$
t/u	$\frac{1-5n}{11n-2}$	$\frac{1-4n}{9n-2}$	$\frac{1-3n}{7n-2}$	$\frac{1-2n}{5n-2}$	$\frac{2n+1}{-3n-2}$	$\frac{3n+1}{-5n-2}$	$\frac{4n+1}{-7n-2}$	$\frac{5n+1}{-9n-2}$	$\frac{6n+1}{-11n-2}$
$\vdots$					$\vdots$				
-6					$K9_3$				
-5				$\vdots$	$K8_3$	$\vdots$			
-4				$K9_6$	$K7_3$	$K9_{15}$			
-3			$\vdots$	$K8_6$	$K6_3$	$K8_{15}$	$\vdots$		
-2			$K9_{23}$	$K7_6$	$K5_1$	$K7_{16}$	$K9_{48}$	$\vdots$	
-1	$\vdots$	$\vdots$	$K8_{21}$	$K6_6$	X	$K5_6$	$K7_{32}$	$K9_{55}$	$\vdots$
$n = 0$	$\cdots\ K6_5$	$K5_5$	$K4_3$	$K3_1$	$K3_1$	$K4_3$	$K5_5$	$K6_5$	$K7_5\ \cdots$
1	$\vdots$	$K8_{43}$	$K6_{16}$	$K4_4$	$K5_4$	$K7_{14}$	$K9_{42}$	$\vdots$	$\vdots$
2		$\vdots$	$K8_{25}$	$K6_7$	$K6_4$	$K8_{14}$	$\vdots$		
3			$K9_{25}$	$K7_7$	$K7_4$	$K9_{14}$			
4			$\vdots$	$K8_7$	$K8_4$	$\vdots$			
5				$K9_7$	$K9_4$				
$\vdots$				$\vdots$	$\vdots$				

(b) Twisted torus knot descriptions for families with $-5 \le k \le -2$.

	k	$T(1-3k, 3-(1-3k)\cdot n, 2, -2)$
$\mathcal{F}_4$	-2	$T(7, 3-7n, 2, -2)$
$\mathcal{F}_{17}$	-3	$T(10, 3-10n, 2, -2)$
	-4	$T(13, 3-13n, 2, -2)$
	-5	$T(16, 3-16n, 2, -2)$

(c) Twisted torus knot descriptions for families with $2 \le k \le 6$.

	k	$T(3k-1, -3-(3k-1)\cdot n, 2, -2)$
$\mathcal{F}_3$	2	$T(5, -3-5n, 2, -2)$
$\mathcal{F}_{11}$	3	$T(8, -3-8n, 2, -2)$
$\mathcal{F}_{28}$	4	$T(11, -3-11n, 2, -2)$
	5	$T(14, -3-14n, 2, -2)$
	6	$T(17, -3-17n, 2, -2)$

Table A.6. Families of knots with slopes $r/s = [-3, k]$ and $t/u = [0, -3, k, n]$.

(a) In this table, $r = 1 - 3k$, $s = k$, $t = 1 + kn$, and $u = -3 + (1 - 3k)n$. Columns for $k = 0, 1$ are omitted, since these correspond to exceptional slopes. Horizontal dots indicate that several more census knots were identified for $k \leq -4$ and $k \geq 5$, but these appear in other tables, so have been omitted to save space. The 4 columns with two distinguished fillings are labelled with their family name, as assigned in Section A.1.

			$\mathcal{F}_{20}$	$\mathcal{F}_3$	$\mathcal{F}_4$	$\mathcal{F}_{26}$		
k	-4	-3	-2	-1	2	3	4	5
r/s	$-13/4$	$-10/3$	$-7/2$	$-4/1$	$-5/2$	$-8/3$	$-11/4$	$-14/5$
t/u	$\frac{1-4n}{13n-3}$	$\frac{1-3n}{10n-3}$	$\frac{1-2n}{7n-3}$	$\frac{1-n}{4n-3}$	$\frac{2n+1}{-5n-3}$	$\frac{3n+1}{-8n-3}$	$\frac{4n+1}{-11n-3}$	$\frac{5n+1}{-14n-3}$
$\vdots$				$\vdots$	$\vdots$			
-5				$K9_4$	$K9_6$			
-4				$K8_4$	$K8_6$	$\vdots$		
-3				$K7_4$	$K7_6$	$K9_{45}$		
-2			$K9_{30}$	$K6_4$	$K6_6$	$K8_{37}$	$\vdots$	
-1		$\vdots$	$K8_{27}$	$K5_4$	$K3_1$	$K6_{21}$	$K8_{55}$	$\vdots$
$n = 0$	$\cdots$ $K7_{27}$	$K6_{14}$	$K5_{14}$	$K3_1$	$K4_4$	$K5_{18}$	$K6_{17}$	$K7_{30}$ $\cdots$
1		$\vdots$ $K8_{50}$	$K6_{11}$	X	$K6_7$	$K8_{35}$	$\vdots$	$\vdots$
2			$K8_{29}$	$K5_1$	$K7_7$	$K9_{44}$		
3			$K9_{31}$	$K6_3$	$K8_7$	$\vdots$		
4			$\vdots$	$K7_3$	$K9_7$			
5				$K8_3$	$\vdots$			
6				$K9_3$				
$\vdots$				$\vdots$				

(b) Twisted torus knot descriptions for families with $-4 \leq k \leq 1$.

	k	$T(1-4k, 4-(1-4k)\cdot n, 2, -2)$
$\mathcal{F}_3$	-1	$T(5, 4-5n, 2, -2)$
$\mathcal{F}_{20}$	-2	$T(9, 4-9n, 2, -2)$
	-3	$T(13, 4-13n, 2, -2)$
	-4	$T(17, 4-17n, 2, -2)$

(c) Twisted torus knot descriptions for families with $2 \leq k \leq 5$.

	k	$T(4k-1, -4-(4k-1)\cdot n, 2, -2)$
$\mathcal{F}_4$	2	$T(7, -4-7n, 2, -2)$
$\mathcal{F}_{26}$	3	$T(11, -4-11n, 2, -2)$
	4	$T(15, -4-15n, 2, -2)$
	5	$T(19, -4-19n, 2, -2)$

TABLE A.7. Families of knots with slopes $r/s = [0, -2, k]$ and $t/u = [-2, k, n]$.

(a) In this table, $r = k$, $s = 1 - 2k$, $t = -2 + (1 - 2k)\,n$, and $u = 1 + kn$. Columns for $k = 0, 1$ are omitted, since these correspond to exceptional slopes. The 6 columns with two distinguished fillings are labelled with their family name, as assigned in Section A.1.

		$\mathcal{F}_{32}$	$\mathcal{F}_{14}$	$\mathcal{F}_{2}$	$\mathcal{F}_{5}$	$\mathcal{F}_{23}$	$\mathcal{F}_{38}$	
k	-4	-3	-2	-1	2	3	4	5
r/s	$-4/9$	$-3/7$	$-2/5$	$-1/3$	$-2/3$	$-3/5$	$-4/7$	$-5/9$
t/u	$\frac{9n-2}{1-4n}$	$\frac{7n-2}{1-3n}$	$\frac{5n-2}{1-2n}$	$\frac{3n-2}{1-n}$	$\frac{-3n-2}{2n+1}$	$\frac{-5n-2}{3n+1}$	$\frac{-7n-2}{4n+1}$	$\frac{-9n-2}{5n+1}$
⋮				⋮	⋮			
-6				$K9_{36}$	$K9_{20}$			
-5			⋮	$K8_{33}$	$K8_{19}$	⋮		
-4			$K9_{80}$	$K7_{30}$	$K7_{23}$	$K9_{75}$		
-3		⋮	$K8_{59}$	$K6_{17}$	$K6_{13}$	$K8_{56}$	⋮	
-2		$K9_{86}$	$K7_{42}$	$K5_{18}$	$K5_{7}$	$K7_{38}$	$K9_{79}$	⋮
-1	⋮	$K8_{43}$	$K6_{16}$	$K4_{4}$	X	$K5_{4}$	$K7_{14}$	$K9_{42}$
$n = 0$	X	X	X	X	X	X	X	X
1	$K8_{21}$	$K6_{6}$	X	X	$K5_{6}$	$K7_{32}$	$K9_{55}$	⋮
2	⋮	$K8_{58}$	$K6_{21}$	$K3_{1}$	$K6_{12}$	$K8_{52}$	⋮	
3		$K9_{89}$	$K7_{43}$	$K5_{14}$	$K7_{22}$	$K9_{73}$		
4		⋮	$K8_{60}$	$K6_{14}$	$K8_{18}$	⋮		
5			$K9_{81}$	$K7_{27}$	$K9_{19}$			
6			⋮	$K8_{31}$	⋮			
7				$K9_{35}$				
⋮				⋮				

(b) Twisted torus knot descriptions for families with $-4 \le k \le -1$.

	k	$T(1-3k, -3+(1-3k)\cdot n, 2, -2)$
$\mathcal{F}_2$	-1	$T(4, -3+4n, 2, -2)$
$\mathcal{F}_{14}$	-2	$T(7, -3+7n, 2, -2)$
$\mathcal{F}_{32}$	-3	$T(10, -3+10n, 2, -2)$
	-4	$T(13, -3+13n, 2, -2)$

(c) Twisted torus knot descriptions for families with $2 \le k \le 5$.

	k	$T(3k-1, 3+(3k-1)\cdot n, 2, -2)$
$\mathcal{F}_5$	2	$T(5, 3+5n, 2, -2)$
$\mathcal{F}_{23}$	3	$T(8, 3+8n, 2, -2)$
$\mathcal{F}_{38}$	4	$T(11, 3+11n, 2, -2)$
	5	$T(14, 3+14n, 2, -2)$

Table A.8. Families of knots with slopes $r/s = [0, -3, k]$ and $t/u = [-3, k, n]$.

(a) In this table, $r = k$, $s = 1 - 3k$, $t = -3 + (1 - 3k)\,n$, and $u = 1 + kn$. The column for $k = 0$ is omitted, since this corresponds to an exceptional slope. The 5 columns with distinguished fillings highlighted are labelled with their family name, as assigned in Section A.1.

		$\mathcal{F}_{34}$	$\mathcal{F}_{8}$	$\mathcal{F}_{0}$	$\mathcal{F}_{14}$	$\mathcal{F}_{39}$	
k	-3	-2	-1	1	2	3	4
r/s	$-3/10$	$-2/7$	$-1/4$	$-1/2$	$-2/5$	$-3/8$	$-4/11$
t/u	$\frac{10n-3}{1-3n}$	$\frac{7n-3}{1-2n}$	$\frac{4n-3}{1-n}$	$\frac{-2n-3}{n+1}$	$\frac{-5n-3}{2n+1}$	$\frac{-8n-3}{3n+1}$	$\frac{-11n-3}{4n+1}$
⋮				⋮			
-7				$K7_5$			
-6				$K6_5$	⋮		
-5			⋮	$K5_5$	$K9_{80}$		
-4			$K9_{66}$	$K4_3$	$K8_{59}$	⋮	
-3		⋮	$K8_{49}$	$K3_1$	$K7_{42}$	$K9_{92}$	
-2		$K9_{88}$	$K7_{37}$	X	$K6_{16}$	$K8_{63}$	⋮
-1	⋮	$K8_{50}$	$K6_{11}$	X	X	$K6_7$	$K8_{35}$
$n = 0$	X	X	X	X	X	X	X
1	$K8_{27}$	$K5_4$	X	$K3_1$	$K6_{21}$	$K8_{55}$	⋮
2	⋮	$K8_{57}$	$K5_{10}$	$K4_3$	$K7_{43}$	$K9_{91}$	
3		$K9_{90}$	$K7_{34}$	$K5_5$	$K8_{60}$	⋮	
4		⋮	$K8_{46}$	$K6_5$	$K9_{81}$		
5			$K9_{61}$	$K7_5$	⋮		
6			⋮	$K8_5$			
7				$K9_5$			
⋮				⋮			

(b) Twisted torus knot descriptions for families with $-3 \le k \le -1$.

	k	$T(1-4k, -4+(1-4k)\cdot n, 2, -2)$
$\mathcal{F}_8$	-1	$T(5, -4+5n, 2, -2)$
$\mathcal{F}_{34}$	-2	$T(9, -4+9n, 2, -2)$
	-3	$T(13, -4+13n, 2, -2)$

(c) Twisted torus knot descriptions for families with $1 \le k \le 4$.

	k	$T(4k-1, 4+(4k-1)\cdot n, 2, -2)$
$\mathcal{F}_0$	1	$T(3, 4+3n, 2, -2)$
$\mathcal{F}_{14}$	2	$T(7, 4+7n, 2, -2)$
$\mathcal{F}_{39}$	3	$T(11, 4+11n, 2, -2)$
	4	$T(15, 4+15n, 2, -2)$

TABLE A.9. Families of knots with slopes $r/s = [-1, -2, k]$ and $t/u = [0, -1, -2, k, n]$.

(a) In this table, $r = 3k - 1$, $s = 1 - 2k$, $t = -2 + (1 - 2k)\,n$, and $u = 3 + (3k - 1)\,n$. Columns for $k = 0, 1$ are omitted, since these correspond to exceptional slopes. Horizontal dots indicate that several more census knots were identified for $k < -4$ and $k > 5$, but these appear in other tables, so have been omitted to save space. The 4 columns with two distinguished fillings are labelled with their family name, as assigned in Section A.1.

			$\mathcal{F}_{35}$	$\mathcal{F}_{10}$	$\mathcal{F}_{11}$	$\mathcal{F}_{36}$		
k	-4	-3	-2	-1	2	3	4	5
r/s	$-13/9$	$-10/7$	$-7/5$	$-4/3$	$-5/3$	$-8/5$	$-11/7$	$-14/9$
t/u	$\frac{9n-2}{3-13n}$	$\frac{7n-2}{3-10n}$	$\frac{5n-2}{3-7n}$	$\frac{3n-2}{3-4n}$	$\frac{-3n-2}{5n+3}$	$\frac{-5n-2}{8n+3}$	$\frac{-7n-2}{11n+3}$	$\frac{-9n-2}{14n+3}$
$\vdots$					$\vdots$			
-4				$\vdots$	$K9_{14}$			
-3				$K9_{13}$	$K8_{14}$	$\vdots$		
-2			$\vdots$	$K8_{13}$	$K7_{14}$	$K9_{70}$	$\vdots$	
-1		$\vdots$	$\vdots$	$K9_{62}$	$K7_{13}$	$K4_3$	$K7_{38}$	$K9_{82}$	$\vdots$	
$n = 0$	$\cdots\ K8_{19}$		$K7_{23}$	$K6_{13}$	$K5_7$	$K5_6$	$K6_{12}$	$K7_{22}$	$K8_{18}$	$\cdots$
1		$\vdots$	$K9_{76}$	$K7_{33}$	X	$K7_{16}$	$K9_{65}$	$\vdots$	$\vdots$	
2			$\vdots$	$K9_{64}$	$K7_{12}$	$K8_{15}$	$\vdots$		
3				$\vdots$	$K8_{12}$	$K9_{15}$			
4					$K9_{12}$	$\vdots$			
$\vdots$					$\vdots$				

(b) Twisted torus knot descriptions for families with $-4 \le k \le -1$.

	k	$T(2-5k, -5+(2-5k)\cdot n, 2, -2)$
$\mathcal{F}_{10}$	-1	$T(7, -5+7n, 2, -2)$
$\mathcal{F}_{35}$	-2	$T(12, -5+12n, 2, -2)$
	-3	$T(17, -5+17n, 2, -2)$
	-4	$T(22, -5+22n, 2, -2)$

(c) Twisted torus knot descriptions for families with $2 \le k \le 5$.

	k	$T(5k-2, 5+(5k-2)\cdot n, 2, -2)$
$\mathcal{F}_{11}$	2	$T(8, 5+8n, 2, -2)$
$\mathcal{F}_{36}$	3	$T(13, 5+13n, 2, -2)$
	4	$T(18, 5+18n, 2, -2)$
	5	$T(23, 5+23n, 2, -2)$

Table A.10. Families of knots with slopes $r/s = [0, -1, -2, k]$ and $t/u = [-1, -2, k, n]$.

(a) In this table, $r = 1 - 2k$, $s = 3k - 1$, $t = 3 + (3k - 1)\,n$, and $u = -2 + (1 - 2k)\,n$. The column for $k = 0$ is omitted, since this corresponds to an exceptional slope. Horizontal dots indicate that several more census knots were identified for $k < -4$ and $k > 5$, but these already appear in other tables, so have been omitted to save space. The 4 columns with two distinguished fillings are labelled with their family name, as assigned in Section A.1. We pay little attention to $\mathcal{F}_0$, since this is the 4th time we have seen it.

			$\mathcal{F}_{40}$	$\mathcal{F}_{15}$	$\mathcal{F}_0$	$\mathcal{F}_{23}$	$\mathcal{F}_{41}$		
k	-4	-3	-2	-1	1	2	3	4	5
r/s	$-9/13$	$-7/10$	$-5/7$	$-3/4$	$-1/2$	$-3/5$	$-5/8$	$-7/11$	$-9/14$
t/u	$\frac{3-13n}{9n-2}$	$\frac{3-10n}{7n-2}$	$\frac{3-7n}{5n-2}$	$\frac{3-4n}{3n-2}$	$\frac{2n+3}{-n-2}$	$\frac{5n+3}{-3n-2}$	$\frac{8n+3}{-5n-2}$	$\frac{11n+3}{-7n-2}$	$\frac{14n+3}{-9n-2}$
$\vdots$					$\vdots$				
-5					$K4_3$	$\vdots$			
-4				$\vdots$	$K3_1$	$K9_{73}$			
-3				$K9_{54}$	X	$K8_{52}$	$\vdots$		
-2			$\vdots$	$K8_{41}$	X	$K7_{32}$	$K9_{87}$	$\vdots$	
-1		$\vdots$	$\vdots$	$K9_{76}$	$K7_{33}$	X	X	$K7_{16}$	$K9_{65}$	$\vdots$	
$n = 0$	$\cdots$	$K8_3$	$K7_3$	$K6_3$	$K5_1$	$K3_1$	$K5_4$	$K6_4$	$K7_4$	$K8_4$	$\cdots$
1		$\vdots$	$K9_{62}$	$K7_{13}$	X	$K4_3$	$K7_{38}$	$K9_{82}$	$\vdots$	$\vdots$	
2			$\vdots$	$K9_{84}$	$K7_{21}$	$K5_5$	$K8_{56}$	$\vdots$		
3				$\vdots$	$K8_{38}$	$K6_5$	$K9_{75}$			
4					$K9_{52}$	$K7_5$	$\vdots$			
5					$\vdots$	$K8_5$				
6						$K9_5$				
$\vdots$						$\vdots$				

(b) Twisted torus knot descriptions for families with $-4 \le k \le -1$.

	k	$T(2-5k, 5-(2-5k)\cdot n, 2, -2)$
$\mathcal{F}_{15}$	-1	$T(7, 5-7n, 2, -2)$
$\mathcal{F}_{40}$	-2	$T(12, 5-12n, 2, -2)$
	-3	$T(17, 5-17n, 2, -2)$
	-4	$T(22, 5-22n, 2, -2)$

(c) Twisted torus knot descriptions for families with $1 \le k \le 5$.

	k	$T(5k-2, -5-(5k-2)\cdot n, 2, -2)$
$\mathcal{F}_0$	1	$T(3, -5-3n, 2, -2)$
$\mathcal{F}_{23}$	2	$T(8, -5-8n, 2, -2)$
$\mathcal{F}_{41}$	3	$T(13, -5-13n, 2, -2)$
	4	$T(18, -5-18n, 2, -2)$
	5	$T(23, -5-23n, 2, -2)$

TABLE A.11. Families of knots with slopes $r/s = [-2, k]$ and $t/u = [-2, -k, 1, 2, n]$.

(a) In this table, $r = 1 - 2k$, $s = k$, $t = (2k-1) + (6k-1)\,n$, and $u = (1-k) - (3k-2)\,n$. Columns for $k = -1, 0, 1$ are omitted, since these correspond to exceptional slopes. The 5 columns with two distinguished fillings are labelled with their family name, as assigned in Section A.1. Those with an asterisk have not been seen in any earlier tables.

			$\mathcal{F}^*_{19}$	$\mathcal{F}_4$	$\mathcal{F}_3$	$\mathcal{F}^*_{12}$	$\mathcal{F}^*_{29}$		
k	-5	-4	-3	-2	2	3	4	5	6
r/s	$-11/5$	$-9/4$	$-7/3$	$-5/2$	$-3/2$	$-5/3$	$-7/4$	$-9/5$	$-11/6$
t/u	$\frac{-31n-11}{17n+6}$	$\frac{-25n-9}{14n+5}$	$\frac{-19n-7}{11n+4}$	$\frac{-13n-5}{8n+3}$	$\frac{11n+3}{-4n-1}$	$\frac{17n+5}{-7n-2}$	$\frac{23n+7}{-10n-3}$	$\frac{29n+9}{-13n-4}$	$\frac{35n+11}{-16n-5}$
$\vdots$					$\vdots$				
-6				$\vdots$	$K9_4$				
-5				$K9_7$	$K8_4$	$\vdots$			
-4			$\vdots$	$K8_7$	$K7_4$	$K9_{17}$			
-3			$K9_{27}$	$K7_7$	$K6_4$	$K8_{17}$	$\vdots$		
-2		$\vdots$	$K8_{26}$	$K6_7$	$K5_4$	$K7_{17}$	$K9_{49}$	$\vdots$	
-1	$\vdots$	$K8_{42}$	$K6_{15}$	$K4_4$	$K3_1$	$K5_{16}$	$K7_{35}$	$K9_{58}$	$\vdots$
$n = 0$	$K9_{51}$	$K7_{28}$	$K5_{15}$	$K3_1$	X	$K3_1$	$K5_{15}$	$K7_{28}$	$K9_{51}$
1	$\vdots$	$\vdots$	$K8_{23}$	$K6_6$	$K5_1$	$K7_{15}$	$K9_{47}$	$\vdots$	$\vdots$
2			$K9_{24}$	$K7_6$	$K6_3$	$K8_{16}$	$\vdots$		
3			$\vdots$	$K8_6$	$K7_3$	$K9_{16}$			
4				$K9_6$	$K8_3$	$\vdots$			
5				$\vdots$	$K9_3$				
$\vdots$					$\vdots$				

(b) Twisted torus knot descriptions for families with $-5 \le k \le -2$. Here $a = |3k-1|$.

	k	$T\big(a, k - a\cdot n, 1-k, -2\big)$
$\mathcal{F}_4$	-2	$T(7, -2-7n, 3, -2)$
$\mathcal{F}^*_{19}$	-3	$T(10, -3-10n, 4, -2)$
	-4	$T(13, -4-13n, 5, -2)$
	-5	$T(16, -5-16n, 6, -2)$

(c) Twisted torus knot descriptions for families with $2 \le k \le 6$. Again, $a = |3k-1|$.

	k	$T\big(a, k + a\cdot n, k, -2\big)$
$\mathcal{F}_3$	2	$T(5, 2+5n, 2, -2)$
$\mathcal{F}^*_{12}$	3	$T(8, 3+8n, 3, -2)$
$\mathcal{F}^*_{29}$	4	$T(11, 4+11n, 4, -2)$
	5	$T(14, 5+14n, 5, -2)$
	6	$T(17, 6+17n, 6, -2)$

Table A.12. Families of knots with slopes $r/s = [-3, k]$ and $t/u = [-3, -k, 1, 1, n]$.

(a) In this table, $r = 1 - 3k$, $s = k$, $t = (3k - 2) + (6k - 1)\,n$, and $u = (1 - k) - (2k - 1)\,n$. Columns for $k = 0, 1$ are omitted, since these correspond to exceptional slopes. The 5 columns with two distinguished fillings are labelled with their family name, as assigned in Section A.1. Those with an asterisk have not been seen in any earlier tables.

		$\mathcal{F}^*_{37}$	$\mathcal{F}^*_{16}$	$\mathcal{F}_3$	$\mathcal{F}_4$	$\mathcal{F}^*_{25}$		
k	-4	-3	-2	-1	2	3	4	5
r/s	$-13/4$	$-10/3$	$-7/2$	$-4/1$	$-5/2$	$-8/3$	$-11/4$	$-14/5$
t/u	$\frac{-25n-14}{9n+5}$	$\frac{-19n-11}{7n+4}$	$\frac{-13n-8}{5n+3}$	$\frac{-7n-5}{3n+2}$	$\frac{11n+4}{-3n-1}$	$\frac{17n+7}{-5n-2}$	$\frac{23n+10}{-7n-3}$	$\frac{29n+13}{-9n-4}$
$\vdots$				$\vdots$				
-6				$K9_3$	$\vdots$			
-5			$\vdots$	$K8_3$	$K9_7$			
-4			$K9_{32}$	$K7_3$	$K8_7$	$\vdots$		
-3		$\vdots$	$K8_{30}$	$K6_3$	$K7_7$	$K9_{43}$		
-2	$\vdots$	$K9_{67}$	$K7_{29}$	$K5_1$	$K6_7$	$K8_{36}$	$\vdots$	
-1	$K8_{45}$	$K6_{18}$	$K4_4$	X	$K4_4$	$K6_{18}$	$K8_{45}$	$\vdots$
$n = 0$	$K9_{69}$	$K7_{36}$	$K5_{17}$	$K3_1$	$K3_1$	$K5_{17}$	$K7_{36}$	$K9_{69}$
1	$\vdots$	$K9_{68}$	$K7_{31}$	$K5_4$	$K6_6$	$K8_{34}$	$\vdots$	$\vdots$
2		$\vdots$	$K8_{32}$	$K6_4$	$K7_6$	$K9_{41}$		
3			$K9_{33}$	$K7_4$	$K8_6$	$\vdots$		
4			$\vdots$	$K8_4$	$K9_6$			
5				$K9_4$	$\vdots$			
$\vdots$				$\vdots$				

(b) Twisted torus knot descriptions for families with $-4 \le k \le -1$. Here $a = |4k - 1|$.

	k	$T\big(a, 1 - 2k + a \cdot n, 1 - 2k, 1\big)$
$\mathcal{F}_3$	-1	$T(5, 3 + 5n, 3, 1)$
$\mathcal{F}^*_{16}$	-2	$T(9, 5 + 9n, 5, 1)$
$\mathcal{F}^*_{37}$	-3	$T(13, 7 + 13n, 7, 1)$
	-4	$T(17, 9 + 17n, 9, 1)$

(c) Twisted torus knot descriptions for families with $2 \le k \le 5$. Again, $a = |4k - 1|$.

	k	$T\big(a, 1 - 2k - a \cdot n, 2k - 1, 1\big)$
$\mathcal{F}_4$	2	$T(7, -3 - 7n, 3, 1)$
$\mathcal{F}^*_{25}$	3	$T(11, -5 - 11n, 5, 1)$
	4	$T(15, -7 - 15n, 7, 1)$
	5	$T(19, -9 - 19n, 9, 1)$

Appendix B. Minimal triangulated fillings

The tables in this appendix show the number of tetrahedra required to realise triangulations of the census knots recognised in Section 2.3, using the triangulations described in Section 2.4.

Each table shows a product of two portions of the Farey sequence in different intervals, with certain slopes highlighted in black. These correspond to the boundary slopes in each of cusp $\mathfrak{c}_1$ and cusp $\mathfrak{c}_2$. In the top left corner of each table we see the name of the parent triangulation, the names of each set of boundary slopes, and the number of tetrahedra in its core.

Rows and columns are labelled by slopes, as well as an integer that represents the number of tetrahedra required to realise a Dehn filling of that slope using the layered solid torus with boundary slopes as indicated. The minimality of a given knot KT_v in the table can be verified by summing the two integers found at the top and left of its column and row, along with the integer in the top-left corner of the table. This should match the integer T in KT_v.

In these tables, rows and columns shaded grey correspond to either an exceptional slope or a boundary slope. Integer slopes and the knots they realise are shaded to indicate that these do not achieve minimality, until the dedicated tables at the end.

Note that not all of the census knots we found actually appear in these tables, since we have omitted sequences of two or more knots that increase steadily by one tetrahedron at a time. This is always indicated by ellipses when relevant.

TABLE B.1. Summary of tables in Appendix B.

Type A families	**Tri.**	**Primary slopes**
Table B.2	$\mathbf{T}_1$	$-7/4 \leq r/s \leq -5/4$
Table B.3	$\mathbf{T}_1$	$-4/5 \leq r/s \leq -1/2$
Table B.4	$\mathbf{T}'_2$	$-1/2 \leq r/s \leq -1/5$
Table B.5	$\mathbf{T}_2$	$-4/1 \leq r/s \leq -7/3$
Table B.6	$\mathbf{T}_3$	$1/3 \leq r/s \leq 2/1$
Type B families		
Table B.7	$\mathbf{T}'_2$	$-3/2 \leq r/s \leq -11/6$
Table B.8	$\mathbf{T}_2$	$-11/5 \leq r/s \leq -5/2$
Type C families		
Table B.9	$\mathbf{T}'_2$	$-5/2 \leq r/s \leq -4/1$
Positive integer families		
Table B.10	$\hat{\mathbf{T}}_4$	$1/1 \leq r/s \leq 5/1$
Negative integer families		
Table B.11	$\hat{\mathbf{T}}_5$	$-7/1 \leq r/s \leq -4/1$

Table B.2. **Type A.** This table shows that minimal triangulations are achieved using triangulation $\mathbf{T}_1$ for all knots in the Type A families $\mathcal{F}_3$, $\mathcal{F}_{10}$, $\mathcal{F}_{11}$, $\mathcal{F}_{24}$, $\mathcal{F}_{28}$, $\mathcal{F}_{35}$, $\mathcal{F}_{36}$.

				$\mathcal{F}_{28}$	$\mathcal{F}_{11}$	$\mathcal{F}_{36}$	$\mathcal{F}_3$	$\mathcal{F}_{35}$	$\mathcal{F}_{10}$	$\mathcal{F}_{24}$	
$\mathbf{T}_1$	$\mathcal{P}_1$	$1/0$	$-2/1$	$-7/4$	$-5/3$	$-8/5$	$-3/2$	$-7/5$	$-4/3$	$-5/4$	$-1/1$
$\mathcal{P}_2$	2	$*$	$*$	2	1	2	0	2	1	2	$*$
$-2/1$	$*$										
$-1/1$	$*$										
$-5/6$	5									$K9_{34}$	
$-4/5$	4								$K7_{12}$	★	
$-7/9$	5								$K8_{12}$	$K9_{39}$	
$-10/13$	6								$K9_{12}$		
$-3/4$	3						$K5_1$	$K7_{33}$	★	$K7_{21}$	
$-11/15$	6								$K9_{13}$		
$-8/11$	5							$K9_{64}$	$K8_{13}$		
$-5/7$	4						$K6_3$	★	$K7_{13}$		
$-7/10$	5						$K7_3$	$K9_{62}$			
⋮	⋮						⋮				
$-2/3$	2				$K5_6$	$K6_{12}$	★	$K6_{13}$	$K5_7$		
⋮	⋮						⋮				
$-7/11$	5					$K9_{65}$	$K7_4$				
$-5/8$	4				$K7_{16}$	★	$K6_4$				
$-8/13$	5				$K8_{15}$	$K9_{70}$					
$-11/18$	6				$K9_{15}$						
$-3/5$	3			$K7_{32}$	★	$K7_{38}$	$K5_4$				
$-10/17$	6				$K9_{14}$						
$-7/12$	5			$K9_{48}$	$K8_{14}$						
$-4/7$	4			★	$K7_{14}$						
$-5/9$	5			$K9_{42}$							
$-1/2$	1			$K5_5$	$K4_3$		$K3_1$				
$0/1$	0										
$1/0$	$*$										

TABLE B.3. **Type A.** This table shows that minimal triangulations are achieved using triangulation $\mathbf{T}_1$ for all knots in the Type A families $\mathcal{F}_0$, $\mathcal{F}_5$, $\mathcal{F}_{15}$, $\mathcal{F}_{23}$, $\mathcal{F}_{30}$, $\mathcal{F}_{38}$, $\mathcal{F}_{40}$, $\mathcal{F}_{41}$.

					$\mathcal{F}_{30}$	$\mathcal{F}_{15}$	$\mathcal{F}_{40}$	$\mathcal{F}_5$	$\mathcal{F}_{41}$	$\mathcal{F}_{23}$	$\mathcal{F}_{38}$	$\mathcal{F}_0$	
$\mathbf{T}_1$	$\mathcal{P}_1$	$1/0$	$-2/1$	$-1/1$	$-4/5$	$-3/4$	$-5/7$	$-2/3$	$-5/8$	$-3/5$	$-4/7$	$-1/2$	$0/1$
$\mathcal{P}_2$	2	$*$	$*$	$*$	4	3	4	2	4	3	4	1	0
$1/0$	$*$												
$-2/1$	$*$											★	
⋮	⋮											⋮	
$-9/5$	3										$K9_{55}$	$K6_5$	
$-7/4$	2									$K7_{32}$	★	$K5_5$	
$-12/7$	3									$K8_{52}$	$K9_{79}$		
$-17/10$	4									$K9_{73}$			
$-5/3$	1							$K5_6$	$K7_{16}$	★	$K7_{14}$	$K4_3$	
$-18/11$	4									$K9_{75}$			
$-13/8$	3								$K9_{87}$	$K8_{56}$			
$-8/5$	2							$K6_{12}$	★	$K7_{38}$			
$-11/7$	3							$K7_{22}$	$K9_{82}$				
⋮	⋮							⋮					
$-3/2$	0					$K5_1$	$K6_3$	★	$K6_4$	$K5_4$		$K3_1$	
⋮	⋮							⋮					
$-10/7$	3						$K9_{76}$	$K7_{23}$					
$-7/5$	2					$K7_{33}$	★	$K6_{13}$					
$-11/8$	3					$K8_{41}$	$K9_{84}$						
$-15/11$	4					$K9_{54}$							
$-4/3$	1				$K7_{12}$	★	$K7_{13}$	$K5_7$					
$-13/10$	4					$K9_{52}$							
$-9/7$	3				$K9_{56}$	$K8_{38}$							
$-5/4$	2				★	$K7_{21}$							
$-6/5$	3				$K9_{40}$								
$-1/1$	$*$												

Table B.4. **Type A.** This table shows that minimal triangulations are achieved using triangulation $\mathbf{T}_2'$ for all knots in the Type A families $\mathcal{F}_0$, $\mathcal{F}_2$, $\mathcal{F}_8$, $\mathcal{F}_{14}$, $\mathcal{F}_{21}$, $\mathcal{F}_{32}$, $\mathcal{F}_{34}$, $\mathcal{F}_{39}$, except for the highlighted knots with integer secondary slopes.

					$\mathcal{F}_0$	$\mathcal{F}_{32}$	$\mathcal{F}_{14}$	$\mathcal{F}_{39}$	$\mathcal{F}_2$	$\mathcal{F}_{34}$	$\mathcal{F}_8$	$\mathcal{F}_{21}$	
$\mathbf{T}_2'$	$\mathcal{P}_1$	$1/0$	$-2/1$	$-1/1$	$-1/2$	$-3/7$	$-2/5$	$-3/8$	$-1/3$	$-2/7$	$-1/4$	$-1/5$	$0/1$
$\mathcal{Q}_2$	2	$*$	$*$	$*$	1	4	3	4	2	4	3	4	0
$1/0$	$*$												
$-6/1$	2											$K7_{20}$	
$-11/2$	3											$K9_{60}$	
$-5/1$	1										$K5_{10}$	★	
$-14/3$	3											$K9_{71}$	
$-9/2$	2										$K7_{34}$	$K8_{40}$	
⋮	⋮										⋮		
$-4/1$	0								$K3_1$	$K5_4$	★	$K5_1$	
⋮	⋮										⋮		
$-11/3$	2									$K8_{57}$	$K7_{37}$		
$-18/5$	3									$K9_{90}$			
$-7/2$	1								$K5_{14}$	★	$K6_{11}$		
$-17/5$	3									$K9_{88}$			
$-10/3$	2								$K6_{14}$	$K8_{50}$			
⋮	⋮								⋮				
$-3/1$	$*$								★				
⋮	⋮								⋮				
$-11/4$	2							$K8_{55}$	$K6_{17}$				
$-19/7$	3							$K9_{91}$					
$-8/3$	1						$K6_{21}$	★	$K5_{18}$				
$-21/8$	3							$K9_{92}$					
$-13/5$	2						$K7_{43}$	$K8_{63}$					
⋮	⋮						⋮						
$-5/2$	0				$K3_1$	$K6_6$	★	$K6_7$	$K4_4$				
⋮	⋮						⋮						
$-12/5$	2					$K8_{58}$	$K7_{42}$						
$-19/8$	3					$K9_{89}$							
$-7/3$	1				$K4_3$	★	$K6_{16}$						
$-16/7$	3					$K9_{86}$							
$-9/4$	2				$K5_5$	$K8_{43}$							
⋮	⋮				⋮								
$-2/1$	$*$				★								

TABLE B.5. **Type A.** This table shows that minimal triangulations are achieved using triangulation $\mathbf{T}_2$ for all knots in the Type A families $\mathcal{F}_4$, $\mathcal{F}_{17}$, $\mathcal{F}_{20}$, $\mathcal{F}_{26}$.

			$\mathcal{F}_3$	$\mathcal{F}_{20}$		$\mathcal{F}_{26}$	$\mathcal{F}_4$	$\mathcal{F}_{17}$	
$\mathbf{T}_2$	$\mathcal{Q}_1$	$1/0$	$-4/1$	$-7/2$	$-3/1$	$-8/3$	$-5/2$	$-7/3$	$-2/1$
$\mathcal{P}_2$	2	$*$	0	1	$*$	1	0	1	$*$
$-2/1$	$*$								
$-1/1$	$*$								
$-1/2$	1						$K3_1$	$K4_3$	
$-4/9$	5							$K8_{21}$	
$-7/16$	6							$K9_{23}$	
$-3/7$	4						$K6_6$	★	
$-8/19$	6							$K9_{25}$	
$-5/12$	5						$K7_6$	$K8_{25}$	
⋮	⋮						⋮		
$-2/5$	3					$K6_{21}$	★	$K6_{16}$	
⋮	⋮						⋮		
$-5/13$	5					$K8_{37}$	$K7_7$		
$-8/21$	6					$K9_{45}$			
$-3/8$	4					★	$K6_7$		
$-7/19$	6					$K9_{44}$			
$-4/11$	5					$K8_{35}$			
$-1/3$	2		$K3_1$	$K5_{14}$		$K5_{18}$	$K4_4$		
$-3/10$	5			$K8_{27}$					
$-5/17$	6			$K9_{30}$					
$-2/7$	4		$K5_4$	★					
$-5/18$	6			$K9_{31}$					
$-3/11$	5		$K6_4$	$K8_{29}$					
$-1/4$	3		★	$K6_{11}$					
$0/1$	0								
$1/0$	$*$								

Table B.6. **Type A.** This table shows that the Type A knots with primary slopes $r/s \in \{1/3, 1/2, 2/3, 3/2\}$, except for those with secondary slopes an integer, have a minimal triangulation realised by $\mathbf{T}_3$.

			$\mathcal{F}_{22}$	$\mathcal{F}_7$	$\mathcal{F}_{33}$	$\mathcal{F}_1$	$\mathcal{F}_{31}$	$\mathcal{F}_6$	
$\mathbf{T}_3$	$\mathcal{R}_1$	$0/1$	$1/3$	$1/2$	$2/3$	$1/1$	$3/2$	$2/1$	$1/0$
$\mathcal{R}_2$	5	$*$	1	0	1	$*$	1	0	$*$
$0/1$	$*$								
$1/3$	1							$K5_9$	★
$2/5$	2							$K6_8$	$K7_{26}$
⋮	⋮							⋮	
$1/2$	0					$K3_2$	$K6_{10}$	★	$K5_8$
⋮	⋮							⋮	
$3/5$	2						$K8_{47}$	$K6_9$	
$5/8$	3						$K9_{63}$		
$2/3$	1					$K4_2$	★	$K5_{13}$	
$5/7$	3						$K9_{59}$		
$3/4$	2					$K5_3$	$K8_{44}$		
⋮	⋮					⋮			
$1/1$	$*$			$K3_2$	$K4_2$	★	$K4_1$	$K2_1$	
⋮	⋮					⋮			
$4/3$	2				$K8_{48}$	$K5_2$			
$7/5$	3				$K9_{72}$				
$3/2$	1			$K6_{10}$	★	$K4_1$			
$8/5$	3				$K9_{72}$				
$5/3$	2			$K7_{24}$	$K8_{51}$				
⋮	⋮			⋮					
$2/1$	0		$K5_9$	★	$K5_{13}$	$K2_1$			
⋮	⋮			⋮					
$5/2$	2		$K8_{39}$	$K7_{18}$					
$8/3$	3		$K9_{57}$						
$3/1$	1		★	$K5_8$					
$7/2$	3		$K9_{53}$						
$4/1$	2		$K7_{25}$						
$1/0$	$*$								

TABLE B.7. **Type B.** This table shows that the knots of Type B with $2 \leq k \leq 6$ achieve minimal triangulations using $\mathbf{T}_2'$.

			$\mathcal{F}_3$	$\mathcal{F}_{12}^*$	$\mathcal{F}_{29}^*$				
$\mathbf{T}_2'$	$\mathcal{P}_1$	$-1/1$	$-3/2$	$-5/3$	$-7/4$	$-9/5$	$-11/6$	$-2/1$	$1/0$
$\mathcal{Q}_2$	2	$*$	0	1	2	3	4	$*$	$*$
$-2/1$	$*$								
$-11/5$	3						$K9_{51}$		
$-20/9$	4					$K9_{58}$			
$-29/13$	5					★			
$-9/4$	2					$K7_{28}$			
$-16/7$	3				$K7_{35}$				
$-39/17$	5				$K9_{49}$				
$-23/10$	4				★				
$-30/13$	5				$K9_{47}$				
$-7/3$	1				$K5_{15}$				
$-12/5$	2			$K5_{16}$					
$-29/12$	4			$K7_{17}$					
⋮	⋮			⋮					
$-17/7$	3			★					
⋮	⋮			⋮					
$-22/9$	4			$K7_{15}$					
$-5/2$	0			$K3_1$					
$-8/3$	2		$K3_1$						
$-19/7$	4		$K5_4$						
⋮	⋮		⋮						
$-11/4$	3		★						
⋮	⋮		⋮						
$-14/5$	4		$K5_1$						
$-3/1$	$*$								
$1/0$	$*$								

Table B.8. **Type B.** This table shows that the knots of Type B with $-5 \leq k \leq -2$ achieve minimal triangulations using $\mathbf{T}_2$.

					$\mathcal{F}^*_{19}$	$\mathcal{F}_4$		
$\mathbf{T}_2$	$\mathcal{Q}_1$	$-2/1$	$-11/5$	$-9/4$	$-7/3$	$-5/2$	$-3/1$	$1/0$
$\mathcal{P}_2$	2	$*$	3	2	1	0	$*$	$*$
$-1/1$	$*$							
$-3/2$	0							
$-8/5$	2					$K4_4$		
$-21/13$	4					$K6_7$		
$\vdots$	$\vdots$					$\vdots$		
$-13/8$	3					★		
$\vdots$	$\vdots$					$\vdots$		
$-18/11$	4					$K6_6$		
$-5/3$	1					$K3_1$		
$-12/7$	3				$K6_{15}$			
$-31/18$	5				$K8_{26}$			
$-50/29$	6				$K9_{27}$			
$-19/11$	4				★			
$-45/26$	6				$K9_{24}$			
$-26/15$	5				$K8_{23}$			
$-7/4$	2				$K5_{15}$			
$-16/9$	4			$K8_{42}$				
$-25/14$	5			★				
$-9/5$	3			$K7_{28}$				
$-20/11$	5							
$-31/17$	6		★					
$-11/6$	4		$K9_{51}$					
$-2/1$	$*$							
$1/0$	$*$							

TABLE B.9. **Type C.** This table shows that all Type C knots achieve minimal triangulations using $\mathbf{T}_2'$, except for those in $\mathcal{F}_3$ and one member of $\mathcal{F}_4$, which have integer filling slopes.

				$\mathcal{F}_4$	$\mathcal{F}^*_{25}$					$\mathcal{F}^*_{37}$	$\mathcal{F}^*_{16}$	$\mathcal{F}_3$	
$\mathbf{T}_2'$	$\mathcal{P}_1$	$-1/1$	$-2/1$	$-5/2$	$-8/3$	$-11/4$	$-14/5$	$-3/1$	$-13/4$	$-10/3$	$-7/2$	$-4/1$	$1/0$
$\mathcal{Q}_2$	2	$*$	$*$	1	2	3	4	0	4	3	2	1	$*$
$-2/1$	$*$												
$\vdots$	$\vdots$											$\vdots$	
$-5/2$	0										$K4_4$	$K3_1$	
$-18/7$	3										$K7_{29}$		
$\vdots$	$\vdots$										$\vdots$		
$-13/5$	2										$\bigstar$		
$\vdots$	$\vdots$										$\vdots$		
$-21/8$	3										$K7_{31}$		
$-8/3$	1									$K6_{18}$	$K5_{17}$		
$-27/10$	4									$K9_{67}$			
$-19/7$	3									$\bigstar$			
$-30/11$	4									$K9_{68}$			
$-11/4$	2								$K8_{45}$	$K7_{36}$			
$-25/9$	4								$\bigstar$				
$-14/5$	3								$K9_{69}$				
$-3/1$	$*$												
$-16/5$	4												
$-29/9$	5						$\bigstar$						
$-13/4$	3					$K8_{45}$	$K9_{69}$						
$-23/7$	4					$\bigstar$							
$-10/3$	2				$K6_{18}$	$K7_{36}$							
$-27/8$	4				$K8_{36}$								
$-44/13$	5				$K9_{43}$								
$-17/5$	3				$\bigstar$								
$-41/12$	5				$K9_{41}$								
$-24/7$	4				$K8_{34}$								
$-7/2$	1			$K4_4$	$K5_{17}$								
$-18/5$	3			$K6_7$									
$\vdots$	$\vdots$			$\vdots$									
$-11/3$	2			$\bigstar$									
$\vdots$	$\vdots$			$\vdots$									
$-15/4$	3			$K6_6$									
$-4/1$	0			$K3_1$									
$1/0$	$*$												

Table B.10. **Integer slopes.** This table shows that all census knots, apart from $K2_1$, with primary slopes an integer $1 \leq r/s \leq 5$ have minimal triangulations realised by $\hat{\mathbf{T}}_4$ (recall Figures 2.17 and 2.18). Integer fillings in $\mathfrak{c}_1$ are achieved using a layered chain, while fillings along secondary slopes in $\mathfrak{c}_2$ are achieved using a layered solid torus.

			$\mathcal{F}_1$	$\mathcal{F}_6$	$\mathcal{F}_{13}$	$\mathcal{F}_{27}$		
$\hat{\mathbf{T}}_4$	$\hat{\mathcal{V}}_1$	$0/1$	$1/1$	$2/1$	$3/1$	$4/1$	$5/1$	$1/0$
$\mathcal{R}_2$	2	0	1	2	3	4	5	$*$
$0/1$	$*$							
$1/5$	3					$K9_{37}$	★	
$1/4$	2				$K7_{19}$	★	$K9_{46}$	
$2/7$	3				$K8_{24}$	$K9_{50}$		
$3/10$	4				$K9_{28}$			
$1/3$	1			$K5_9$	★	$K7_{25}$		
$4/11$	4				$K9_{29}$			
$3/8$	3				$K8_{28}$			
$2/5$	2			$K6_8$	$K7_{26}$			
⋮	⋮			⋮				
$1/2$	0		$K3_2$	★	$K5_8$			
⋮	⋮			⋮				
$3/5$	2			$K6_9$				
$2/3$	1		$K4_2$	$K5_{13}$				
$3/4$	2		$K5_3$					
⋮	⋮		⋮					
$1/1$	$*$		★	$K2_1$				
$1/0$	$*$							

TABLE B.11. **Integer slopes.** This table shows that all census knots with primary slopes $-7 \leq {}^{r}/_{s} \leq -4$ have minimal triangulations realised by $\hat{\mathbf{T}}_5$ (recall Figures 2.19 and 2.20). Integer fillings in $\mathfrak{c}_1$ are achieved using a layered chain, while fillings along secondary slopes in $\mathfrak{c}_2$ are achieved using a layered solid torus.

				$\mathcal{F}_{18}$	$\mathcal{F}_9$	$\mathcal{F}_3$	
$\hat{\mathbf{T}}_5$	$\hat{\mathcal{U}}_1$	$1/0$	$-7/1$	$-6/1$	$-5/1$	$-4/1$	$-3/1$
$\mathcal{R}'_2$	2	$*$	3	2	1	0	1
$1/0$	$*$						
$-1/1$	$*$						
$-1/2$	0						
$-1/3$	1					$K3_1$	
$-2/7$	3					$K5_4$	
$-3/11$	4					$K6_4$	
$\vdots$	$\vdots$					$\vdots$	
$-1/4$	2				$K5_{10}$	★	
$\vdots$	$\vdots$					$\vdots$	
$-2/9$	4				$K7_9$	$K6_3$	
$-3/14$	5				$K8_{11}$		
$-4/19$	6				$K9_{11}$		
$-1/5$	3			$K7_{20}$	★	$K5_1$	
$-3/16$	6				$K9_{10}$		
$-2/11$	5			$K9_{26}$	$K8_8$		
$-1/6$	4		$K9_{38}$	★	$K7_8$		
$-1/7$	5			$K9_{18}$			
$0/1$	$*$						

Appendix C. Gammas in L and M

This appendix contains substitutions for the A-polynomial calculations in Chapter 4.

In order to express equations (4.10) and (4.12) entirely in terms of L and M we need the variables $\gamma_{1/0}, \gamma_{1/1}, \gamma_{0/1}, \gamma_{-1/1}$ and $\gamma_{1/2}$ in terms of L and M. These are summarised below. With these substitutions, equations (4.10) and (4.12) become formulas for rational functions that contain the geometric factor of the A-polynomial for the twisted torus knots $T(5, 1-5m, 2, 2)$.

$$\gamma_{1/0} = M^{-1}(L-M)^{-1}(L+M)^{-1}(L-M^2)(L+M^2)$$

$$\begin{aligned}\gamma_{1/1} = &-M^{-4}(L-M)^{-6}(L+M)^{-6}\left(L^6M + L^5M^4 - 2L^5M^2 + L^5\right.\\
&-L^4M^5 - 2L^4M^3 + 2L^2M^7 + L^2M^5 - LM^{10} + 2LM^8 - LM^6 - M^9\left.\right)\\
&\left(L^6M - L^5M^4 + 2L^5M^2 - L^5 - L^4M^5 - 2L^4M^3 + 2L^2M^7 + L^2M^5\right.\\
&\left.+LM^{10} - 2LM^8 + LM^6 - M^9\right)\end{aligned}$$

$$\begin{aligned}\gamma_{0/1} = &-L^{-1}M^{-6}(M-1)^{-1}(M+1)^{-1}(L-M)^{-9}(L+M)^{-9}\\
&\left(L^{10}M^2 - L^8M^7 + 3L^8M^5 - 7L^8M^4 - 3L^8M^3 + 3L^8M^2 + L^8M - L^8\right.\\
&- L^6M^{10} + L^6M^9 + 7L^6M^8 - 3L^6M^7 + 3L^6M^6 + 3L^6M^5 + L^6M^4\\
&- L^6M^3 + L^4M^{13} - L^4M^{12} - 3L^4M^{11} - 3L^4M^{10} + 3L^4M^9 - 7L^4M^8\\
&- L^4M^7 + L^4M^6 + L^2M^{16} - L^2M^{15} - 3L^2M^{14} + 3L^2M^{13} + 7L^2M^{12}\\
&\left.-3L^2M^{11} + L^2M^9 - M^{14}\right)\\
&\left(L^{10}M^2 + L^8M^7 - 3L^8M^5 - 7L^8M^4 + 3L^8M^3 + 3L^8M^2 - L^8M - L^8\right.\\
&- L^6M^{10} - L^6M^9 + 7L^6M^8 + 3L^6M^7 + 3L^6M^6 - 3L^6M^5 + L^6M^4\\
&+ L^6M^3 - L^4M^{13} - L^4M^{12} + 3L^4M^{11} - 3L^4M^{10} - 3L^4M^9 - 7L^4M^8\\
&+ L^4M^7 + L^4M^6 + L^2M^{16} + L^2M^{15} - 3L^2M^{14} - 3L^2M^{13} + 7L^2M^{12}\\
&\left.+3L^2M^{11} - L^2M^9 - M^{14}\right)\end{aligned}$$

$$
\begin{aligned}
\gamma_{-1/1} = {} & L^{-2}M^{-8}(M-1)^{-2}(M+1)^{-2}(L-M)^{-12}(L+M)^{-12} \\
& \big(-L^3M^{22} + L^2M^{21} + 5L^3M^{20} + LM^{20} - 2L^4M^{19} - 3L^2M^{19} - M^{19} \\
& - 14L^3M^{18} - LM^{18} + L^6M^{17} + 5L^4M^{17} + 9L^2M^{17} + 2L^7M^{16} \\
& + 6L^5M^{16} + 12L^3M^{16} - 2L^6M^{15} - 18L^4M^{15} - 14L^7M^{14} + 2L^5M^{14} \\
& - 3L^3M^{14} + L^8M^{13} + 20L^6M^{13} - 7L^4M^{13} + L^9M^{12} + 12L^7M^{12} \\
& - 7L^5M^{12} + L^3M^{12} - L^{10}M^{11} - 17L^8M^{11} + 17L^6M^{11} + L^4M^{11} \\
& - L^{11}M^{10} + 7L^9M^{10} - 12L^7M^{10} - L^5M^{10} + 7L^{10}M^9 - 20L^8M^9 \\
& - L^6M^9 + 3L^{11}M^8 - 2L^9M^8 + 14L^7M^8 + 18L^{10}M^7 + 2L^8M^7 \\
& - 12L^{11}M^6 - 6L^9M^6 - 2L^7M^6 - 9L^{12}M^5 - 5L^{10}M^5 - L^8M^5 \\
& + L^{13}M^4 + 14L^{11}M^4 + L^{14}M^3 + 3L^{12}M^3 + 2L^{10}M^3 - L^{13}M^2 \\
& -5L^{11}M^2 - L^{12}M + L^{11}\big)\big(L^3M^{22} + L^2M^{21} - 5L^3M^{20} - LM^{20} \\
& - 2L^4M^{19} - 3L^2M^{19} - M^{19} + 14L^3M^{18} + LM^{18} + L^6M^{17} + 5L^4M^{17} \\
& + 9L^2M^{17} - 2L^7M^{16} - 6L^5M^{16} - 12L^3M^{16} - 2L^6M^{15} - 18L^4M^{15} \\
& + 14L^7M^{14} - 2L^5M^{14} + 3L^3M^{14} + L^8M^{13} + 20L^6M^{13} - 7L^4M^{13} \\
& - L^9M^{12} - 12L^7M^{12} + 7L^5M^{12} - L^3M^{12} - L^{10}M^{11} - 17L^8M^{11} \\
& + 17L^6M^{11} + L^4M^{11} + L^{11}M^{10} - 7L^9M^{10} + 12L^7M^{10} + L^5M^{10} \\
& + 7L^{10}M^9 - 20L^8M^9 - L^6M^9 - 3L^{11}M^8 + 2L^9M^8 - 14L^7M^8 \\
& + 18L^{10}M^7 + 2L^8M^7 + 12L^{11}M^6 + 6L^9M^6 + 2L^7M^6 - 9L^{12}M^5 \\
& - 5L^{10}M^5 - L^8M^5 - L^{13}M^4 - 14L^{11}M^4 + L^{14}M^3 + 3L^{12}M^3 \\
& +2L^{10}M^3 + L^{13}M^2 + 5L^{11}M^2 - L^{12}M - L^{11}\big)
\end{aligned}
$$

$$
\begin{aligned}
\gamma_{1/2} = {} & L^{-2}M^{-11}(M-1)^{-2}(M+1)^{-2}(L-M)^{-17}(L+M)^{-17} \\
& \big(-L^4M^{30} - L^5M^{28} + 7L^4M^{28} + L^3M^{28} + 2L^2M^{28} - L^6M^{26} \\
& + 4L^5M^{26} - 28L^4M^{26} - 3L^3M^{26} - 6L^2M^{26} - LM^{26} - M^{26} \\
& + 3L^8M^{24} + 2L^7M^{24} + 16L^6M^{24} - 13L^5M^{24} + 52L^4M^{24} + 11L^3M^{24} \\
& + 13L^2M^{24} + 2L^9M^{22} - 27L^8M^{22} - L^7M^{22} - 35L^6M^{22} + L^5M^{22} \\
& - 64L^4M^{22} - 2L^3M^{22} + 4L^{10}M^{20} - 16L^9M^{20} + 70L^8M^{20} + 40L^7M^{20} \\
& + 53L^6M^{20} - 27L^5M^{20} - L^4M^{20} + 3L^3M^{20} - 3L^{12}M^{18} - 2L^{11}M^{18} \\
& - 18L^{10}M^{18} - 5L^9M^{18} - 115L^8M^{18} + 10L^7M^{18} + 53L^6M^{18} \\
& - 3L^5M^{18} - L^4M^{18} - L^3M^{18} - L^{13}M^{16} + 23L^{12}M^{16} + 34L^{11}M^{16} \\
& + 41L^{10}M^{16} - 80L^9M^{16} - 25L^8M^{16} + 53L^7M^{16} - 3L^6M^{16} + 3L^5M^{16} \\
& - 3L^{14}M^{14} + 3L^{13}M^{14} - 53L^{12}M^{14} + 25L^{11}M^{14} + 80L^{10}M^{14} \\
& - 41L^9M^{14} - 34L^8M^{14} - 23L^7M^{14} + L^6M^{14} + L^{16}M^{12} + L^{15}M^{12} \\
& + 3L^{14}M^{12} - 53L^{13}M^{12} - 10L^{12}M^{12} + 115L^{11}M^{12} + 5L^{10}M^{12} \\
& + 18L^9M^{12} + 2L^8M^{12} + 3L^7M^{12} - 3L^{16}M^{10} + L^{15}M^{10} + 27L^{14}M^{10} \\
& - 53L^{13}M^{10} - 40L^{12}M^{10} - 70L^{11}M^{10} + 16L^{10}M^{10} - 4L^9M^{10} \\
& + 2L^{16}M^8 + 64L^{15}M^8 - L^{14}M^8 + 35L^{13}M^8 + L^{12}M^8 + 27L^{11}M^8 \\
& - 2L^{10}M^8 - 13L^{17}M^6 - 11L^{16}M^6 - 52L^{15}M^6 + 13L^{14}M^6 - 16L^{13}M^6 \\
& - 2L^{12}M^6 - 3L^{11}M^6 + L^{19}M^4 + L^{18}M^4 + 6L^{17}M^4 + 3L^{16}M^4 \\
& + 28L^{15}M^4 - 4L^{14}M^4 + L^{13}M^4 - 2L^{17}M^2 - L^{16}M^2 - 7L^{15}M^2 \\
& + L^{14}M^2 + L^{15}\big)\big(L^4M^{30} - L^5M^{28} - 7L^4M^{28} + L^3M^{28} - 2L^2M^{28} \\
& + L^6M^{26} + 4L^5M^{26} + 28L^4M^{26} - 3L^3M^{26} + 6L^2M^{26} - LM^{26} + M^{26} \\
& - 3L^8M^{24} + 2L^7M^{24} - 16L^6M^{24} - 13L^5M^{24} - 52L^4M^{24} + 11L^3M^{24} \\
& - 13L^2M^{24} + 2L^9M^{22} + 27L^8M^{22} - L^7M^{22} + 35L^6M^{22} + L^5M^{22} \\
& + 64L^4M^{22} - 2L^3M^{22} - 4L^{10}M^{20} - 16L^9M^{20} - 70L^8M^{20} + 40L^7M^{20} \\
& - 53L^6M^{20} - 27L^5M^{20} + L^4M^{20} + 3L^3M^{20} + 3L^{12}M^{18} - 2L^{11}M^{18} \\
& + 18L^{10}M^{18} - 5L^9M^{18} + 115L^8M^{18} + 10L^7M^{18} - 53L^6M^{18} \\
& - 3L^5M^{18} + L^4M^{18} - L^3M^{18} - L^{13}M^{16} - 23L^{12}M^{16} + 34L^{11}M^{16} \\
& - 41L^{10}M^{16} - 80L^9M^{16} + 25L^8M^{16} + 53L^7M^{16} + 3L^6M^{16} + 3L^5M^{16} \\
& + 3L^{14}M^{14} + 3L^{13}M^{14} + 53L^{12}M^{14} + 25L^{11}M^{14} - 80L^{10}M^{14} \\
& - 41L^9M^{14} + 34L^8M^{14} - 23L^7M^{14} - L^6M^{14} - L^{16}M^{12} + L^{15}M^{12} \\
& - 3L^{14}M^{12} - 53L^{13}M^{12} + 10L^{12}M^{12} + 115L^{11}M^{12} - 5L^{10}M^{12} \\
& + 18L^9M^{12} - 2L^8M^{12} + 3L^7M^{12} + 3L^{16}M^{10} + L^{15}M^{10} - 27L^{14}M^{10} \\
& - 53L^{13}M^{10} + 40L^{12}M^{10} - 70L^{11}M^{10} - 16L^{10}M^{10} - 4L^9M^{10} \\
& - 2L^{16}M^8 + 64L^{15}M^8 + L^{14}M^8 + 35L^{13}M^8 - L^{12}M^8 + 27L^{11}M^8 \\
& + 2L^{10}M^8 - 13L^{17}M^6 + 11L^{16}M^6 - 52L^{15}M^6 - 13L^{14}M^6 \\
& - 16L^{13}M^6 + 2L^{12}M^6 - 3L^{11}M^6 + L^{19}M^4 - L^{18}M^4 + 6L^{17}M^4 \\
& - 3L^{16}M^4 + 28L^{15}M^4 + 4L^{14}M^4 + L^{13}M^4 - 2L^{17}M^2 + L^{16}M^2 \\
& - 7L^{15}M^2 - L^{14}M^2 + L^{15}\big)
\end{aligned}
$$